Search for Neutral Higgs Bosons in e^+e^- Collisions

D I S S E R T A T I O N

zur Erlangung des akademischen Grades
doctor rerum naturalium
(dr. rer. nat.)
im Fach Physik

eingereicht an der
Mathematisch-Naturwissenschaftlichen Fakultät I
Humboldt-Universität zu Berlin

von
Herr Dipl.-Phys. Alexei Raspereza
geboren am 7.12.1972 in Brest, Weissrussland

Präsident der Humboldt-Universität zu Berlin:
Prof. Dr. J. Mlynek

Dekan der Mathematisch-Naturwissenschaftlichen Fakultät I:
Prof. Dr. Ronacher

Gutachter:

1. Prof. Dr. Eva-Maria Kabuss
2. Prof. Dr. Thomas Hebbeker
3. Prof. Dr. Peter Zerwas

eingereicht am:	30. März 2002
Tag der mündlichen Prüfung:	12. Juli 2002

Abstract

This thesis is devoted to the search for neutral Higgs bosons predicted by various theoretical models. The Higgs boson arises as a result of spontaneous breaking of SU(2) symmetry leading to the generation of masses of fermions and weak bosons. The search is done in all experimentally related channels using the data collected at center-of-mass energies $\sqrt{s}$ up to 209 GeV in the years 1998-2000 with the L3 detector at the Large Electron Positron collider, LEP. Here the study of the final states characterised by four jets is described in detail. For other final states the analyses are briefly reviewed and the results are reported. The data are compared with the expectation from the Standard Model background processes and with various signal hypotheses. A model independent search for neutral Higgs bosons is also performed. No evidence for the production of Higgs bosons is found. New mass limits are determined superseding previous mass limits established by L3 and other experiments.

First I describe the analysis searching for the Standard Model Higgs Boson. Its production at LEP is expected mainly via the Higgs-strahlung process, $e^+e^- \to Z^* \to HZ$. In the mass range accessible at LEP the Standard Model Higgs Boson is predicted to decay dominantly into a pair of b and anti-b quarks, hence the dedicated analyses are optimised for the $H \to b\bar{b}$ decay mode. The $HZ \to q\bar{q}q\bar{q}$ channel is investigated and then combined with the $HZ \to q\bar{q}\nu\bar{\nu}$, $HZ \to q\bar{q}\ell^+\ell^-(\ell = e, \mu, \tau)$ and $HZ \to \tau^+\tau^-q\bar{q}$ channels leading to a lower mass limit of

$$m_H > 112.0 \text{ GeV}$$

at 95 % C.L.. The results of the search are also interpreted in terms of limits on the HZZ coupling.

In the Minimal Supersymmetric Standard Model (MSSM) the Higgs sector is extended to five physical states. The Higgs-strahlung process $e^+e^- \to hZ$ is complemented by the mechanism of the Higgs boson pair production $e^+e^- \to hA$. Therefore, for the interpretation of the results in the framework of the MSSM the Standard Model analyses are combined with the $hA \to b\bar{b}\tau^+\tau^-$ ($hA \to \tau^+\tau^-b\bar{b}$), $hA \to b\bar{b}b\bar{b}$ and $hZ \to AAq\bar{q}$ channels. Three benchmark MSSM scenarios denoted "$m_h - max$", "no mixing" and "large-μ" are considered. Using L3 data the lower bounds on the Higgs boson masses

$$m_h > 84.5 \text{ GeV}, \qquad m_A > 86.3 \text{ GeV}$$

are derived at 95 % C.L. for tanβ >0.7. For the "m_h − max", "no mixing" and "large-μ" scenarios, ranges $0.55 \leq \tan\beta \leq 2.2$, $0.4 \leq \tan\beta \leq 4.9$ and $0.7 \leq \tan\beta \leq 6.2$, respectively, are ruled out.

A model independent search for the $e^+e^- \to hZ$ process with subsequent decay of h into hadrons is carried out in the four-jet channel. The results of the analysis are then combined with the $hZ \to q\bar{q}\nu\bar{\nu}$ and $hZ \to q\bar{q}\ell^+\ell^-(\ell = e, \mu, \tau)$ channels. A limit on the hZZ coupling as a function of the Higgs boson mass is derived. The results of L3 combined search establish a 95% C.L. lower mass limit

$$m_h > 97 \text{ GeV}$$

for a hadronically decaying Higgs boson assuming the cross section of the $e^+e^- \to hZ$ process to be equal to the value predicted by the Standard Model and the branching fraction of the Higgs boson into hadrons equal to 100%.

Analyses are developed to search exclusively for the $hA \to b\bar{b}b\bar{b}$, $hA \to q\bar{q}q'\bar{q}'$, $hA \to b\bar{b}\tau^+\tau^-$ and $hA \to q\bar{q}\tau^+\tau^-$ final states. Results of these analyses are translated into a 95 % C.L. upper limit on the hAZ coupling as a function of Higgs boson masses.

Searches for neutral Higgs bosons carried out by the L3 collaboration are combined with searches performed in other LEP experiments. The results of this combination are reported.

The perspectives of Higgs boson searches at TEVATRON and LHC are briefly reviewed.

The prospects of Higgs physics at a future linear e^+e^- collider are discussed. The potential of the TESLA detector foreseen at the TESLA linear collider for the determination of Higgs boson properties is studied. The Higgs boson masses m_H = 120, 150 and 180 GeV are considered. It is shown that a precision of 40 - 70 MeV in the measurement of the Higgs boson mass can be achieved. A model independent method to measure the $e^+e^- \to HZ$ cross section is proposed. The method is based on the study of the inclusive $HZ \to X\ell^+\ell^-(\ell = e, \mu)$ channels. The relative error in the determination of the cross section varies between 2.6% and 3.8% for m_H ranging from 120 GeV to 180 GeV. For the four-fermion and six-fermion final states arising from the $e^+e^- \to HZ$ process the accuracy of the measurement of a topological cross section defined as the product of the $e^+e^- \to HZ$ cross section and the branching fraction of the specific final state is investigated. The relative uncertainty of this measurement varies from 1.1% for the $HZ \to b\bar{b}q\bar{q}$ channel at m_H = 120 GeV to 13.0% for the $HZ \to W^+W^-\ell^+\ell^-(\ell = e, \mu; W \to q\bar{q}')$ channel at m_H = 120 GeV. These and other measurements will allow to determine the profile of the Higgs boson and give insight into the structure of the Higgs sector in nature.

Keywords:
Standard Model, Higgs bosons, Minimal Supersymmetric Standard Model, Searches

Zusammenfassung

Diese Arbeit beschreibt die Suche nach dem Higgs Boson, welches in vielen theoretischen Modellen der Teilchenphysik vorhergesagt wird. Das Higgs Boson ist die Konsequenz der spontanen Symmetriebrechung, welche den Teilchen Masse verleiht. Zur Suche werden e^+e^- Annihilationen bei Schwerpunktenergien bis 209 GeV analysiert, welche vom Experiment L3 am Speicherring LEP in den Jahren 1998 bis 2000 registriert wurden. Die Suche erfolgte in allen relevanten Endzuständen, wobei der Endzustand mit vier hadronischen Jets im Detail behandelt wird.

Die Daten werden mit den Erwartungen eines Signals in verschiedenen Modellen bei Berücksichtigung der bekannten Untergrundprozesse verglichen oder es wird modellunabhängig nach der Erzeugung skalarer Teilchen gesucht.

Die Produktion von Higgs Bosonen konnte nicht nachgewiesen werde. Die Daten wurden daher benutzt, um neue Grenzen für Parameter der Modelle oder der Kopplungen zu setzen.

Als erstes wird die Suche nach dem Higgs Boson im Standard Modell der elektroschwachen Wechselwirkung beschrieben. Die Produktion des Higgs Bosons wird bei LEP Energien über die Higgs-Strahlung, $e^+e^- \to Z^* \to HZ$, und der Zerfall des Higgs Bosons in ein Paar von b-Quarks, $H \to b\bar{b}$, vorhergesagt. Die Analysen beruhen daher wesentlich auf der Erkennung von B-Hadronen. Der $HZ \to q\bar{q}q\bar{q}$ Endzustand wird im Detail untersucht, und die Ergebnisse werden mit den anderen Kanälen $HZ \to q\bar{q}\nu\bar{\nu}$, $HZ \to q\bar{q}\ell^+\ell^-(\ell = e, \mu, \tau)$ and $HZ \to \tau^+\tau^- q\bar{q}$ kombiniert. Die untere Massengrenze für das Higgs Boson wird zu

$$m_H > 112.0 \text{ GeV},$$

auf 95% Vertrauensniveau, bestimmt. Ausserdem werden Grenzen auf die HZZ Kopplung abgeleitet.

Im minimalen supersymmetrischen Modell (MSSM) werden fünf Higgs Bosonen vorhergesagt. Zur Higgs-Strahlung kommt die Paarproduktion von Higgs Bosonen, $e^+e^- \to hA$, hinzu. Die Ergebnisse der Suche im Standard Modell werden durch die Suche in den Endzuständen $hA \to b\bar{b}\tau^+\tau^-$ ($hA \to \tau^+\tau^- b\bar{b}$), $hA \to b\bar{b}b\bar{b}$ und $hZ \to AAq\bar{q}$ ergänzt. Im Rahmen von drei Standard-Szenarien, benannt als "$m_h - max$", "no mixing" und "large-μ" werden untere Grenzen auf die Higgs Boson Massen von

$$m_h > 84.5 \text{ GeV}, \qquad m_A > 86.3 \text{ GeV}$$

für tanβ >0.7 abgeleitet. Weiterhin werden im "$m_h - max$" Szenario $0.55 \leq \tan\beta \leq 2.2$, im "no mixing" Szenario $0.4 \leq \tan\beta \leq 4.9$ und im "large-μ" Szenario $0.7 \leq \tan\beta \leq 6.2$ ausgeschlossen.

Eine modellunabhängige Suche nach dem Prozess $e^+e^- \to hZ$ wird für den vier-Jet Endzustand durchgeführt. In Kombination mit den Ergebnissen von den anderen Kanälen, $hZ \to q\bar{q}\nu\bar{\nu}$ und $hZ \to q\bar{q}\ell^+\ell^-(\ell = e, \mu, \tau)$, werden Grenzen für die hZZ Kopplung bestimmt. Wird die hZZ Kopplung auf den Wert im Standard Modell gesetzt und der Zerfall des Higgs Bosons zu 100% in Hadronen angenommen, ergibt sich als Grenze der Higgs Boson Masse

$$m_h > 97 \text{ GeV}.$$

Modellunabhängige obere Grenzen für die hAZ Kopplung werden aus der Suche nach der Paarerzeugung von Higgs Bosonen in $hA \to q\bar{q}q'\bar{q}'$, $hA \to b\bar{b}\tau^+\tau^-$ und $hA \to q\bar{q}\tau^+\tau^-$ in Abhängigkeit von den Higgs Boson Massen abgeleitet.

Die Resultate aus der Kombination aller LEP Experimente werden für die oben genannten Analysen vorgestellt.

Die Perspektiven der Higgs Boson Suche an den TEVATRON und LHC Speicherringen werden diskutiert und die Higgs Boson Physik an künftigen e^+e^- Linearbeschleunigern behandelt. Ein Linearbeschleuniger wie TESLA wäre ideal für Untersuchungen eines leichten Higgs Bosons. Für ein Higgs Boson mit einer Masse zwischen 120 und 180 GeV kann m_H mit einer Präzision von 40 bis 70 MeV bestimmt werden. Im gleichen Massenbereich ist die Messung des Wirkungsquerschnitts, weitgehend modellunabhängig, mit einem relativen Fehler von 2.6 bis 3.8 % möglich. In vier-Fermion und sechs-Fermion Endzuständen werden topologische Wirkungsquerschnitte, definiert als Produkt des totalen Wirkungsquerschnitts für $e^+e^- \to HZ$ mit dem Verzweigungsverhältnis eines Zerfallskanals, untersucht. Für den Messfehler werden 1.1% für $HZ \to b\bar{b}q\bar{q}$ und 13% für $HZ \to W^+W^-\ell^+\ell^-(\ell = e, \mu; W \to q\bar{q}')$ bei $m_H = 120$ GeV abgeschätzt. Die Gesamtheit dieser und weiterer Messungen erlaubt eine genaue Bestimmung des Higgs Boson Profils und gibt Aufschluss über die Struktur des Higgs Sektors in der Natur.

Schlagwörter:
Standardmodell, Higgs Bosonen, Minimales Supersymmetrisches Standardmodell, Suchen

Contents

List of Figures

List of Tables

Chapter 1

Introduction

Particle physics attempts to describe the universe in terms of fundamental constituents and interactions between them. Over the past few decades physicists made an impressive breakthrough in understanding the structure of matter and basic principles governing the fundamental laws of nature. The accumulation of extensive knowledge in the field of particle physics wouldn't be possible without the complementarity of theoretical and experimental studies. Various theories have been developed to describe the physics phenomena observed at experiments and to make suggestions on further experimental investigations. The experiments either verify the validity of the theoretical models or rise new questions and problems that have to be tackled by theoreticians. Deeper understanding of the fundamental particles can be achieved by investigating their interactions at very high energies. Experiments carried out at particle accelerators provide an excellent opportunity for such investigations. One of these accelerators is the Large Electron Positron Collider (LEP) at the European Laboratory for Particle Physics (CERN, Geneva).

Nowadays, a theory called Standard Model (SM) [1] almost perfectly describes the experimental observations made at LEP and other particle accelerators. It postulates as the fundamental constituents of matter fermions (spin-1/2 particles) interacting with each other via gauge bosons (spin-1 particles). Fermions, classified into quarks and leptons, appear in three families and undergo four distinct interactions which differ by strength and by distance at which these interactions manifest themselves. These are strong, electromagnetic, weak and gravitational interactions. The existence of gauge bosons logically follows from the principle of gauge invariance. The SM is invariant under the $U(1)_Y \otimes SU(2)_L \otimes SU(3)_C$ gauge group. The $U(1)_Q$ group of the electromagnetism is a subgroup of $U(1)_Y \otimes SU(2)_L$. Electromagnetic forces are mediated by massless gauge bosons called photons. They are described within the framework of a theory called Quantum Electrodynamics (QED). The SU(2) gauge group is associated with weak interactions. Massive W and Z bosons play here the role of weak force carriers. Finally, the SU(3) group represents the sector of strong interactions described by Quantum Chromodynamics (QCD). Only quarks are "sensitive" to strong forces mediated by gluons.

The SM has been very successful in accounting for various experimental observations as well as in its predictions of new phenomena. One of the striking successes of the SM is

the discovery of W and Z bosons made at CERN's proton-antiproton collider in 1983 [4]. Another examples of experimental validation of the SM are the observation of gluons in 1979 at the PETRA e^+e^- collider (DESY, Hamburg) [6] and the discovery of the top quark, the heaviest fermion predicted by the SM, at the TEVATRON proton-antiproton collider (Fermilab, Batavia) in 1995 [7].

In fact, the gauge symmetry of the SM forbids masses for all particles. However from experiment we know that only gluons, the photon and perhaps neutrinos[1] are massless. All other particles are massive. To overcome this inconsistency between experimental observations and the requirement of the gauge invariance the Higgs mechanism [9] is invented allowing for the generation of particle masses and keeping the gauge invariance. One scalar Higgs doublet is introduced and its vacuum expectation value ν breaks the SU(2) symmetry. The masses of quarks, leptons and weak gauge bosons are proportional to ν. The Higgs mechanism gives rise to one more particle - the Higgs boson. This particle has been so far elusive for experimental detection.

One Higgs doublet is the minimum which is required to generate fermion and boson masses. There are extensions of the minimal SM postulating additional Higgs multiplets. Two Higgs doublet models (2HDM) [12] are particularly attractive since two Higgs doublets are required in the Minimal Supersymmetric Standard Model, a more general theory than the SM. In the 2HDM after spontaneous symmetry breaking five Higgs particles arise: two neutral CP-even Higgs bosons, h and H; one neutral CP-odd Higgs boson A and two charged Higgs bosons $H^{\pm}$.

It should be noted that the SM doesn't deny the previously developed less general theories but rather logically includes them into the framework of a more general model. Previous theories are just particular cases having their own "windows" of applicability. Moreover, there are strong conceptual indications that the SM itself is not a complete self-consistent theory and in its turn represents a particular case, applicable only within a limited energy scale, of a more general theory. The inability of the SM to accommodate in a consistent way quantum gravity is one of these indications. The SM is characterised by nineteen arbitrary parameters. In the ultimate theory these parameters should not appear as totally free and there should be a way to understand their values. Three gauge couplings defining the strength of the electromagnetic, weak and strong interactions are slowly-varying functions of the energy scale. They are found to point towards unification at scales of energy $M_{GUT} \sim 10^{14}$-10^{16} GeV (Grand Unification Theories: GUTs). The idea of grand unification is too attractive to be ignored. It provides the basis for understanding of the common origin of the electromagnetic, weak and strong interactions and for establishing relations between different parameters of the SM. But there are a few obstacles on the way to the unification of gauge interactions. First, the attempt to incorporate the SM in a more general theory unifying interactions at large energy scales inevitably encounters the so-called "hierarchy problem" [13] - a problem related to the presence of fundamental scalar fields with quadratic mass divergences. Second, when the evolution of gauge couplings is calculated from the low-energy to high-energy scale only with the particle content of the SM unification doesn't occur in a single point.

[1] Recent non-accelerator observations suggest that there are oscillations between neutrinos belonging to different families. Such oscillations imply the difference in mass for neutrinos of different families [8].

One of the most attractive extensions of the SM where the problems mentioned are solved in a consistent way is Supersymmetry (SUSY) [15]. It establishes the symmetry between bosons and fermions. The Minimal Supersymmetric extension of the Standard Model (MSSM) [16] doubles the number of elementary particles by assigning for each SM particle a partner called sparticle that differs only in spin by half a unit. In the MSSM the Higgs sector comprises two doublets and is characterised by five physical states which are identical to those in the general 2HDM.

Over the past decade searches for Higgs bosons of different theoretical models have been carried out at the TEVATRON and LEP. From 1989 until 1995 LEP operated at center-of-mass energies close to the Z-resonance and the data collected during this period by the LEP experiments - ALEPH, DELPHI, L3 and OPAL - were used to verify the SM and to search for new particles including Higgs bosons. In 1995 the second phase of LEP operation (LEP2) started. The energy of colliding electron and positron beams was gradually increasing thus expanding the kinematic domain for Higgs searches. In the year 2000 LEP has been pushed to the limit of its performance resulting to the extension of the center-of-mass energy range up to 209 GeV. The L3 detector collected during the year 2000 more than 200 pb^{-1} of data at center-of-mass energies between 200 and 209 GeV.

The searches for neutral Higgs bosons of various theoretical models with the L3 detector at the highest energies attained by LEP frame the main theme of this thesis. Although the author of this thesis analysed also the data collected in the years 1998 and 1999 at center-of-mass energies between 189 GeV and 202 GeV, this thesis is mainly based on the results obtained from the data of the year 2000. The combination of Higgs searches performed by the four LEP collaborations essentially improves the search sensitivity. The results of LEP combined searches for neutral Higgs bosons are reported in this thesis.

Higgs searches remain one of the most important parts of the scientific program at TEVATRON. The Large Hadron Collider (LHC), the successor of LEP at CERN, is expected to be brought into operation in the year 2006. This machine will provide another opportunity for the discovery of Higgs bosons.

Once the Higgs boson is found, the accurate determination of its profile will become of immediate concern. A linear $\mathrm{e}^+\mathrm{e}^-$ collider perfectly suits for this task. The TESLA[2] project [19] recently worked out at DESY is one of the attempts to design and construct a linear $\mathrm{e}^+\mathrm{e}^-$ collider and a corresponding detector. I complemented this thesis with studies of the potential of the TESLA detector for the precise determination of the SM Higgs boson properties.

[2] The abbreviation TESLA stands for Tera electronvolt Electron-positron Superconducting Linear Accelerator

Chapter 2

Concepts of Particle Physics

The development of the extensive knowledge in the field of particle physics wouldn't be possible without complementarity of theoretical and experimental investigations.

Theoretical physics is the discipline which tries to understand and explain accumulated empirical information, to associate experimentally established laws of nature with fundamental principles, to classify physical objects and interactions between them, to draw conclusions and to make predictions which can be tested by experiments. From theoretical point of view the value of a theory is determined by its simplicity, i.e. by the minimal number of fundamental principles (basic assumptions) necessary to explain the variety of physical phenomena observed in the nature.

To understand the relation between fundamental principles and physical laws let us consider one example. An elegant idea was proposed by the theoretician Emmy Noether known as Noether's theorem. It states that well-known conservation laws result from the symmetries existing in the nature. For instance, the conservation of momentum of a freely propagating particle logically follows from the symmetry under space translation. In other words, the laws of motion shouldn't change if we translate objects in space. Similarly, the conservation of energy results from the time-translation symmetry. The example given above demonstrates how the fundamental principle of space-time symmetry explains the momentum-energy conservation.

From the experimental point of view the value of a theory is determined on how accurately it describes experimental data. But the role of the theories is not restricted by only the explanation of experimentally observed phenomena. Experimenters expect from theoreticians further predictions and suggestions which could drive experimental research in the right direction. In this sense the value of a theory is defined also by its potential to predict new interesting phenomena which can be experimentally verified.

This chapter is dedicated to the discussion of the main theoretical concepts of the particle physics.

2.1 The Minimal Standard Model

The minimal theory which describes best the phenomena observed so far in the world of elementary particles is called the Standard Model (SM) [1]. It is the quantum field the-

ory of strong, electromagnetic and weak interactions. Based on the fundamental idea of gauge symmetry, the SM has successfully passed many tests made at LEP and other particle accelerators. The SM is based on the gauge group $U(1)_Y \otimes SU(2)_L \otimes SU(3)_C$. The $U(1)_Q$ group of electromagnetism appears in the SM as a subgroup of $U(1)_Y \otimes SU(2)_L$ and in this sense electromagnetic and weak forces are unified. Strong interactions are described by a theory called Quantum Chromodynamics (QCD). The latter is invariant under the $SU(3)_C$ gauge group.

2.1.1 Symmetry and Gauge Invariance

One of the fundamental ideas forming the conceptual basis of the SM is the principle of gauge invariance. The realisation of this principle in the SM naturally introduces the interaction between fermions (spin 1/2 particles) through exchange by gauge bosons (spin 1 particles).

Let us consider this principle in detail using as an example QED, the theory describing electromagnetic interactions. In a quantum field theory particles are represented as fields $\Psi(\tilde{x}, t)$ in space and time. QED postulates that phase transformation

$$\Psi(\tilde{x}, t) \rightarrow \Psi'(\tilde{x}, t) = e^{i\chi(\tilde{x},t)}\Psi(\tilde{x}, t), \tag{2.1}$$

denoted as a local gauge transformation, must not affect the evolution equation for physical objects. In other words, the Lagrangian, the mathematical object describing the evolution of a fermion field, must remain unchanged under a local gauge transformation. However, if we consider the Lagrangian of a free fermion with mass m

$$\mathcal{L} = i\bar{\Psi}\gamma^\mu\partial_\mu\Psi - m\bar{\Psi}\Psi, \tag{2.2}$$

we realise that it is not invariant under a local gauge transformation given by Equation (2.1). To fulfil the requirement of gauge invariance one must rewrite the derivative by introducing vector gauge field A_μ

$$D_\mu \equiv \partial_\mu - ieA_\mu. \tag{2.3}$$

Defining the gauge transformation for A_μ as

$$A_\mu \rightarrow A_\mu + \frac{1}{e}\partial_\mu\chi, \tag{2.4}$$

one obtains a new Lagrangian

$$\mathcal{L} = i\bar{\Psi}\gamma^\mu D_\mu\Psi - m\bar{\Psi}\Psi, \tag{2.5}$$

which has the desired invariance under a transformation given by Equation (2.1). The requirement of a local gauge invariance has lead to the introduction of a vector field A_μ which can be associated to the photon. Adding the kinetic term for the photon field we obtain the final Lagrangian of QED:

$$\mathcal{L} = \bar{\Psi}(i\gamma^\mu\partial_\mu - m)\Psi + e\bar{\Psi}\gamma^\mu A_\mu\Psi - \frac{1}{4}F_{\mu\nu}F^{\mu\nu}. \tag{2.6}$$

Note that the total QED Lagrangian doesn't contain a gauge boson mass term of type $m_\gamma^2 A_\mu A^\mu$. The appearance of such a term in the Lagrangian would inevitably break the gauge invariance of the theory since the transformation rules (2.4) result into:

$$A_\mu A^\mu \to A_\mu A^\mu + \frac{2}{e} A^\mu \partial_\mu \chi + \frac{1}{e^2} \partial_\mu \chi \partial^\mu \chi. \tag{2.7}$$

Fortunately there is no need to introduce a gauge boson mass term in the QED Lagrangian since experimental physics suggests that photon is massless. A completely different situation occurs in the weak sector of the SM where the gauge bosons Z and W are massive.

2.1.2 Particles and Lagrangian in the Standard Model

The spectrum of particles in the SM comprises fermions which are matter constituents and gauge bosons which play the role of force carriers between fermions. Fermions are classified into quarks, participating both in strong and electroweak interactions, and leptons, undergoing only electroweak interactions. Quarks and leptons appear in three families. The u and d quarks, constituents of the proton and neutron, the electron and neutrino, emitted in β decays of atomic nuclei, form the first family of fermions. Quarks and charged leptons of the second and third family are unstable and decay weakly either into fermions of "lower" families (weak decays of quarks belonging to the second and third families) or into fermions of "lower" families and the neutrino of the same family (decays of muons and τ-leptons).

The electroweak sector of the Standard Model is based on the $U(1)_Y \otimes SU(2)_L$ gauge group generated by the hypercharge Y and the weak isospin $\tilde{T}$. The latter is expressed in terms of Pauli matrices $\tilde{\sigma}$ as:

$$\tilde{T} = \frac{1}{2} \tilde{\sigma} \tag{2.8}$$

The hypercharge and the third component of the isospin, T_3, are related to the electromagnetic charge in the following way:

$$Q = Y + T_3. \tag{2.9}$$

Each fermion family is made of five different representations of the Standard Model gauge group:

$$Q_L^i(2,3)^w_{+1/6}, \quad L_L^i(2,1)^w_{-1/2}, \quad u_R^i(1,3)^w_{+2/3}, \quad d_R^i(1,3)^w_{-1/3}, \quad \ell_R^i(1,1)^w_{-1}. \tag{2.10}$$

The notation means that, for example, the left-handed up- and down-type quarks of the i-th family, Q_L^i, form a doublet (2) of the $SU(2)_L$ group, carry hypercharge $+1/6$ and are in a triplet (3) under the $SU(3)_C$ group of strong interactions discussed in this section later on. The symbol L_L^i stands for the isospin doublet composed of the left-handed charged lepton ℓ_L^i and the neutrino ν_L^i. The symbols u_R^i, d_R^i, ℓ_R^i stand for the right-handed up- and down-type quarks and the right-handed charged leptons. The right-handed fermions are singlets under the $SU(2)_L$ group. The index "w" indicates weak interaction eigenstates. It should be noted that physical (mass) eigenstates of down-type quarks, $d_L^{i\prime}$,

are related to weak eigenstates, d_L^{iw}, through the Cabibbo-Kobayashi-Maskawa (CKM) mixing matrix [20]:

$$d_L^{iw} = \sum_{j=1}^{3} V_{CKM}^{ij} d_L^{j'}. \tag{2.11}$$

As one can see from (2.10) left-handed fermions form weak isospin doublets while right-handed are transformed under the same group as singlets. As we'll see later placing right-handed and left-handed fermions into different multiplets of the $SU(2)_L$ group is dictated by the necessity to accommodate parity violation within the framework of the SM. The properties of fermions are summarised in Table 2.1.

	Family					
	1	2	3	T_3	Y	Q
Leptons	$\begin{pmatrix} \nu_e \\ e \end{pmatrix}_L$	$\begin{pmatrix} \nu_\mu \\ \mu \end{pmatrix}_L$	$\begin{pmatrix} \nu_\tau \\ \tau \end{pmatrix}_L$	$1/2$ $-1/2$	$-1/2$ $-1/2$	0 -1
	e_R	μ_R	τ_R	0	-1	-1
Quarks	$\begin{pmatrix} u \\ d' \end{pmatrix}_L$	$\begin{pmatrix} c \\ s' \end{pmatrix}_L$	$\begin{pmatrix} t \\ b' \end{pmatrix}_L$	$1/2$ $-1/2$	$1/6$ $1/6$	$2/3$ $-1/3$
	u_R	c_R	t_R	0	$2/3$	$2/3$
	d_R	s_R	b_R	0	$-1/3$	$-1/3$

Table 2.1: Multiplet and quantum number assignments for the fermions in the Standard Model. The prime indicates that the weak eigenstates of the quarks are not their mass eigenstates. The quark mixing is described by the Cabibbo-Kobayashi-Maskawa (CKM) matrix. The indices $L(R)$ denote left(right)-handed fermions.

The requirement of $U(1)_Y \otimes SU(2)_L$ gauge invariance naturally leads to the introduction of four gauge boson fields. One of them, B_μ, is associated with the hypercharge Y and three others, W_μ^i (i=1..3), with the weak isospin $\tilde{T}$. The Lorentz derivative ∂_μ for the fermion field must be replaced by a covariant derivative which in case of $U(1)_Y \otimes SU(2)_L$ gauge symmetry reads:

$$D_\mu = \partial_\mu - ig_1 Y B_\mu - ig_2 \tilde{T} \cdot \tilde{W}_\mu. \tag{2.12}$$

The g_1 and g_2 are $U(1)_Y$ and $SU(2)_L$ coupling constants, respectively. With introducing the covariant derivative the part of the Lagrangian describing massless fermion fields and their interactions with gauge fields acquires the form:

$$i\sum_f \bar{\Psi}\gamma^\mu D_\mu \Psi = i\sum_f \bar{\Psi}\gamma^\mu \partial_\mu \Psi + g_1 Y \sum_f \bar{\Psi}\gamma^\mu \Psi B_\mu + g_2 \sum_f \bar{\Psi}_L \gamma^\mu \tilde{T} \cdot \tilde{W}_\mu \Psi_L. \tag{2.13}$$

Now we can rotate the weak bosons to the physical basis which contains two charged bosons $W_\mu^\pm$, a neutral boson Z_μ and the photon A_μ. The relations transforming interaction eigenstates of gauge bosons to their physical eigenstates read:

$$W^\pm = \frac{1}{\sqrt{2}}(W^1 \pm iW^2), \tag{2.14}$$

$$\begin{pmatrix} \mathrm{Z} \\ \mathrm{A} \end{pmatrix} = \begin{pmatrix} \cos\theta_\mathrm{w} & -\sin\theta_\mathrm{w} \\ \sin\theta_\mathrm{w} & \cos\theta_\mathrm{w} \end{pmatrix} \begin{pmatrix} \mathrm{W}^3 \\ \mathrm{B} \end{pmatrix}, \tag{2.15}$$

with θ_w denoting the mixing angle in the neutral weak boson sector. It is expressed in terms of coupling constants as:

$$\cos\theta_\mathrm{w} = \frac{\mathrm{g_1}}{\sqrt{\mathrm{g_1^2} + \mathrm{g_2^2}}}. \tag{2.16}$$

Interaction	Boson	Q	m
Electromagnetic	γ	0	0
Weak	W	±1	80.4 GeV
	Z	0	91.2 GeV
Strong	g	0	0

Table 2.2: Gauge bosons of the Standard Model. Electromagnetic charge is given in units of positron charge.

After transforming weak bosons to the physical basis the Lagrangian (2.13) acquires the form where all known electroweak interactions between fermions and bosons are represented by separate terms:

$$\begin{aligned}
\mathcal{L}_\mathrm{f} = \quad & \mathrm{i}\textstyle\sum_\mathrm{f} \bar{\Psi}\gamma^\mu\partial\mu\Psi && \textit{free fermions} \\
& -\mathrm{e}\textstyle\sum_\mathrm{f} \mathrm{Q_f}\bar{\Psi}\gamma^\mu\Psi\mathrm{A}^\mu && \textit{electromagnetic interactions} \\
& -\tfrac{\mathrm{g_2}}{2\cos\theta_\mathrm{w}}\textstyle\sum_\mathrm{f} \bar{\Psi}\gamma_\mu(\mathrm{g_V} - \mathrm{g_A}\gamma_5)\Psi\mathrm{Z}^\mu && \textit{weak neutral-current interactions} \\
& -\tfrac{\mathrm{g_2}}{\sqrt{2}}\textstyle\sum_\mathrm{f} \bar{\Psi}_\mathrm{L}\gamma_\mu(\sigma_+\mathrm{W}^{\mu+} + \sigma_-\mathrm{W}^{\mu-})\Psi_\mathrm{L} && \textit{weak charged-current interactions}
\end{aligned}$$

In these relations $\mathrm{Q_f}$ denotes fermion electromagnetic charges, $\mathrm{g_V} = \mathrm{T_f^3} - 2\mathrm{Q_f}\sin^2\theta_\mathrm{w}$ and $\mathrm{g_A} = \mathrm{T_f^3}$ are coupling constants corresponding to the parts of the neutral-current which transform like vector and axial vector, respectively. The matrices $\sigma_\pm = \frac{1}{2}(\sigma_1 \pm \mathrm{i}\sigma_2)$ realise the transitions between up-type and down-type fermions which occur in the weak charged-current interactions like, for instance, the decay of neutron: $\mathrm{n} \to \mathrm{p}^+ + \mathrm{e}^- + \bar{\nu}_\mathrm{e}$.

Note that by placing left-handed fermions into $\mathrm{SU(2)_L}$ doublets and right-handed fermions into $\mathrm{SU(2)_L}$ singlets we managed to accommodate parity violation. The weak charged-current interactions include only left-handed fermion fields.

The total electroweak Lagrangian includes also the gauge boson kinetic and self-interaction terms as expected in the non-abelian $\mathrm{SU(2)_L}$ group:

$$\mathcal{L}_\mathrm{G} = -\frac{1}{4}\tilde{\mathrm{W}}_{\mu\nu}\tilde{\mathrm{W}}^{\mu\nu} - \frac{1}{4}\mathrm{B}_{\mu\nu}\mathrm{B}^{\mu\nu}, \tag{2.17}$$

where

$$\tilde{W}_{\mu\nu} = \partial_\mu \tilde{W}_\nu - \partial_\nu \tilde{W}_\mu + g_2 \tilde{W}_\mu \times \tilde{W}_\nu, \tag{2.18}$$

$$B_{\mu\nu} = \partial_\mu B_\nu - \partial_\nu B_\mu. \tag{2.19}$$

Quantum Chromodynamics (QCD), the gauge field theory that describes the interactions of quarks and gluons, is another component of the SM. Experimental observations suggest that quarks don't exist as free particles. Strong forces bind them into objects called baryons formed by three quarks or mesons which are made of a quark and an antiquark. This fact was a hint for theoreticians to build QCD on the basis of the $SU(3)_C$ gauge group. Here C refers to the colour - the quantum number conserved in strong interactions - and 3 is the number of quark colour states. Within the framework of QCD mesons are colour singlets formed by a quark and an antiquark:

$$M = \sum_i \bar{q}^i q_i, \tag{2.20}$$

while baryons are colour singlets made of three quarks:

$$B = \sum_{ijk} \epsilon^{ijk} q_i q_j q_k, \tag{2.21}$$

where indices i, j and k run over the three colour states of quarks and ϵ^{ijk} is the completely antisymmetric Levi-Civita tensor.

Strong interactions are mediated by 8 gluons associated with 8 Gell-Mann matrices λ_a (a=1..8), the generators of the $SU(3)_C$ group. The covariant derivative for a quark field q in case of QCD reads:

$$D_\mu q = \left(\partial_\mu + \frac{i g_3}{2} \lambda_a G^a_\mu\right) q, \tag{2.22}$$

where G^a_μ denote eight gluon fields and g_3 is the strong coupling constant. Free quarks and their interactions with gluons are described by the $i\bar{q}\gamma^\mu D_\mu q$ term. The QCD Lagrangian includes also the gluon kinetic and self-interaction terms:

$$\mathcal{L}^{QCD}_G = -\frac{1}{4} F^a_{\mu\nu} F^{\mu\nu}_a. \tag{2.23}$$

The strength tensor of the gluon field is expressed as:

$$F^a_{\mu\nu} = \partial_\mu G^a_\nu - \partial_\nu G^a_\mu + g_3 f^{abc} G_{b\mu} G_{c\nu}. \tag{2.24}$$

The third term in (2.24) represents a bilinear form determined by the structure constants, f^{abc} (a,b,c=1..8), of the $SU(3)_C$ group.

2.1.3 Gauge Invariance of the SM

The SM Lagrangian must respect the symmetry under the $U(1)_Y \otimes SU(2)_L \otimes SU(3)_C$ If the quarks and leptons undergo a local position-dependent phase rotation:

$$\Psi'(x) = U(x)\Psi(x) = \exp\left[\frac{i}{2}\left(\theta^a(x)\lambda_a + \beta^b(x)\sigma_b + Y\alpha(x)\right)\right]\Psi \ (a = 1..8,\ b = 1..3), \tag{2.25}$$

and gauge fields are transformed into:

$$G'_\mu = U(x)G_\mu U(x)^{-1} + \frac{i}{g_3}\left[\partial_\mu U(x)\right]U(x)^{-1} \quad \text{(gluon field)}, \tag{2.26}$$

$$W'_\mu = U(x)W_\mu U(x)^{-1} + \frac{i}{g_2}\left[\partial_\mu U(x)\right]U(x)^{-1} \quad \text{(isospin field)}, \tag{2.27}$$

$$B'_\mu = U(x)B_\mu U(x)^{-1} + \frac{i}{g_1}\left[\partial_\mu U(x)\right]U(x)^{-1} \quad \text{(hypercharge field)}, \tag{2.28}$$

then the SM Lagrangian must remain invariant. This requirement is fulfilled provided that the Lagrangian doesn't contain fermion and boson mass terms of the form $m_f\bar{\Psi}\Psi$, $m_B^2 B_\mu B^\mu$, $m_W^2 W_\mu W^\mu$ and $m_g^2 G_\mu G^\mu$. And, indeed, the gauge transformations (2.25-2.28) leave the Lagrangian having none of fermion and gauge boson mass terms,

$$\mathcal{L} = \bar{\Psi}\gamma^\mu D_\mu \Psi - \frac{1}{4}\tilde{W}_{\mu\nu}\tilde{W}^{\mu\nu} - \frac{1}{4}B_{\mu\nu}B^{\mu\nu} - \frac{1}{4}F^a_{\mu\nu}F^{\mu\nu}_a, \tag{2.29}$$

invariant. In Equation (2.29) the covariant derivative contains all the terms associated with the SM gauge group. The presence of fermion and boson mass terms would break the $U(1)_Y \otimes SU(2)_L \otimes SU(3)_C$ symmetry of the Lagrangian (2.29). Thus, to preserve the gauge symmetry without complicating the theoretical model one has to assume that all fermions and bosons are massless. But from experiment we know that only gluons, photon and, perhaps, neutrinos are massless. All other particles are massive.

2.1.4 Higgs mechanism

Spontaneous Symmetry Breaking

The Higgs mechanism [9] is introduced to assign masses to W and Z bosons while keeping invariance under $SU(2)_L$ group. The same mechanism is used for generation of fermion masses. In this section I discuss the general idea of Spontaneous Symmetry Breaking. Let us start from the consideration of complex scalar Higgs field, Φ, with the potential:

$$V(\Phi) = \frac{\lambda}{2}\left(\Phi^*\Phi - r^2\right)^2. \tag{2.30}$$

The potential given by (2.30) is invariant under the U(1) group and is characterised by one maximum at $\Phi = 0$ and minima constituting a circle with the radius r in (ReΦ,ImΦ) plane which can be parametrised as $\Phi = r \cdot \exp(i\alpha)$. This is shown in Figure 2.1. The the vacuum corresponds to a certain choice within these minima.

Let vacuum be the state with zero phase: $\alpha = 0$. The U(1) symmetry of the Higgs potential is not kept for the chosen vacuum state. In other words, the vacuum state has a lower symmetry than the potential itself. This phenomenon is known in physics under the name of "Spontaneous Symmetry Breaking".

Physical states of the Higgs field are just space-time dependent excitations near the vacuum configuration:

$$\Phi(x) = r + h(x) + i\xi(x). \tag{2.31}$$

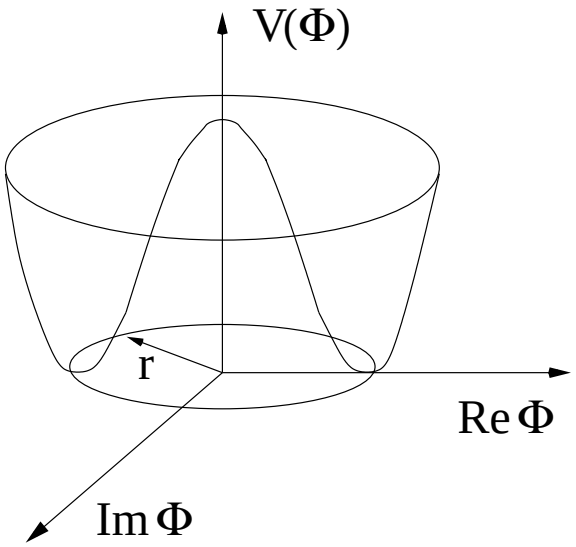

Figure 2.1: The Higgs potential in the case of single complex scalar field.

The Lagrangian of the complex scalar Higgs field

$$\mathcal{L}_{\text{Higgs}} = \frac{1}{2}\partial_\mu \Phi^* \partial^\mu \Phi - \mathrm{V}(\Phi) \tag{2.32}$$

can be expressed in terms of excitation states as:

$$\mathcal{L}_{\text{Higgs}} = \partial_\mu \mathrm{h} \partial^\mu \mathrm{h} + \partial_\mu \xi \partial^\mu \xi - \frac{\lambda}{2}\Big((\mathrm{h}^2+\xi^2)^2 + 4\mathrm{r}\mathrm{h}(\mathrm{h}^2+\xi^2) + 4\mathrm{r}^2\mathrm{h}^2\Big). \tag{2.33}$$

The obvious global U(1) invariance of the Lagrangian given by (2.32) is well hidden in Equation (2.33). The coefficients in front of the bilinear terms determine the masses of the physical fields. So we got a theory of two particles with masses:

$$\begin{aligned} \mathrm{m}_\mathrm{h}^2 &= 4\lambda \mathrm{r}^2, \\ \mathrm{m}_\xi^2 &= 0. \end{aligned} \tag{2.34}$$

The "radial" excitation of the Higgs field is characterised by a mass determined by the parameter λ and the vacuum expectation value r while the excitation that corresponds to the motion along the valley of minima is massless. It is referred to as Goldstone boson. As we will see later, in the SM Goldstone bosons are "gauged away" and become longitudinal polarisations of W and Z bosons. The terms in Equation (2.33) containing higher orders of h and ξ describe self-interactions of h and ξ fields and interactions between them.

Generation of Masses in the SM

I have just discussed the model where the Higgs field is characterised by two degrees of freedom: the complex field Φ is represented by a combination of the two real fields, ϕ_1 and ϕ_2 ($\Phi = \phi_1 + \mathrm{i}\phi_2$). Increasing the number of real fields by two we arrive at the case of the SM which postulates the existence of a quartet of real fields ϕ_i (i=1..4) described by the Lagrangian:

$$\mathcal{L}(\phi_\mathrm{i}) = \sum_{\mathrm{i}=1,4} \frac{1}{2}\partial_\mu \phi_\mathrm{i} \partial^\mu \phi_\mathrm{i} - \mathrm{V}\left(\phi_\mathrm{i}\right), \tag{2.35}$$

where the potential $V(\phi_i)$ has the form:

$$V(\phi_i) = \frac{\lambda}{4}\left(\sum_{i=1,4}\phi_i^2 - \frac{\mu^2}{\lambda}\right)^2. \tag{2.36}$$

Potential (2.36) has O(4) symmetry and is characterised by the continuous minima at

$$\sum_{i=1,4}\phi_i^2 = \frac{\mu^2}{\lambda}. \tag{2.37}$$

We can always rotate the vacuum state, corresponding to one of these minima, to the basis where $\phi_1 = \phi_2 = \phi_3 = 0$ and $\phi_4 = \mu/\sqrt{\lambda}$. The four real fields ϕ_i can be sorted into a doublet of complex fields Φ:

$$\Phi = \begin{pmatrix} \phi^+ \\ \phi^0 \end{pmatrix} = \frac{1}{\sqrt{2}}\begin{pmatrix} \phi_2 + i\phi_1 \\ \phi_4 + i\phi_3 \end{pmatrix}. \tag{2.38}$$

This field referred hereafter to as the Higgs field respects $SU(2)_L$ isospin symmetry of the SM. In terms of Φ the Lagrangian takes the form:

$$\mathcal{L} = \partial_\mu\Phi^\dagger\partial^\mu\Phi - V(\Phi^\dagger\Phi), \tag{2.39}$$

with the potential:

$$V(\Phi^\dagger\Phi) = \lambda\left(\Phi^\dagger\Phi - \frac{\mu^2}{2\lambda}\right)^2, \tag{2.40}$$

and the vacuum state chosen for the Higgs field reads:

$$<0|\Phi|0> = \frac{1}{\sqrt{2}}\begin{pmatrix} 0 \\ \nu \end{pmatrix}, \tag{2.41}$$

where $\nu = \mu/\sqrt{\lambda}$ is the vacuum expectation value of the Higgs field. The choice of vacuum state given by Equation (2.41) is not random. Setting the ϕ^+ component of the Higgs field to zero is dictated by the necessity to ensure the conservation of the electromagnetic charge [22]. The specific choice of the vacuum state reduces the O(4) symmetry of Equation (2.37) down to a O(1) symmetry which corresponds to the $U(1)_Q$ group of electromagnetism. As we saw in the previous section the Higgs particle is interpreted as a space-time dependent "radial" fluctuation of field Φ near the vacuum configuration:

$$\Phi = \frac{1}{\sqrt{2}}\begin{pmatrix} 0 \\ \nu + h(x) \end{pmatrix}. \tag{2.42}$$

The Lagrangian expressed in terms of the vacuum expectation value ν and the physical state h,

$$\mathcal{L}_{\text{Higgs}} = \frac{1}{2}\partial_\mu h\partial^\mu h - \lambda\nu^2h^2 - \lambda\nu h^3 - \frac{\lambda}{4}h^4, \tag{2.43}$$

effectively describes the scalar particle with mass proportional to ν:

$$m_h = \sqrt{2\lambda}\nu. \tag{2.44}$$

The scalar particle described by Lagrangian (2.43) is referred to as the Standard Model Higgs boson. The terms proportional to h^3 and h^4 describe self-interaction of the field h.

To assign masses for gauge bosons one has to introduce interactions of gauge bosons with the Higgs doublet. In the Lagrangian language this means the replacement of the Lorentz derivative for the field Φ by the covariant derivative given by Equation (2.12),

$$\partial_\mu \Phi^\dagger \partial^\mu \Phi \rightarrow D_\mu \Phi^\dagger D^\mu \Phi. \tag{2.45}$$

Let us also take into consideration massless Goldstone bosons associated with three remaining degrees of freedom of the Higgs doublet:

$$\Phi = \frac{1}{\sqrt{2}} \begin{pmatrix} \eta_1(x) + i\eta_2(x) \\ \nu + h(x) + i\xi(x) \end{pmatrix}. \tag{2.46}$$

Inserting this expression for the field Φ into (2.45) and using identities given by (2.14) and (2.15) we obtain:

$$\begin{aligned} & D_\mu \Phi^\dagger D^\mu \Phi \Longrightarrow \\ & \left.\begin{array}{r} \frac{1}{4}(g_2\nu)^2 W'^+_\mu W'^{-\mu} \\ \frac{1}{8}\nu^2(g_1^2+g_2^2) Z'_\mu Z'^\mu \end{array}\right\} \; W \text{ and } Z \text{ mass terms}, \\ & \left.\begin{array}{r} \frac{1}{2}g_2^2 \nu W'^+_\mu W'^{-\mu} h \\ \frac{1}{4}\nu(g_1^2+g_2^2) Z'_\mu Z'^\mu h \end{array}\right\} \; \text{trilinear couplings of } W \text{ and } Z \text{ to } h, \\ & \left.\begin{array}{r} \frac{1}{4}g_2^2 W'^+_\mu W'^{-\mu} h^2 \\ \frac{1}{8}(g_1^2+g_2^2) Z'_\mu Z'^\mu h^2 \end{array}\right\} \; \text{quartic couplings of } W \text{ and } Z \text{ to } h. \end{aligned} \tag{2.47}$$

Note that Relations (2.47) involve redefined W and Z fields:

$$W'^\pm_\mu = W^\pm_\mu \pm \frac{2}{g_2(\nu+h)} \partial_\mu(\eta_1 \pm i\eta_2), \qquad Z'_\mu = Z_\mu + \frac{2}{(\nu+h)\sqrt{g_1^2+g_2^2}} \partial_\mu \xi. \tag{2.48}$$

Looking at (2.48) one can see that Goldstone bosons have become longitudinal polarisations[1] of the W and Z fields. Inspecting the mass terms in (2.47) we can conclude that masses of W and Z bosons are proportional to ν:

$$m_W = \frac{1}{2}\nu g_2, \tag{2.49}$$

$$m_Z = \frac{1}{2}\nu\sqrt{g_1^2+g_2^2}, \tag{2.50}$$

[1]The Lorentz derivative ∂_μ is equivalent to the momentum operator, P_μ, and therefore terms proportional to $\partial_\mu(\eta_1 \pm i\eta_2)$ and $\partial_\mu \xi$ are regarded as longitudinal polarisation states of the W and Z fields, respectively.

while the photon remains massless:

$$\mathrm{m}_\gamma = 0. \tag{2.51}$$

The last equation is derived from the fact that there is no term of the form $\mathrm{A}_\mu\mathrm{A}^\mu$ in Equation (2.47). It can be shown that masses of the Z and W bosons are related to the weak mixing angle θ_w:

$$\cos\theta_\mathrm{w} = \frac{\mathrm{m_W}}{\mathrm{m_Z}}. \tag{2.52}$$

A useful quantity which is often referred to is $\rho = \mathrm{m_W}/\mathrm{m_Z}\cos\theta_\mathrm{w}$. As can be seen from Equation (2.52), the SM predicts $\rho = 1$. The experimental observations confirm this prediction. Any other theory suggesting the mass generation has to reproduce this experimental result.

Fermion masses are obtained by adding the so-called Yukawa term to the SM Lagrangian. This term respects $\mathrm{U(1)_Y} \otimes \mathrm{SU(2)_L}$ gauge invariance and describes the interaction of the Higgs doublet with the fermion fields:

$$\mathcal{L}_\mathrm{Yukawa} = \sum_{\mathrm{ij}} \left(\mathrm{Y}_\ell^{\mathrm{ij}} \bar{\mathrm{L}}_\mathrm{L}^{\mathrm{i}} \Phi \ell_\mathrm{R}^{\mathrm{j}} + \mathrm{Y}_\mathrm{u}^{\mathrm{ij}} \bar{\mathrm{Q}}_\mathrm{L}^{\mathrm{i}} \Phi_\mathrm{c} \mathrm{u}_\mathrm{R}^{\mathrm{j}} + \mathrm{Y}_\mathrm{d}^{\mathrm{ij}} \bar{\mathrm{Q}}_\mathrm{L}^{\mathrm{i}} \Phi \mathrm{d}_\mathrm{R}^{\mathrm{j}} \right) + \mathrm{h.c.}, \tag{2.53}$$

where the charge-conjugate Higgs doublet Φ_c, expressed as:

$$\Phi_\mathrm{c} = -\mathrm{i}\sigma_2\Phi^* = \begin{pmatrix} -\Phi_0^* \\ \Phi^- \end{pmatrix}, \tag{2.54}$$

is introduced to generate masses of up-type quarks. The notations $\mathrm{L}_\mathrm{L}^{\mathrm{i}}$, $\mathrm{Q}_\mathrm{L}^{\mathrm{i}}$, $\ell_\mathrm{R}^{\mathrm{i}}$, $\mathrm{u}_\mathrm{R}^{\mathrm{i}}$ and $\mathrm{d}_\mathrm{R}^{\mathrm{i}}$ have the same meaning as in (2.10). The indexes i and j run over three fermion families and $\mathrm{Y}_\ell^{\mathrm{ij}}$, $\mathrm{Y}_\mathrm{u}^{\mathrm{ij}}$ and $\mathrm{Y}_\mathrm{d}^{\mathrm{ij}}$ are general complex 3×3 matrices. In terms of ν and h, the Yukawa interactions acquire the following form:

$$\begin{aligned} \mathcal{L}_\mathrm{Yukawa} = {} & \tfrac{\nu}{\sqrt{2}} \mathrm{Y}_\ell^{\mathrm{ij}} \bar{\ell}_\mathrm{L}^{\mathrm{iw}} \ell_\mathrm{R}^{\mathrm{jw}} + \tfrac{\nu}{\sqrt{2}} \mathrm{Y}_\mathrm{u}^{\mathrm{ij}} \bar{\mathrm{u}}_\mathrm{L}^{\mathrm{iw}} \mathrm{u}_\mathrm{R}^{\mathrm{jw}} + \tfrac{\nu}{\sqrt{2}} \mathrm{Y}_\mathrm{d}^{\mathrm{ij}} \bar{\mathrm{d}}_\mathrm{L}^{\mathrm{iw}} \mathrm{d}_\mathrm{R}^{\mathrm{jw}} + \mathrm{h.c.} + \\ & \tfrac{\mathrm{h}}{\sqrt{2}} \mathrm{Y}_\ell^{\mathrm{ij}} \bar{\ell}_\mathrm{L}^{\mathrm{iw}} \ell_\mathrm{R}^{\mathrm{jw}} + \tfrac{\mathrm{h}}{\sqrt{2}} \mathrm{Y}_\mathrm{u}^{\mathrm{ij}} \bar{\mathrm{u}}_\mathrm{L}^{\mathrm{iw}} \mathrm{u}_\mathrm{R}^{\mathrm{jw}} + \tfrac{\mathrm{h}}{\sqrt{2}} \mathrm{Y}_\mathrm{d}^{\mathrm{ij}} \bar{\mathrm{d}}_\mathrm{L}^{\mathrm{iw}} \mathrm{d}_\mathrm{R}^{\mathrm{jw}} + \mathrm{h.c.}, \end{aligned} \tag{2.55}$$

where the first line represents fermion mass terms and the second one describes the interaction between the Higgs particle and the fermion fields. The superscript "w" refers to the interaction basis. The mass basis corresponds, by definition, to diagonal mass matrices. We can always find unitary matrices $\mathrm{V_{fL}}$ and $\mathrm{V_{fR}}$ such that

$$\mathrm{V_{fL}} \mathrm{Y_f} \mathrm{V_{fR}^\dagger} = \mathrm{Y_f'}, \tag{2.56}$$

with $\mathrm{Y_f'}$ diagonal and real, $\mathrm{Y_f'^{ij}} = \delta^{\mathrm{ij}} \mathrm{c_f^i}$. The mass eigenstates are then identified as

$$\begin{aligned} \mathrm{d}_\mathrm{L}^{\mathrm{i}\prime} &= (\mathrm{V_{dL}})^{\mathrm{ij}} \mathrm{d}_\mathrm{L}^{\mathrm{jw}}, & \mathrm{d}_\mathrm{R}^{\mathrm{i}\prime} &= (\mathrm{V_{dR}})^{\mathrm{ij}} \mathrm{d}_\mathrm{R}^{\mathrm{jw}}, \\ \mathrm{u}_\mathrm{L}^{\mathrm{i}\prime} &= (\mathrm{V_{uL}})^{\mathrm{ij}} \mathrm{u}_\mathrm{L}^{\mathrm{jw}}, & \mathrm{u}_\mathrm{R}^{\mathrm{i}\prime} &= (\mathrm{V_{uR}})^{\mathrm{ij}} \mathrm{u}_\mathrm{R}^{\mathrm{jw}}, \\ \ell_\mathrm{L}^{\mathrm{i}\prime} &= (\mathrm{V_{\ell L}})^{\mathrm{ij}} \ell_\mathrm{L}^{\mathrm{jw}}, & \ell_\mathrm{R}^{\mathrm{i}\prime} &= (\mathrm{V_{\ell R}})^{\mathrm{ij}} \ell_\mathrm{R}^{\mathrm{jw}}, \\ \nu_\mathrm{L}^{\mathrm{i}\prime} &= (\mathrm{V_{\nu L}})^{\mathrm{ij}} \nu_\mathrm{L}^{\mathrm{jw}}. \end{aligned} \tag{2.57}$$

Note that, since the neutrinos are massless, $V_{\nu L}$ is arbitrary. The charged-current interactions for quarks have the following form in the mass basis:

$$\mathcal{L}_W = -\frac{g_2}{\sqrt{2}}\bar{u}_L^{i\prime}\gamma_\mu(V_{uL}V_{dL}^\dagger)^{ij}d_L^{j\prime}W^{\mu+} + \text{h.c.}, \tag{2.58}$$

where $(V_{uL}V_{dL}^\dagger)$ is the CKM matrix (see Equation (2.11)) describing the mixing in the quark sector. Similarly, the mixing matrix in the lepton sector is $(V_{\nu L}V_{\ell L}^\dagger)$. However, we can use the arbitrariness of $V_{\nu L}$ to choose $V_{\nu L} = V_{\ell L}$, and the mixing matrix becomes a unit matrix. We can conclude that the masslessness of neutrinos (if true) implies that there is no mixing in the lepton sector.

In the mass basis, fermion mass terms and terms describing the interaction of the Higgs particle with the fermion fields read

$$\left.\begin{aligned} &\tfrac{c_\ell^i}{\sqrt{2}}\nu\left(\bar{\ell}_L'\ell_R' + \bar{\ell}_R'\ell_L'\right)\\ &\tfrac{c_u^i}{\sqrt{2}}\nu\left(\bar{u}_L'u_R' + \bar{u}_R'u_L'\right)\\ &\tfrac{c_d^i}{\sqrt{2}}\nu\left(\bar{d}_L'd_R' + \bar{d}_R'd_L'\right)\end{aligned}\right\} \; fermion\ mass\ terms,$$

$$\left.\begin{aligned} &\tfrac{c_\ell^i}{\sqrt{2}}h\left(\bar{\ell}_L'\ell_R' + \bar{\ell}_R'\ell_L'\right)\\ &\tfrac{c_u^i}{\sqrt{2}}h\left(\bar{u}_L'u_R' + \bar{u}_R'u_L'\right)\\ &\tfrac{c_d^i}{\sqrt{2}}h\left(\bar{d}_L'd_R' + \bar{d}_R'd_L'\right)\end{aligned}\right\} \; fermion\ interactions\ with\ h. \tag{2.59}$$

From (2.59) we can conclude that fermion masses are:

$$m_\ell^i = \frac{c_\ell^i\nu}{\sqrt{2}}, \qquad m_u^i = \frac{c_u^i\nu}{\sqrt{2}}, \qquad m_d^i = \frac{c_d^i\nu}{\sqrt{2}}. \tag{2.60}$$

One should point out one more important consequence of Spontaneous Symmetry Breaking. From Equations (2.47) and (2.59) it follows that the heavier particle is, the stronger it couples to the Higgs boson. Hence, the latter prefers to decay into more massive particles provided that such decay is kinematically allowed. This feature is used in analyses used to search for the SM Higgs boson at LEP.

2.2 General Two Higgs Doublet Models

One Higgs doublet is the minimum which is needed to generate boson and fermion masses. However there is no strong theoretical argument favouring this minimal choice. There are extensions of the Standard Model with additional Higgs singlets, doublets and even triplets with respect to the $SU(2)_L$ group [23]. I will restrict myself to the

discussion of general Two Higgs Doublet Models (2HDM) [12]. These models are very attractive extensions of the minimal SM for the following reasons:

- They add new phenomena (e.g. charged Higgs bosons) with the fewest new parameters.
- The two Higgs doublet models are built in such a way that they satisfy the experimental constraint of $\rho \approx 1$ and ensure the absence of tree level flavour-changing neutral currents (FCNC) which haven't been observed experimentally.
- At least two doublets of scalar Higgs fields are required in "low-energy" supersymmetric models[2] .

Table 2.3 summarises the four different types of the 2HDM depending on how each of two Higgs doublets couples to different types of fermions. The numbers (1 or 2) show

	Type I	Type I′	Type II	Type II′
u (up-type quarks)	2	2	2	2
d (down-type quarks)	2	2	1	1
ℓ (charged leptons)	2	1	1	2

Table 2.3: Four distinct structures of the 2HDM.

which Higgs doublet couples to which fermion type. In the model of type I, the first doublet does not couple at all to fermions, while the second behaves like the doublet in the minimal model. The 2HDM of type II corresponds to the case when the first doublet couples to down-type quarks and charged leptons and the second to up-type quarks. Models I′ and II′ are rarely mentioned in the literature and discussed only in the context of the charged Higgs sector [24]. Requiring each fermion type indicated in Table 2.3 to couple to no more than one Higgs doublet ensures the absence of tree level FCNC [25].

The potential describing two complex $\mathrm{SU(2)_L}$ doublet scalar fields Φ_1 and Φ_2 is given by [26]:

$$\begin{aligned} \mathrm{V}(\Phi_1,\Phi_2) \;=\; & \lambda_1(\Phi_1^\dagger\Phi_1-\nu_1^2)^2+\lambda_2(\Phi_2^\dagger\Phi_2-\nu_2^2)^2 \\ & +\lambda_3\left[(\Phi_1^\dagger\Phi_1-\nu_1^2)+(\Phi_2^\dagger\Phi_2-\nu_2^2)\right]^2 \\ & +\lambda_4\left[(\Phi_1^\dagger\Phi_1)(\Phi_2^\dagger\Phi_2)-(\Phi_1^\dagger\Phi_2)(\Phi_2^\dagger\Phi_1)\right] \\ & +\lambda_5\left[\mathrm{Re}(\Phi_1^\dagger\Phi_2)-\nu_1\nu_2\cos\xi\right]^2+\lambda_6\left[\mathrm{Im}(\Phi_1^\dagger\Phi_2)-\nu_1\nu_2\sin\xi\right]^2, \end{aligned} \tag{2.61}$$

where the λ_i are real parameters, ν_1 and ν_2 are vacuum expectation values of the two doublets. The phase ξ is introduced to accommodate CP-violation in the Higgs sector.

[2]Supersymmetric models will be discussed in the next sections.

The vacuum corresponds to the particularly chosen ground state of the Potential (2.61) when fields Φ_1 and Φ_2 have the form:

$$< \Phi_1 >= \begin{pmatrix} 0 \\ \nu_1 \end{pmatrix}, \qquad < \Phi_2 >= \begin{pmatrix} 0 \\ \nu_2 e^{i\xi} \end{pmatrix}. \tag{2.62}$$

A detailed discussion on CP violation in the Higgs sector can be found in Reference [27]. It will not be considered in this thesis and the phase ξ is set to zero. One of the most important parameters in 2HDM is the ratio of vacuum expectation values defined as:

$$\tan\beta = \frac{\nu_2}{\nu_1}. \tag{2.63}$$

After spontaneous symmetry breaking three out of eight degrees of freedom constituting the Higgs sector of 2HDM become longitudinal polarisations of W and Z bosons. The remaining five give rise to the following particles:

a pair of charged Higgs bosons

$$H^{\pm} = -\Phi_1^{\pm}\sin\beta + \Phi_2^{\pm}\cos\beta \tag{2.64}$$

with mass squared ${m_{H^{\pm}}}^2 = \lambda_4(\nu_1^2 + \nu_2^2)$,

a CP-odd neutral scalar Higgs boson

$$A = \sqrt{2}(-\mathrm{Im}\Phi_1^0\sin\beta + \mathrm{Im}\Phi_2^0\cos\beta) \tag{2.65}$$

with mass squared ${m_A}^2 = \lambda_6(\nu_1^2 + \nu_2^2)$ and

two CP-even neutral scalar Higgs bosons

$$H = \sqrt{2}\left[(\mathrm{Re}\Phi_1^0 - \nu_1)\cos\alpha + (\mathrm{Re}\Phi_2^0 - \nu_2)\sin\alpha\right], \tag{2.66}$$

$$h = \sqrt{2}\left[-(\mathrm{Re}\Phi_1^0 - \nu_1)\sin\alpha + (\mathrm{Re}\Phi_2^0 - \nu_2)\cos\alpha\right], \tag{2.67}$$

where α is the mixing angle which depends on the components of the mass-squared matrix of these two scalars:

$$\mathcal{M} = \begin{pmatrix} \mathcal{M}_{11} & \mathcal{M}_{12} \\ \mathcal{M}_{12} & \mathcal{M}_{22} \end{pmatrix} = \begin{pmatrix} 4\nu_1^2(\lambda_1+\lambda_3) + \nu_2^2\lambda_5 & (4\lambda_3+\lambda_5)\nu_1\nu_2 \\ (4\lambda_3+\lambda_5)\nu_1\nu_2 & 4\nu_2^2(\lambda_2+\lambda_3) + \nu_1^2\lambda_5 \end{pmatrix}. \tag{2.68}$$

The physical masses of the CP-even Higgs bosons are given by:

$$m_{H,h}^2 = \frac{1}{2}\left[\mathcal{M}_{11} + \mathcal{M}_{22} \pm \sqrt{(\mathcal{M}_{11} - \mathcal{M}_{22})^2 + 4\mathcal{M}_{12}^2}\right]. \tag{2.69}$$

The mixing angle α is obtained from:

$$\begin{aligned} \sin 2\alpha &= \frac{2\mathcal{M}_{12}}{\sqrt{(\mathcal{M}_{11} - \mathcal{M}_{22})^2 + 4\mathcal{M}_{12}^2}}, \\ \cos 2\alpha &= \frac{\mathcal{M}_{11} - \mathcal{M}_{22}}{\sqrt{(\mathcal{M}_{11} - \mathcal{M}_{22})^2 + 4\mathcal{M}_{12}^2}}. \end{aligned} \tag{2.70}$$

CP-conserving 2HDM introduces six additional free parameters:

- the mixing angle, α;
- the ratio of vacuum expectation values, $\tan\beta$;
- four Higgs boson masses: $m_{H^\pm}$, m_A, m_h and m_H.

The gauge bosons become massive due to their interactions with Higgs doublets. The generated masses of the gauge bosons are related to the vacuum expectation values and the coupling constants g_1 and g_2 as follows:

$$m_W = g_2\sqrt{\frac{\nu_1^2+\nu_2^2}{2}}, \qquad m_Z = \sqrt{\frac{(\nu_1^2+\nu_2^2)(g_1^2+g_2^2)}{2}}, \qquad m_\gamma = 0. \tag{2.71}$$

Fermion masses arise due to the Yukawa couplings. The explicit expressions for fermion masses depend on the type of 2HDM. As an example I'll consider the "relationships"between fermions and Higgs doublets within the framework of 2HDM of type II. In this model, masses of down-type quarks and charged leptons are determined by the profile of the first Higgs doublet - its vacuum expectation value ν_1 and its Yukawa couplings to the down-type quarks, c_{1d}, and charged leptons, $c_{1\ell}$:

$$m_d = \frac{c_{1d}\nu_1}{\sqrt{2}}, \tag{2.72}$$

$$m_\ell = \frac{c_{1\ell}\nu_1}{\sqrt{2}}. \tag{2.73}$$

The up-type quarks acquire mass through their interaction with the second Higgs doublet. Consequently, the masses of up-type quarks depend on the vacuum expectation value ν_2 and Yukawa couplings of the field Φ_2 to the up-type quarks, c_{2u}:

$$m_u = \frac{c_{2u}\nu_2}{\sqrt{2}}. \tag{2.74}$$

Rotating the weak eigenstates of the Higgs bosons to their mass eigenstates one obtains the dependence of the Higgs boson couplings to the fermions and gauge bosons on the parameters β and α. This is illustrated in Table 2.4. In the 2HDM there are additional trilinear couplings between the Z boson and the neutral Higgs particles as illustrated in Figure 2.2. These couplings depend on parameters α and β in the following way:

$$g_{ZhA} \sim \cos(\beta-\alpha), \tag{2.75}$$

$$g_{ZHA} \sim \sin(\beta-\alpha). \tag{2.76}$$

	h	H	A
W^+W^-	$\sin(\beta-\alpha)$	$\cos(\beta-\alpha)$	0
ZZ	$\sin(\beta-\alpha)$	$\cos(\beta-\alpha)$	0
$u\bar{u}$ (up-type quarks)	$\cos\alpha/\sin\beta$	$\sin\alpha/\sin\beta$	$\cot\beta$
$d\bar{d}$ (down-type quarks)	$\sin\alpha/\cos\beta$	$\cos\alpha/\cos\beta$	$\tan\beta$
$\ell\ell$ (charged leptons)	$\sin\alpha/\cos\beta$	$\cos\alpha/\cos\beta$	$\tan\beta$

Table 2.4: The dependence of fermion and gauge boson couplings to the neutral Higgs bosons on parameters α and β in 2HDM of type II. In the CP-conserving 2HDM the CP-odd Higgs boson A is decoupled from W and Z bosons.

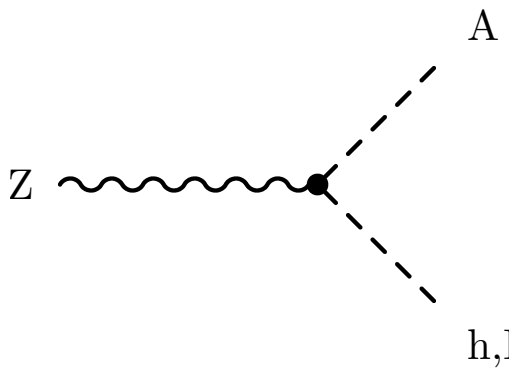

Figure 2.2: Feynman graph illustrating trilinear couplings between Z, h(H) and A bosons.

2.3 Supersymmetry

2.3.1 Defects of the SM

Despite the phenomenological success of the SM, there are strong conceptual indications that this model is not the ultimate, self-contained theory. Even if one accepts very strange set of group representations that are required by the SM, there are at least nineteen absolutely arbitrary parameters, three gauge couplings, $g_{1,2,3}$, one CP-violating non-perturbative QCD vacuum angle θ_{QCD} [28], six quark and three charged lepton masses with three charged weak mixing angles and one CP-violating phase δ, and two parameters: (μ,λ) or (m_H,m_W) to characterise the Higgs sector. Moreover, many more parameters are needed if one wishes to accommodate non-accelerator observations For example, neutrino masses and mixing require at least seven additional parameters: three masses, three mixing angles and one CP-violating phase. Cosmological inflation implies at least one new mass scale of order 10^{16} GeV, the cosmological baryon asymmetry introduces one or more additional parameters, and the cosmological constant may be non-zero. In a fundamental physical model all these parameters should not appear as totally free. The ultimate theory should provide a way to understand their values and perhaps establish relations between them.

Another shortcoming of the SM comes from its inability to include in a consistent

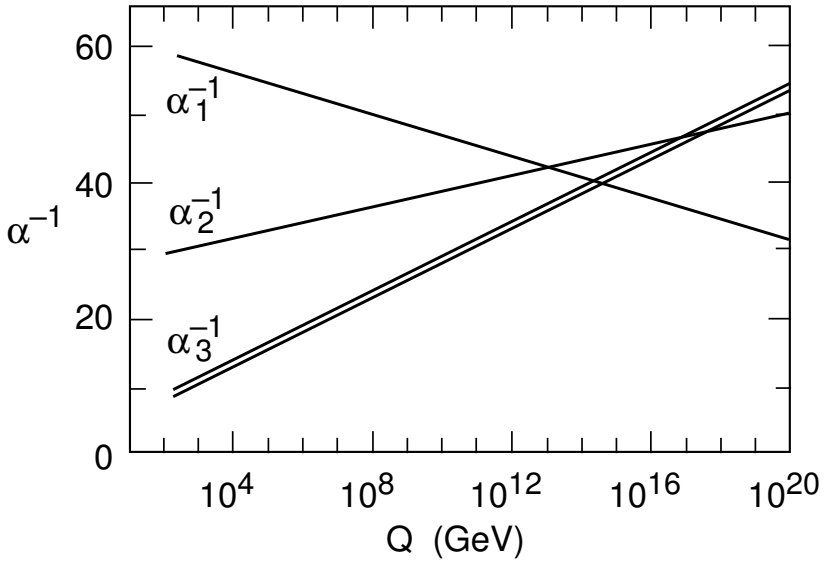

Figure 2.3: Evolution of the gauge couplings to high energy scales. The parameters α_i are defined as $\alpha_\mathrm{i} = \mathrm{g}_\mathrm{i}^2/4\pi$. The dependence of α_i on the energy scale Q is computed with only the particle content of the SM. The unification of the gauge couplings does not occur in a single point.

way gravity. The gravitational interactions are well described classically by the General Theory of Relativity. But the attempt to include the gravity within the framework of quantum physics results into a non-renormalisable theory. Radiative corrections become more and more divergent at higher orders of perturbation theory. At energies attainable at contemporary accelerators the gravitational interactions are essentially negligible due to the extremely small Newton constant, $\mathrm{G_N} \sim 10^{-38}$ GeV^{-2}. However their strength grows up quadratically with energy and gravitational interactions become strong at the so-called Planck scale, $\mathrm{M_P} = \sqrt{\hbar \mathrm{c}^5/\mathrm{G_N}} \sim 10^{19}$ GeV.

The ultimate self-consistent theory is supposed to give the answers to the following questions:

1. What is the origin of six flavours of both quarks and leptons and what explains their weak charged-current mixing and CP-violation?

2. Do particle masses really originate from a Higgs mechanism and why their values are much lower than Planck scale and vary in a wide range from 0.5 MeV to 175 GeV?

3. Is there a way to introduce gravity as a renormalisable quantum field theory?

4. Can all the interactions be unified?

Radiative corrections make gauge couplings dependent on the energy scale. This dependence is given by the Renormalisation Group Equations [29]. Theoretical calculation shows that the three gauge couplings approach each other at the energy scale

$M_{GUT} \sim 10^{14}$-10^{16} GeV favouring the positive answer to question 4, and so-called Grand Unification Theories (GUT) [30] aim at these energy scales. However, unification of gauge couplings doesn't occur in a single point if their dependence on the energy scale is computed with the particle content of the SM as demonstrated in Figure 2.3.

It is natural to assume that the SM is an effective theory which is valid up to some energy scale Λ beyond which a more general theory is valid. One may feel tempted to associate Λ with the Planck or GUT scale. However, there is a threat from radiative corrections to the masses of the scalar fields. Each of the one-loop diagrams depicted in Figure 2.4 is individually quadratically divergent, implying

$$\delta m_H^2 \sim O\left(\frac{\lambda^2}{16\pi^2}\right) \int^{\Lambda} \frac{d^4k}{k^2} \sim O\left(\frac{\lambda^2}{16\pi^2}\right) \Lambda^2, \tag{2.77}$$

where λ is the fermion (boson) trilinear coupling to the scalar field. Equation (2.77) is derived by setting the cutoff parameter to the energy scale Λ where the SM breaks up and must be substituted by a new theory. If we assume that $\Lambda \backsimeq M_{GUT}$ or $\Lambda \backsimeq M_P$

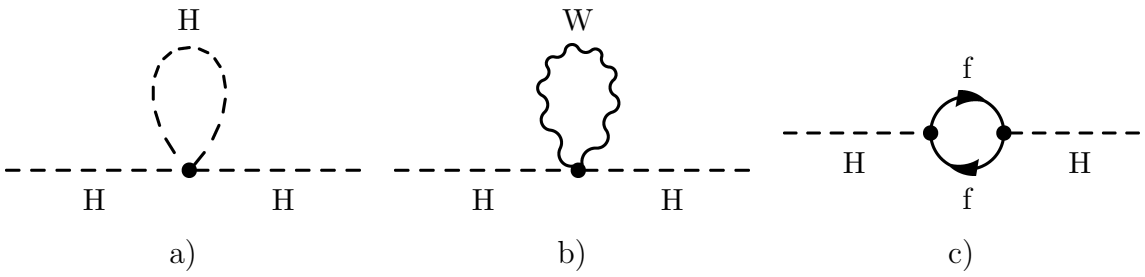

Figure 2.4: Quantum corrections to the Higgs boson mass arising from a) Higgs boson loop; b) gauge boson loop; c) fermion loop.

then the quantum corrections given by (2.77) are much larger than the physical value of the scalar boson mass, $m_H \sim 10^2$ GeV. Fermion and gauge boson masses are protected from quadratic divergences by chiral and gauge symmetry, respectively. However, since quarks, leptons and weak bosons acquire their mass due to the vacuum expectation value of the scalar field, the entire mass spectrum is sensitive to energy scale Λ. This conceptual inconsistency is known in physics under the name of "hierarchy" or "naturalness" problem. Keeping the radiative corrections small with respect to much larger energy scales requires an unnatural procedure known as "fine-tuning" which implies iterative adjustment of the model parameters when going to higher orders in perturbation theory. A more elegant solution would be a symmetry principle allowing the masses of scalar fields to remain of the order of electroweak scale: $\delta m_H^2 \sim m_H^2$.

The problems that I've just discussed are solved in a natural way by Supersymmetry (SUSY). In the next section I will outline the basic ideas underlying SUSY.

2.3.2 Supersymmetry: Basic Ideas

The Supersymmetry is a symmetry which links fermions and bosons by placing them into one supermultiplet. The transformations between bosons and fermions are realised

via so-called spin-$\frac{1}{2}$ operators, S_α (where α is spinorial index). These operators are of fermionic character. Together with the Poincare group they constitute the supersymmetry algebra [32]. Introducing supersymmetry algebra has very important consequence in a theory. Being realised locally, SUSY naturally accommodates Einstein's General Theory of Relativity and postulates gravity as an interaction mediated by gauge bosons called gravitons [33].

Another attractive feature of SUSY is that it offers an elegant solution for the "hierarchy problem" exploiting the fact that the fermion and boson loops illustrated in Figure 2.4 have opposite signs. If there is an equal number of fermions and bosons, and if boson and fermion trilinear couplings to the scalar fields are degenerated as supposed in a supersymmetric theory, the quadratic divergences in Equation (2.77) cancel:

$$\delta m_H^2 = -\frac{\lambda_F^2}{16\pi^2}\left(\Lambda^2 + M_F^2\right) + \frac{\lambda_B^2}{16\pi^2}\left(\Lambda^2 + M_B^2\right) = O\left(\frac{\lambda^2}{16\pi^2}\right)|M_B^2 - M_F^2|, \tag{2.78}$$

where $\lambda = \lambda_F = \lambda_B$ is the universal fermion and boson coupling to the scalar field and M_F and M_B are masses of fermion and boson fields, respectively. Cancellation of quadratic divergences makes it possible to keep the radiative corrections to the masses of scalar fields of the order of electroweak scale provided that:

$$\delta m_H^2 \sim |M_B^2 - M_F^2| \lesssim 1\mathrm{TeV}^2. \tag{2.79}$$

The most trivial supersymmetric theory which contains only one Weyl fermion ψ and one scalar complex field ϕ and ignores interaction is described by the following Lagrangian [34]:

$$\mathcal{L} = \partial_\mu \phi^* \partial^\mu \phi + i\psi^+ \bar{\sigma} \cdot \partial \psi, \tag{2.80}$$

where $\bar{\sigma} = (1, \tilde{\sigma})$. The simplest supersymmetry transformation laws are:

$$\delta_\eta \phi = \sqrt{2}\eta^T C \psi, \qquad \delta_\eta \psi = \sqrt{2} i \cdot \partial \phi C \eta^*, \tag{2.81}$$

where η is an infinitesimal spinor parameter and $C = -i\sigma^2 = C^*$ is the charge-conjugation matrix. It is easy to check that under (2.81) the Lagrangian (2.80) changes by a total derivative $\partial_\mu(...)$, and hence the action $A = \int d^4x \mathcal{L}(x)$ is invariant. Lagrangian (2.80) can be easily extended to include interactions,

$$\mathcal{L} = \partial_\mu \phi^* \partial^\mu \phi + i\psi^+ \bar{\sigma} \cdot \partial \psi + F^+ F + \left(F \frac{\partial W}{\partial \phi} - \frac{1}{2}\psi^T C \psi \frac{\partial^2 W}{\partial \phi^2} + \text{h.c.}\right), \tag{2.82}$$

with the supersymmetry transformations:

$$\delta_\eta \phi = \sqrt{2}\eta^T C \psi, \qquad \delta_\eta \psi = \sqrt{2} i \bar{\sigma} \cdot \partial \phi C \eta^* + \eta F, \qquad \delta_\eta F = -\sqrt{2} i \eta^+ \bar{\sigma} \cdot \partial \psi. \tag{2.83}$$

The field F is called auxiliary. It has no kinetic term and therefore may be eliminated by using an equation of motion:

$$F^+ = -\frac{\partial W}{\partial \phi}. \tag{2.84}$$

Thus all the interactions are characterised by the analytic function $\mathrm{W}(\phi)$ which is called the superpotential. To keep the theory renormalisable, the superpotential has to be at most a cubic function of ϕ:

$$\mathrm{W}(\phi) = \sum_{\mathrm{i}=1,3} \omega_{\mathrm{i}} \phi^{\mathrm{i}}. \tag{2.85}$$

The superpotential

$$\mathrm{W}(\phi) = \frac{\mathrm{m}}{2}\phi^2 - \frac{\lambda}{3}\phi^3, \quad \lambda > 0 \tag{2.86}$$

leads to a theory which resembles the SM deprived of gauge fields. And indeed, the resulting Lagrangian derived from (2.86),

$$\begin{aligned} \mathcal{L} = & \\ \mathrm{i}\psi^{+}\sigma \cdot \partial\psi - \tfrac{\mathrm{m}}{2}\left(\psi^{\mathrm{T}}\mathrm{C}\psi - \psi^{+}\mathrm{C}\psi^{*}\right) & \} \text{ massive fermion field} \\ +\partial_{\mu}\phi^{*}\partial^{\mu}\phi - \mathrm{V}(\phi) & \} \text{ scalar field} \\ +\lambda\left[\psi^{\mathrm{T}}\mathrm{C}\psi\phi - \phi^{*}\psi^{+}\mathrm{C}\psi^{*}\right] & \} \text{ interaction} \end{aligned} \tag{2.87}$$

describes a massive fermion field, a complex scalar field with the potential:

$$\begin{aligned} \mathrm{V}(\phi) &= \mathrm{m}^2\phi\phi^{*} - \lambda\mathrm{m}\left(\phi^2\phi^{*} + \phi\phi^{*2}\right) + \lambda^2\left(\phi\phi^{*}\right)^2 \\ &= \mathrm{m}^2|\phi|^2 - 2\lambda\mathrm{m}|\phi|^3\cos\alpha + \lambda^2|\phi|^4, \quad \phi = |\phi|\exp(\mathrm{i}\alpha) \end{aligned} \tag{2.88}$$

and Yukawa-like interaction between fermion and scalar fields. The Potential (2.88) has two minima: one at $\phi = 0$ and another at non-zero field strength, $\phi = \mathrm{m}/\lambda$, as shown in Figure 2.5. The simplest supersymmetric model considered above can be generalised to accommodate the SM gauge group with its representations and to account for three fermion families. The combination of the SUSY concept with building blocks of the SM is realised in the most economical way in the Minimal Supersymmetric Standard Model which is described in the next section.

2.3.3 The Minimal Supersymmetric Standard Model

The Minimal Supersymmetric extension of the Standard Model (MSSM) [16] postulates two types of supermultiplets:

- **the chiral supermultiplet** includes a single spin-$\frac{1}{2}$ Weyl fermion and a complex scalar field;
- **the gauge supermultiplet** comprises a vector gauge boson and a spin-$\frac{1}{2}$ Majorana particle.

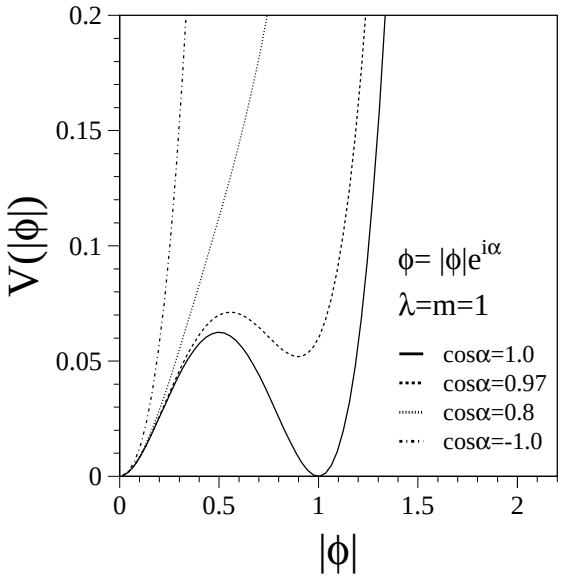

Figure 2.5: The dependence of the potential given by (2.88) on the absolute value of the scalar field, $|\phi|$ at four representative values of the phase α: $\phi = |\phi| \exp(\mathrm{i}\alpha)$. The potential has two minima at $\phi = 0$ and m/λ.

In the MSSM each of the known fundamental particles acquires a superpartner with spin differing by half a unit. The supersymmetry generators act independently of any internal symmetry, implying that particles in the same supermultiplet have identical electromagnetic charge, weak isospin and colour degrees of freedom and consequently belong to the same representation of the SM gauge group. The SM fermions reside in chiral supermultiplets together with their supersymmetric partners: **scalar quarks** and **scalar leptons** or **squarks** and **sleptons**. The left-handed and right-handed states of the quarks and leptons are separate two-component Weyl fermions with different gauge transformation properties in the SM, so each must have its own complex scalar partner, $\tilde{\mathrm{f}}_{\mathrm{L}}$ and $\tilde{\mathrm{f}}_{\mathrm{R}}$. The MSSM requires two Higgs doublets $\mathrm{H_u}$ and $\mathrm{H_d}$ with opposite hypercharges in order to give masses both to up-type and down-type fermions. The Higgs supermultiplets, which are of chiral structure, contain spin-$\frac{1}{2}$ fermions called Higgsinos, $\tilde{\mathrm{H}}_{\mathrm{u}}, \tilde{\mathrm{H}}_{\mathrm{d}}$, which generate so-called triangle anomalies [35]. These can be cancelled among themselves provided that there is an even number of Higgs supermultiplets.

The chiral supermultiplets are classified according to their transformation properties under the SM gauge group as illustrated in Table 2.5. The standard convention is that all chiral multiplets are defined in terms of left-handed Weyl spinors, so that the weak-isospin singlets are considered as the conjugates of the right-handed quarks and leptons.

The SM gauge bosons are placed in gauge supermultiplets along with their superpartners: spin-$\frac{1}{2}$ Majorana particles called gauginos. The gauge bosons $\mathrm{W}^{\pm}, \mathrm{W}^0$ and B are assigned with spin-$\frac{1}{2}$ superpartners $\tilde{\mathrm{W}}^{\pm}, \tilde{\mathrm{W}}^0$ and $\tilde{\mathrm{B}}$ called **winos** and **bino** whereas the octet of gluons is complemented with eight spin-$\frac{1}{2}$ gluinos, $\tilde{\mathrm{g}}$. Table 2.6 summarises gauge supermultiplets in the MSSM.

The particle spectrum of the MSSM affects the evolution of gauge couplings. If we assume that masses of scalar partners of the SM particles are of order 10^2 GeV and modify the Renormalisation Group Equations accordingly to the particle content of the MSSM, the running gauge couplings meet in a single point at a scale of $\sim 10^{16}$ GeV as

Names		spin 0	spin $\frac{1}{2}$	$SU(3)_C$ multiplets	$SU(2)_L$ multiplets	$U(1)_Y$ hypercharge
squarks, quarks	Q	$(\tilde{u}_L, \tilde{d}_L)$	(u_L, d_L)	3	2	$+\frac{1}{6}$
(×3 families)	$\bar{U}$	$\tilde{u}^*_R$	$u^\dagger_R$	$\bar{3}$	1	$-\frac{2}{3}$
	$\bar{D}$	$\tilde{d}^*_R$	$d^\dagger_R$	$\bar{3}$	1	$+\frac{1}{3}$
sleptons, leptons	L	$(\tilde{\nu}, \tilde{\ell}_L)$	(ν, ℓ_L)	1	2	$-\frac{1}{2}$
(×3 families)	$\bar{E}$	$\tilde{\ell}^*_R$	$\ell^\dagger_R$	1	1	$+1$
Higgs, higgsinos	H_u	(H^+_u, H^0_u)	$(\tilde{H}^+_u, \tilde{H}^0_u)$	1	2	$+\frac{1}{2}$
	H_d	(H^0_d, H^-_d)	$(\tilde{H}^0_d, \tilde{H}^-_d)$	1	2	$-\frac{1}{2}$

Table 2.5: Chiral supermultiplets in the MSSM.

Names	spin $\frac{1}{2}$	spin 1	$SU(3)_C$ multiplets	$SU(2)_L$ multiplets	$U(1)_Y$ hypercharge
gluino, gluon	$\tilde{g}$	g	8	1	0
winos, W bosons	$\tilde{W}^\pm\ \tilde{W}^0$	$W^\pm\ W^0$	1	3	0
bino, B boson	$\tilde{B}^0$	B^0	1	1	0

Table 2.6: Gauge supermultiplets in the MSSM.

shown in Figure 2.6. Thus, the MSSM can be considered as a first step towards Grand Unification Theories.

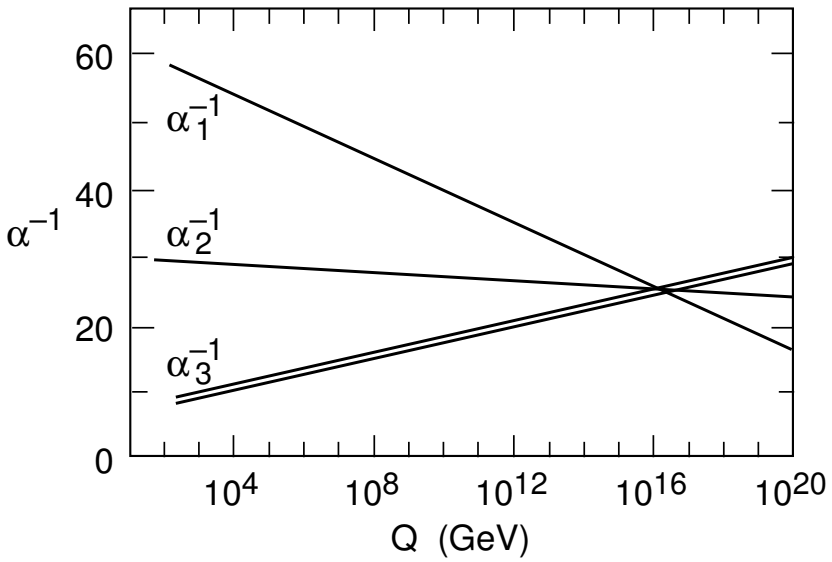

Figure 2.6: Evolution of the gauge couplings with energy scale calculated with the particle content of the MSSM. The gauge couplings are unified at a scale of $\sim 10^{16}$ GeV.

Now let us consider the construction of the MSSM Lagrangian which inherits the phenomenology of the SM. The Lagrangian (2.82) can be easily extended to account for several chiral supermultiplets:

$$\begin{aligned}\mathcal{L} &= \partial_\mu \phi_{\mathrm{j}}^* \partial^\mu \phi_{\mathrm{j}} + \mathrm{i}\psi_{\mathrm{j}}^+ \bar{\sigma}\cdot\partial\psi_{\mathrm{j}} + \mathrm{F}_{\mathrm{j}}^+ \mathrm{F}_{\mathrm{j}} \\ &+ \left(\mathrm{F}_{\mathrm{j}} \tfrac{\partial \mathrm{W}}{\partial \phi_{\mathrm{j}}} - \tfrac{1}{2}\psi_{\mathrm{j}}^{\mathrm{T}} \mathrm{C} \psi_{\mathrm{k}} \tfrac{\partial^2 \mathrm{W}}{\partial\phi_{\mathrm{j}}\partial\phi_{\mathrm{k}}} + \mathrm{h.c.}\right), \\ \mathrm{F}_{\mathrm{j}}^+ &= -\tfrac{\partial \mathrm{W}}{\partial \phi_{\mathrm{j}}},\end{aligned} \tag{2.89}$$

where j and k are indexing the chiral supermultiplets and ϕ and ψ are generic symbols for bosonic and fermionic components of the chiral supermultiplet, respectively. The supersymmetric generalisation of the Yukawa interactions is achieved by introducing the superpotential:

$$W_{Yukawa} = \lambda_{\mathrm{u}}^{\mathrm{jk}} \tilde{\mathrm{u}}_{\mathrm{R}}^{*\mathrm{j}} \mathrm{H_u}\cdot\tilde{\mathrm{Q}}_{\mathrm{L}}^{\mathrm{k}} \lambda_{\mathrm{d}}^{\mathrm{jk}} \tilde{\mathrm{d}}_{\mathrm{R}}^{*\mathrm{j}} \mathrm{H_d}\cdot\tilde{\mathrm{Q}}_{\mathrm{L}}^{\mathrm{k}} \lambda_{\ell}^{\mathrm{jk}} \tilde{\ell}_{\mathrm{R}}^{*\mathrm{j}} \mathrm{H_d}\cdot\tilde{\mathrm{E}}_{\mathrm{L}}^{\mathrm{k}}, \tag{2.90}$$

where $\lambda_{\mathrm{u}}^{\mathrm{jk}}$, $\lambda_{\mathrm{d}}^{\mathrm{jk}}$ and $\lambda_{\ell}^{\mathrm{jk}}$ are 3x3 matrices and $\tilde{\mathrm{Q}}_{\mathrm{L}}^{\mathrm{i}}, \tilde{\mathrm{u}}_{\mathrm{R}}^{*\mathrm{i}}, \tilde{\mathrm{d}}_{\mathrm{R}}^{*\mathrm{i}}, \tilde{\mathrm{L}}_{\mathrm{L}}^{\mathrm{i}}, \tilde{\ell}_{\mathrm{R}}^{*\mathrm{i}}$ denote scalar fermions of the i-th family which constitute five different representations of the $\mathrm{U(1)_Y}\otimes\mathrm{SU(2)_L}\otimes\mathrm{SU(3)_C}$ gauge group as indicated in Table 2.5. Being inserted into the second line of Equation (2.89) the superpotential (2.90) gives rise to the terms describing the well-known Yukawa interactions between Higgs bosons and fermions. Introducing gauge interactions requires modification of the first line of (2.89) to:

$$\begin{aligned}\mathcal{L}_{\mathrm{kin}} = \;& \mathrm{D}_\mu \phi_{\mathrm{j}}^* \mathrm{D}^\mu \phi_{\mathrm{j}} + +\mathrm{i}\psi_{\mathrm{j}}^+ \sigma^\mu \mathrm{D}_\mu \psi_{\mathrm{j}} + \mathrm{F}_{\mathrm{j}}^+ \mathrm{F}_{\mathrm{j}} \\ & -\mathrm{i}\sqrt{2}\mathrm{g_A}\left(\phi_{\mathrm{j}}^* (\lambda_{\mathrm{A}}^{\mathrm{a}})^{\mathrm{T}} \mathrm{t}_{\mathrm{A}}^{\mathrm{a}} \mathrm{C}\psi_{\mathrm{j}} - \psi_{\mathrm{j}}^+ \mathrm{t}_{\mathrm{A}}^{\mathrm{a}} \mathrm{C} (\lambda_{\mathrm{A}}^{\mathrm{a}})^* \phi_{\mathrm{j}}\right) + \mathrm{g_A} \mathrm{P}_{\mathrm{A}}^{\mathrm{a}} \phi_{\mathrm{j}}^* \mathrm{t}_{\mathrm{A}}^{\mathrm{a}} \phi_{\mathrm{j}},\end{aligned} \tag{2.91}$$

where the Lorentz derivative ∂_μ is replaced by the covariant derivative D_μ of the form (2.12); the $\mathrm{t}_{\mathrm{A}}^{\mathrm{a}}$ are generators of the SM gauge group A (A=$\mathrm{U(1)_Y}$, $\mathrm{SU(2)_L}$, $\mathrm{SU(3)_C}$; a=1 for $\mathrm{U(1)_Y}$, a=3 for $\mathrm{SU(2)_L}$, and a=8 for $\mathrm{SU(3)_C}$); $\mathrm{g_A}$ is the coupling of the gauge group A and $\lambda_{\mathrm{A}}^{\mathrm{a}}$ are the spinors describing gauginos associated with generators $\mathrm{t}_{\mathrm{A}}^{\mathrm{a}}$ of the gauge group A. Equation (2.91) implies summation over all the gauge groups, A, all the group generator indexes, a, and all the chiral supermultiplets, j. The auxiliary fields $\mathrm{P}_{\mathrm{A}}^{\mathrm{a}}$ can be eliminated using their equations of motion:

$$\mathrm{P}_{\mathrm{A}}^{\mathrm{a}} = -\mathrm{g_A}\phi_{\mathrm{j}}^* \mathrm{t}_{\mathrm{A}}^{\mathrm{a}} \phi_{\mathrm{j}}. \tag{2.92}$$

For each gauge group the following Lagrangian terms, involving the relevant gauge supermultiplets, are introduced:

$$\mathcal{L}_{\mathrm{gauge}} = -\frac{1}{4}\left(\mathrm{F}_{\mathrm{A}\mu\nu}^{\mathrm{a}}\right)^2 + \mathrm{i}(\lambda_{\mathrm{A}}^{\mathrm{a}})^+ \sigma^\mu \mathrm{D}_\mu \lambda_{\mathrm{A}}^{\mathrm{a}} + \frac{1}{2}(\mathrm{D}_{\mathrm{A}}^{\mathrm{a}})^2. \tag{2.93}$$

The full supersymmetric generalisation of the Standard Model Lagrangian can be written in the form:

$$\mathcal{L}_{\mathrm{SUSY}} = \mathcal{L}_{\mathrm{gauge}} + \mathcal{L}_{\mathrm{kin}} + \mathcal{L}_{\mathrm{Yukawa}} + \mathcal{L}_{\mu}, \tag{2.94}$$

which includes all the terms that were discussed plus $\mathcal{L}_\mu$ associated to a gauge invariant term that we can add to the superpotential:

$$W_\mu = \mu \mathrm{H_u} \cdot \mathrm{H_d}. \tag{2.95}$$

The parameter μ is the only new parameter which is added so far to the SM.

The Lagrangian (2.94) conserves the discrete quantum number:

$$\mathrm{R} = (-1)^{\mathrm{L}+3\mathrm{B}+2\mathrm{S}}, \tag{2.96}$$

where L is the lepton number, B is the baryon number and S is the spin. This quantity is called **R-parity**. It can be easily checked that R=+1 for the leptons, quarks, gauge and Higgs bosons while R=-1 for their supersymmetric companions. The MSSM in which R-parity is conserved leads to the following phenomenological predictions:

1. SUSY particles can be produced only in pairs;
2. SUSY particles decay to SM particle(s) and supersymmetric one and at the end of the decay chain the lightest supersymmetric particle (LSP) is produced;
3. the LSP must be stable.

The theory described by the Lagrangian (2.94) has exact supersymmetry predicting that supersymmetric particles degenerate in mass with their SM partners. However, this prediction contradicts experimental observations. No SUSY particles have been observed so far at particle accelerators meaning that if SUSY particles exist, they must have larger masses than the SM particles. Therefore, one has to admit that supersymmetry must be broken. Several models have been developed to explain the dynamics of supersymmetry breaking. A detailed description of these models can be found elsewhere [36]. Hereafter I will consider supersymmetry breaking from the phenomenological point of view. Supersymmetry breaking is implemented by adding so-called **soft supersymmetry breaking** terms to the Lagrangian (2.94). These terms are:

$$\mathcal{L}_{\mathrm{soft}} = -\mathrm{M}_{\mathrm{j}}^2 |\phi_{\mathrm{j}}|^2 - \mathrm{M}_{\mathrm{a}}^{\mathrm{A}} (\lambda_{\mathrm{A}}^{\mathrm{a}})^{\mathrm{T}} \mathrm{C} \lambda_{\mathrm{A}}^{\mathrm{a}} + \mathrm{B}\mu \mathrm{H_u} \cdot \mathrm{H_d} + A\, W_a, \tag{2.97}$$

where W_a is the superpotential (2.90) plus other possible analytic terms cubic in the scalar fields ϕ_{j}. The terms (2.97) ensure the mass splitting between particles residing in the same supermultiplet and move superpartners of the SM particles to higher mass scales. All the coefficients in (2.97) have the dimensions of (mass) and (mass)^2. The "softness" of these terms implies that they do not regenerate quadratic mass divergences of the scalar or any other fundamental field in the theory. It is $\mathcal{L}_{\mathrm{soft}}$ which introduces most of new SUSY parameters, 104 in total, whereas the Lagrangian of unbroken SUSY contains only one additional parameter, μ.

The MSSM makes many interesting phenomenological predictions that can be probed at currently operating accelerators or at forthcoming experimental facilities. A detailed discussion of different aspects of the MSSM and its phenomenological consequences can be found elsewhere [33]. I will focus on the Higgs sector of the MSSM since it is of primary interest for the topic of this thesis.

2.3.4 The Higgs Sector and Electroweak Symmetry Breaking in the MSSM

It should be noted at this point that SUSY provides the mechanism to Electroweak (EW) Symmetry Breaking. The Higgs sector of the MSSM corresponds to a 2HDM of type II. The Higgs potential derived from the superpotential and the relevant terms of $\mathcal{L}_{\text{soft}}$ reads:

$$\begin{aligned} V_H = m_1^2|H_d|^2 + m_2^2|H_u|^2 - m_3^2\left(\epsilon_{ab}H_d^a H_u^b + h.c\right) \\ +\tfrac{g_1^2+g_2^2}{8}\left(|H_u|^2 - |H_d|^2\right)^2 + \tfrac{g_2^2}{2}|H_u^* H_d|^2 \end{aligned} \tag{2.98}$$

where $m_1^2 = \mu^2 + m_{H_d}^2$, $m_2^2 = \mu^2 + m_{H_u}^2$, $m_3^2 = \mu B$ and ϵ_{ab} is antisymmetric spinorial tensor. Now, let us investigate the conditions ensuring EW Symmetry breaking. For the potential to be bounded from below, we have to require that

$$\mathcal{S} = m_1^2 + m_2^2 - 2|m_3^2| \geq 0. \tag{2.99}$$

In order to get non-vanishing vacuum expectation values we must destabilise the origin in field space:

$$\mathcal{B} = m_1^2 m_2^2 - m_3^4 \leq 0. \tag{2.100}$$

To fulfil these relations one or both $m_{H_{u,d}}^2$ must be negative.

The vacuum expectation values of the Higgs doublets ν_1 and ν_2 are related to the parameters m_1^2, m_2^2 and m_3^2 in the following way:

$$\sin 2\beta = -\frac{2m_3^2}{m_1^2 + m_2^2}, \qquad \nu_1^2 + \nu_2^2 = \frac{3}{g_1^2 + g_2^2}\frac{m_1^2 - m_2^2\tan\beta}{\tan^2\beta - 1}. \tag{2.101}$$

The W and Z masses are expressed accordingly to the general 2HDM relations given by (2.71).

It should be noted that in SUSY EW Symmetry Breaking is achieved in a more natural way than in the SM. The Yukawa interactions of the Higgs doublets with heavy fermions, for example top quark, tend to drive $m_{H_{u,d}}^2$ to smaller values at smaller renormalisation scales. Even if $m_{H_{u,d}}^2 > 0$ at the input energy scale, for instance GUT scale, one or both $m_{H_{u,d}}^2$ may acquire negative values at the EW scale which is necessary to ensure EW Symmetry Breaking. Thus, in SUSY it is possible to generate EW Symmetry Breaking radiatively [37] whereas in the SM this is done "by hand". After EW Symmetry Breaking occurs five physical Higgs particles emerge: two neutral CP-even bosons h and H ($m_h < m_H$), a neutral CP-odd boson A and a pair of charged bosons $H^\pm$. Their tree level masses are given by:

$$m_A^2 = \frac{2|\mu|B}{\sin 2\beta}, \tag{2.102}$$

$$m_{H^\pm}^2 = m_A^2 + m_W^2, \tag{2.103}$$

$$m_{h,H}^2 = \frac{1}{2}\left[m_A^2 + m_Z^2 \mp \sqrt{\left(m_A^2 + m_Z^2\right)^2 - 4m_A^2 m_Z^2\cos^2 2\beta}\right]. \tag{2.104}$$

From Equation (2.104) it follows that at tree level the mass of the lightest neutral Higgs boson is smaller than the mass of the Z boson, $m_h < m_Z|\cos 2\beta|$. However, radiative corrections, in particular from the top-quark and scalar top quark loops, considerably affect the masses of the Higgs bosons. After having taken these radiative corrections into account the upper bound on m_h can be pushed up to about 135 GeV [38,39]. The masses of up-type quarks are generated via Yukawa interactions with the H_u doublet and masses of down-type quarks and charged leptons arise from Yukawa interactions with H_d.

2.3.5 Constraint MSSM and Benchmark Scenarios

The search for the neutral Higgs bosons is performed in the context of the constraint MSSM assuming the degeneracy of all the sfermion masses and the unification of all the Higgs-sfermion trilinear couplings at the EW scale and the unification of U(1) and SU(2) gaugino mass parameters at the GUT scale. These assumptions have a little impact on the Higgs boson phenomenology but reduce the number of free parameters to 7. These are: the universal sfermion mass parameter, M_{SUSY}; the common Higgs-sfermion trilinear coupling, $\mathcal{A}$; the supersymmetric Higgs mass parameter, μ; the SU(2) gaugino mass parameter, M_2; the gluino mass parameter, M_3; m_A and tanβ . The U(1) gaugino mass parameter, M_1, is derived from M_2 using the GUT relation: $M_1 = M_2(5\sin^2\theta_w/3\cos^2\theta_w)$.

As was already mentioned, the radiative corrections to m_h can be quite large. They are strongly dependent on top quark mass, M_{SUSY} and the mixing between left-handed and right-handed components of the scalar top quark.

Three benchmark scenarios are considered [40]. The first one, denoted "no mixing" scenario, corresponds to vanishing mixing between left-handed and right-handed components of scalar top quark. The MSSM parameters are chosen as follows: M_{SUSY} = 1 TeV; M_2 = 200 GeV; μ = -200 GeV; the scalar top mixing parameter defined as

$$X_t = \mathcal{A} - \mu \cot\beta$$

is set to zero. The gluino mass M_3 is fixed to 800 GeV and has a little effect on the Higgs boson phenomenology in this scenario. Keeping these parameters fixed, a scan over two remaining parameters tanβ and m_A is performed in the ranges: $0.5 \leq$ tan$\beta \leq 30$ and 10 GeV $\leq m_A \leq$ 1 TeV. The search for neutral Higgs bosons is performed assuming that the widths of h and A bosons are considerably smaller than the experimental mass resolutions. This assumption is valid for tan$\beta < 30$ in this scenario and hence higher values of tanβ are not scanned.

The second scenario called "m_h − max" is designed to yield the maximal upper theoretical bound on m_h as function of tanβ . The values of the MSSM parameters are set to the same values as in the "no mixing" scheme, with exception of the X_t parameter which is fixed to $2M_{SUSY}$ following the conventions of the two-loop diagrammatic approach [39,41]. The scan over tanβ and m_A is performed in the same ranges as in the "no mixing" scenario. The values of tanβ exceeding 30 are not considered to satisfy the assumptions made on the decay widths.

The third MSSM scheme termed "large-μ" scenario corresponds to the following choice of the MSSM parameters: M_{SUSY} = 400 GeV; M_2 = 400 GeV; μ = 1 TeV; X_t =

-300 GeV; $M_3 = 200$ GeV. The m_A is scanned in the range from 10 to 400 GeV for tanβ slices between 0.7 and 50. The values of tanβ less than 0.7 are not scanned because of instability of the theoretical calculations. On the other hand, the assumption that the widths of the Higgs bosons are small compared to experimental mass resolutions is valid at tanβ values up to 50. A more specific features of the "large-μ" scenario are discussed later on in the section devoted to production and decays of MSSM Higgs bosons at LEP.

The mass of the top quark which essentially affects the calculation of radiative corrections to m_h is taken to be 174.3 GeV, the current average of TEVATRON measurement [43].

The dependence of m_h on m_A at two representative tan β values, 2 and 25, is shown in Figures 2.7a, 2.7b and 2.7c for the "no mixing", "m_h -max" and "large-μ" scenario, respectively.

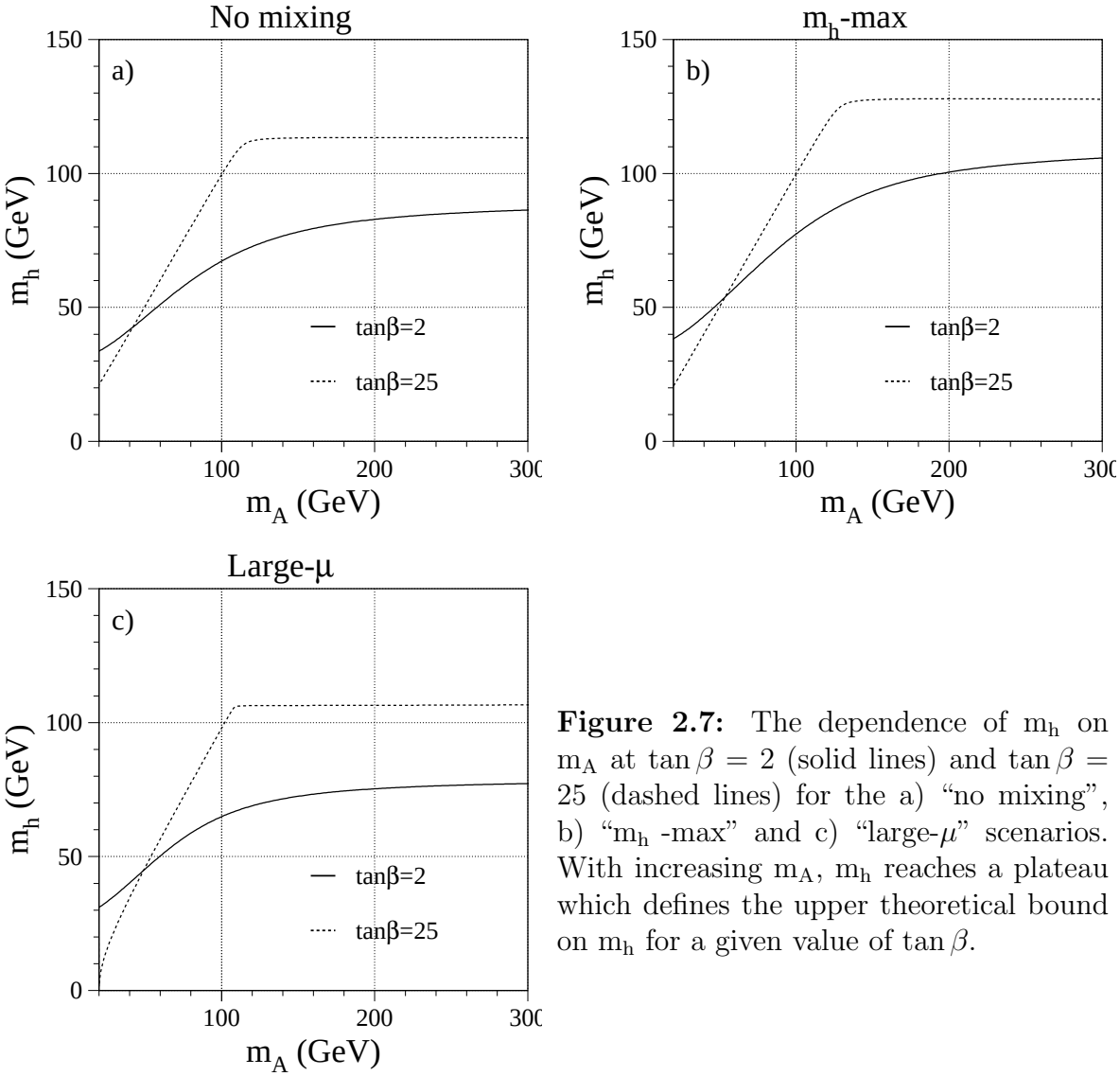

Figure 2.7: The dependence of m_h on m_A at tan $\beta = 2$ (solid lines) and tan $\beta = 25$ (dashed lines) for the a) "no mixing", b) "m_h -max" and c) "large-μ" scenarios. With increasing m_A, m_h reaches a plateau which defines the upper theoretical bound on m_h for a given value of tan β.

Chapter 3

Higgs Bosons at LEP

After having reviewed the Higgs sector in the SM and its extensions the possible production scenarios in e^+e^- collisions at LEP and the main decay channels of neutral Higgs bosons are discussed in this chapter. During the last two years of operation LEP produced e^+e^- collisions at center-of-mass energies around 200 GeV allowing for the detection of neutral Higgs bosons with masses of order 100 GeV. In the following sections the considerations are conducted according to this mass scale.

3.1 Production and Decays of the SM Higgs Boson at LEP

At LEP the production of the SM Higgs boson is expected mainly through the Higgs-strahlung process illustrated in Figure 3.1. Electron and positron annihilate into virtual Z which then emits the Higgs boson and becomes on-shell. The cross section of the Higgs-strahlung mechanism is described by the following formula [44]:

$$\sigma(e^+e^- \to HZ) = \frac{G_F^2 m_Z^4}{24\pi s}(g_{Ve}^2 + g_{Ae}^2)\lambda^{\frac{1}{2}}\frac{\lambda + 12m_Z^2/s}{(1 - m_Z^2/s)^2}, \tag{3.1}$$

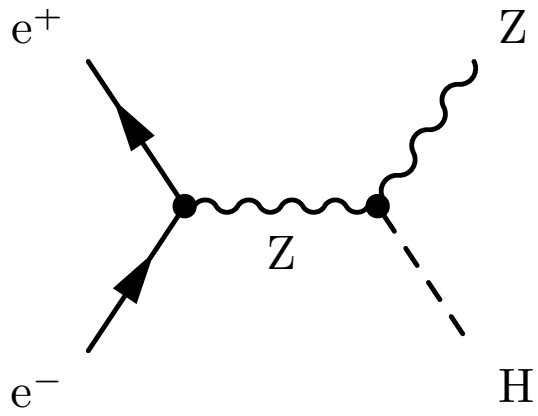

Figure 3.1: Higgs-strahlung: The Higgs boson is produced together with the Z boson.

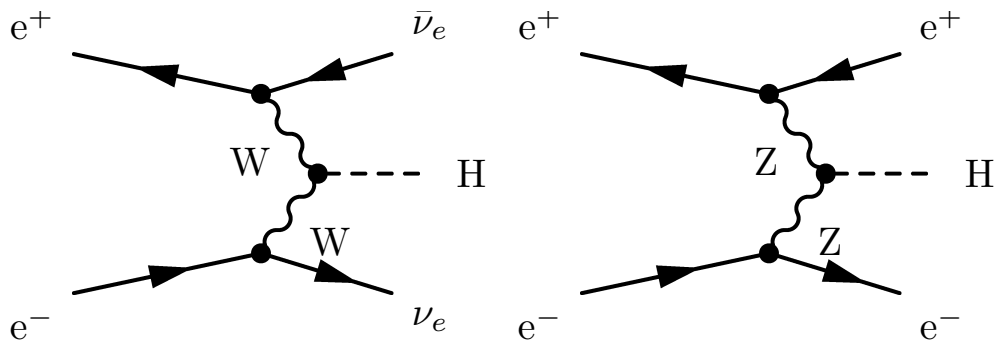

Figure 3.2: WW and ZZ fusion diagrams: They are suppressed by an additional power of the electroweak coupling with respect to the Higgs-strahlung process.

where $\sqrt{s}$ is the center-of-mass energy, $g_{Ae} = -1/2$ and $g_{Ve} = -1/2 + 2\sin^2\theta_w$ are the neutral current couplings of the electron and $\lambda = (1 - m_H^2/s - m_Z^2/s)^2 - 4m_H^2 m_Z^2/s^2$ is the two-particle phase space function. It should be noted that the formula given by (3.1) does not include the effect of finite width of the Z boson, Γ_Z. Therefore, it predicts that the cross section approaches zero in the vicinity of the HZ kinematic limit, $\sqrt{s} - m_Z - m_H = 0$. The WW and ZZ fusion processes depicted in Figure 3.2 contribute to the production of the Higgs boson with smaller cross sections.

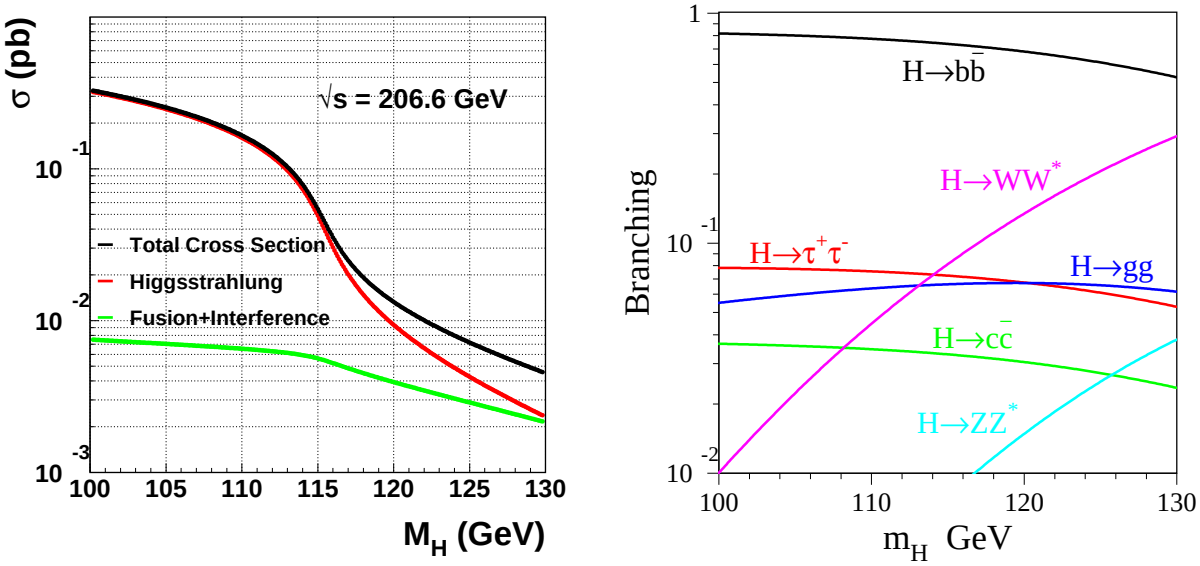

a) b)

Figure 3.3: The production and decays of the SM Higgs Boson. a) The cross sections of the production mechanisms and b) the decay branching fractions as a function of m_H.

Figure 3.3a illustrates the evolution of the cross sections of the Higgs boson production mechanisms with the Higgs boson mass at $\sqrt{s} = 206.6$ GeV. In this figure the dependence of the Higgs-strahlung cross section now takes Γ_Z into account and predicts very small but non-zero cross section beyond the HZ kinematic limit, when the Z boson is produced off-shell.

The angular distribution of the H and Z particles in the Higgs-strahlung process is determined by the spin-parity quantum numbers of the Higgs boson, $J^P = 0^+$, and given by [44]:

$$\frac{d\sigma}{d\cos\Theta} \sim \lambda \sin^2\Theta + 8m_Z^2/s, \tag{3.2}$$

where Θ is the polar angle between the momentum vector of the Higgs boson and the electron beam axis. At high energies, $\sqrt{s} \gg m_H + m_Z$, when the Higgs-strahlung process takes place far above the kinematic threshold the Z boson is produced longitudinally polarised and the angular distribution approaches asymptotically the $\sin^2\Theta$ dependence. At the threshold where λ approaches zero, the angular distribution becomes independent of $\cos\Theta$.

The lifetime of the Higgs boson depends on its mass, m_H. The heavier the Higgs boson is, the more decay channels open and therefore the larger its decay width, Γ_H, becomes. Consequently, the lifetime of the Higgs boson decreases with increasing m_H. At $m_H \sim 100$ GeV Γ_H is predicted to be few MeV. Hence the Higgs boson decays practically at the production point into lighter particles. Analyses aimed to search for the SM Higgs boson make use of its specific decay modes distinguishing it from other particles. The Higgs boson prefers to decay into more massive particles provided that the decay is kinematically allowed.

From the Yukawa couplings the partial decay widths of the Higgs boson to fermions can be derived. The width into leptons is given by [45]:

$$\Gamma(H \to \ell^+\ell^-) = \frac{G_F m_\ell^2}{4\sqrt{2}\pi} m_H, \tag{3.3}$$

with $\ell = e, \mu, \tau$. Since the electron and the muon are much lighter than the tau lepton

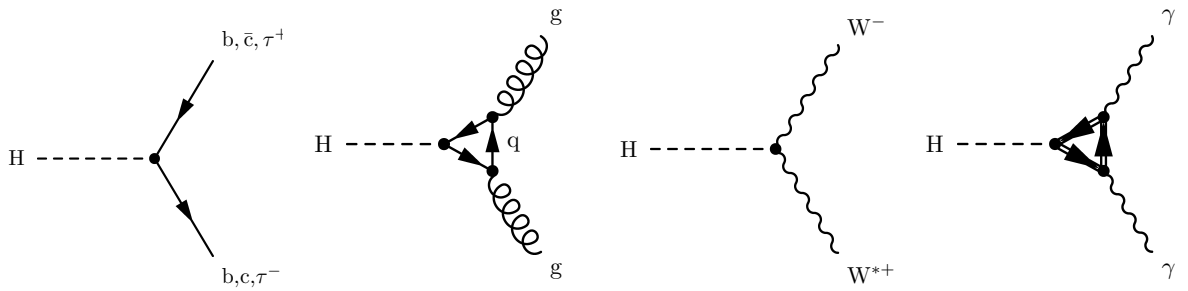

Figure 3.4: Higgs boson decay modes. The decay into gluons is realised by heavy quark loops. Decays into photons are possible via quark or $W^\pm$ loops.

($m_e \approx 0.5$ MeV, $m_\mu \approx 105$ MeV, $m_\tau \approx 1777$ MeV), the decay of the Higgs into muons is suppressed by a factor of 3×10^{-3} compared to the decay into tau leptons and the electron decay by a factor of 8×10^{-8}.

For the Higgs decay into quarks, the colour factor ($N_C = 3$) and QCD corrections have to be taken into account [46]:

$$\Gamma(H \to q\bar{q}) = \frac{3G_F}{4\sqrt{2}\pi} m_q^2(m_H) m_H \cdot \delta(\alpha_s, m_H, m_t). \tag{3.4}$$

Here, δ is a function of the strong interaction coupling α_s. The quark masses have to be taken at the mass scale m_H. Due to the colour factor three and the larger b quark mass the Higgs boson decay into $b\bar{b}$ is enhanced by about one order of magnitude with respect to the $H \to \tau^+\tau^-$ decay. The decay into $c\bar{c}$ is smaller in the mass range of interest due to the relatively small mass m_c of about 0.6 GeV [47].

The channel $H \to WW^*$ becomes relevant for Higgs boson masses $m_H > m_W$ when one of the W bosons can be produced on mass shell. The partial width for this channel is given by the following equation [44]:

$$\Gamma(H \to WW^*) = \frac{3G_F^2 m_W^4}{16\pi^3} m_H R(x), \tag{3.5}$$

where R(x) is a function which depends on the ratio $x = m_W^2/m_H^2$. In the range of the Higgs boson masses investigated at LEP, the decay of the Higgs boson into WW^* occurs far below the kinematic threshold and its rate is smaller compared to the rate of the kinematically allowed decays into heavy fermions. Due to the larger mass of the Z boson and the reduced neutral current couplings compared to the W mass and charged couplings, respectively, the branching fraction of the decay to ZZ^* is one order of magnitude lower with respect to the $H \to WW^*$ channel.

At tree level, no decays into gluons or photons occur. However, the massless gauge bosons can be produced at one loop level as shown in Figure 3.4. The branching fractions of the Higgs boson as a function of the Higgs boson mass are shown in Figure 3.3b.

3.2 Production and Decays of Neutral Higgs Bosons in the 2HDM and MSSM

In the 2HDM the production of the light and heavy neutral CP-even Higgs bosons, h and H, through the Higgs-strahlung mechanism:

$$e^+e^- \to Z^* \to hZ(HZ) \tag{3.6}$$

is complemented with the processes

$$e^+e^- \to Z^* \to hA(HA). \tag{3.7}$$

The cross sections of the processes (3.6) and (3.7) are related to the cross section of

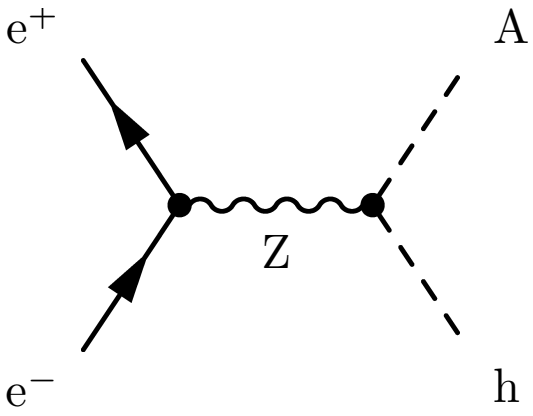

Figure 3.5: Associated pair production in the 2HDM: The CP-even Higgs boson h is produced together with the CP-odd Higgs boson A.

the Higgs-strahlung process in the SM, $\sigma_{\mathrm{HZ}}^{\mathrm{SM}}$, and the 2HDM parameters α and β in the following way:

$$\sigma_{\mathrm{hZ}} = \sin^2(\beta-\alpha)\sigma_{\mathrm{HZ}}^{\mathrm{SM}} \tag{3.8}$$

$$\sigma_{\mathrm{HZ}} = \cos^2(\beta-\alpha)\sigma_{\mathrm{HZ}}^{\mathrm{SM}} \tag{3.9}$$

$$\sigma_{\mathrm{hA}} = \cos^2(\beta-\alpha)\bar{\lambda}_{\mathrm{hA}}\sigma_{\mathrm{HZ}}^{\mathrm{SM}} \tag{3.10}$$

$$\sigma_{\mathrm{HA}} = \sin^2(\beta-\alpha)\bar{\lambda}_{\mathrm{HA}}\sigma_{\mathrm{HZ}}^{\mathrm{SM}} \tag{3.11}$$

The factor $\bar{\lambda}$, defined as

$$\bar{\lambda}_{\mathrm{hA,HA}} = \frac{\lambda_{\mathrm{hA,HA}}^{3/2}}{\lambda_{\mathrm{hZ,HZ}}^{1/2}\left[12\mathrm{m}_{\mathrm{Z}}^2/\mathrm{s}+\lambda_{\mathrm{hZ,HZ}}\right]}, \tag{3.12}$$

accounts for the correct suppression of the P-wave cross section near the kinematic threshold. The quantity $\lambda_{\mathrm{ij}} = [1-(\mathrm{m_i}+\mathrm{m_j})^2/\mathrm{s}]\,[1-(\mathrm{m_i}-\mathrm{m_j})^2/\mathrm{s}]$ is the usual momentum factor of the two particle phase space. The angular distributions exhibit the standard behaviour expected for the Higgs-strahlung mechanism and the spin-zero associated pair production process [44]:

$$\frac{d\sigma}{d\cos\Theta} \sim \begin{cases} \lambda_{\mathrm{hZ,HZ}}\sin^2\Theta + 8\mathrm{m}_{\mathrm{Z}}^2/\mathrm{s} & \text{for } \mathrm{e^+e^-} \to \mathrm{hZ(HZ)}, \\ \sin^2\Theta & \text{for } \mathrm{e^+e^-} \to \mathrm{hA(HA)}. \end{cases} \tag{3.13}$$

The couplings of the Higgs bosons to fermions involve as a scale factor geometric functions of the parameters α and β as can be seen from Table 2.4. Consequently, the corresponding partial widths are proportional to the square of these factors and in the case of the type II model read:

$$\begin{aligned} &\Gamma_{\mathrm{h}\ell\ell} = \tfrac{\sin^2\alpha}{\cos^2\beta}\,\Gamma_{\mathrm{h}\ell\ell}^{\mathrm{SM}}, \quad \Gamma_{\mathrm{hu\bar{u}}} = \tfrac{\cos^2\alpha}{\sin^2\beta}\,\Gamma_{\mathrm{hu\bar{u}}}^{\mathrm{SM}}, \quad \Gamma_{\mathrm{hd\bar{d}}} = \tfrac{\sin^2\alpha}{\cos^2\beta}\,\Gamma_{\mathrm{hd\bar{d}}}^{\mathrm{SM}}, \\ &\Gamma_{\mathrm{H}\ell\ell} = \tfrac{\cos^2\alpha}{\sin^2\beta}\,\Gamma_{\mathrm{h}\ell\ell}^{\mathrm{SM}}, \quad \Gamma_{\mathrm{Hu\bar{u}}} = \tfrac{\sin^2\alpha}{\cos^2\beta}\,\Gamma_{\mathrm{hu\bar{u}}}^{\mathrm{SM}}, \quad \Gamma_{\mathrm{Hd\bar{d}}} = \tfrac{\cos^2\alpha}{\sin^2\beta}\,\Gamma_{\mathrm{hd\bar{d}}}^{\mathrm{SM}}, \\ &\Gamma_{\mathrm{A}\ell\ell} = \tan^2\beta\,\Gamma_{\mathrm{h}\ell\ell}^{\mathrm{SM}}, \quad \Gamma_{\mathrm{Au\bar{u}}} = \cot^2\beta\,\Gamma_{\mathrm{hu\bar{u}}}^{\mathrm{SM}}, \quad \Gamma_{\mathrm{Ad\bar{d}}} = \tan^2\beta\,\Gamma_{\mathrm{hd\bar{d}}}^{\mathrm{SM}}, \end{aligned} \tag{3.14}$$

with Γ^{SM}_{Hff} denoting the partial width of the SM Higgs boson decay into the corresponding fermion antifermion pair.

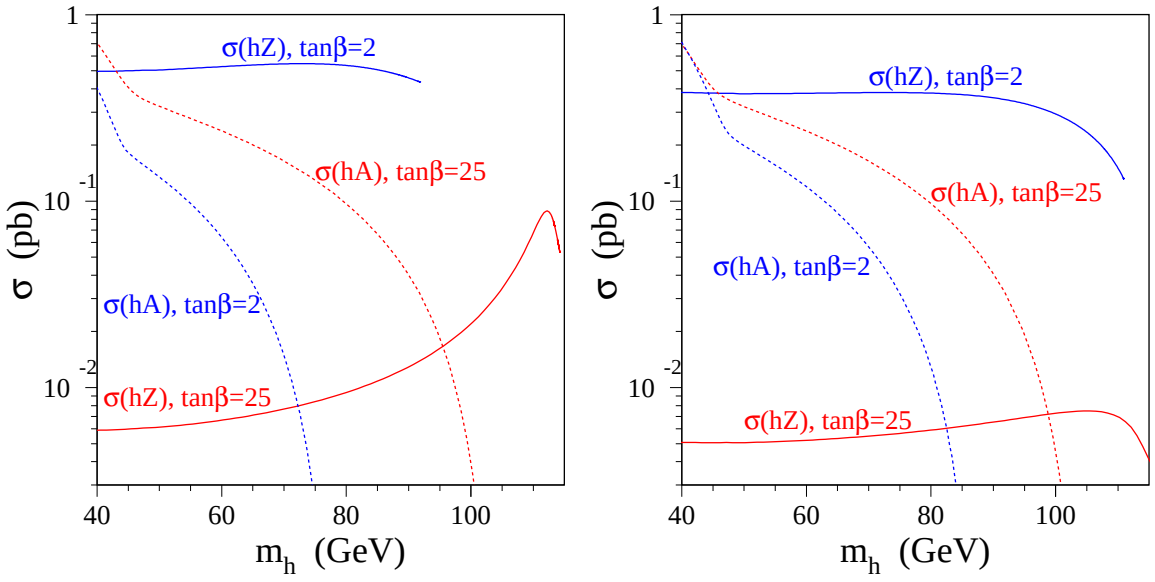

a) "No mixing" scenario b) "m_h-max" scenario

Figure 3.6: The cross section of the hZ and hA production at $\sqrt{s}$=206 GeV in a) "no mixing" and b) "m_h-max" scenarios for tanβ = 2 and 25. Curves stop at values corresponding to the upper theoretical bounds on m_h for a given tanβ value. The point $m_h \approx 45$ GeV corresponds to $m_h + m_A \sim m_Z$. This causes the sudden change in the $e^+e^- \to hA$ cross section evolution as for $m_h \leq 45$ GeV the hA production is dominated by the radiative return to the Z resonance, which cannot kinematically contribute beyond this point.

There are no strong theoretical arguments favouring a particular choice of the parameters α and β and thus predicting specific branching fractions for the Higgs bosons in 2HDM. Due to the fact that up-type and down-type fermions couple to the Higgs bosons in a different way, scenarios are possible in 2HDM in which couplings of the Higgs bosons to down-type fermions are reduced while couplings to up-type fermions are enhanced. An extreme scenario is realised by setting tanβ to very low values, tanβ $\ll$1, cotβ $\gg$1. In this case h and A decays into $c\bar{c}$ and via charm and top quark loops into a gluon pair are significantly enhanced and supplant decays to $b\bar{b}$ and $\tau^+\tau^-$.

The structure of the Higgs sector in the MSSM corresponds to the 2HDM of type II. Hence the production mechanisms for the neutral Higgs bosons of the MSSM are identical to those described above. The dependence of the $e^+e^- \to hZ$ and $e^+e^- \to hA$ cross sections on m_h is shown in Figure 3.6 at two representative tanβ values, 2 and 25, for the "m_h-max" and "no mixing" scenarios. At tan$\beta \gtrsim 10$ and $m_h \lesssim 100$ GeV, the quantity $\sin^2(\beta - \alpha)$ is close to zero and only associated Higgs boson pair production contributes

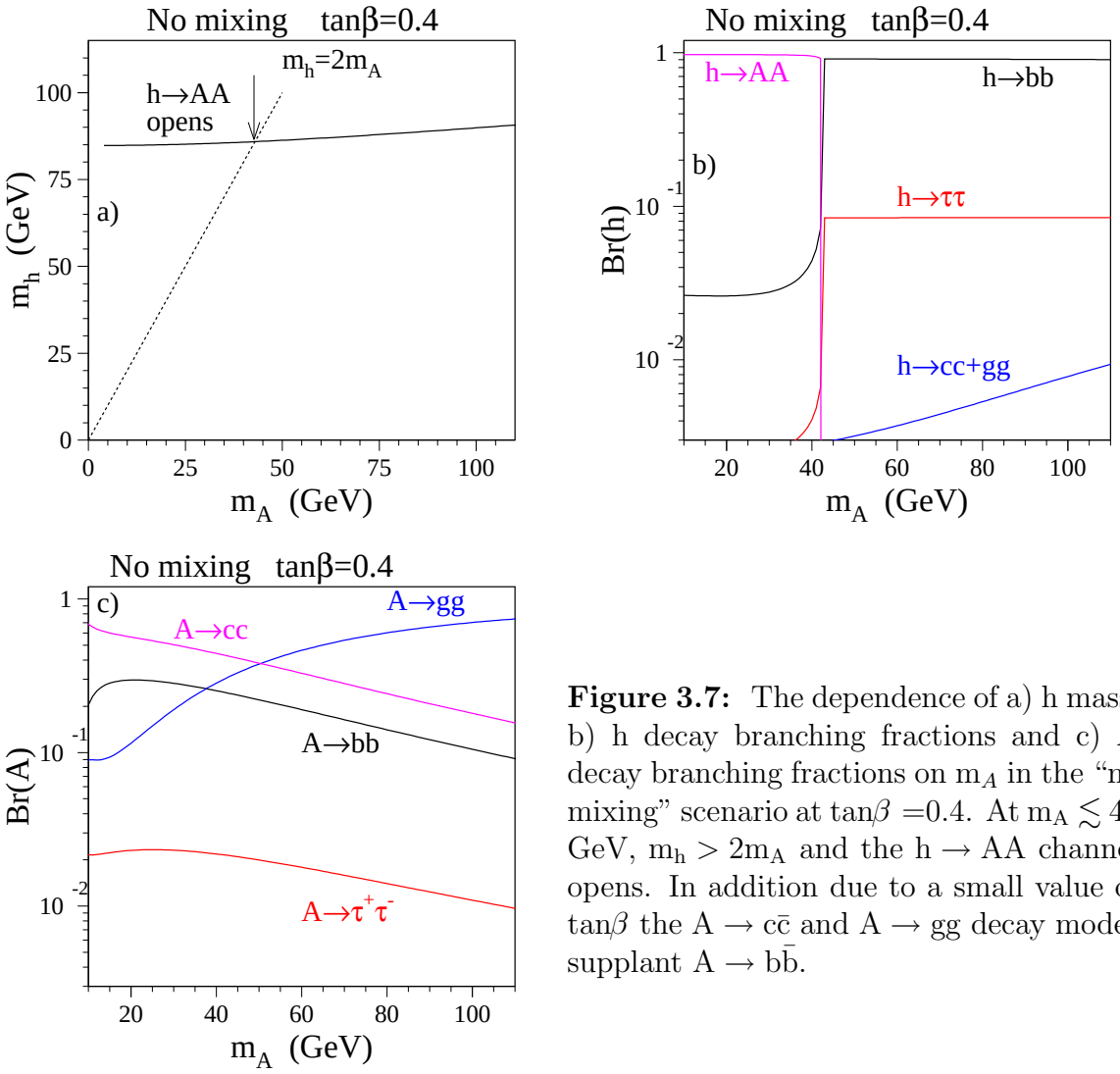

Figure 3.7: The dependence of a) h mass, b) h decay branching fractions and c) A decay branching fractions on m_A in the "no mixing" scenario at tanβ =0.4. At $m_A \lesssim 42$ GeV, $m_h > 2m_A$ and the $h \to AA$ channel opens. In addition due to a small value of tanβ the $A \to c\bar{c}$ and $A \to gg$ decay modes supplant $A \to b\bar{b}$.

to the signal. For these models, m_h is predicted to be close to m_A, $m_h \approx m_A$. The difference in mass reaches not more than 5 GeV. With decreasing tanβ and increasing m_h, the quantity $\sin^2(\beta - \alpha)$ increases leading to the rise of the $e^+e^- \to hZ$ cross section and fall of the $e^+e^- \to hA$ cross section. As a consequence, at a certain point the Higgs-strahlung mechanism becomes dominant. The $e^+e^- \to hZ$ process prevails, for instance, in the mass range $m_h \gtrsim 90$ GeV at tan$\beta \approx 8$ and $m_h \gtrsim 60$ GeV at tan$\beta \approx 4$.

For a larger part of MSSM parameter space the decay of h and A to $b\bar{b}$ is dominant followed by the decay to $\tau^+\tau^-$. However, at certain conditions other decay modes can be enhanced. As an example, Figure 3.7 illustrates the situation when the channel $h \to AA$ opens and in addition $A \to c\bar{c}$ and $A \to gg$ decay modes supplant $A \to b\bar{b}$.

In the "large-μ" scenario the maximum allowed value of m_h is less than 108 GeV for any tanβ value, thus making the light Higgs boson, h, kinematically accessible at the highest LEP energies over the entire $(\tan\beta, m_A)$ plane. For some choices of m_A and tanβ , the $e^+e^- \to hZ$ cross section is suppressed by a small value of $\sin^2(\beta - \alpha)$, and the $e^+e^- \to hA$ process is kinematically inaccessible. For these models, however, the heavy

Higgs boson, H, has the mass less than 109 GeV and can be produced with relatively high cross section via the Higgs-strahlung process as illustrated in Figure 3.8a. The detection of Higgs boson signal in the "large-μ" scenario is complicated by the pathological regions in the $(\tan\beta, \mathrm{m_A})$ plane where the decay of either h or H to $\mathrm{b\bar{b}}$ is suppressed due to large corrections from SUSY loop processes [48,49]. This situation is illustrated in Figure 3.8b. The suppression of the $\mathrm{h(H)} \to \mathrm{b\bar{b}}$ decay mode is accompanied by an enhancement of the $\mathrm{h(H)} \to \mathrm{c\bar{c}}, \mathrm{gg}, \mathrm{WW}^*, \tau^+\tau^-$ channels. For many of these models, the decay into a tau-lepton pair is also suppressed providing an additional experimental challenge.

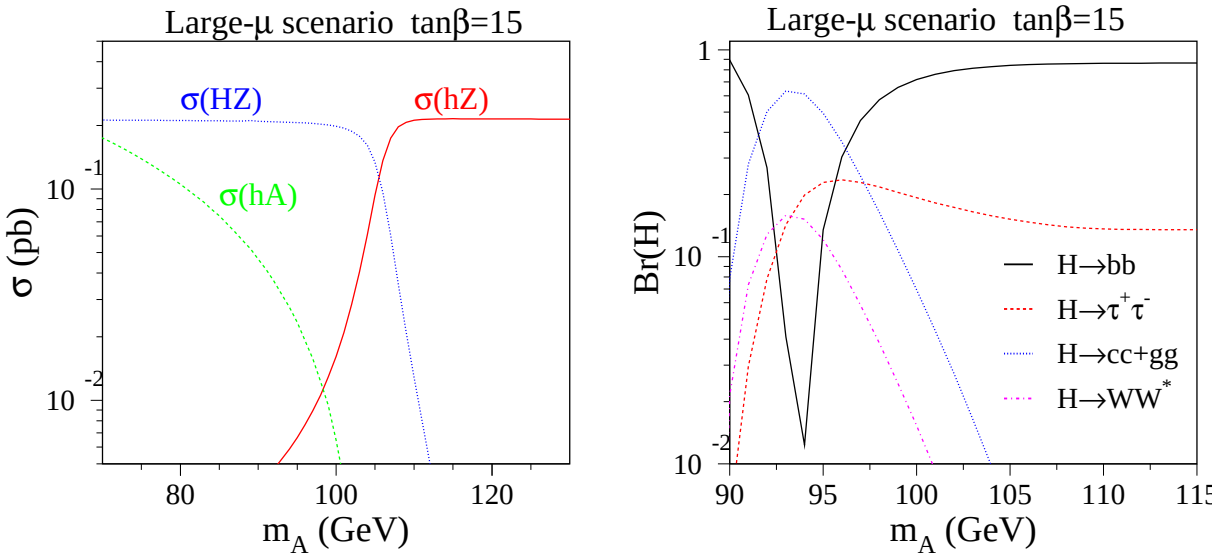

Figure 3.8: a) The cross sections of the processes contributing to the Higgs boson signal at $\sqrt{s} = 206$ GeV and b) the branching fractions of the heavy Higgs boson H as a function of m_A in the "large-μ" scenario at $\tan\beta = 15$. At $m_A \lesssim 110$ GeV, m_H is about 108 GeV and H becomes accessible at LEP via the $\mathrm{e^+e^-} \to \mathrm{HZ}$ process. At m_A values around 94 GeV, the $H \to b\bar{b}$ decay is suppressed whereas $H \to c\bar{c}, gg, WW^*$ decays are enhanced.

3.3 Limits on the Higgs Boson Mass

Theoretical Bounds on the Higgs boson mass

Although the Standard Model does not predict the mass of the Higgs boson, constraints on it can be deduced from theoretical arguments.

For internal consistency of the SM, the perturbation approach has to be valid. Processes mediated by the Higgs boson are needed to compensate for the increasing cross

section of the scattering of the longitudinally polarised W bosons. However, if $m_H \gtrsim 1$ TeV, the coupling of the Higgs boson to W bosons becomes so large that a perturbation approach fails. Therefore, the consistency requires an upper limit of $m_H \lesssim 1$ TeV [50].

More stringent theoretical bounds are based on the assumption that the SM is an effective theory valid up to a certain renormalisation scale Λ. Higher order corrections modify the Higgs potential (2.40) in the following way [51]:

$$V(\Phi^\dagger\Phi) = \lambda\left(\Phi^\dagger\Phi - \frac{\mu^2}{2\lambda}\right)^2 + V_1\left(\Lambda, m_t, m_H\right), \tag{3.15}$$

where the additional term depends on m_H, m_t and Λ. Vacuum stability requires that $V_1\left(\Lambda, m_t, m_H\right)$ should not destroy the shape of the potential. The vacuum is stable, i.e. the potential has an absolute minimum at non-zero field strength, if the Higgs boson mass is high enough to keep the coefficient in front of $\left(\Phi^\dagger\Phi\right)^2$ positive even after corrections. This theoretical argument bounds the Higgs boson mass from below. An upper limit on m_H is obtained considering the Higgs self coupling λ. The latter grows with increasing m_H and at a certain point becomes divergent at the renormalisation scale Λ. In an effective field theory the Higgs boson self couplings must be finite. From this requirement an upper limit on Higgs mass is derived as a function of Λ [52].

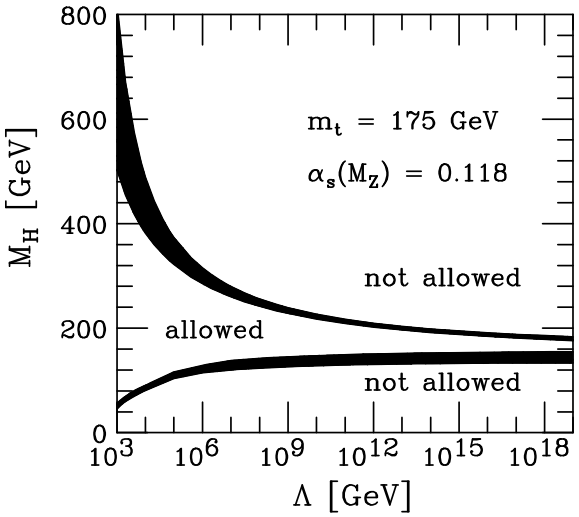

Figure 3.9: The allowed Higgs boson mass range as a function of the scale Λ defining the validity range of the Standard Model.

If the mass of the top quark is set to the experimentally measured value of about 175 GeV, the allowed Higgs boson mass window would be only 130 - 200 GeV if the SM is required to be valid up to the Planck scale ($\Lambda = 10^{19}$ GeV). However, if the validity range of the SM is required only up to $\Lambda \approx 1$ TeV, the Higgs boson mass can vary in the range 55 - 700 GeV. The allowed range of m_H as a function of Λ is shown in Figure 3.9.

In the MSSM, m_h is restricted at tree level to be smaller than m_Z. Radiative corrections, however, alter this limit. The theoretically forbidden regions in the ($\tan\beta$,m_h) plane are shown in Figure 3.10 for the three MSSM scenarios considered in this thesis.

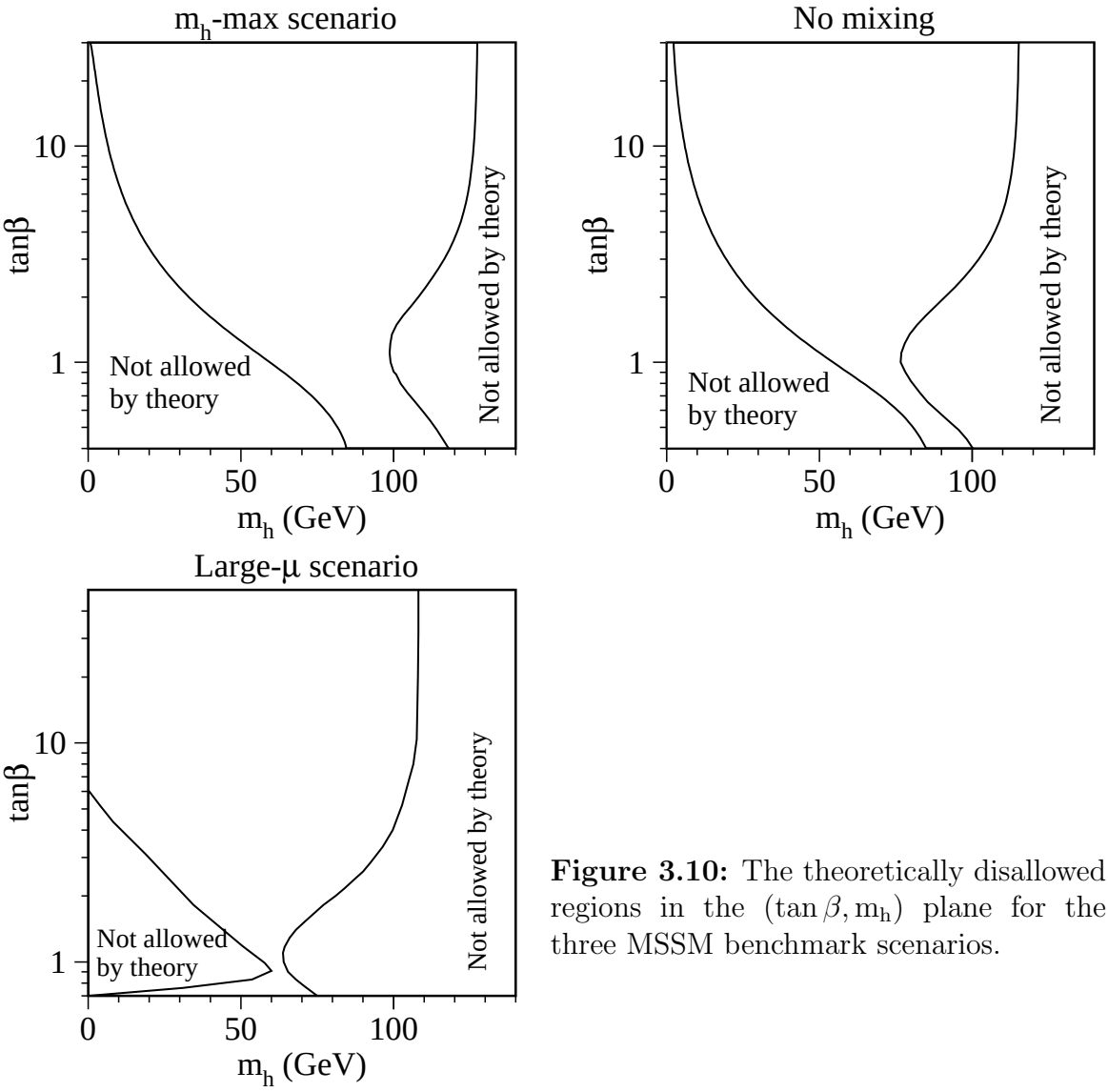

Figure 3.10: The theoretically disallowed regions in the $(\tan\beta, \mathrm{m_h})$ plane for the three MSSM benchmark scenarios.

Indirect Experimental Limits

Many observable quantities measured with high precision at LEP and in other experiments are sensitive to radiative corrections involving the Higgs boson. Two examples for Feynman diagrams are depicted in Figure 3.11. In first order these radiative corrections are logarithmically dependent on $\mathrm{m_H}$. Hence the Higgs boson mass can be predicted by fitting electroweak data with $\mathrm{m_H}$ as a free parameter. The error on the fit result is currently dominated by the uncertainty on $\alpha(\mathrm{m_Z}^2)$ which arises from the uncertainty of the light quark contribution to the photon vacuum polarisation $\Delta^{(5)}_{\mathrm{had}}(\mathrm{m_Z^2})$:

$$\alpha(\mathrm{m_Z^2}) = \frac{\alpha(0)}{1 - \Delta\alpha_\ell(\mathrm{m_Z^2}) - \Delta\alpha^{(5)}_{\mathrm{had}}(\mathrm{m_Z^2}) - \Delta\alpha_{\mathrm{top}}(\mathrm{m_Z^2})}, \tag{3.16}$$

where $\alpha(0) = 1/137.036$. The top quark contribution, $\Delta\alpha_{\mathrm{top}}(\mathrm{m_Z^2})$ = -0.00007, depends on the mass of the top quark, and is therefore determined inside the electroweak li-

braries [53]. The leptonic contribution, $\Delta\alpha_\ell(m_Z^2)$, is calculated to third order [54] to be 0.03150, with negligible uncertainty. A serious problem for the determination of $\Delta^{(5)}_{had}(m_Z^2)$ is the low energy contribution of the five light quarks u, d, s, c and b which cannot be reliably calculated using perturbative QCD. This is solved by combining the measurements of electron-positron annihilations into hadrons. In the updated combination of the electroweak measurements [55] the old value $\Delta^{(5)}_{had}(m_Z^2)$=0.02804±0.0065 [56] is substituted by the new evaluation 0.02761±0.0036 which takes into account the recent results by the BES collaboration [57]. There are also several evaluations of $\Delta^{(5)}_{had}(m_Z^2)$ which are more theory-driven. One of the most recent of these [58] also includes the recent results from BES, yielding 0.02738±0.00020. The dependence of χ^2 of the fit on m_H is illustrated in Figure 3.11. From this dependence the constraints $m_H = 88^{+53}_{-35}$ GeV or $m_H < 196$ GeV at 95 % C.L. are obtained [55].

Clearly, despite of all the interesting arguments made by theorists or derived from measurements taking into account some underlying theory, the direct measurement remains the most convincing step to confirm or to rule out the existence of Higgs bosons.

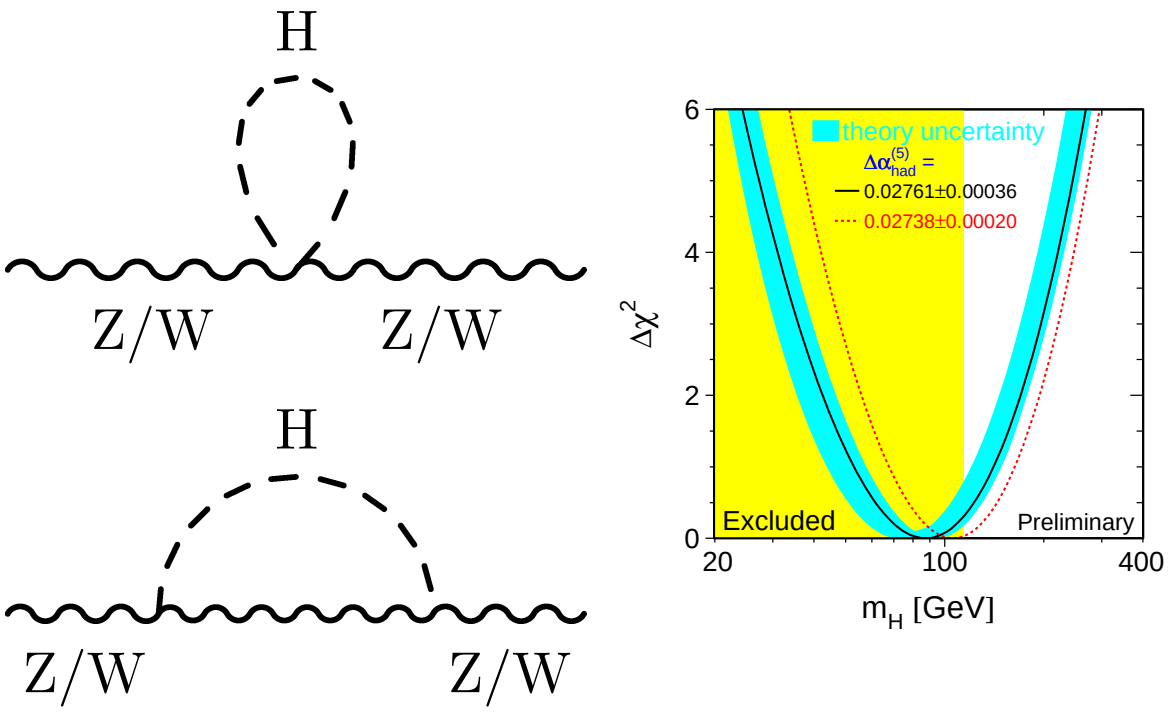

Figure 3.11: The Higgs boson enters via loop corrections into the electroweak fits (left). The Higgs boson mass can be derived by fitting the electroweak observables measured at LEP and at other accelerators (right).

Limits from Direct Searches

When this thesis was started, the four LEP collaborations performed searches for neutral Higgs bosons in the data taken at center-of-mass energies up to 202 GeV[1] [59, 60, 61, 62, 63]. No hints of the Higgs boson signal were found and the results of the searches were translated into mass limits for the SM Higgs boson and neutral Higgs bosons of the MSSM. These limits are summarised in Table 3.1.

	ALEPH	DELPHI	L3	OPAL
Lower limit on the SM Higgs mass m_H (GeV)	107.7	107.3	107.0	103.0
Lower limits on masses of neutral Higgs bosons of the MSSM				
m_h (GeV)	91.2	85.9	83.4	79.0
m_A (GeV)	91.6	86.5	83.8	80.1

Table 3.1: Limits on Higgs boson masses at 95% C.L. obtained from direct searches at $\sqrt{s} \leq 202$ GeV by the four LEP collaborations.

The search for the neutral Higgs boson has also been performed at the TEVATRON $p\bar{p}$ collider by the CDF and D0 collaborations in the processes $q\bar{q} \rightarrow HZ$ and $q\bar{q} \rightarrow HW$ [64]. Four final states were studied:

- $HZ \rightarrow b\bar{b}\ell^+\ell^-(\ell = e, \mu)$;
- $HZ \rightarrow b\bar{b}\nu\bar{\nu}$;
- $HW \rightarrow b\bar{b}\ell\nu(\ell = e, \mu)$;
- $HZ(HW) \rightarrow b\bar{b}q\bar{q}$.

However, the sensitivity of this search does not reach the SM expectations for a signal: an upper 95 % C.L. limit on the quantity $\sigma(p\bar{p} \rightarrow HV) \times Br(H \rightarrow b\bar{b})$ (where V stands for W and Z) is much higher compared to the values predicted by the SM as shown in Figure 3.12.

[1] The author of this thesis also participated in the analysis of these data.

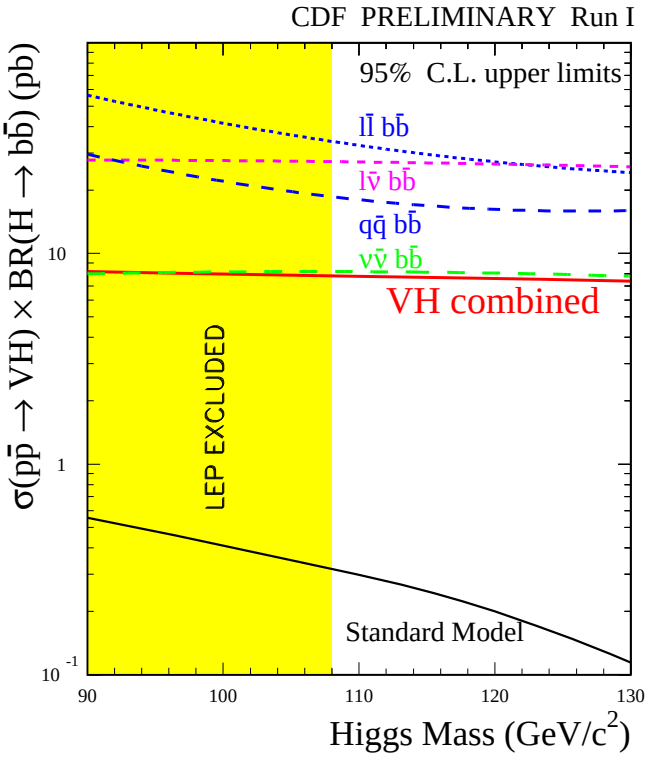

Figure 3.12: Upper 95 % C.L. limit set by CDF on the product of HV (V is W and Z) production cross section and branching fraction of $H \to b\bar{b}$ compared to the SM prediction. The shaded area corresponds to the combined LEP limit obtained from the data collected at $\sqrt{s}$ up to 202 GeV.

Chapter 4

The Experiment

4.1 The e^+e^- Collider LEP

The Large Electron Positron Collider LEP (Figure 4.1), situated at the European Laboratory for Particle Physics (CERN) near Geneva, was constructed to investigate electroweak interactions in e^+e^- collisions.

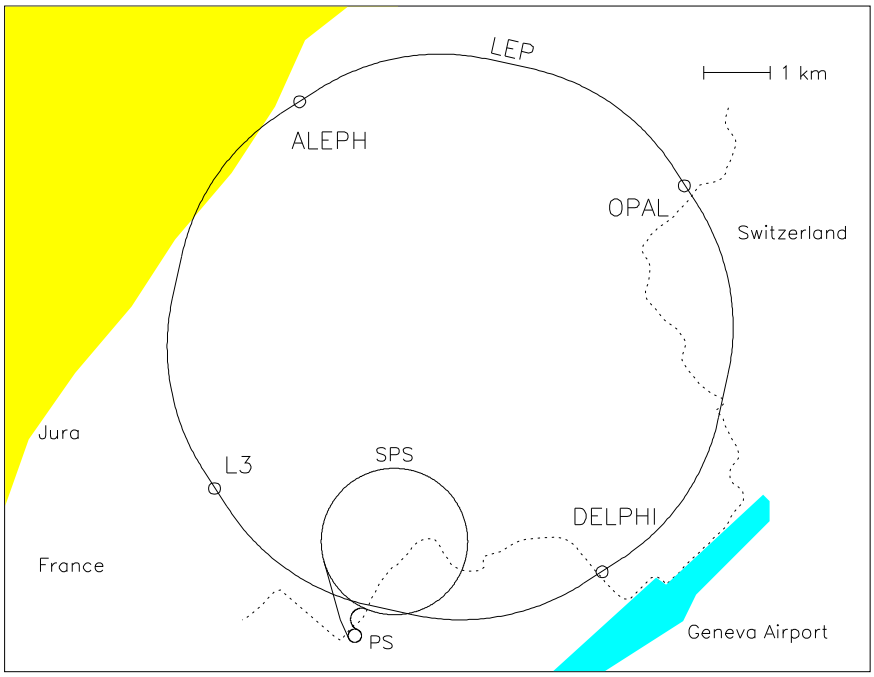

Figure 4.1: The LEP accelerator and storage ring.

LEP has a circumference of about 27 km. Electrons and positrons are accelerated in opposite directions. They are forced to collide in four interaction regions. There the experiments ALEPH [65], DELPHI [66], L3 [67] and OPAL [68] are located which

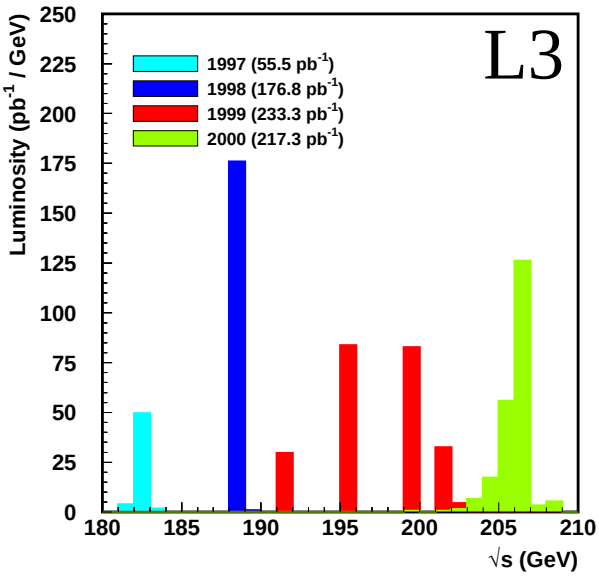

Figure 4.2: The integrated luminosities collected by the L3 detector from 1997 to 2000.

detect e^+e^- annihilation events and perform energy and momentum measurements of the produced particles. In the first phase (1989-1995), LEP was running at a center-of-mass energy close to the mass of the Z boson ($m_Z = 91.187$ GeV). The data collected during this period were used for precise measurements of the Standard Model parameters as well as for the search for new particles. Starting from autumn 1995, the centre-of-mass energy was continuously increased. In 1996 it reached the threshold of $W^{\pm}$-pair production allowing for the precise determination of important parameters such as mass, couplings and branching fractions of the $W^{\pm}$ bosons.

There are two different acceleration schemes used. In the first, electrons and positrons are arranged in 2×4 bunches along the LEP ring. The distance between two bunches, i. e. the time difference between two potential collisions is 22 μs. In the second scheme, the so called bunch train regime, the bunches are replaced by trains of up to 4 smaller bunchlets, which have a distance of 250 ns in time. Therefore, collisions may occur more frequently than in the first scheme. For the operation of LEP at the Z peak, the bunch train scheme leads to an increase in luminosity. For running at higher energies, there are usually only 4 bunches used per beam which contain however a much higher current. The total current at high energies amounts about 5 to 6 mA at the beginning of a fill. Figure 4.2 shows typical integrated luminosities collected by each of the four LEP experiments at different $\sqrt{s}$ during the last four years of LEP operation. In the year 2000, the four experiments collected data at center-of-mass energies between 200 and 209 GeV, integrating approximately 870 pb^{-1} of luminosity, with about 510 pb^{-1} above 206 GeV.

4.2 The L3 Detector

The L3 detector depicted in Figure 4.3 is a general purpose detector with special emphasis on the precise energy measurement of photons, electrons and muons. The whole detector is installed in a 12 m inner diameter solenoidal magnet, which provides an uniform magnetic field of 0.5 T along the beam axis. The major components of the detector are the following:

- the Silicon Microvertex Detector (SMD)
- the Central Tracking Chambers consisting of a time expansion chamber (TEC) and the z chambers
- the Electromagnetic Calorimeter (BGO)
- the Scintillators
- the Hadron Calorimeter (HCAL)
- the Muon Chambers

The origin of the right handed coordinate system is in the geometric centre of the detector. The positive z axis coincides with the direction of the electron beam. The y axis points vertically upwards and the x axis towards the centre of the LEP ring. The distance between a point in the x-y plane and the geometric centre of the detector is the radius r. The azimuthal angle between the radius vector $\vec{r}$ and the positive x axis is denoted with ϕ. The polar angle between the direction of a particle and the electron beam direction is called Θ.

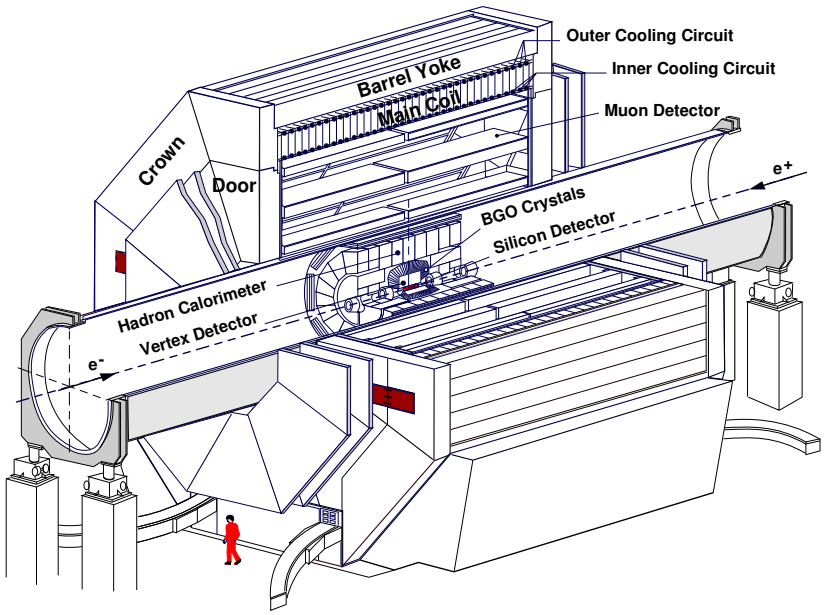

Figure 4.3: The L3 detector at LEP.

4.2.1 The Silicon Microvertex Detector

The Silicon Microvertex Detector (SMD) is directly attached to the beryllium beam pipe of LEP which has a radius of 5.3 cm. This detector is used to measure charged particles at a close distance to the interaction point to resolve possible secondary vertices which arise from the decay of short living particles such as hadrons containing b quarks.

The SMD depicted in Figure 4.4 is made up of two cylindrical layers. The mean radius of the cylinders amounts to 6 cm and 8 cm respectively. The length of the SMD is 30 cm which yields to a polar angle coverage of $22° \leq \Theta \leq 158°$. Each of the layers has 12 modules (ladders) which are made up of two electrically independent half-ladders. The half-ladders consist of 2 double-sided silicon sensors. Each of these sensors is 70 mm long, 40 mm wide and made from 300 μm high purity n-type silicon. On one side (junction side) of the sensors there are implantation strips every 25 μm with a readout pitch of 50 μm. They run parallel to the beam axis and allow therefore the determination of the rϕ coordinate. On the other side the implantation strips are arranged perpendicular to the junction side strips with a pitch of 50 μm. The readout pitch is 200 μm for $0.53 \leq |\cos\Theta| \leq 0.93$ and 150 μm for $|\cos\Theta| \leq 0.53$. These strips are used for the z measurement. A resolution of 7.5 μm in rϕ and 14.3 μm in z is obtained [69].

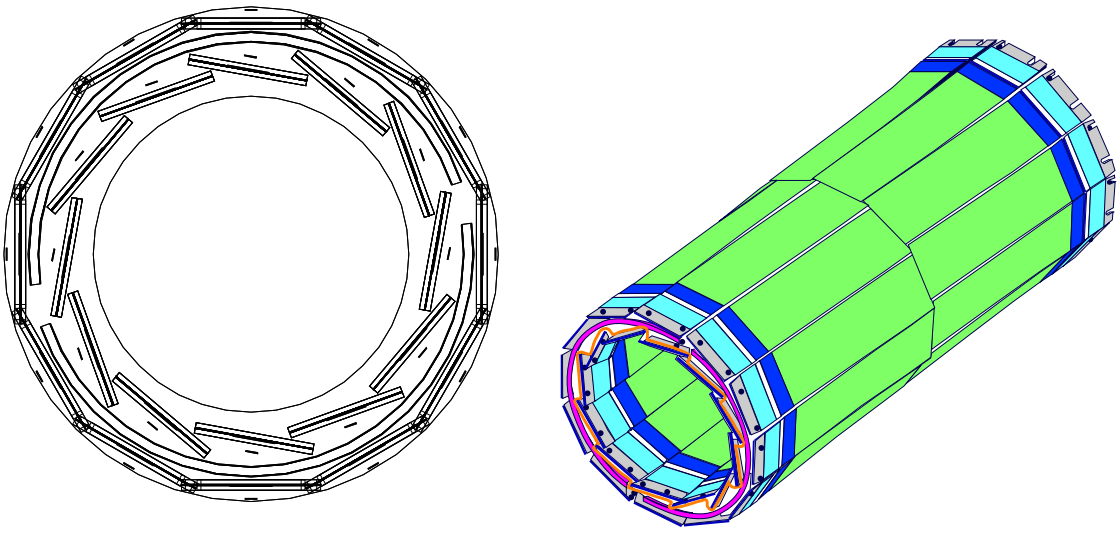

Figure 4.4: The Silicon Microvertex detector.

4.2.2 The Central Tracking Chambers

The central tracking chambers allow the reconstruction of charged tracks in rϕ and z. For the rϕ measurement two concentric drift chambers are used which operate in the time expansion mode. This is illustrated in Figure 4.5. The drift chambers are subdivided into sectors. The anode and cathode wires are drawn in z direction. The inner drift

chamber consists of 12 sectors with 8 anode wires each. The outer drift chamber is subdivided into 24 sectors with 54 wires each. The inner and the outer radius of the TEC is 9.15 cm and 45.6 cm respectively. The length is 126 cm.

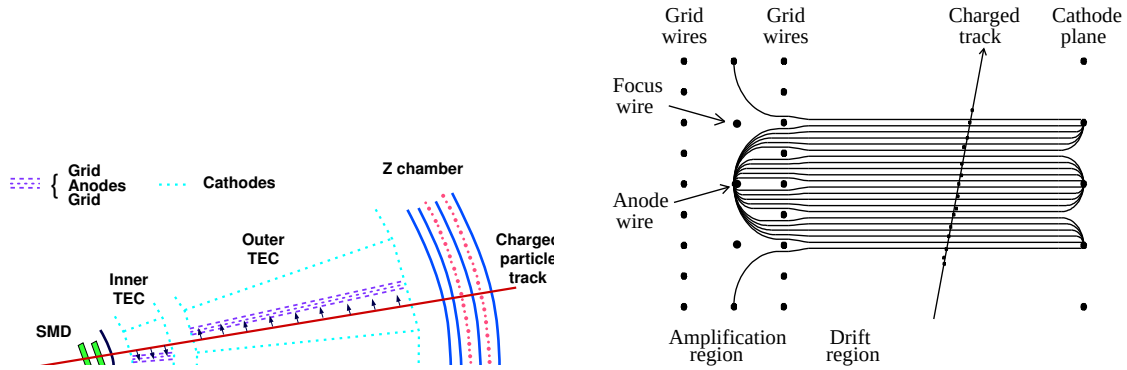

Figure 4.5: Left: rϕ view of the central tracker consisting of SMD, TEC and the Z detector. Right: drift field in the TEC.

The anode planes are screened by grid planes which divide the drift regions in areas of different field strength. The small field strength between the cathode and the grid plane leads to a small drift velocity which results in a very good spatial resolution. In the region of the high field strength gas amplification occurs and the electron avalanche is detected by the anodes. In order to resolve the left right ambiguity additional wires in the grid plane are read out. The gas mixture consists of 80 % CO_2 and 20 % Isobutan. The drift velocity is 6 μm/ns. In rϕ a resolution of (50-60) μm is obtained. Some anode wires are read out on both sides. These signals are used to obtain a rough z coordinate (resolution some cm) by means of the charge division principle.
Particles with a polar angle between 42° and 138° will pass the z chambers. This detector supplements the measurements of TEC and SMD with a z coordinate at r = 50 cm. It consists of two multiwire proportional chambers with cathode readout. The anode wires are aligned in z direction. The two chambers contain two cathode layers each. The cathode layers are made of 240 strips with a pitch of 4.45 mm. The strips of two of the layers are arranged perpendicular to the z direction (z layer) and the strips of the other two layers run under a stereo angle of ±69°. The gas mixture consists of 80 % Argon, 16 % CO_2 and 4 % Isobutan. A charged particle traversing the chamber ionises the gas. The resulting electron avalanche around the anode wire induces image charges on the cathode layers. The relative amount of the signal measured on the individual cathode strips is used for the coordinate determination. The ϕ component of the stereo layer allows the matching of the cluster with a TEC track. The z layers are used for the measurement of the z coordinate. The resolution varies depending on the polar angle. At $\cos\Theta = 0$ the resolution is about 200 μm whereas at $|\cos\Theta| = 0.74$ the resolution is

1000 μm. The special design of the readout electronics can be used to tag the interacting bunchlet when LEP is operating in the Bunch Train Mode [70].

4.2.3 The Electromagnetic Calorimeter

The electromagnetic calorimeter (BGO) allows the very precise measurement of electrons and photons with energies between 100 MeV and 100 GeV. It consists of bismuth germanate ($Bi_4Ge_3O_{12}$) crystals pointing to the interaction region as can be seen in Figure 4.6. The crystals have a length of 24 cm, a front face of 2×2 cm^2 and a rear face of 3×3 cm^2. In the central part of the detector (barrel) there are 7680 crystals. They cover the polar angle $42° \leq \Theta \leq 138°$. In the forward-backward region (endcap) of the detector there are 1527 BGO crystals which cover the angles $11.6° \leq \Theta \leq 38°$ and $142° \leq \Theta \leq 168.4°$. The scintillation light of the BGO crystals is collected by two photodiodes which are mounted at the rear face of the crystals. The energy resolution is 5 % at 100 MeV and less than 2 % at energies larger than 1 GeV [71].

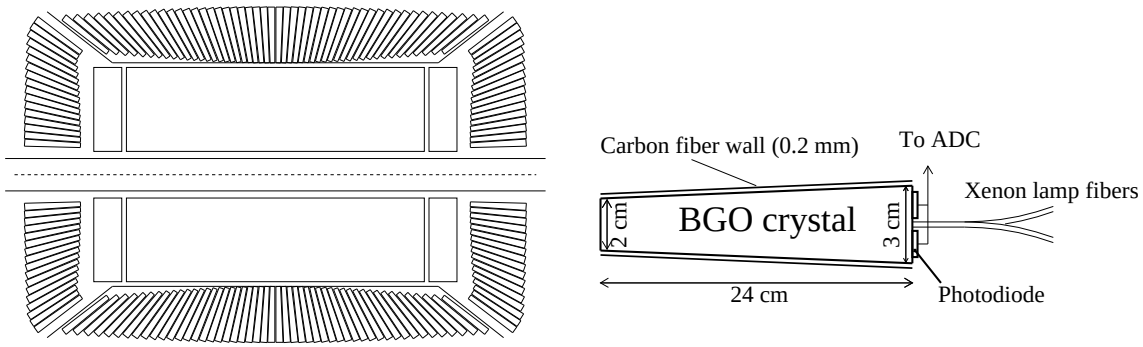

Figure 4.6: Left: the arrangement of the BGO crystals. The front faces of 2×2 cm^2 point to the interaction point. Right: a BGO crystal. The scintillation light is collected by two photodiodes on the rear site.

The gaps between the barrel and the endcap BGO crystals are filled with lead-scintillating fibre calorimeters (SPACAL) [72]. They consists of 24 modules (bricks) containing a lead structure filled with scintillating fibres. The scintillation light is collected by phototriodes glued on the rear site of the bricks. The resolution of the SPACAL is 15 % at 45 GeV.

4.2.4 The Scintillators

The scintillator system consists of 30 single plastic counters which are located between the electromagnetic and the hadron calorimeter. They allow the discrimination of cosmic

muons. If LEP operates in the Bunch Train Mode they are used to tag the bunchlet. The time resolution is about 460 ps.

4.2.5 The Hadron Calorimeter

The energy of hadrons is measured in the hadron calorimeter. As in the case of the BGO, it also consists of a barrel and two endcap parts. The barrel calorimeter allows the energy measurement within $35° \leq \Theta \leq 145°$ whereas the endcap calorimeters cover the angles $5.5° \leq \Theta \leq 35°$ and $145° \leq \Theta \leq 174.5°$ in the forward-backward region of the detector.

The central part of the hadron calorimeter contains 9 rings with 16 modules. These modules consist of uranium absorber plates with a width of 5.5 mm interspersed with proportional wire chambers. There are in total 7968 chambers in the barrel part. The two endcaps are each built up of one outer and two inner rings. Each of these rings contains 12 modules.
The material which a particle arising from the interaction point has to traverse depends on the polar angle and varies between 6 and 7 nuclear absorption lengths. A muon filter, mounted on the inside wall of the support tube, adds an additional absorption length which suppresses the flow of secondary particles produced in the hadron calorimeter into the muon chambers. The hadron jet energy resolution of the calorimeter is $(55/\sqrt{\mathrm{E}}+8)\%$, where E is measured in GeV. The direction of the jet axis can be measured with a resolution of about 2.5°.

4.2.6 The Muon Detector

The muon detector is the largest part in the L3 experiment. It envelopes all other detector components. It was designed to measure muon momenta with very high precision. The barrel part of the detector covers the polar angle range from 44° to 136°. It consists of two halves with a gap at z=0. Each of the halves is subdivided into octants. As illustrated in Figure 4.7 (left) each octant consists of five precision drift chambers (P-chambers) which are arranged in three layers. The outer and inner chambers contain 16 wires each whereas the middle chambers are equipped with 24 wires. In order to determine the z-coordinate of a muon track, there is a set of Z-chambers mounted on the top and the bottom of the inner and the outer layer. The design momentum resolution for muons measured in all 3 layers is $\sigma_\mathrm{p}/\mathrm{p} \approx 2.5\%$ at 45 GeV.

The barrel part of the muon detector is complemented with a forward backward spectrometer covering the polar angles $24° \leq \Theta \leq 44°$ and $136° \leq \Theta \leq 156°$. Three rings consisting of 16 drift chambers are attached to the magnet doors as shown in Figure 4.7. They are triggered by Resistive Plate Counters (RPCs) which are mounted at the rings. The magnet doors are wrapped up with coils producing a toroidal magnetic field of 1.2 T. The momentum resolution depends on the polar angle or more precisely spoken on whether the inner and middle layers of the barrel detector were also hit by the muon. The momentum resolution varies from 6% at $\Theta = 43°$ to 35% at $\Theta = 28°$ [73].

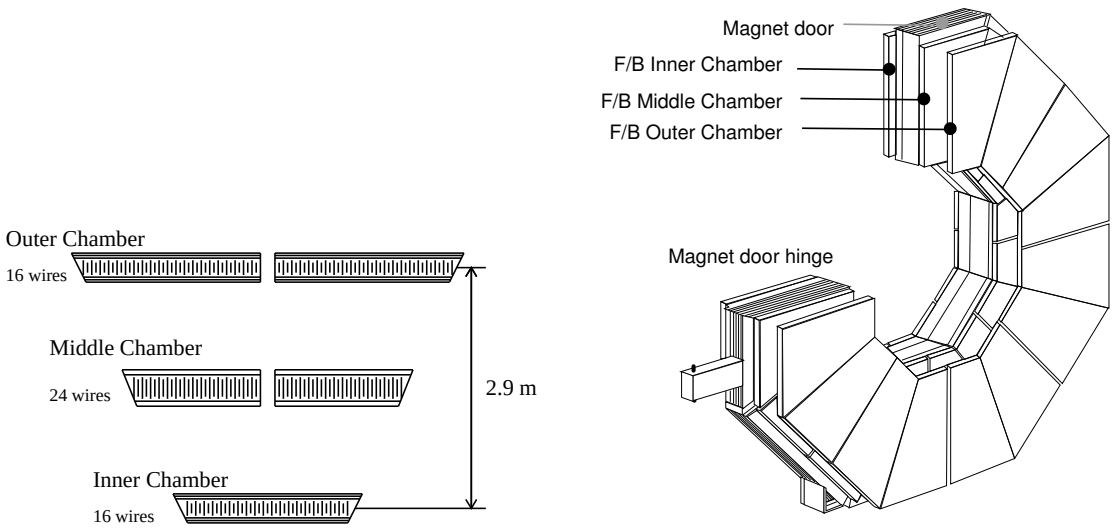

Figure 4.7: Left: the structure of a muon octant in the barrel. Right: The forward-backward muon chambers.

4.2.7 The Luminosity Monitor

A precise knowledge of the luminosity is very important for most of the measurements made at LEP. This is achieved by measuring low angle Bhabha scattering and comparing the measured rate with a precise theoretical calculation [74]. The L3 luminosity monitor consists of two electromagnetic calorimeters complemented with two silicon trackers (SLUM). These two sets are located at $z = \pm 2.7$ m (Figure 4.8) and cover the polar angles 24.93 mrad $\leq \Theta \leq$ 69.94 mrad.

4.2.8 The Trigger System

An efficient trigger system is needed to separate interesting physics events from those events which just contain energy deposits caused by beam-gas, beam-wall interactions, synchrotron radiation or detector noise. All subdetectors are prepared for data taking by the beam crossing signal ($\approx$ 1.7 μs before the electron and positron bunches are expected to collide).

The number of events written to tape is reduced in 3 steps. The first step (level-1 Trigger) takes individual information from the subdetectors into account. These are track information from the TEC (TEC trigger), energy deposits in the calorimeters (energy trigger), scintillator hits (scintillator trigger), energy deposits in the luminosity monitor (luminosity trigger) and tracks in the muon chamber (muon trigger). If one of these triggers has fired, the event is passed to the level-2 trigger, where more time is available to make a first cross check between the individual triggers. This removes already a large fraction of the background events mentioned above. If an event was accepted by more than one trigger, the event is not rejected. At the trigger level-3 the full information of an event is available. The correlation between the individual subdetector information is exploited and tighter requirements on the individual decisions

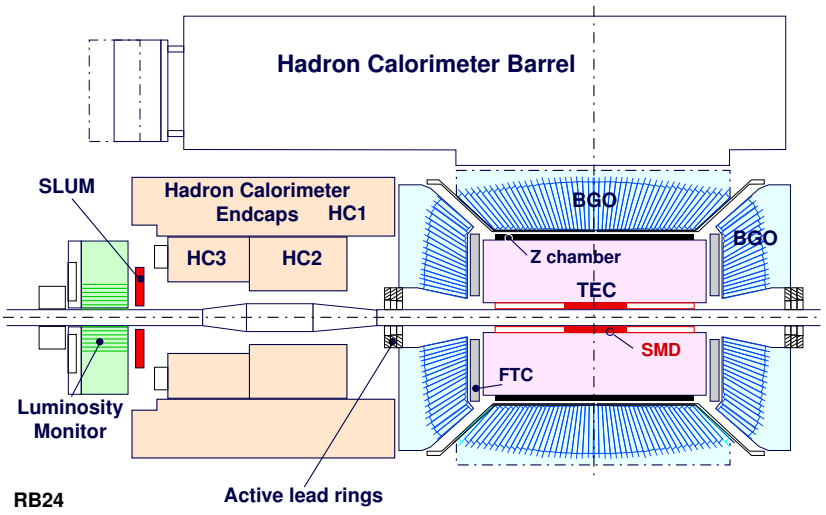

Figure 4.8: Layout of the luminosity monitor. The luminosity is measured by using low angle Bhabha scattering.

can be made. Events with multiple positive decisions on trigger level-1 or with luminosity trigger are not rejected. All events passing the trigger level-3 decision are written to tape.

Chapter 5

Experimental Conditions and Analysis Procedures

In Chapter 3 the mechanisms of Higgs boson production at LEP were discussed. However, there are many other processes resulting from e^+e^- collisions. These processes can potentially mimic a signal and therefore must be considered as background. A sensitivity of the search for a signal in experimental data depends on how well the signal is separated from background. Hence a dedicated analyses must exploit particular signatures of the signal final states distinguishing them from the background topologies to achieve the efficient signal selection while keeping the acceptance for the background events as low as possible.

In this chapter the signal topologies and main background processes are discussed, experimental conditions, at which analyses were performed, are presented, the analysis strategy common for all search channels is reviewed and the statistical method used to evaluate the presence of a signal in experimental data is described.

5.1 Signal Topologies

The search for the SM Higgs boson in the Higgs-strahlung process is based on the study of four distinct topologies determined by the decay products of the H and Z bosons:

- $HZ \to q\bar{q}q\bar{q}$ (four-jet channel);
- $HZ \to q\bar{q}\nu\bar{\nu}$ (missing energy channel);
- $HZ \to q\bar{q}\ell^+\ell^-$, $(\ell = e, \mu)$ (semileptonic channel);
- $HZ \to q\bar{q}\tau^+\tau^-(\tau^+\tau^- q\bar{q})$ (tau channels).

With the exception of the $HZ \to \tau^+\tau^- q\bar{q}$ channel, all the analyses are optimised for $H \to b\bar{b}$ decay mode which dominates in the mass range of interest. The selection efficiency for events with the $H \to c\bar{c}$ and $H \to gg$ decays is also estimated.

The signature of the pure hadronic final state, $HZ \to q\bar{q}q\bar{q}$, is four high multiplicity hadronic jets and the presence of b hadron decay products, in particular, in jets assigned

to the Higgs boson. The invariant mass of the dijet system recoiling against the Higgs boson must be consistent with the mass of the Z boson, m_Z .

The $HZ \to q\bar{q}\nu\bar{\nu}$ signal topology is characterised by large missing energy and two acoplanar hadronic jets containing the decay products of b hadrons. The missing mass in such events has to be compatible with m_Z .

The semileptonic final states, $HZ \to q\bar{q}\ell^+\ell^-$, are searched for in events which contain two isolated electrons or muons and two hadronic jets initiated by b quarks. The invariant mass of lepton pair must be consistent with m_Z .

Finally tau channels are characterised by four jets two of which have low multiplicity as expected for tau jets. The invariant mass of two hadronic jets in the $HZ \to \tau^+\tau^- q\bar{q}$ channel or tau jet pair in the $HZ \to q\bar{q}\tau^+\tau^-$ channel must be compatible with m_Z . In the $HZ \to q\bar{q}\tau^+\tau^-$ final state hadronic jets should contain decay products of b hadrons.

All enumerated signal topologies are displayed in Figure 5.1.

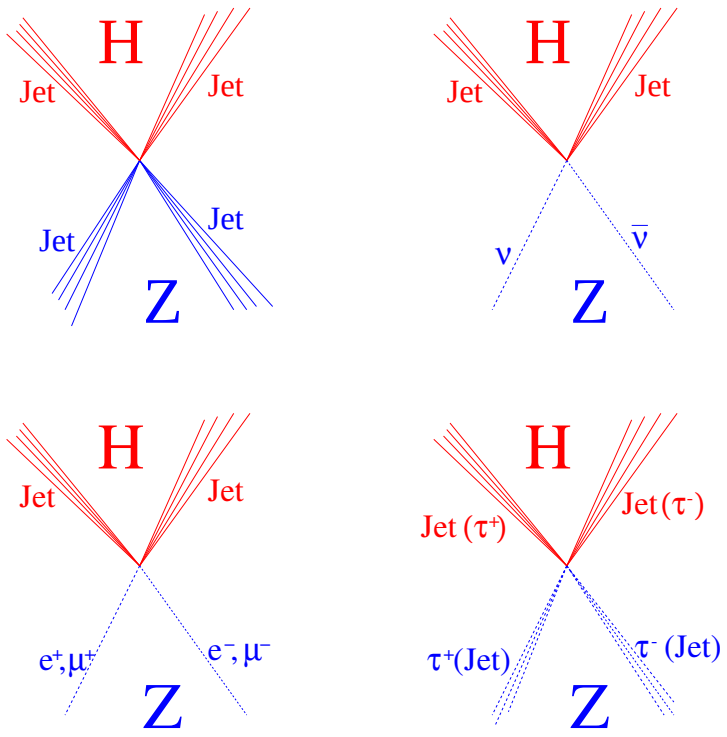

Figure 5.1: Signal topologies associated with the HZ production.

The processes of WW and ZZ fusion contribute, with smaller rate, to the $q\bar{q}\nu\bar{\nu}$ and $q\bar{q}e^+e^-$ final states, respectively. However, final states arising from the fusion processes are a bit different from similar final states associated with the Higgs-strahlung production mechanism. For instance, in WW and ZZ fusion processes the missing mass and invariant mass of the electron positron pair are not necessarily close to m_Z and the corresponding mass constraints cannot be exploited anymore. Therefore, the $HZ \to q\bar{q}\nu\bar{\nu}$ and $HZ \to q\bar{q}e^+e^-$ analyses are less effective in discriminating WW and ZZ fusion processes from background.

In the search for the neutral Higgs bosons of the MSSM, signal topologies associated with the Higgs-strahlung process are complemented with the hA $\rightarrow$ $b\bar{b}b\bar{b}$ and hA $\rightarrow$ $b\bar{b}\tau^+\tau^-$ (hA $\rightarrow$ $\tau^+\tau^-b\bar{b}$) search channels illustrated in Figure 5.2 and the six-jet channel hZ $\rightarrow$ AAq$\bar{q}$ $\rightarrow$ q$\bar{q}$q$'\bar{q}'$q$''\bar{q}''$ when it becomes relevant.

Finally, analyses have been developed to search for the Higgs-strahlung and Higgs pair production processes with subsequent hadronic decays of the Higgs bosons not necessarily into $b\bar{b}$. In these analyses we do not require the presence of b hadron decay products in the jets assigned to the Higgs boson.

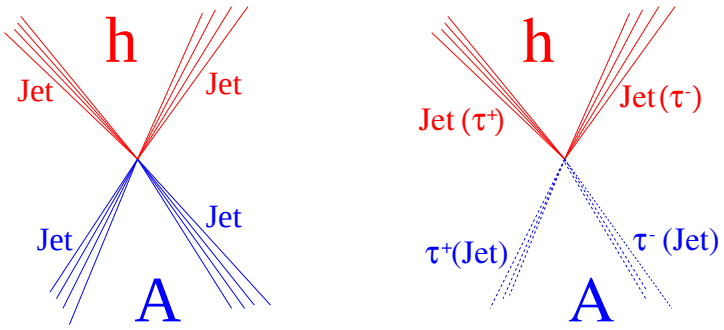

Figure 5.2: Signal topologies associated with the hA production.

5.2 Main Background Processes

Interactions between electrons and positrons proceed via various processes. Many of them have topologies similar to the searched signal. For analyses presented here these processes must be considered as a background. For the most important processes contributing to the background for Higgs boson searches, the dependence of the cross section on the center-of-mass energy is given in Figure 5.3. In the vicinity of the kinematic threshold the $e^+e^- \rightarrow HZ$ cross section is several orders of magnitude lower than the cross sections of the relevant background reactions. Hence it is a real challenge for experimentalists to find the Higgs boson in such a severe background environment.

All processes occurring in e^+e^- interactions can be divided into three classes. The first class contains the processes arising from so-called **two-photon interactions** in which a fermion-antifermion pair is produced through the exchange of two virtual photons as depicted in Figure 5.4. The cross section of two-photon interaction processes at LEP is very high, but their particular features allow to suppress them at an early stage of the analysis. The electron and positron are scattered at very low polar angles and then either escape into the beam pipe, carrying away almost the entire initial energy, or are absorbed by the luminosity monitor.

Annihilations into a **fermion-antifermion pair** constitute the second class of backgrounds. These reactions proceed via the exchange of a virtual Z or γ as illustrated

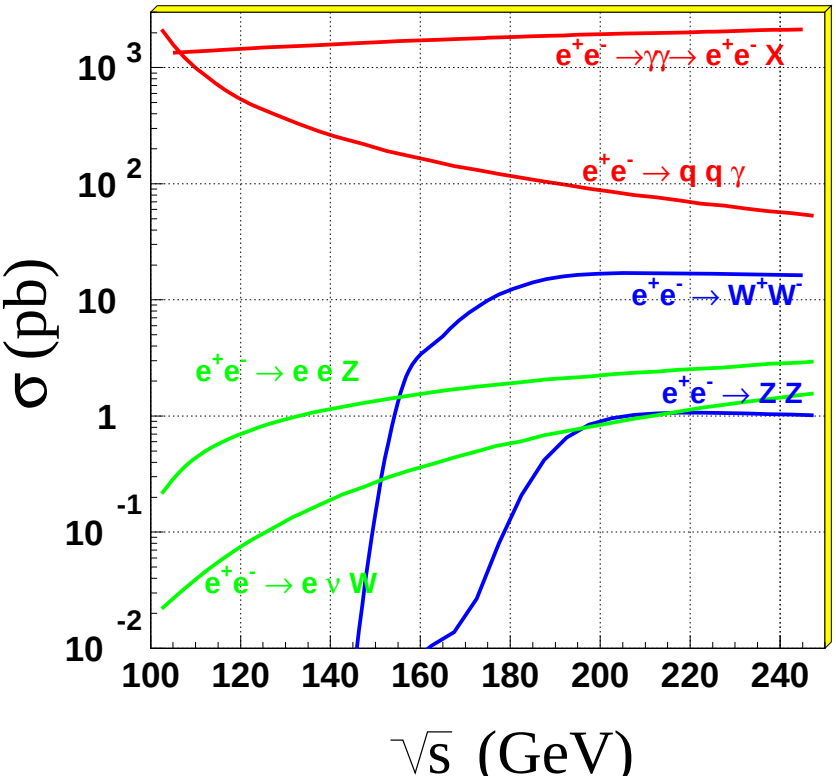

Figure 5.3: The cross section dependence on the center-of-mass energy for the processes contributing to the background for Higgs boson searches.

in Figure 5.5a. For e^+e^- final states there is also an additional t-channel contribution shown in Figure 5.5b.

The production of two fermions can be accompanied by the radiation of a real photon off the initial state electron or positron. In this case the effective center-of-mass energy is reduced so that a real Z boson can be produced instead of a virtual. This type of reactions, called **radiative return to the Z resonance**, is depicted in Figure 5.6. The

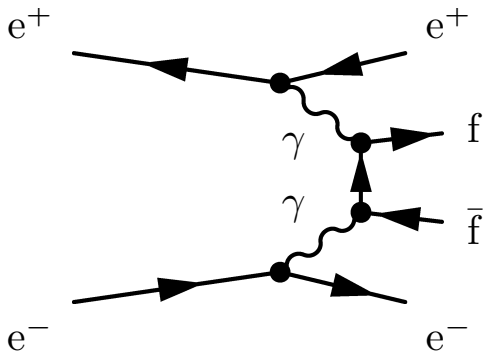

Figure 5.4: Feynman diagram for two photon interaction

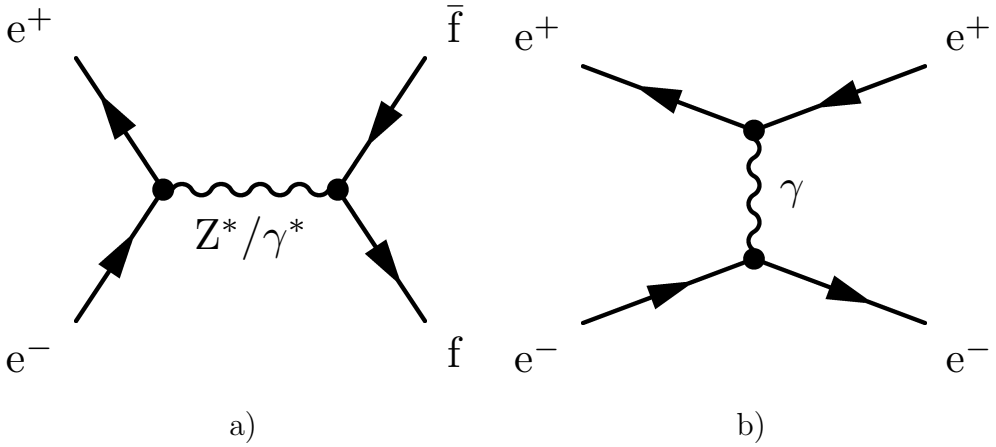

Figure 5.5: Two fermion processes: a) s-channel; b) e^+e^- production via t-channel.

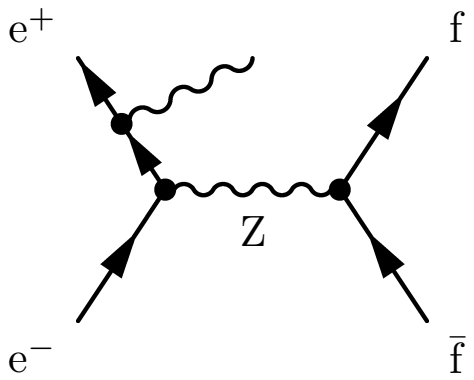

Figure 5.6: Radiative return to the Z resonance. In the case of initial state radiation the event is unbalanced if the photon escapes unobserved the detector.

emitted photon escapes very often undetected into the beam pipe and therefore, these events have large longitudinal momentum imbalance.

The most important two-fermion production for us is the one leading to a quark anti-quark pair in a final state. It has a high cross section of ~ 90 pb at center-of-mass energies around 200 GeV and is characterised by high multiplicity. The hadronisation of quarks results mainly into a two jet configuration. However, radiation of gluons by the quark or anti-quark can generate additional jets.

The **four-fermion** final states make up the third class of background reactions. They result from gauge boson pair production or single gauge boson production processes. The W-pairs are produced in the s-channel through virtual γ or Z exchange as illustrated in Figure 5.7a, or in the t-channel via ν_e exchange as shown in Figure 5.7b.

The W bosons can decay into a lepton and an anti-lepton, $W^- \to \ell^- \nu_\ell$ ($\ell = e, \mu, \tau$) or into a quark and an anti-quark, $W^+ \to u\bar{d}$ or $c\bar{s}$ [1]. The decay $W^+ \to t\bar{b}$ is kinematically

[1] The charge conjugated decays are also possible.

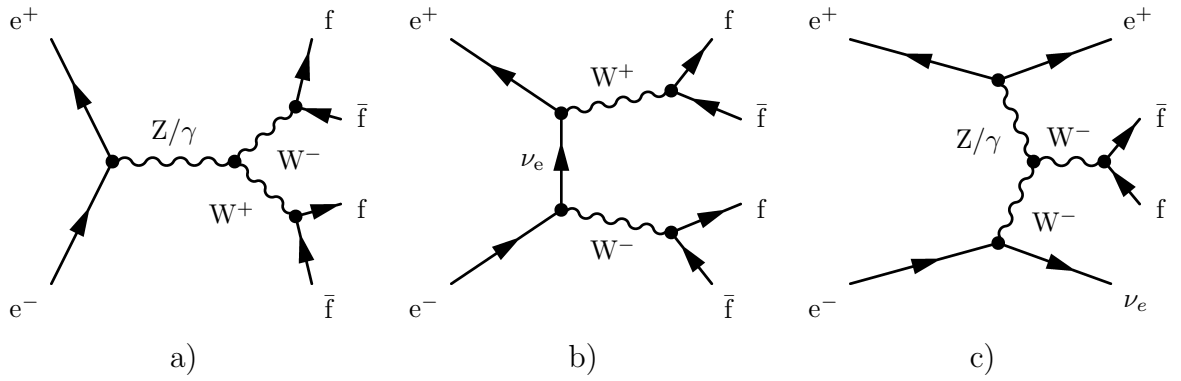

Figure 5.7: W-pair production a) in s-channel and b) in t-channel. c) Single W production.

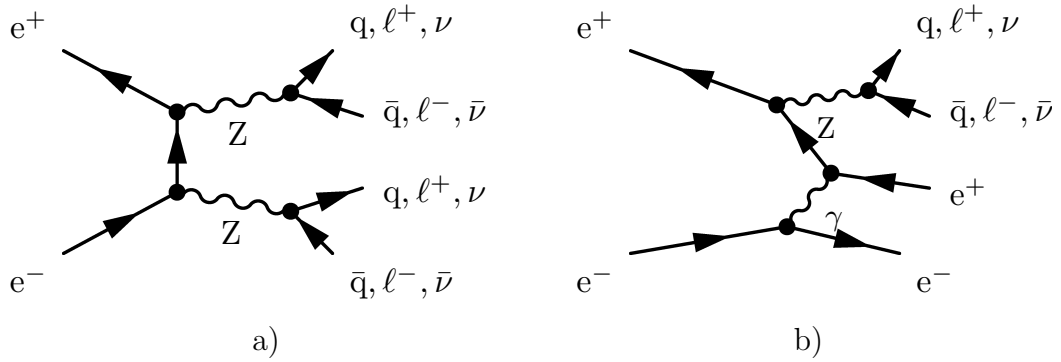

Figure 5.8: a) Z-pair production and b) single Z production.

not allowed.

Pairs of Z bosons are produced via ν_e exchange in the t-channel as illustrated in Figure 5.8a. Z bosons then decay into fermion and antifermion of the same flavour: $Z \to q\bar{q}$ ($q = u, d, s, c, b$); $Z \to \ell^+\ell^-(\ell = e, \mu, \tau)$; $Z \to \nu_\ell\bar{\nu}_\ell$. The W^+W^- and ZZ production cross sections exhibit a typical threshold behaviour with increasing center-of-mass energy. At $\sqrt{s} \sim 200$ GeV the cross section $\sigma(W^+W^-)$ reaches the value ∼17 pb. At the same energy the ZZ production has a more than one order of magnitude lower cross section.

Single production of W and Z bosons proceeds via Feynman diagrams displayed in Figures 5.7c and 5.8b, respectively. In these reactions, the W is produced in association with an $e^\pm$ and a neutrino while the production of Z is accompanied by an electron-positron pair. There is a considerable missing energy in $W^\mp e^\pm \nu$ events since the $e^\pm$ usually escapes undetected into the beam pipe. The Zee process is characterised by the presence of an energetic electron and positron which either vanish unobserved into the beam pipe or are detected as isolated huge energy deposits in the electromagnetic

calorimeter.

5.3 Data and Monte Carlo Samples

The analyses presented in this thesis are performed on the data collected by the L3 detector in the year 2000. The center-of-mass energy of this data sample spreads from 200 GeV to 209 GeV [2]. In the vicinity of the kinematic threshold the cross section of the Higgs-strahlung process is very sensitive to the center-of-mass energy. In order to reduce the systematic effect connected with the beam energy spread, the entire 2000 year data sample is divided into eight subsets which are analysed separately. The integrated luminosities and the effective, i.e. luminosity-weighted, center-of-mass energies corresponding to these subsets are given in Table 5.1.

$\sqrt{s}$ (GeV)	203.8	205.1	206.3	206.6	208.0	208.6
$\mathcal{L}$ (pb^{-1})	7.6	68.1	66.9	63.7	8.2	0.1

Table 5.1: The effective center-of-mass energies, $\sqrt{s}$, and corresponding integrated luminosities, $\mathcal{L}$ in the data sample of the year 2000.

The cross sections for the Higgs-strahlung and associated Higgs boson pair production processes are calculated using the HZHA generator [75]. Efficiencies are determined using Monte Carlo samples of signal events generated with the PYTHIA package [76]. Since the cross section of the Higgs-strahlung process depends strongly on $\sqrt{s}$ samples of Higgs-strahlung events are simulated at each center-of-mass energy shown in Table 5.1. Higgs-strahlung events are simulated in the mass range from 60 to 95 GeV in steps of 5 GeV and from 100 to 120 GeV in steps of 1 GeV. For each mass and each search channel between 2000 and 10000 events are generated. For the $HZ \to q\bar{q}q\bar{q}$ channel the Monte Carlo statistics amounts to $\sim$ 3500 events for each mass and each center-of-mass energy. The Monte Carlo samples of $e^+e^- \to hA$ events are simulated using the HZHA generator. About 2500 events are generated both for $hA \to b\bar{b}b\bar{b}$ and $hA \to b\bar{b}\tau^+\tau^-$ channels for m_h and m_A between 50 and 100 GeV in steps of 5 GeV.

The background estimates rely on the following Monte Carlo programs: KK2f [78] for $e^+e^- \to q\bar{q}(\gamma)$, KORALW [79] for $e^+e^- \to W^+W^-$, PHOJET [80] for two-photon interactions ($e^+e^- \to e^+e^-q\bar{q}$) and EXCALIBUR [81] for other four-fermion final states. The number of simulated events for the main background processes is at least 100 times the number of collected data events.

The response of the L3 detector is simulated using the GEANT program [82], taking into account the effects of multiple scattering, energy loss and showering in the detector. Hadronic interaction in the detector are modelled using the GHEISHA [83] program. Time dependent detector inefficiencies, as monitored during the data-taking period, are also taken into account.

[2] Although the data sample of the year 2000 includes also relatively small amount of luminosity, $\mathcal{L} \sim 2$ pb^{-2}, collected at $\sqrt{s} < 203$ GeV, the energy range for this data sample is referred hereafter to as $\sqrt{s} = 203$-209 GeV.

5.4 Search Strategy

All the search channels are analysed in three stages. First, a selection of events with high multiplicity, preserving most of the Higgs signal, is applied to reduce the large background from two-photon interaction and dilepton final states. In a second stage, variables having discriminating power between signal and background processes are used to construct a signal likelihood in the $HZ \to q\bar{q}q\bar{q}$ channel or fed into a neural network in the $HZ \to q\bar{q}\nu\bar{\nu}$ channel to further discriminate between signal and background events. In the case of semileptonic and tau channels a fine-tuned selection based on a traditional cut technique is used. The third stage is the construction of the final discriminant. It is combined from event shape variables, information about the flavour content of the jets and from the mass information. The latter is contained either in the reconstructed mass of the dijet or ditau system assigned to the Higgs boson or in a computed probability quantifying the consistency of an event with the tested Higgs boson mass hypothesis.

The final discriminants are computed in the same way for data, for the expected background and for the expected signal, at each tested Higgs boson mass hypothesis. Then the spectra of these final discriminants are used to examine the data for their consistency with the background hypothesis and with the signal hypothesis.

5.5 Statistical Method

A detailed description and justification of statistical method adopted for the interpretation of data in the context of Higgs boson searches can be found in Reference [84]. I will just briefly outline the main ideas of this method.

The distributions of final discriminants, constructed in each search channel and at each $\sqrt{s}$ for a given Higgs boson mass hypothesis, are combined into one array of analysis bins. Each analysis bin "i" is characterised by the number of observed candidates, n_i, the number of expected background events, b_i and the number of expected signal events, s_i. The array of analysis bins is used to compute the likelihood ratio Q. This is the ratio of the likelihood of observing the data in the presence of both signal and background ("signal+background" hypothesis) to the likelihood of observing the data in the presence of only the background ("background-only" hypothesis). Assuming that each analysis bin obeys Poisson statistics, the likelihood ratio is defined as

$$Q = \frac{\prod_{i=1}^{N} e^{-(s_i+b_i)} \frac{(s_i+b_i)^{n_i}}{n_i!}}{\prod_{i=1}^{N} e^{-b_i} \frac{b_i^{n_i}}{n_i!}}. \tag{5.1}$$

Here, i=1..N runs over all analysis bins. The statistical estimator used to evaluate the presence of a signal in the data is the logarithm of the likelihood ratio

$$-2 \ln Q = 2 \sum_i \Big[s_i - n_i \ln(1 + s_i/b_i) \Big]. \tag{5.2}$$

Note that each event contributes to -2lnQ with a weight $1 + s/b$, where s/b is the signal-to-background ratio of the bin where the event occurs. With the definition of

the statistical estimator given by Equation (5.2) negative values of -2lnQ favour the "signal+background" hypothesis whereas positive values favour the "background-only" hypothesis.

In the next step we perform a large number of Monte Carlo experiments under the "background-only" and the "signal+background" hypotheses. In Monte Carlo trials the number of events in each bin "i" is generated assuming Poisson statistics with mean value $(s_i + b_i)$ and b_i for the "signal+background" and the "background-only" hypotheses, respectively. The outcome of the Monte Carlo experiments is two distributions of -2lnQ, one for the "signal+background" hypothesis and another for the "background-only" hypothesis as shown in Figure 5.9. The systematic errors on the expected background and signal rates are incorporated into the statistical procedures in the following way. For the subset of bins with correlated systematic errors the normalisation of the signal

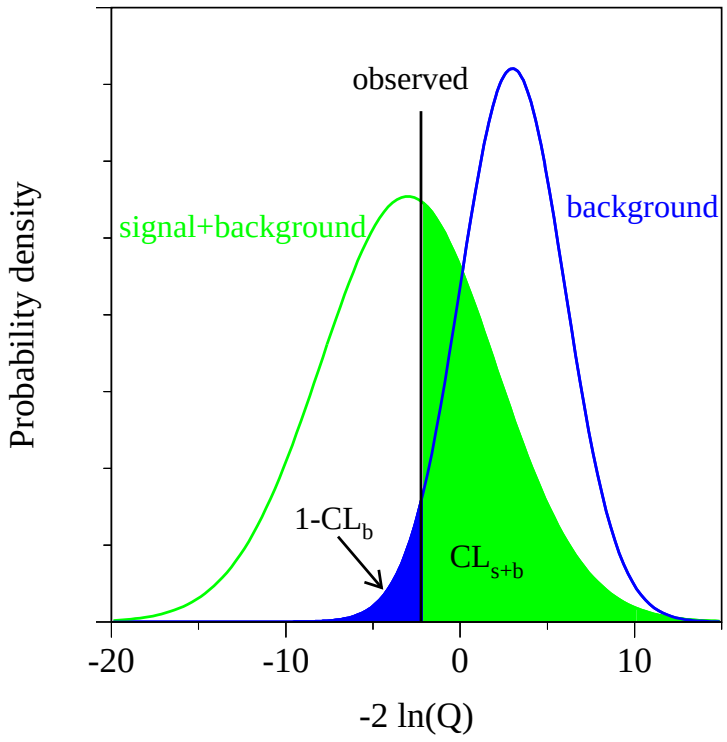

Figure 5.9: Definition of confidence levels.

and background is changed using a Gaussian distribution accordingly to the evaluated systematic errors on the number of expected signal and background events.

The observed value of the logarithm of the likelihood ratio is then compared to the spectra of -2lnQ obtained for the "signal+background" and "background-only" hypotheses. The definition of confidence levels is illustrated in Figure 5.9. The confidence level for the "background-only" hypothesis, $(1 - \mathrm{CL_b})$, is the probability of observing in a sample of simulated "background-only" experiments a more signal-like value of -2lnQ than observed in the data. The distribution of $(1 - \mathrm{CL_b})$ in a spectrum of simulated "background-only" experiments is uniform between 0 and 1, thus its median expected value is 0.5. The $(1 - \mathrm{CL_b})$ values of 0.16 and 0.84 (0.025 and 0.975) correspond to the

68% (95%) probability intervals centred on the background expected median value. Hereafter these intervals are referred to as 1σ (2σ) bands with respect to "background-only" hypothesis. The observation of the $(1 - \mathrm{CL_b})$ value of $2.7{\cdot}10^{-3}(5.7{\cdot}10^{-7})$ means that there is an excess of 3(5) standard deviations in the data compared to the expectation from the background. Similarly, the confidence level for "signal+background" hypothesis, $\mathrm{CL_{s+b}}$, is defined as probability of observing in a spectrum of "signal+background" experiments a less signal-like value of -2lnQ than in the data. To avoid bias due to statistical fluctuations, the third quantity, $\mathrm{CL_s} = \mathrm{CL_{s+b}}/\mathrm{CL_b}$, is introduced and used to exclude the signal hypothesis. Observation of a $\mathrm{CL_s}$ value smaller than 5 % means that the signal hypothesis is ruled out at 95 % confidence level. Bins of final discriminants with a signal-to-background ratio smaller than 0.05 are not considered in calculation of confidence levels as they degrade the analysis performance once systematic errors are included.

Qualitatively, the search sensitivity, is determined by how well the -2lnQ distribution for the "signal+background" hypothesis is separated from that for the "background-only" hypothesis. If there is only a tiny overlap between these distributions, the signal is well distinguishable from the background and the search sensitivity is high. If there is a huge overlap between these distributions, the signal is poorly separated from the background. Quantitatively, the search sensitivity can be expressed in terms of the expected median confidence level, $\mathrm{CL_{med}}$, which is defined as $\mathrm{CL_{s+b}}/\mathrm{CL_b}$ corresponding to the median value of -2lnQ in an ensemble of "background-only" experiments. The lower the value of $\mathrm{CL_{med}}$ is obtained the better the separation between signal and background is achieved and the more performant the analysis is considered to be. Thus, optimisation of the analysis performance implies the adjustment of the selection criteria in order to minimise $\mathrm{CL_{med}}$.

Chapter 6

Analysis Tools

The accumulation of raw experimental information proceeds in the following way:

- interesting events are triggered and recorded during data taking;
- tracks and calorimetric clusters are reconstructed with the standard reconstruction software;
- tracks reconstructed with the inner tracking system are associated with calorimetric clusters or muon chamber tracks.

Any analysis of experimental data relies upon a set of algorithms designed to properly reconstruct events recorded by the detector. These algorithms are applied at different stages of the event reconstruction procedure to gradually transform fragmented raw information, like reconstructed tracks and calorimetric clusters into physical quantities such as jet four-momenta, dijet masses, momenta of isolated leptons and photons.

The purpose of this chapter is to describe the most important algorithms related to the event reconstruction procedure.

6.1 Jet Clustering

At the first stage of the reconstruction of hadronic events, we deal with a large number of particles which left their traces in the detector in the form of reconstructed tracks and energy depositions in the calorimeter. These particles are just descendants of the primary objects created in e^+e^- collisions. To reveal the physical origin of an event one needs to retrieve the information about these "parent" objects. This is achieved by applying the procedure of unifying the energy deposits in the detector into larger units. In L3 this procedure is realised using the Durham jet reconstruction algorithm [85]. The momenta of the tracks reconstructed by the inner tracker and muon chambers and calorimetric energy depositions determine the initial set of particles. For each pair of particles i and j, a quantity

$$y_{ij} = \frac{2\min(E_i^2, E_j^2)}{E_{vis}^2}\Big(1 - \cos\theta_{ij}\Big) \tag{6.1}$$

is determined, where E_i and E_j are the energies of the two particles, $\cos\theta_{ij}$ is the opening angle between them and E_{vis} is the whole energy deposited in the detector called also visible energy. The pair with the smallest y_{ij} is combined into a new particle by summing up the four momenta of the particles i and j:

$$\begin{aligned} \tilde{P}_{ij} &= \tilde{P}_i + \tilde{P}_j, \\ E_{ij} &= E_i + E_j. \end{aligned} \tag{6.2}$$

The list of particles is updated and the procedure described above is repeated unless the smallest y_{ij} at the current iteration exceeds some predefined threshold y_{cut}. Proceeding in this way we can cluster each event into a certain number of pseudo-particles (jets) by adjusting the cut-off parameter y_{cut}. The value of y_{cut} for which an event goes from four-jet to three-jet topology is denoted Y_{34}. It quantifies the consistency of an event with the four-jet configuration.

6.2 Kinematic fit

Once we structured the event into the four-jet topology, a kinematic fit is performed to improve the dijet mass resolution. This implies the variation of the measured quantities defining the event configuration under certain constraints.

The fit is performed with fixed jet velocities, leading to a cancellation of possible systematic effects arising from the energy scale uncertainty. Thus we are left with twelve independent quantities which describe a four-jet event. These are the energy of each of the four jets, E_i, their polar angles, θ_i, and azimuthal angles, ϕ_i. These quantities are varied to minimise a χ^2 function defined in the following way:

$$\chi^2 = (\tilde{V} - \tilde{V}^0)^T \hat{W} (\tilde{V} - \tilde{V}^0), \tag{6.3}$$

where $\tilde{V}$ is the vector of varied quantities, $\tilde{V}^0$ is the vector composed of their measured values and $\hat{W}$ is the global error matrix describing the four-jet system. It is assumed to be diagonal, meaning that the measurements of the jets are uncorrelated. The errors on the measured jet quantities are taken to be

$$\begin{aligned} \frac{\sigma_{E_i}}{E_i} &= \frac{0.55}{\sqrt{E_j/\mathrm{GeV}}} \oplus 0.05 \ , \\ \sigma_{\theta_i} &= 0.017 \ \ (\mathrm{rad}), \\ \sigma_{\phi_i} &= \frac{\sigma_{\theta_i}}{2\sin\theta_i} \ \ (\mathrm{rad}). \end{aligned} \tag{6.4}$$

This parametrisation was obtained by investigating the invariant masses in four-jet events at 130 GeV $< \sqrt{s} <$ 172 GeV [86]. Recently, more accurate resolution functions of jet measurements were derived from Monte Carlo studies of $q\bar{q}\gamma$ and WW samples at $\sqrt{s}$ around 200 GeV [87]. The jets' energies and angles are not independent quantities.

They must fulfil at least the requirement of energy-momentum conservation:

$$\begin{aligned} \textstyle\sum_i E_i &= \sqrt{s}, \\ \textstyle\sum_i \tilde{P}_i &= 0, \end{aligned} \tag{6.5}$$

where $\tilde{P}_i$ is the momentum of the i-th jet. Furthermore, as was already mentioned the minimisation of the χ^2 function is performed with fixed jet velocities. Therefore the momentum of the i-th jet is related to its energy as:

$$|\tilde{P}_i| = E_i \frac{|\tilde{P}_i^0|}{E_i^0}, \tag{6.6}$$

where $\tilde{P}_i^0$ and E_i^0 are measured values of corresponding quantities. The minimisation of χ^2 under constraints is performed using the method of the Lagrange multipliers. The detailed description of the kinematic fit algorithm employed in L3 can be found in Reference [88].

Since the energy-momentum conservation requirement includes four constraints, the kinematic fit is called four-constraint (4C) fit. This requirement can be complemented by additional constraints. For instance, in the $HZ \to q\bar{q}q\bar{q}$ and $HZ \to q\bar{q}\ell^+\ell^-$ analyses it is reasonable to constraint the invariant mass of the dijet or dilepton systems, presumably arising from the decay of the Z boson, to m_Z . These cases correspond to the so-called five constraint (5C) kinematic fit. The invariant mass of the jets recoiling against the Z boson is then compared to the tested Higgs boson mass hypothesis.

In the $HZ \to q\bar{q}q\bar{q}$ analysis there are six possibilities to assign four jets to the Higgs and Z bosons. Therefore it is relevant to examine all jet combinations for their compatibility with the HZ production hypothesis. It is done by performing a six constraint (6C) fit with the additional requirement that the invariant mass of the dijet system recoiling against the Z boson equals to the tested Higgs boson mass. The probability associated with a χ^2 of the 6C kinematic fit quantifies the consistency of the jet combination with the considered Higgs boson mass hypothesis.

The interpretation of an event under the hypothesis that two particles of equal masses are produced is one of the important analysis steps in the four-jet channel. This gives additional distinguishing power between the HZ signal and hadronic decays of W- and Z-pairs. The equal mass constraint is added to the requirement of energy-momentum conservation and a 5C fit is performed for each jet combination. Then the jet pairing with the best χ^2 is chosen. The mass of this pairing is reconstructed and then exploited to separate the signal from hadronic decays of W- and Z-pairs.

The effect of the kinematic fit on the mass resolution[1] can be illustrated with the Monte Carlo sample of hadronic decays of pair produced h and A Higgs bosons with equal masses, $m_h = m_A = 70$ GeV. Figure 6.1a shows the distribution of the Higgs boson mass reconstructed as a half of the sum of the measured dijet masses. The jet

[1]The mass resolution is defined as the width of a Gaussian function approximating a peak in the reconstructed mass spectrum.

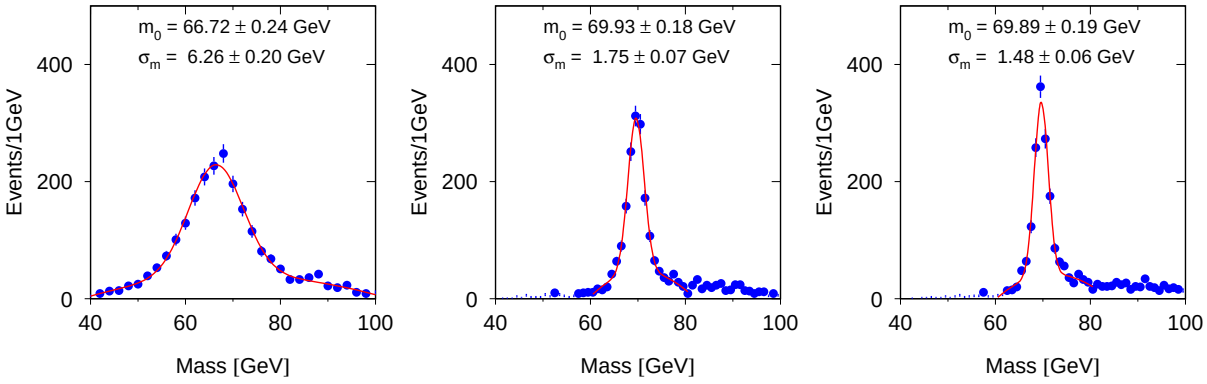

Figure 6.1: Effect of kinematic fit on the mass resolution.

pairing with minimal dijet mass difference is chosen. In this case the mass resolution constitutes $\sigma_{\mathrm{m}} \sim 6.3$ GeV. Then a 4C fit is performed and the same mass reconstruction procedure is applied with the exception that the measured dijet masses are replaced by their fitted values. This improves the mass resolution to $\sigma_{\mathrm{m}} \sim 1.8$ GeV as can be seen in Figure 6.1b. Finally, a 5C fit assuming equal mass is performed further improving the resolution to $\sigma_{\mathrm{m}} \sim 1.5$ GeV as depicted in Figure 6.1c.

6.3 B-tagging

In Chapter 3 we saw that for both the Standard Model and for a large part of the parameter space in the MSSM in the mass range investigated at LEP neutral Higgs bosons are predicted to decay dominantly into b quarks. On the other hand, well known background processes result into a much lower production rates of b quarks in comparison with lighter quarks. Thus, the SM Higgs boson and neutral Higgs bosons of the MSSM can be distinguished from the background processes by their decays into b quarks. The identification of b quarks or b-tagging is based on specific features distinguishing b jets from the jets initiated by light flavour quarks. The main purpose of this section is to explain the algorithm of tagging b quarks.

A comparison between the properties of b hadrons and the hadrons composed of only lighter quarks is given in Table 6.1. First of all, it is known that b hadrons have a longer life-time compared to many other particles. Hence, b jets likely contain secondary vertices located away from the $\mathrm{e^+e^-}$ interaction point. Meanwhile, the exceptionally long-lived particles, like $\mathrm{K^0_S}$ or Λ^0, decay in average much farther away from the $\mathrm{e^+e^-}$ interaction point thus making them easy to reject. As one can see from Table 6.1 some of the hadrons containing a c quark have a comparable decay length with b hadrons. Further discrimination is achieved due to the fact that b jets have larger multiplicities and b hadrons are characterised by smaller boosts compared to hadrons containing a c quark. Finally, since in many cases b hadrons decay semileptonically, the presence of a high energy prompt lepton in the jet would favour the b quark hypothesis.

	Lifetime (ps)	Typical boost $\gamma\beta$ $\sqrt{s} = 91.2$ GeV	Typical decay length $\gamma\beta c\tau$ (mm) $\sqrt{s} = 91.2$ GeV
$B^{\pm}$	1.65±0.04	6	3.0
B^0	1.56±0.04	6	2.8
B_s^0	1.54±0.07	6	2.8
$D^{\pm}$	1.057±0.015	12	3.8
D^0	0.415±0.004	12	1.5
$D_s^{\pm}$	0.467±0.017	11.5	1.6
$\Lambda_c^{\pm}$	0.206±0.012	10	0.6
τ-lepton	0.29±0.02	25.5	2.2
K_S^0	89.27±0.09	6	160
Λ^0	263±2	2.5	197

Table 6.1: Typical decay lengths and boosts of b hadrons and other particles [89].

A detailed description of the b-tagging procedure employed in L3 can be found in Reference [90]. I will just briefly outline the main ideas underlying the algorithm of b quark identification.

The b-tagging procedure starts with the reconstruction of the e^+e^- collision point. The primary interaction vertex is searched for by minimising a χ^2 function which contains two terms:

$$\chi^2_{\text{vert}} = \chi^2_{\text{beam}} + \chi^2_{\text{tracks}}. \tag{6.7}$$

The term χ^2_{beam} is determined by the beam position and dimensions in the $r\phi$ plane as monitored during data taking. In other words we constrain the primary vertex to the beam spot envelope in the projection orthogonal to the beam axis. The term χ^2_{tracks} is determined by track parameters reconstructed by combined measurements with SMD and TEC. For each track the distance of closest approach (DCA) to the searched primary vertex is calculated at each step of the χ^2_{vert} minimisation procedure. The χ^2_{tracks} is defined as error weighted quadratic sum of these DCA's. Tracks that significantly worsen χ^2_{vert} are excluded from the procedure of the primary vertex reconstruction.

Once the primary vertex is reconstructed, the jet clustering algorithm is applied and the event is forced into the desired number of jets. The crossing point of each track with the jet momentum vector is determined in the $r\phi$ and the sz[2] planes.

The distance between this crossing point and the primary vertex define decay lengths in two projections, $L_{r\phi}$ and L_{sz}. It should be noted that both $L_{r\phi}$ and L_{sz} are signed quantities. A positive sign is given if the track crosses the jet momentum vector in the supposed direction of the initial quark flight. Otherwise, $L_{r\phi}$ and L_{sz} acquire negative values[3]. The quantities $L_{r\phi}$ and L_{sz}, and their errors are used to calculate a

[2] The sz plane is defined as "unfolded"cylindrical surface in which the helic track trajectory lies.
[3] Negative values of the decay length are possible due to finite SMD resolution.

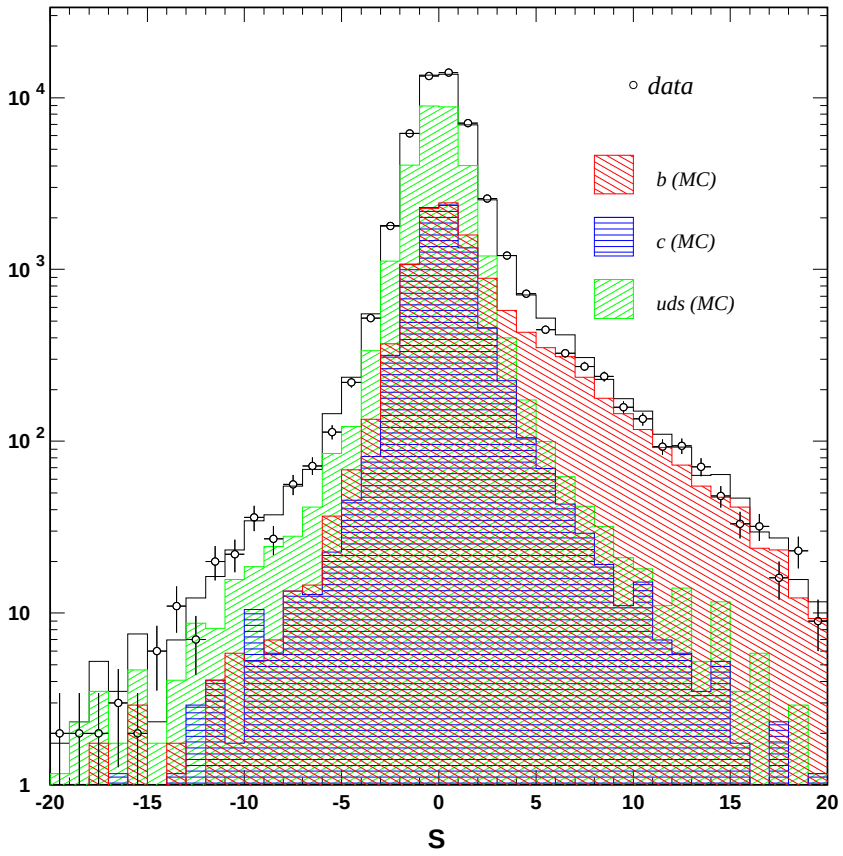

Figure 6.2: Decay length significance distribution. The data sample of hadronic events, collected during a calibration run at $\sqrt{s} = 91.2$ GeV, is represented by points. The corresponding Monte Carlo sample, broken down by the flavour content of the final state, is represented by histograms.

three-dimensional decay length variable, L. The precision of the determination of L is accounted for by introducing a quantity called decay length significance. It is defined as the ratio of the decay length to the corresponding error, $s = L/\sigma_L$. The decay length significance is calculated for different track categories depending on the availability of SMD and Z-chamber information. For the tracks belonging to the jets initiated by light flavour quarks, the s distribution is narrow and almost symmetric with a slight preference for positive values as can be seen in Figure 6.2. For tracks in b jets, the s distribution has a pronounced asymmetry with positive values of the decay length significance prevailing. This effect is explained by two factors. First, the asymmetry is caused by longer decay lengths of b hadrons. Second, smaller boosts and larger masses of b hadrons result in average in larger angles between the direction of the b hadron flight and momentum vectors of the decay products. This allows to determine the decay length with smaller error. As a consequence the decay length significance acquires larger values thus making the distribution broader. The negative side of the distribution is fitted with an arbitrary function. The resolution function R(s) obtained from this fit is then used to calculate track probabilities P(s) for the positive side. The probability that a track with the decay

length significance larger than s originates from the primary vertex is then:

$$P(s) = \frac{\int_s^\infty R(s')ds'}{\int_0^\infty R(s')ds'}. \tag{6.8}$$

The individual track probabilities are weighted depending on the decay length resolution and their momenta and are finally combined into a weighted probability P_n^w, where n denotes the number of tracks which are included. For a detailed discussion on the derivation of this quantity see Reference [90]. Jets with b quarks will have low values in P_n^w.

To profit from other properties distinguishing b jets from the lighter quark jets, an artificial neural network [91] is applied which combines decay length information

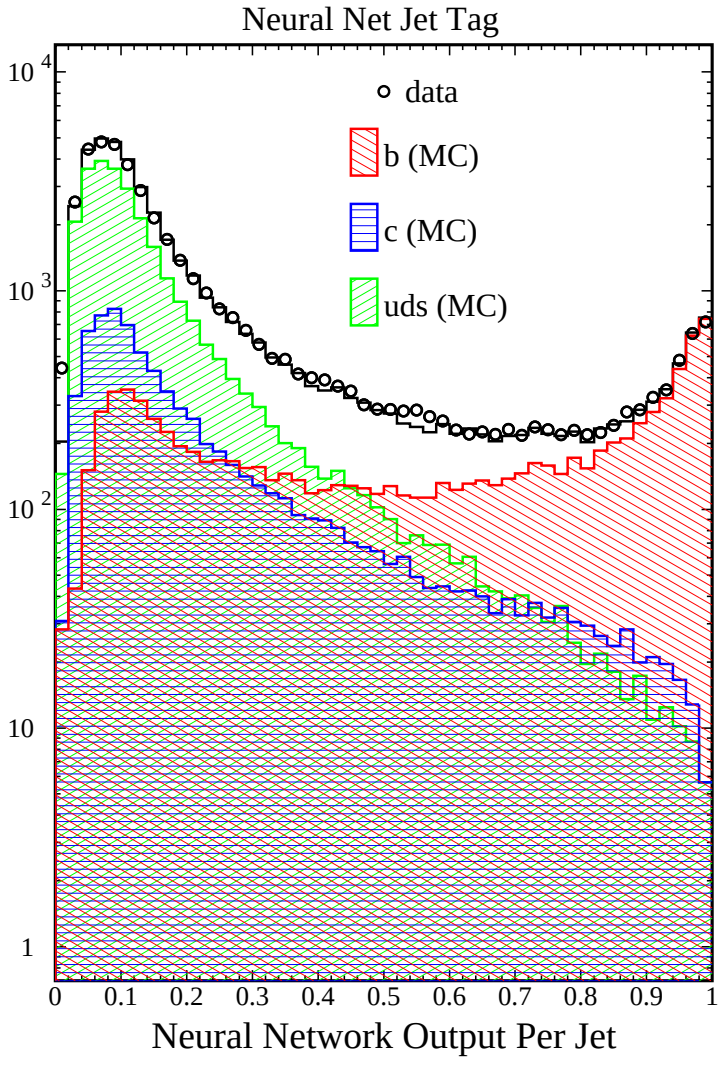

Figure 6.3: The distribution of b-tag NNet output per jet. The data sample of hadronic events, collected during a calibration run at $\sqrt{s} = 91.2$ GeV, is represented by points. The corresponding Monte Carlo sample, broken down by the flavour content of the final state, is represented by histograms.

contained in P_n^w, the multiplicity and kinematic characteristics of the jet, information about secondary vertices and energetic prompt leptons. The neural network (NNet) is trained to separate b jets from the light flavour jets. Values of NNet output close to 1 favour the b jet hypothesis while the values close to zero indicate that the jet likely originates from a light flavour quark. The NNet output per jet is usually referred to as jet b-tag. Its distribution is shown in Figure 6.3 for the sample of hadronic events collected during a calibration run at $\sqrt{s} = 91.2$ GeV and for the corresponding Monte Carlo sample broken down by the flavour content of the final state. To evaluate the presence of b hadrons in the event, a quantity called global event b-tag is introduced. First, for each jet a probability to originate from the light flavour quark is computed by comparing the value of jet b-tag with the Monte Carlo distribution containing only jets originating from light flavour quarks. The event b-tag is then defined as the negative logarithm of the combined individual jet probabilities.

The b-tagging performance for the data taken in the year 2000 at $\sqrt{s} > 203$ GeV is verified with a control sample of $e^+e^- \to q\bar{q}\gamma$ events. The efficiency for tagging light flavour hadrons is checked with a sample of $W^+W^- \to q\bar{q}\ell\nu$ events. The selection of these samples is described in appendix A. The agreement of data with the simulation of Standard Model processes in the jet b-tag variable is shown in Figure 6.4 for $e^+e^- \to q\bar{q}\gamma$ and $W^+W^- \to q\bar{q}\ell\nu$ events. The data distributions are well described by the Monte Carlo simulation.

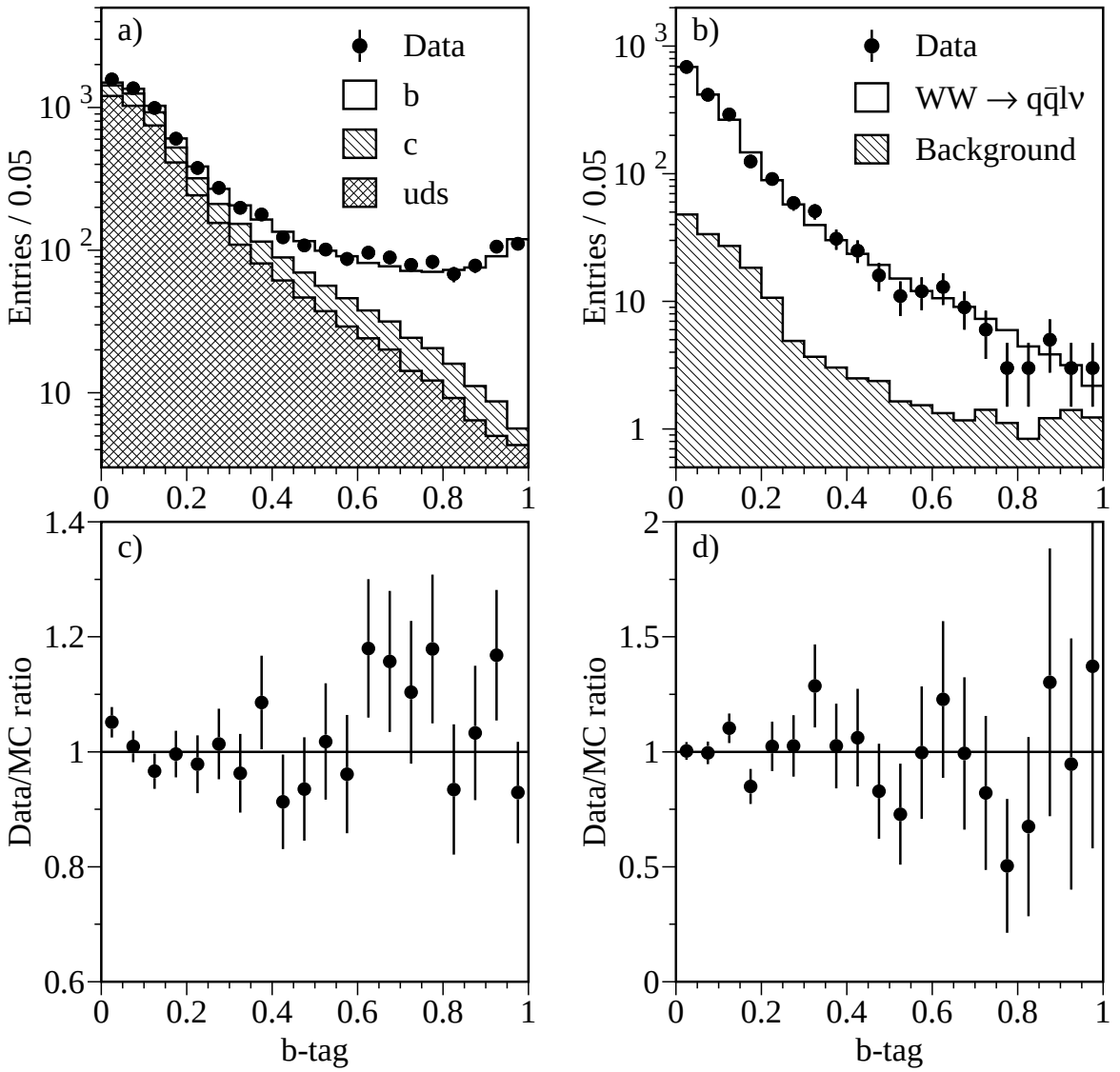

Figure 6.4: Distribution of the neural network jet b-tag variable in a sample of a) $e^+e^- \to q\bar{q}\gamma$ and b) $W^+W^- \to q\bar{q}\ell\nu$ events from the high-energy data collected in the year 2000. Two entries per event contribute to the distributions. The data are compared to the simulation of Standard Model processes. The bin-by-bin ratio of the data to the simulated events is displayed in c) and d).

Chapter 7

Search for the SM Higgs Boson

As discussed in Section 5.1 the search for the SM Higgs boson relies upon the investigation of four distinct topologies. In this section the analysis searching for the SM Higgs boson in the four-jet channel is described in detail, other search channels are briefly reviewed and the combined results are discussed.

7.1 The $HZ \to q\bar{q}q\bar{q}$ Channel

The signature of the $HZ \to q\bar{q}q\bar{q}$ final state is four high-multiplicity hadronic jets and the presence of b hadrons, in particular in the jets expected to stem from the Higgs boson. The invariant mass of the jets assigned to the Z boson must be compatible with the Z mass. An event compatible with the signal topology in the $HZ \to q\bar{q}q\bar{q}$ channel is displayed in Figure 7.1.

The dominant backgrounds arise from $q\bar{q}\gamma$ final states and hadronic decays of W- and Z-pairs.

First, a preselection of high-multiplicity hadronic events is applied. At least 15 tracks and 20 calorimetric clusters are required. The visible energy, E_{vis}, must exceed 60% and be less than 140% of the center-of-mass energy. The energy imbalance perpendicular to beam direction must be less than 30%.

To reject radiative returns to the Z with photons escaping in the beam pipe the quantity $\Delta E_l/|m_{vis} - m_Z|$ must be less than 0.5, where m_{vis} is the visible mass of the event and ΔE_l is the energy imbalance along the beam direction. In addition, events with an isolated photon of more than 20 GeV energy are rejected.

Gauge boson pair production with one of the bosons decaying leptonically is suppressed by rejecting events containing an electron or muon with an energy larger than 40 GeV.

Remaining two-jet events are further suppressed by the requirement Y_{34} >0.002. Background originating from two-photon interactions is suppressed by the requirement $|\cos\Theta_T| < 0.95$, where $\cos\Theta_T$ is the cosine of the polar angle of the event thrust vector.

Events passing this preselection are then forced into a four-jet topology using the Durham algorithm and subject of a 4C kinematic fit.

The numbers of events obtained from ZZ, WW and $q\bar{q}\gamma$ Monte Carlo simulations and

selected in data for all center-of-mass energies are given in Table 7.1. The contributions from other background sources are negligible. The sum of the number of events from all background sources is in good agreement with the number of events in data. The signal preselection efficiency is larger than 90% for Higgs boson masses above 95 GeV.

$\sqrt{s}$ (GeV)	203.8	205.1	206.3	206.6	208.0	208.6
ZZ	5.0	37.0	36.7	35.1	4.5	0.05
WW	48.8	444.5	433.1	412.4	52.9	0.64
$q\bar{q}\gamma$	18.3	164.9	160.7	153.0	19.4	0.24
Total background	72.1	646.4	630.5	600.5	76.8	0.93
Data	79	651	682	599	84	1

Table 7.1: The numbers of events expected from the different background sources, their sum and the number of events selected in data for all center-of-mass energies after the preselection.

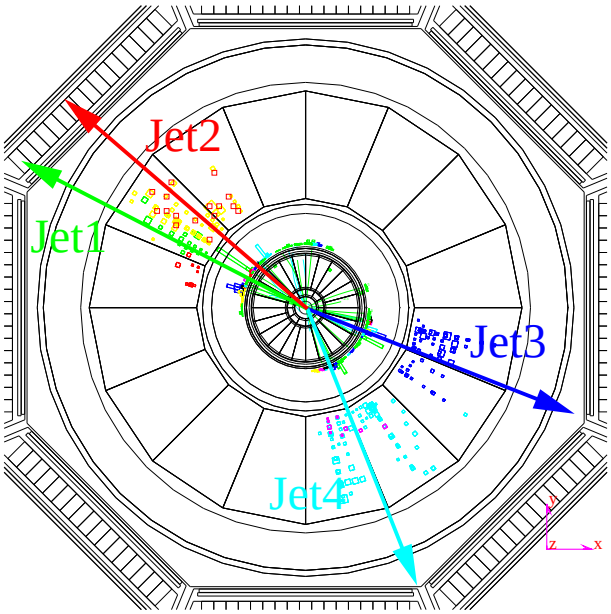

Figure 7.1: Typical $HZ \to q\bar{q}q\bar{q}$ candidate. The event is compatible with a four-jet topology. Jets 2 and 3 are assigned to the Higgs boson. Their b-tag values are 0.93 and 0.63 favouring the b quark hypothesis. The invariant masses of the dijet systems are $m_{14} = 95.2$ GeV and $m_{23} = 104.2$ GeV. The hypothetical mass of the Higgs boson is calculated as $m_H = m_{12} + m_{34} - m_Z = 108.2$ GeV. The compatibility with the ZZ and WW production hypotheses was tested with a 6C fit constraining both dijet masses to m_Z or m_W. This procedure was performed for each jet combination. Probabilities associated with the best χ^2 of the fit are 1.5% and 0.07% for the ZZ and WW hypotheses, respectively. The event was recorded by the L3 detector at $\sqrt{s} = 206.4$ GeV.

After the preselection the most discriminating variables are combined into one discriminant which is then used to select events into the final sample. This discriminant is constructed using the binned likelihood technique [92]. Each final state is considered as an event class j (j=HZ, ZZ, WW, $q\bar{q}\gamma$). For each class probability density functions $f^j(x_i)$ are derived from Monte Carlo, where x_i denotes one of the variables, which have discriminating power between the signal and background classes. The probability of an

event to belong to the event class j, based solely on the value of the variable x_i, is defined as:

$$p^j(x_i) = \frac{f^j(x_i)}{\sum_k f^k(x_i)}, \tag{7.1}$$

where k runs over all classes.

Finally, the individual probabilities are combined into a likelihood. The likelihood, L_{HZ}, that an event belongs to the signal class, is given by the following equation:

$$L_{HZ} = \frac{\prod_i p^{HZ}(x_i)}{\sum_k \prod_i p^k(x_i)}, \tag{7.2}$$

where i runs over all variables considered and k over all event classes. Two kinds of variables are used to calculate the likelihood L_{HZ}. These are first topological and kinematic event characteristics:

- number of tracks, N_{TRK};
- global event b-tag, B_{TAG};
- maximal jet energy difference, normalised to the center-of-mass energy, $\Delta E_{jet}^{max}/\sqrt{s}$;
- minimal jet energy, normalised to the center-of-mass energy, $E_{jet}^{min}/\sqrt{s}$;
- logarithm of jet resolution parameter Y_{34};
- maximal jet triplet boost, γ_{triple}, which is defined as the maximum three-jet boost obtained from the four possibilities to construct a different one-jet against three-jet constellation in a 4-jet event [93];
- minimum opening angle between any two jets, Θ_{jj}^{min};
- event sphericity [76].

Second, the dijet masses and the cosine of the production polar angle assuming the production of a pair of bosons, $\cos\Theta_{2B}$, are exploited. Four jets can be combined to three different dijet pairings. The invariant masses of both dijet systems are compared to the expectation from the ZZ and WW final states allowing to identify background from these channels. The motivation for using the production polar angle is given by the scalar nature of the Higgs boson, which implies a polar angle distribution strongly different from the one of W or Z boson pair production.

Firstly, a 5C kinematic fit imposing energy and momentum conservation and the requirement that the dijet masses are equal is performed. The combination with the best χ^2 is taken and the invariant mass, m_{eq}^{5C}, is used as discriminating variable along with the probability associated with the best χ^2 of the fit, P_{2B}. Moreover, for this dijet pairing the polar production angle, Θ_{2B}, is reconstructed and is also included into L_{HZ}.

The distributions of the variables used to construct L_{HZ} and the distribution of L_{HZ} are shown in Figures 7.2, 7.3 and 7.4 for data and Monte Carlo samples at $\sqrt{s} = 206.6$ GeV. The difference in the shapes of the signal and the background distributions is nicely seen.

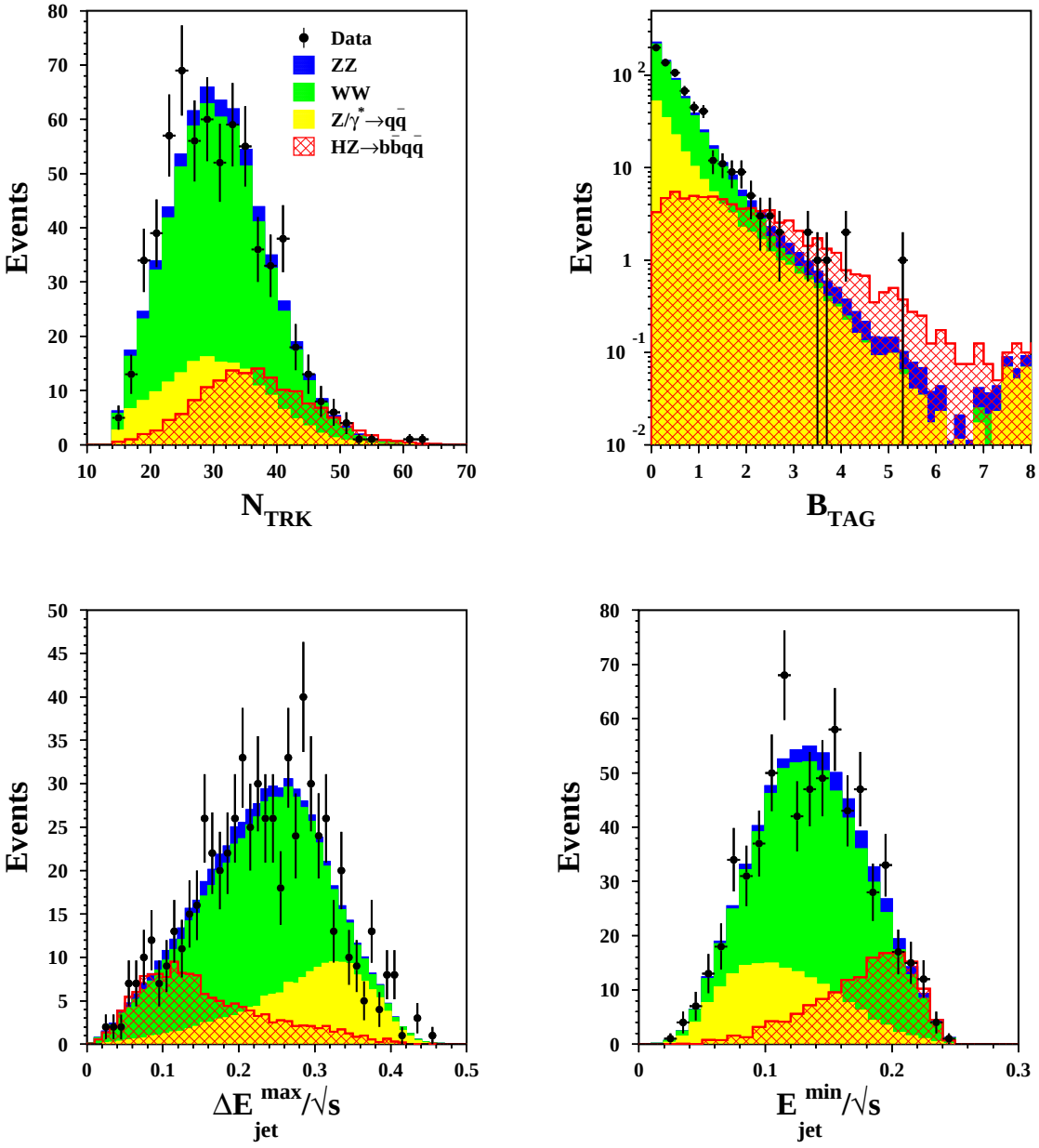

Figure 7.2: Distributions of variables from the $\sqrt{s} = 206.6$ GeV data used to construct the signal likelihood: number of tracks (top left); global event b-tag (top right); maximum jet energy difference normalised to the center-of-mass energy (bottom left); minimum of the jet energies normalised to center-of-mass energy (bottom right). Also shown are the expectations from the different background sources and from a signal. The signal, shown with arbitrary normalisation, corresponds to 115 GeV Higgs boson mass.

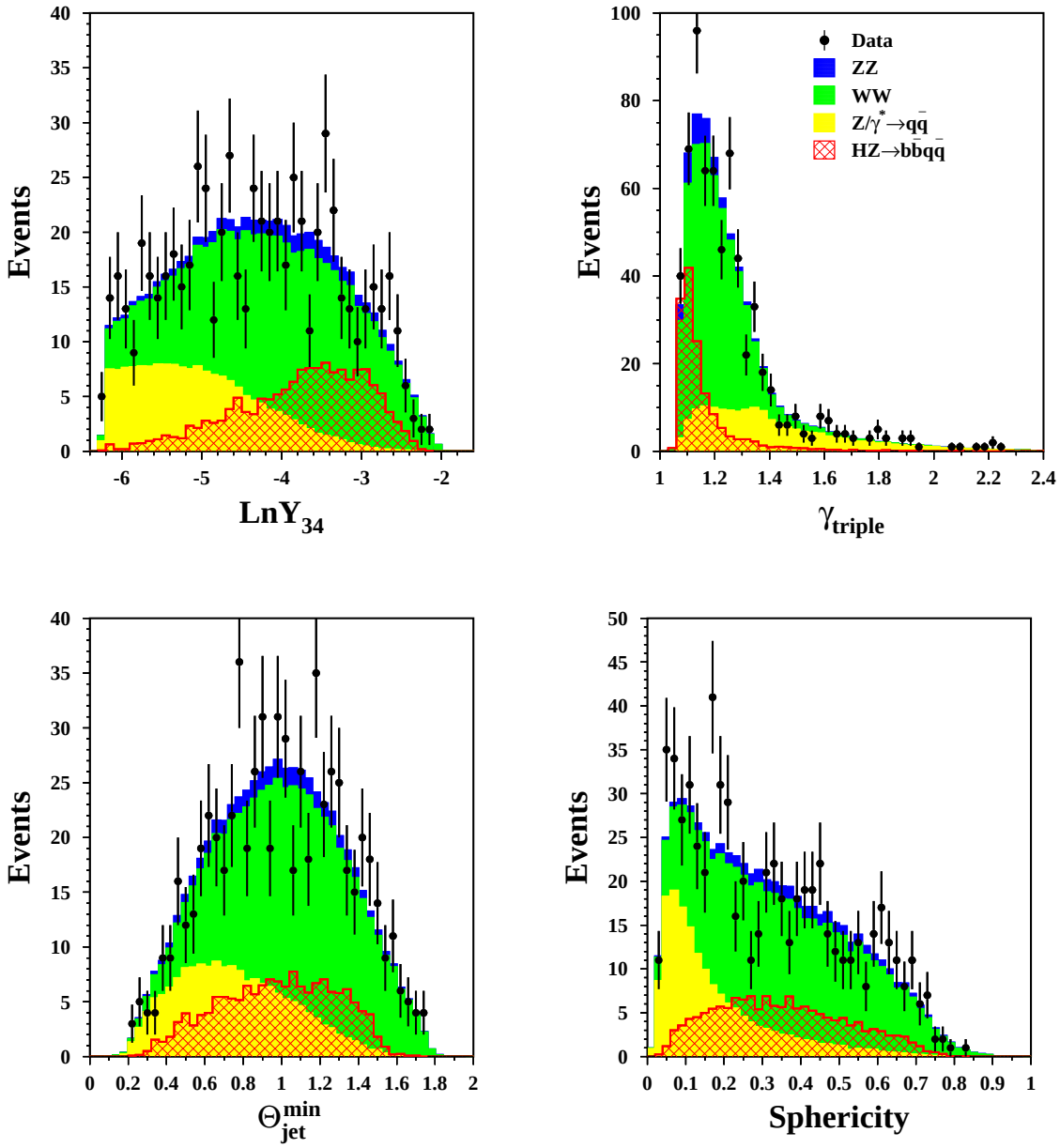

Figure 7.3: Distributions of variables from the $\sqrt{s} = 206.6$ GeV data used to construct the signal likelihood: logarithm of the Y_{34} parameter (top left); maximal jet triplet boost (top right); minimum jet-jet opening angle (bottom left); event sphericity (bottom right); Also shown are the expectations from the different background sources and from a signal. The signal, shown with arbitrary normalisation, corresponds to 115 GeV Higgs boson mass.

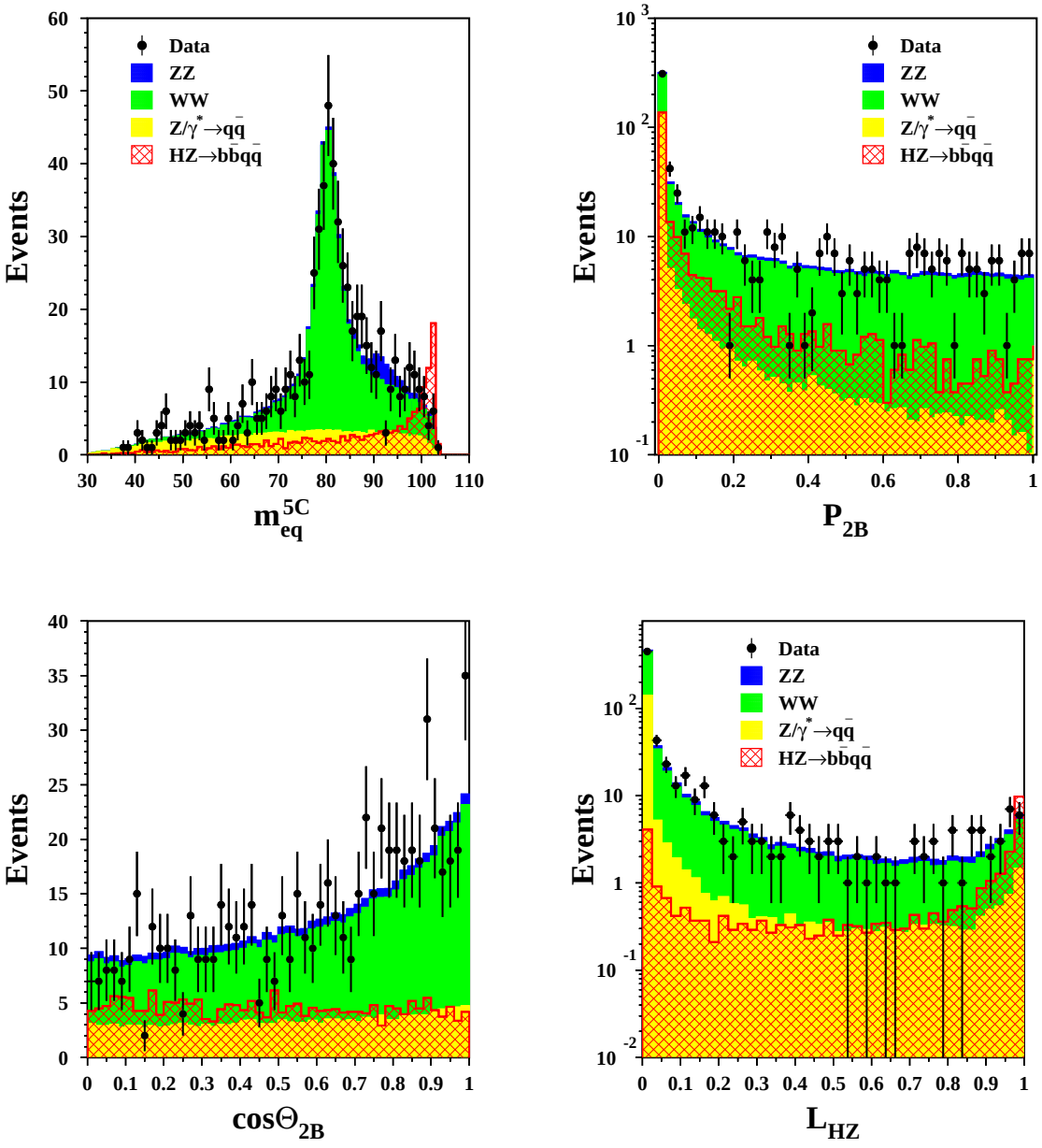

Figure 7.4: Distributions of variables from the $\sqrt{s} = 206.6$ GeV data used to construct the signal likelihood: mass from the 5C fit with equal dijet mass constraint (top left); $P_{2B}(\chi^2)$ for gauge boson pair production (top right); cosine of polar production angle of the boson (bottom left). Signal likelihood, L_{HZ}, distribution from the $\sqrt{s} = 206.6$ GeV data set (bottom right). Also shown are the expectations from the different background sources and from a signal. The signal, shown with arbitrary normalisation, corresponds to 115 GeV Higgs boson mass.

Events are selected into the final sample if the value of L_{HZ} is greater than a certain threshold, which is optimised for each center-of-mass energy and each Higgs boson mass hypothesis. The typical values of this threshold lie between 0.4 and 0.6 depending on $\sqrt{s}$ and m_H. In addition, the compatibility of each event with the probed Higgs boson mass hypothesis is tested by considering the following quantity:

$$\chi^2_{HZ} = \left(\Sigma_i - (m_H + m_Z)\right)^2/\sigma^2_\Sigma + \left(\Delta_i - |m_H - m_Z|\right)^2/\sigma^2_\Delta, \tag{7.3}$$

where Σ_i and Δ_i are the dijet mass sum and dijet mass difference of the i-th pairing after the 4C fit and σ_Σ and σ_Δ are the corresponding resolutions. The σ_Σ and σ_Δ are found to be almost independent of mass hypothesis ($\sigma_\Sigma = 4$ GeV, $\sigma_\Delta/\sigma_\Sigma = 4.6$) if the process $e^+e^- \to HZ$ occurs far above the kinematic threshold, $m_Z + m_H \leq \sqrt{s} - 20$ GeV. With approaching the kinematic threshold, $m_Z + m_H > \sqrt{s} - 20$ GeV, quantities σ^2_Σ and σ^2_Δ become strongly dependent on mass hypothesis and are parametrised as:

$$\sigma_\Sigma = 2.6\ \text{GeV} + 0.07 \cdot \left(\sqrt{s} - m_Z - m_H\right), \tag{7.4}$$

$$\frac{\sigma_\Delta}{\sigma_\Sigma} = 6.0 - 0.07\ [\text{GeV}^{-1}] \cdot \left(\sqrt{s} - m_Z - m_H\right)/\text{GeV}. \tag{7.5}$$

The jet pairing with the best χ^2 is chosen and the probability associated with the χ^2, $P(\chi^2_{HZ})$, is computed. Finally, only events with $P(\chi^2_{HZ}) > 10^{-2}$ are accepted.

For these events now the final discriminant, D_{HZ}, is constructed using the same likelihood technique as described above. At first, the events are classified into three categories depending on the ranking of the values of b-tags of the two jets assigned to the Higgs boson. The first category contains events for which non of these jets has the highest value among four jet b-tags. The second category is composed of events for which one of these jets has the highest b-tag value while another has one of two lowest b-tag values. The third category contains events for which the two jets assigned to the Higgs boson have the highest b-tag values. The quantity $\log_{10}P(\chi^2_{HZ})$, the b-tags of the individual jets and the event category are combined to D_{HZ}. Their distributions are shown in Figures 7.5 and 7.6. Since $P(\chi^2_{HZ})$ is used, D_{HZ} becomes mass dependent and must be recalculated for each Higgs boson mass hypothesis. The number of events observed in data, background and signal expectations and signal efficiency, as a function of m_H, are given in Table 7.2 for the entire data sample of the year 2000. Qualitatively evaluating this table one can conclude that the data show preference for the SM background hypothesis.

The final discriminants constructed at different center-of-mass energies are combined into one array by merging bins with close signal-to-background ratio, s/b. This is demonstrated in Figures 7.7 and 7.8 for Higgs boson mass hypotheses $m_H = 110$ GeV and $m_H = 115$ GeV. The behaviour of the commulative distribution obtained from the data is well described by the SM background.

$\sqrt{s}$ = 203 - 209 GeV					
m_H =	80 GeV	90 GeV	100 GeV	110 GeV	115 GeV
Final selection					
Data	207	149	133	124	85
Background	186.6	141.5	140.9	124.1	77.3
Signal	43.7	35.2	30.0	13.1	2.6
Efficiency, %	50	54	66	63	49
s/b > 0.5					
Data	25	15	11	5	0
Background	18.8	17.8	12.0	4.5	0.6
Signal	21.4	16.7	14.6	5.4	0.6
Efficiency, %	25	26	32	26	10

Table 7.2: The number of data events selected into final sample and retained after applying a cut on the final discriminant corresponding to a signal-to-background ratio, s/b, greater than 0.5, expected background, expected signal and signal efficiency as a function of m_H.

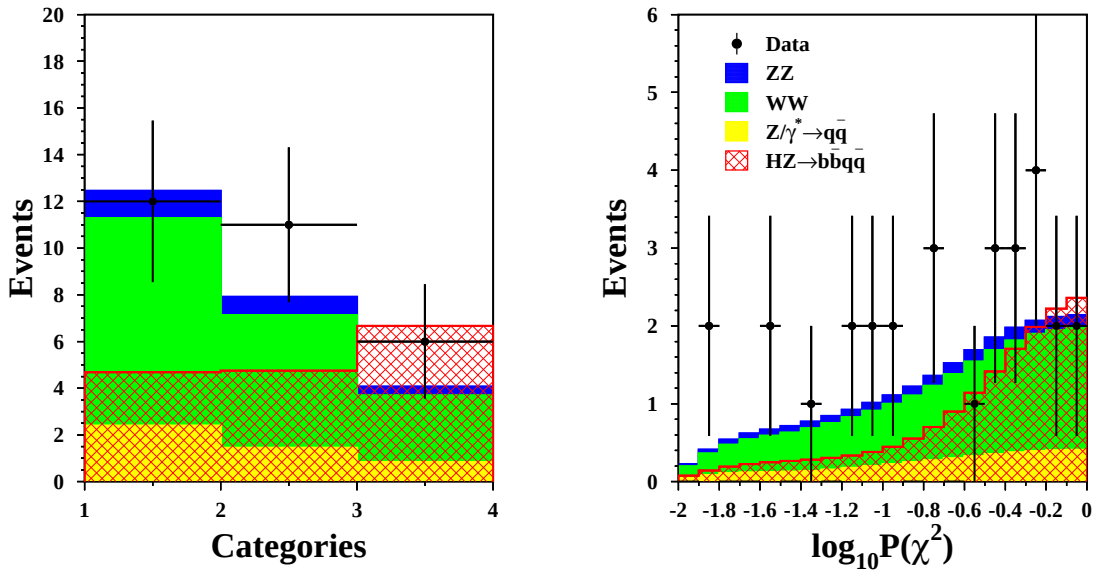

Figure 7.5: Distributions from the $\sqrt{s} = 206.6$ GeV data of: event categories using the ranking of the b-tags from the jets assigned to the Higgs boson (left) and the logarithm of $P(\chi^2)$ for a Higgs mass hypothesis of 115 GeV (right); Also shown are the expectations from the different background sources and from a signal. The signal, multiplied by a factor of 15, corresponds to 115 GeV Higgs boson mass.

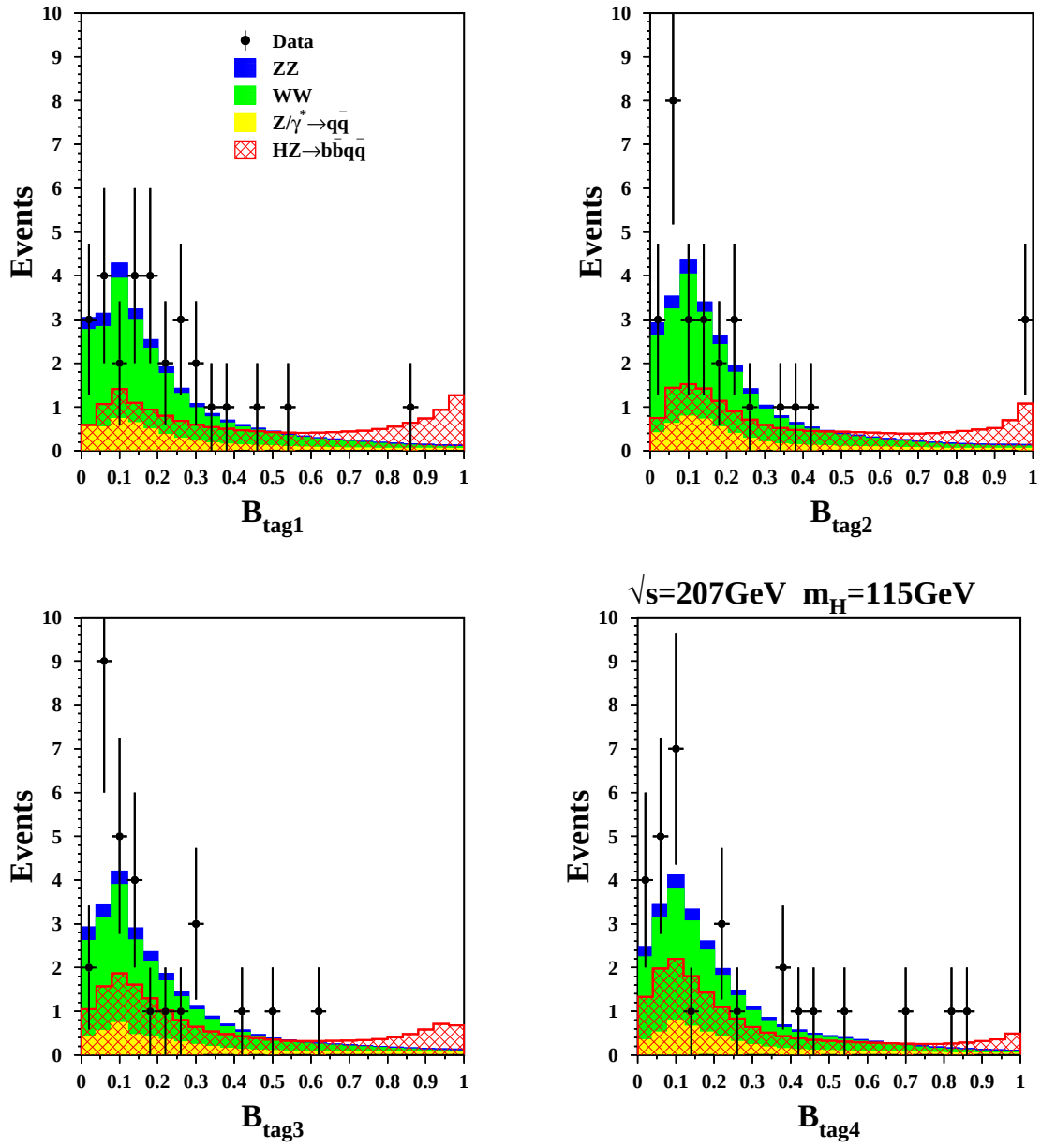

Figure 7.6: Distributions from the $\sqrt{s} = 206.6$ GeV data of: b-tag of the highest energetic jet (top left); b-tag of the second energetic jet (top right); b-tag of the third energetic jet (bottom left); b-tag of the lowest energetic jet (bottom right). Also shown are the expectations from the different background sources and from a signal. The signal, multiplied by a factor of 15, corresponds to 115 GeV Higgs boson mass.

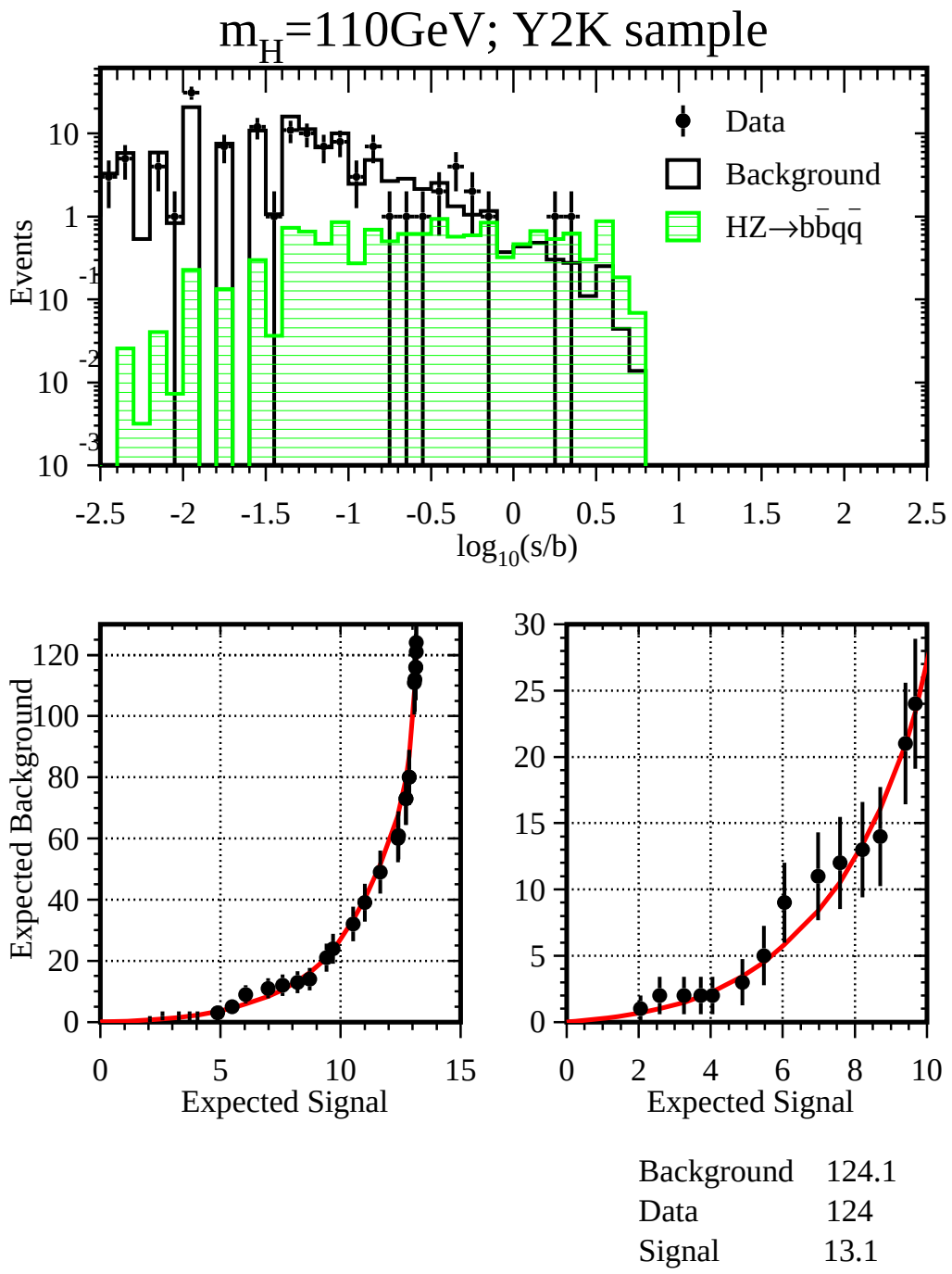

Figure 7.7: Distribution of $\log_{10}$(s/b) for the full data sample (top). The bottom left distribution is obtained by integrating the upper distribution from the right to left side. The bottom right plot is a zoomed part of the bottom left one containing the region of high signal purity. Dots are data and the line is the expectation from the background. The Higgs boson mass hypothesis is 110 GeV.

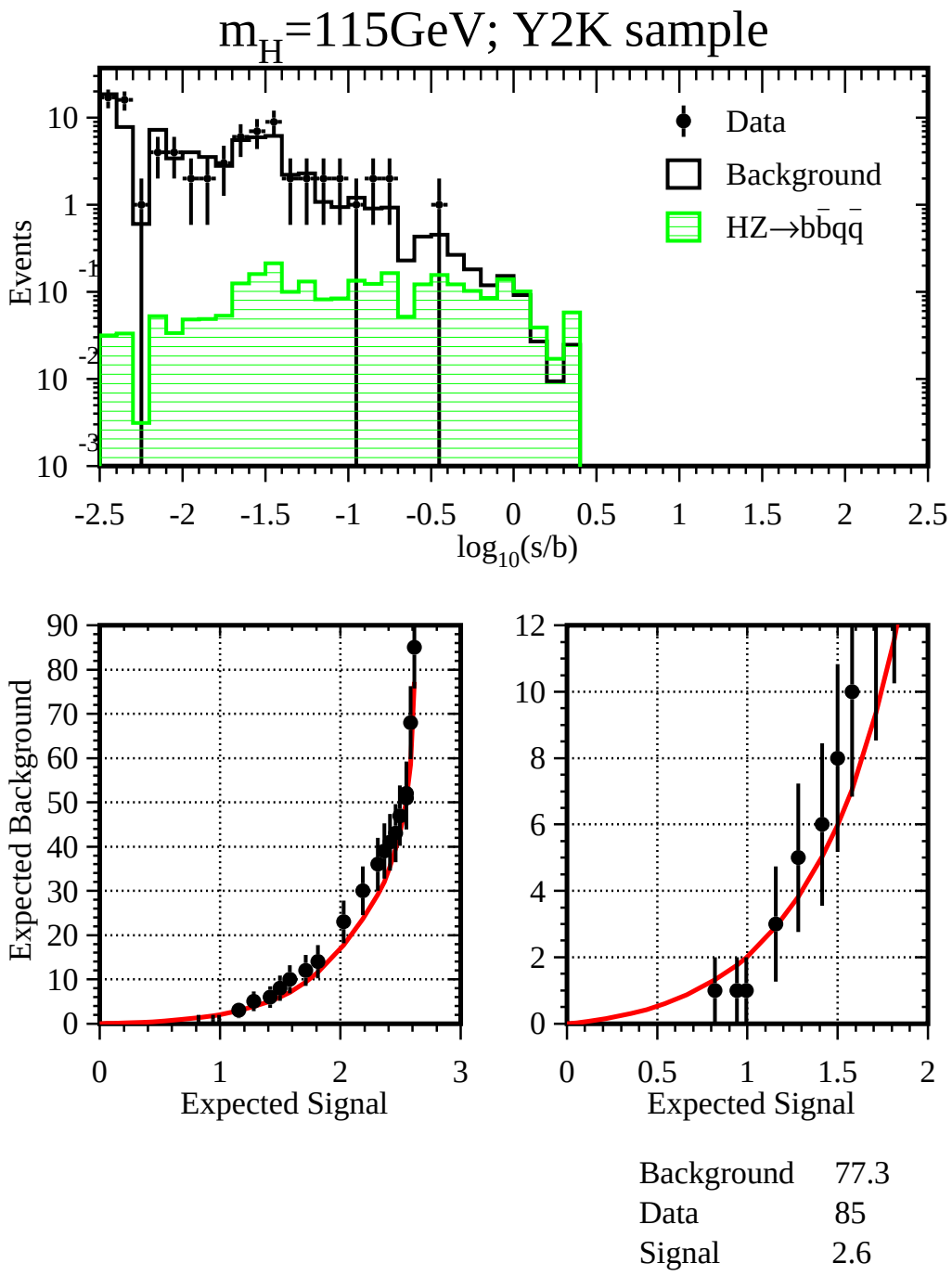

Figure 7.8: The distribution of $\log_{10}(s/b)$ for the full data sample (top). The bottom left distribution is obtained by integrating the upper distribution from the right to left side. The bottom right plot is a zoomed part of the bottom left one containing the region of high signal purity. Dots are data and the line is the expectation from the background. The Higgs boson mass hypothesis is 115 GeV.

7.2 The $HZ \to q\bar{q}\nu\bar{\nu}$ Channel

The $HZ \to q\bar{q}\nu\bar{\nu}$ analysis is based on the selection of events with two jets containing b hadrons, with large missing energy and with missing mass consistent with m_Z. The dominant backgrounds arise from the $WW \to q\bar{q}\ell\nu$, $ZZ \to q\bar{q}\nu\bar{\nu}$ and $q\bar{q}(\gamma)$ final states. In the first step of the analysis, high multiplicity hadronic events are selected and forced into two jets using the Durham algorithm. To suppress $q\bar{q}\gamma$ background, events with energetic isolated photon are rejected. Two-photon interactions are eliminated by requiring the dijet invariant mass to exceed 40 GeV. The W-pair and $q\bar{q}\gamma$ backgrounds are reduced by requiring the visible mass to be less than 140 GeV and the mass recoiling against the hadronic system to lie between 50 GeV and 130 GeV. The longitudinal missing energy must be less than 60 % of the LEP energy and the missing momentum vector must be at least 16^o away from the beam axis. The energy in the forward luminosity calorimeter must be smaller than 20 GeV and the acollinearity is required to be smaller than 65^o. After this set of cuts, there are 123 events in the data, while 130 are expected from background. The expectation from signal amounts to 4.3 and 1.3 events for m_H = 110 GeV and 115 GeV, respectively. A kinematic fit imposing four-momentum conservation and constraining the missing mass to m_Z is performed to improve the resolution of dijet mass measurement. The dijet mass obtained after the kinematic fit is regarded as the reconstructed Higgs boson mass. In the next step artificial neural network is used to discriminate the signal from the background. This network exploits variables such as jet b-tags, transverse momentum imbalance, jet masses, missing mass and χ^2 of the kinematic fit. The output of the neural network is then combined with the reconstructed Higgs boson mass to build the final discriminant. The distributions of the reconstructed Higgs boson mass and the neural network output for events selected in the final sample for $\sqrt{s} > 206$ GeV, compared to the expectation from the SM processes, are shown in Figure 7.9.

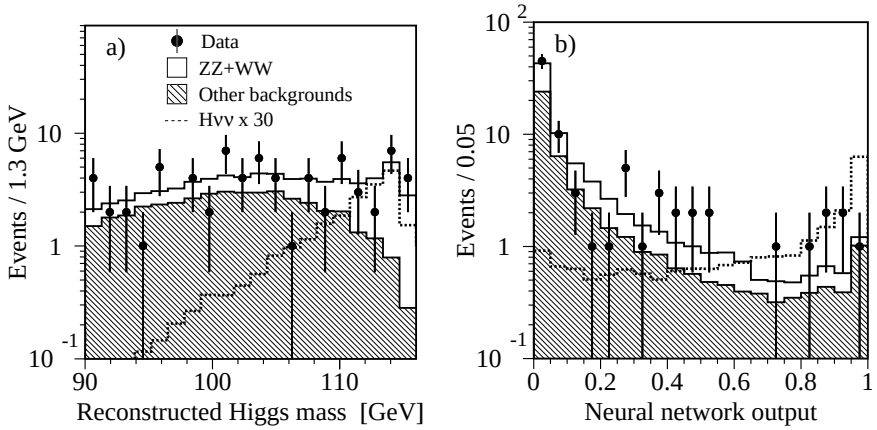

Figure 7.9: Distributions of a) the reconstructed Higgs boson mass, b) the neural network output, for events selected in the $HZ \to q\bar{q}\nu\bar{\nu}$ search channel. The points represent the data collected at $\sqrt{s} > 206$ GeV. The open and hatched histograms are the expected backgrounds. The dashed line is the expected Higgs signal with $m_H = 115$ GeV, multiplied by a factor of 30.

7.3 The $HZ \to q\bar{q}\ell^+\ell^-(\ell = e, \mu, \tau)$ and $HZ \to \tau^+\tau^- q\bar{q}$ Channels

The signatures of the $HZ \to q\bar{q}e^+e^-$ and $HZ \to q\bar{q}\mu^+\mu^-$ processes are a pair of high energy electrons or muons with an invariant mass compatible with m_Z and two hadronic jets with b quark content. In $HZ \to q\bar{q}\tau^+\tau^-$ events the tau pair invariant mass must also be compatible with m_Z. For these events, the mass resolution is worse than in the $HZ \to q\bar{q}\ell^+\ell^-$ $(\ell = e, \mu)$ channels due to the missing neutrinos from the tau decays. Events with Higgs boson decaying into tau leptons, $HZ \to \tau^+\tau^- q\bar{q}$, have similar signature to the $HZ \to q\bar{q}\tau^+\tau^-$ events, with the difference that the invariant mass of the two hadronic jets must be consistent with m_Z and that the b quark content of the events is reduced. The main background comes from $ZZ \to q\bar{q}\ell^+\ell^-$, $WW \to q\bar{q}\ell\nu$ and $q\bar{q}(\gamma)$ final states. For the $HZ \to q\bar{q}e^+e^-$ channel, Zee production represents an additional source of background. The dedicated analyses aim to select high multiplicity events. In the $HZ \to q\bar{q}\ell^+\ell^-$ $(\ell = e, \mu)$ analyses two well identified electrons or muons are also required. In the tau analyses, tau leptons are identified via their decays into electrons or muons, or as isolated low-multiplicity jets with one or three tracks and unit charge. The identified leptons must be well isolated from the hadronic jets. The procedure of lepton identification as well as selection criteria are described in detail in Reference [94].

For all $HZ \to q\bar{q}\ell^+\ell^-$ selections, the invariant mass of the lepton pair after 4C fit must be consistent with m_Z within a mass range depending on the dilepton mass resolution. In the $HZ \to \tau^+\tau^- q\bar{q}$ selection the mass of the two hadronic jets after 4C kinematic fit must be consistent with m_Z.

Events retained by both $HZ \to q\bar{q}\tau^+\tau^-$ and $\tau^+\tau^- q\bar{q}$ selections are uniquely classified as $HZ \to q\bar{q}\tau^+\tau^-$ or $\tau^+\tau^- q\bar{q}$ candidates exploiting b-tag and mass information. After the $HZ \to q\bar{q}\ell^+\ell^-$ selections, 18 events are observed with 16.7 expected from background processes and 1.7 and 0.32 signal events expected for $m_H = 110$ GeV and 115 GeV, respectively. After the $HZ \to \tau^+\tau^- q\bar{q}$ selection, 8 events are observed with 7.8 expected from background and 0.66 and 0.15 signal events expected for $m_H = 110$ GeV and 115 GeV respectively.

It is found that the best mass resolution in the $HZ \to q\bar{q}e^+e^-$ analysis is obtained if the Higgs boson mass is reconstructed after 4C fit as the mass recoiling against the dilepton system. In the $HZ \to q\bar{q}\mu^+\mu^-$, $HZ \to q\bar{q}\tau^+\tau^-(\tau^+\tau^- q\bar{q})$ analyses the mass resolution is improved by applying the 5C fit constraining the mass of the system presumably stemming from the Z to m_Z. The invariant mass of the system recoiling against the Z is considered as the reconstructed Higgs boson mass.

The distributions of the dilepton mass and the reconstructed Higgs boson mass in the $HZ \to q\bar{q}e^+e^-$ and $HZ \to q\bar{q}\mu^+\mu^-$ channels are shown in Figures 7.10a and 7.10b, respectively. The distributions of the reconstructed Higgs boson mass in the $HZ \to q\bar{q}\tau^+\tau^-$ and $HZ \to \tau^+\tau^- q\bar{q}$ channels are shown in Figures 7.10c and 7.10d, respectively.

In the $HZ \to q\bar{q}\ell^+\ell^-$ selections, the the reconstructed Higgs boson mass is combined with the b-tag values of the two hadronic jets, to form the final discriminant. For the $HZ \to \tau^+\tau^- q\bar{q}$ selection, the reconstructed Higgs boson mass is used as the final discriminant.

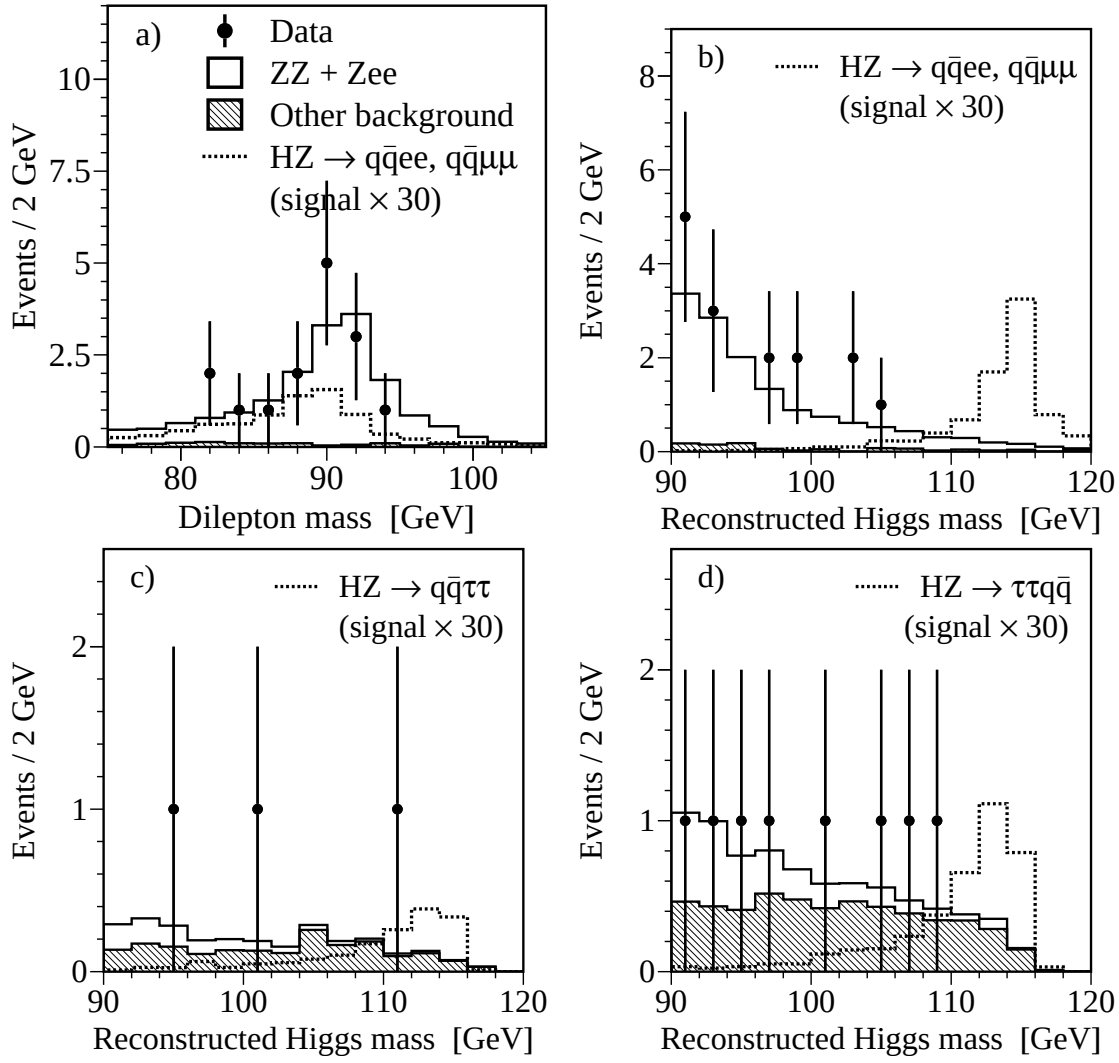

Figure 7.10: Distributions of a) the dilepton mass and b) the reconstructed Higgs mass in the HZ → $q\bar{q}e^+e^-$ and HZ → $q\bar{q}\mu^+\mu^-$ channels. The reconstructed Higgs boson mass in c) HZ → $q\bar{q}\tau^+\tau^-$ and d) HZ → $\tau^+\tau^-q\bar{q}$ channels. The points represent the data. The open and hatched histograms are the expected backgrounds. The dashed line is the expected Higgs signal with $m_H = 115$ GeV, multiplied by a factor of 30.

7.4 L3 Combined Results of the SM Higgs Search

The number of selected events in all search channels after applying cut on signal-to-background ratio of s/b > 0.05 is presented in Table 7.3 for $m_H = 110$ GeV and 115 GeV[1]. The number of signal events includes also fusion processes as well as charm and gluonic Higgs boson decays. Figure 7.11 shows the observed value of -2lnQ compared to expectation from "background-only" and "signal+background" hypotheses, as a function of the tested Higgs mass, for each of four search channels. At high tested Higgs masses, $m_H > 95$ GeV, data in the HZ → $q\bar{q}q\bar{q}$, HZ → $q\bar{q}\ell^+\ell^-$ and HZ → $\tau^+\tau^-q\bar{q}$ channels are

[1]These two mass hypotheses are very close to the upper limit of the search sensitivity in L3.

found to agree with the SM background hypothesis within one standard deviation. A slight excess of events above one standard deviation from the background is observed in the $HZ \to q\bar{q}\nu\bar{\nu}$ channel for m_H above 100 GeV.

$\sqrt{s} = 203 - 209$ GeV	Mass hypothesis					
	$m_H = 110$ GeV			$m_H = 115$ GeV		
Selection	N_D	N_B	N_S	N_D	N_B	N_S
$HZ \to q\bar{q}q\bar{q}$	49	51.5	11.7	12	9.4	1.8
$HZ \to q\bar{q}\nu\bar{\nu}$	13	10.7	3.3	5	3.3	0.66
$HZ \to q\bar{q}e^+e^-$	0	0.66	0.58	0	0.38	0.14
$HZ \to q\bar{q}\mu^+\mu^-$	0	0.38	0.45	0	0.26	0.11
$HZ \to q\bar{q}\tau^+\tau^-$	0	0.53	0.19	1	0.14	0.03
$HZ \to \tau^+\tau^- q\bar{q}$	3	2.3	0.51	0	0.84	0.15
Total	65	66.1	16.7	18	14.3	2.9

Table 7.3: The number of observed candidates (N_D), expected background (N_B) and expected signal (N_S) events for the data collected by L3 in the year 2000, after a cut on the final discriminant corresponding to a signal-to-background ratio greater than 0.05. This cut is used to calculate the confidence levels.

The characteristics of the most significant candidates for $m_H \geq 110$ GeV are detailed in Table 7.4. These events are selected requiring the maximum value of the event weight $1 + s/b$ in the mass range $m_H \geq 110$ GeV to be larger than 0.5.

In Figures 7.12a and 7.12b the observed value of -2lnQ for all channels combined is compared to the expected distributions of -2lnQ for the "background-only" and "signal+background" hypotheses at tested Higgs boson masses of 110 GeV and 115 GeV, respectively. The dependence of the observed and expected -2lnQ on m_H after combining

Channel	m_H^{rec} (GeV)	$\sqrt{s}$ (GeV)	$(s/b)_{110}$	$(s/b)_{115}$	$(s/b)_{max}$	m_H^{max}
$HZ \to q\bar{q}\nu\bar{\nu}$	115.0	206.4	0.39	0.70	0.77	114.3
$HZ \to q\bar{q}q\bar{q}$	108.2	206.4	1.90	0.36	2.96	107.9
$HZ \to q\bar{q}\nu\bar{\nu}$	110.1	206.4	1.39	0.23	1.39	110.0
$HZ \to q\bar{q}\nu\bar{\nu}$	107.1	206.6	0.94	0.20	2.31	107.6
$HZ \to q\bar{q}q\bar{q}$	109.9	206.6	0.73	0.13	1.12	109.3
$HZ \to q\bar{q}q\bar{q}$	107.1	204.7	2.20	0.01	2.67	106.9

Table 7.4: Characteristics of the most significant candidates for $m_H \geq 110$ GeV, selected requiring that maximal value of event weight $1 + s/b$ in the mass range $m_H \geq 110$ GeV be larger than 0.5. The quantities m_H^{rec} and $\sqrt{s}$ are the reconstructed Higgs mass and center-of-mass energy at which the event was recorded, respectively. The quantities $(s/b)_{110}$ and $(s/b)_{115}$ are s/b values at Higgs mass hypotheses of 110 GeV and 115 GeV, respectively. The quantities $(s/b)_{max}$ and m_H^{max} are the maximum value of s/b and the Higgs mass hypothesis for which this value is obtained. The events are sorted in descending order of $(s/b)_{115}$.

all channels is shown in Figure 7.12c. As can be seen no indication of signal is found in the combined data sample.

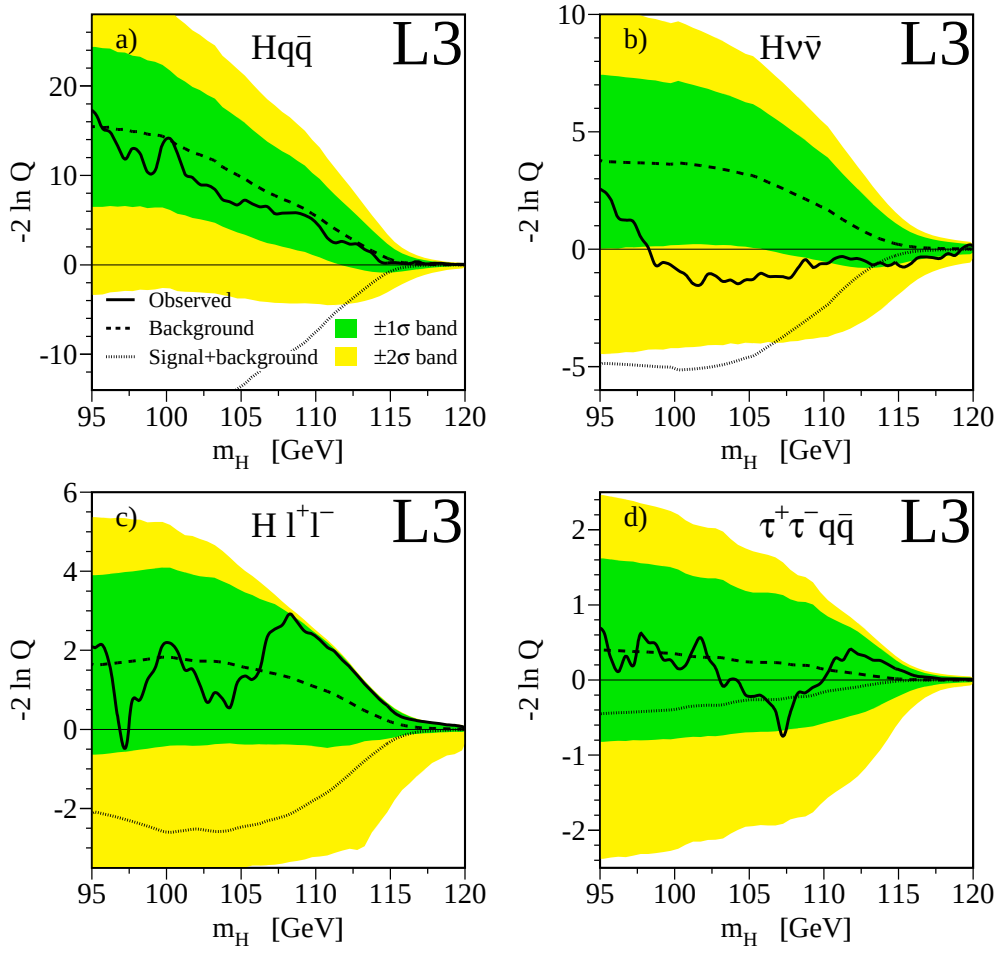

Figure 7.11: The log-likelihood ratio, -2lnQ, as function of the Higgs mass hypothesis, m_H, for the search channels a) $HZ \to q\bar{q}q\bar{q}$, b) $HZ \to q\bar{q}\nu\bar{\nu}$, c) $HZ \to q\bar{q}\ell^+\ell^-$, d) $HZ \to \tau^+\tau^-q\bar{q}$. The solid line shows the observed -2lnQ. The dashed line corresponds to the expectation from the "background-only" hypothesis. The shaded areas represent 1σ and 2σ bands with respect to the "background-only" hypothesis. The dotted line is the expectation from the "signal+background" hypothesis.

The statistical and systematic uncertainties on the signal and background predictions are incorporated in the calculation of confidence levels as described in Section 5.5. The following sources of errors are considered.

Energy Scale:
A global energy shift of ±2% corresponding to the maximal error in the calibration method [95] was applied leading to the uncertainty on the number of background events from 3% to 10% above and beyond the HZ kinematic threshold. The uncertainty on the number of signal events varies from 2% to 3% above and beyond the HZ kinematic threshold.

Background Normalisation:
Following the suggestion of the LEP ZZ working group, the following uncertainties on the background cross section are assumed: 2% on WW and 5% on $q\bar{q}\gamma$, ZZ and Zee.

Theoretical Signal Uncertainty:
Theoretical error on the Higgs boson production cross section due to uncertainties in m_t and α_s [96], amounts to $\approx 0.1\%$. Theoretical error on the Higgs boson decay branching fractions constitutes 1% [97].

Luminosity Error:
The relative uncertainty in the luminosity measurement is 0.3%.

Simulation of Selection Variables:
The systematics effects potentially originating from event selection variables are estimated with the event reweighting method [98]. For each variable a weight depending on the value of the variable is introduced to bring the simulated distribution in agreement with distribution observed in data. The corrections to the estimated background and signal are then determined and added in quadrature for all variables. This results into an uncertainty on the number of background events between 1% and 10% and on the number of signal events between 2% and 5% above and beyond the HZ kinematic threshold.

B-tag Related Systematics:
The systematic effect due to b-tagging is studied using independent reference samples as described in Section 6.3. Good agreement between data and Monte Carlo is found in the spectrum of the jet b-tag variable and the related systematic error is estimated to be negligible.

Overall Systematic Uncertainty:
Assuming that systematic errors from different sources are uncorrelated total systematic uncertainties are estimated to range from 6% to 15% on the number of background events and from 3% to 6% on the number of signal events above and beyond the HZ kinematic threshold.

Statistics of Simulated Samples:
Statistical uncertainties due to finite number of simulated Monte Carlo events are evaluated to be up to 8% for the background and 4% for the signal. However, they are completely uncorrelated between different bins in the individual channels and have little effect on the calculation of confidence levels.

The results of the SM Higgs searches performed by L3 at lower center-of-mass energies [62] are also included in the calculation of confidence levels. The confidence level for the "background-only" hypothesis, $(1 - CL_b)$, as a function of tested Higgs boson mass is shown in Figure 7.13 for the full data sample collected at $\sqrt{s}$ between 189 GeV and 209 GeV in the years 1998 - 2000. An excesses of more than one but less than two standard deviations from the SM background expectation are observed at low Higgs masses, $m_H < 78$ GeV and at $m_H \sim 99$ GeV. The first excess is dominated by candidates in the $HZ \to q\bar{q}q\bar{q}$ channel in the data of the year 2000. The second one is mainly caused by significant $HZ \to q\bar{q}e^+e^-$ and $HZ \to q\bar{q}\mu^+\mu^-$ candidates recorded at $\sqrt{s}$ between 192

GeV and 202 GeV in 1999. Apart from these two excesses which are far below the expectation for the signal the combined data are found to be consistent within 1 standard deviation with the background.

The data are used then to exclude a SM Higgs boson. Figure 7.14 shows the dependence of the CL_s and CL_{med} confidence levels on m_H. Values of m_H below 110 GeV are excluded in the SM with a confidence level greater than 99 %. The observed lower limit on m_H is 112.0 GeV at 95 % C.L., for an expected lower limit of 112.4 GeV.

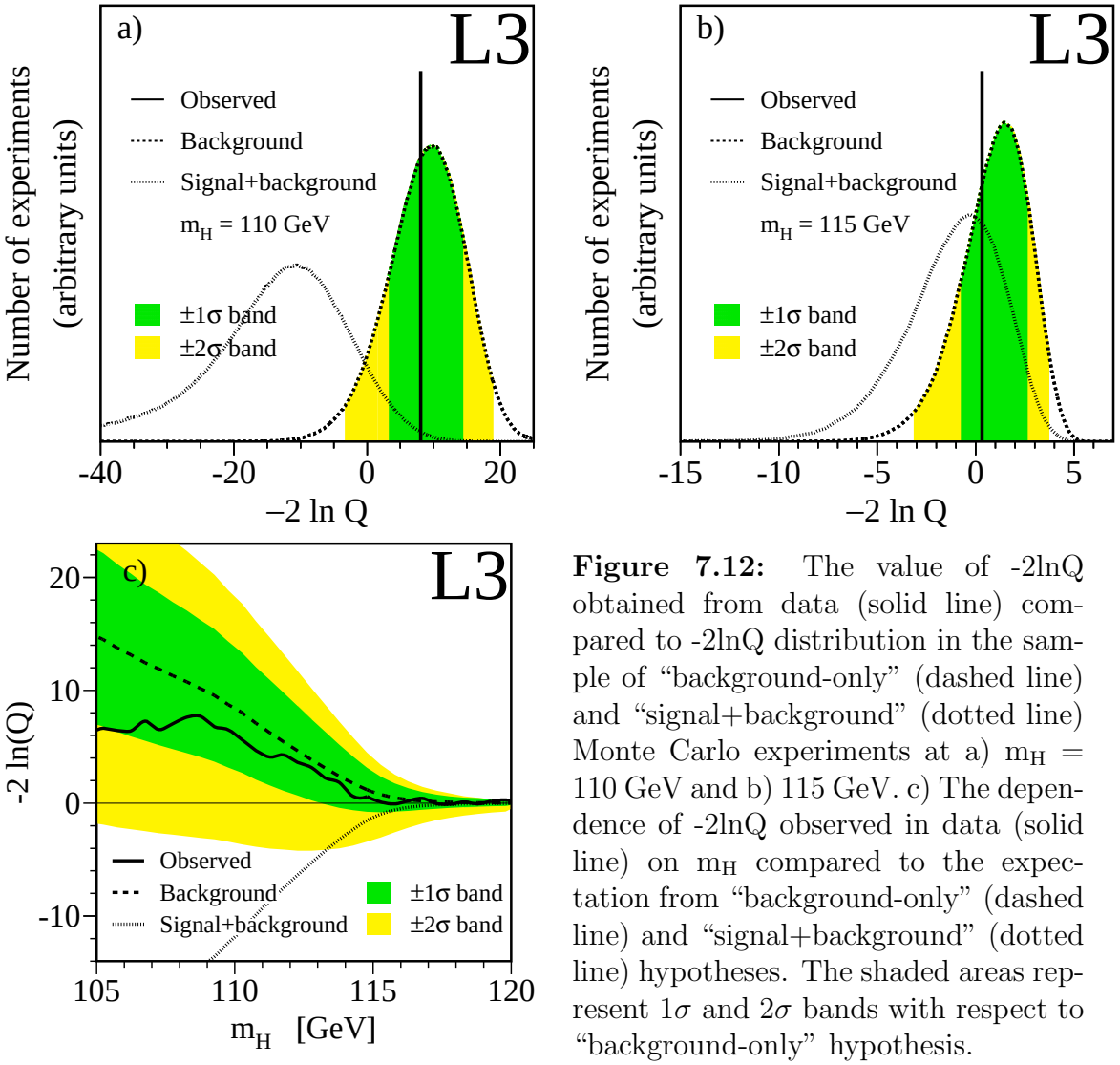

Figure 7.12: The value of -2lnQ obtained from data (solid line) compared to -2lnQ distribution in the sample of "background-only" (dashed line) and "signal+background" (dotted line) Monte Carlo experiments at a) m_H = 110 GeV and b) 115 GeV. c) The dependence of -2lnQ observed in data (solid line) on m_H compared to the expectation from "background-only" (dashed line) and "signal+background" (dotted line) hypotheses. The shaded areas represent 1σ and 2σ bands with respect to "background-only" hypothesis.

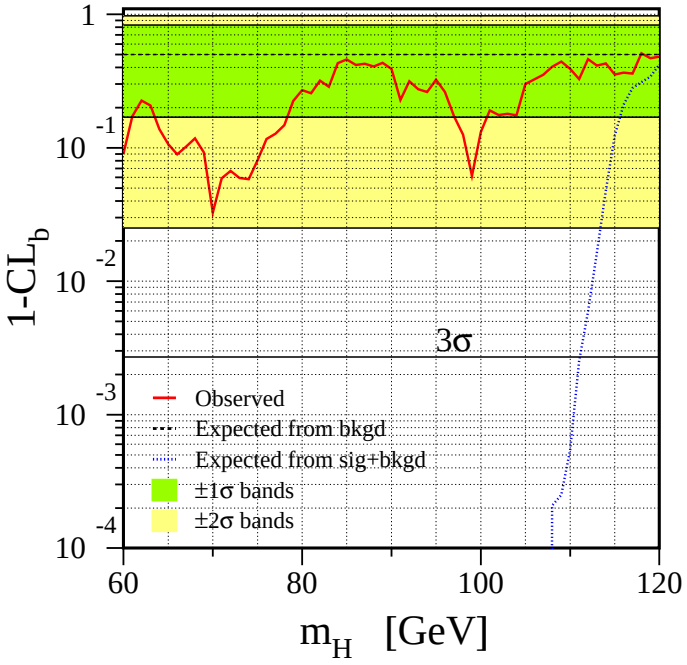

Figure 7.13: Confidence level for background hypothesis, $(1 - \mathrm{CL_b})$, observed in data (solid line), expected from "background-only" hypothesis (dashed line) and from "signal+background" hypothesis (dotted line) as a function of $\mathrm{m_H}$. The shaded areas represent 1σ and 2σ bands centred on the background expected median value.

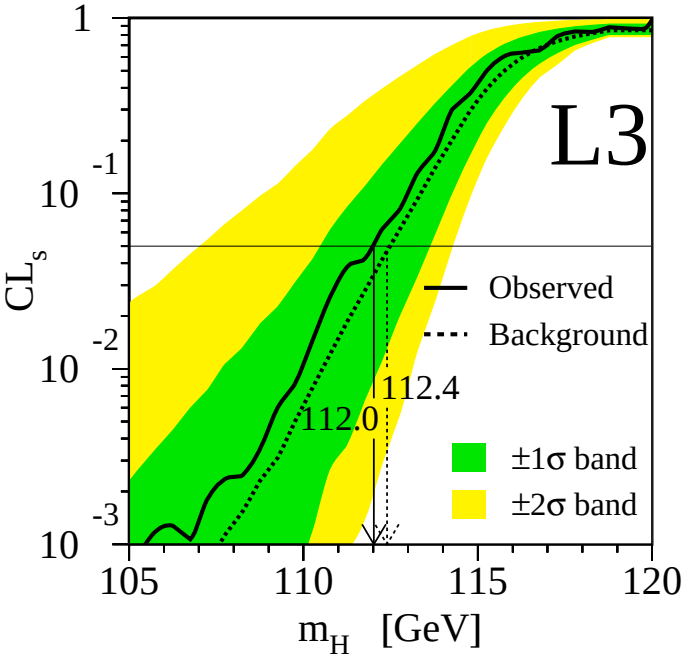

Figure 7.14: The confidence level observed in data, $\mathrm{CL_s}$, (solid line) and the expected median confidence level, $\mathrm{CL_{med}}$, (dashed line) as a function of $\mathrm{m_H}$. The shaded areas represent 1σ and 2σ bands centred on the background expected median value.

Chapter 8

Search for Neutral Higgs Bosons of the MSSM

The search for MSSM Higgs bosons is performed exploiting final states resulting from the $e^+e^- \to hZ$ and $e^+e^- \to hA$ processes. Like in the SM Higgs search, four event topologies arising from the Higgs-strahlung process are studied: $hZ \to b\bar{b}q\bar{q}$, $hZ \to b\bar{b}\nu\bar{\nu}$, $hZ \to b\bar{b}\ell^+\ell^-$ and $hZ \to \tau^+\tau^- q\bar{q}$. For the hA production, the following decay modes are investigated: $hA \to b\bar{b}b\bar{b}$, $hA \to b\bar{b}\tau^+\tau^-$[1]. The analyses $hZ \to b\bar{b}\nu\bar{\nu}$ and $hZ \to b\bar{b}\ell^+\ell^-(\ell = e, \mu)$ are the same as devised for the SM Higgs search. The analyses $hZ \to b\bar{b}q\bar{q}$ and $hZ \to b\bar{b}\tau^+\tau^-, \tau^+\tau^- q\bar{q}$ have been optimised to account for overlap with the similar modes in the hA channel. To cover the region of low $\tan\beta$ and low m_A , a dedicated analysis is elaborated to search for the $hZ \to AAq\bar{q}$ final states.

8.1 The $hZ \to b\bar{b}q\bar{q}$ and $hA \to b\bar{b}b\bar{b}$ Channels

The strategy of the search for neutral Higgs bosons of the MSSM in the four-jet channel is illustrated in Figure 8.1. First, a preselection of high multiplicity hadronic events common for $hZ \to b\bar{b}q\bar{q}$ and $hA \to b\bar{b}b\bar{b}$ channels is applied. At the next stage events are uniquely assigned either to the hZ or hA analysis branch exploiting kinematic information. Once an event is assigned to one of the two analysis branches, it obeys selection criteria established for a given branch. At the final stage of the analysis the final discriminant specific for each analysis branch is constructed exploiting mass, kinematic and b-tag information.

The preselection criteria are identical to those described in Section 7.1. Therefore the numbers of events expected from different background processes and preselected in data are the same as given in Table 7.1. The $hZ \to b\bar{b}q\bar{q}$ and $hA \to b\bar{b}b\bar{b}$ preselection efficiencies are larger than 85 % for all tested Higgs boson mass hypotheses.

After preselection events are forced into a four-jet topology using the Durham algorithm and a 4C kinematic fit is performed. Each event is tested for its compatibility with hZ and hA production hypotheses exploiting the dijet masses. The procedure is similar to that described in Section 7.1. For every pairing a mass χ^2 variables are calculated as

[1]The decay mode $hA \to \tau^+\tau^- b\bar{b}$ is also considered

follows:

$$\chi^2_{hZ} = \frac{(\Sigma_i - m_h - m_Z)^2}{\sigma^2_\Sigma} + \frac{(\Delta_i - |m_h - m_Z|)^2}{\sigma^2_\Delta}, \tag{8.1}$$

$$\chi^2_{hA} = \frac{(\Sigma_i - m_h - m_A)^2}{\sigma^2_\Sigma} + \frac{(\Delta_i - |m_h - m_A|)^2}{\sigma^2_\Delta}, \tag{8.2}$$

The dijet mass sum and dijet mass difference resolutions are parametrised in the same way as in the SM Higgs search. For each hypothesis the lowest χ^2 is chosen and the probability $P(\chi^2)$ is calculated.

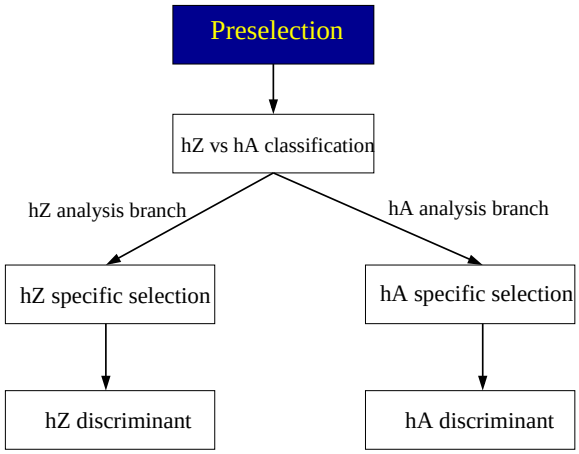

Figure 8.1: The diagram, illustrating the strategy of the search for neutral Higgs bosons of the MSSM in the four-jet channel.

Since Higgs bosons are scalars, the distribution in the production polar angle Θ differ both between hZ and hA final states and between these processes and gauge boson pair production. The angle Θ_{hA} is obtained for the hA hypothesis from the dijet pairing with minimal χ^2_{hA} as the polar angle between the presumable momentum of the h boson and the beam axis. The variables $\log_{10}P(\chi^2_{hZ})$, $\log_{10}P(\chi^2_{hA})$ and $|\cos\Theta_{hA}|$ are used in the next steps of the analysis.

In order to assign events either for the hZ or for the hA analysis branch, a likelihood, L^c_{hZ}, is constructed assuming two event classes, hA and hZ, and exploiting the following variables: N_{TRK}, B_{TAG}, $\log_{10}P(\chi^2_{hZ})$, $\log_{10}P(\chi^2_{hA})$, $|\cos\Theta_{hA}|$ and γ_{triple}. An event is classified to the hZ branch if $L^c_{hZ} = 1 - L^c_{hA} > 0.5$, otherwise an event is assigned to the hA branch. The distributions of some variables entering the classification likelihood are shown for data and Monte Carlo samples in Figures 8.2-8.4. The distributions of L^c_{hZ} for data and Monte Carlo samples obtained at (m_h, m_A) = (90,90) GeV and (m_h, m_A) = (85,110) GeV are presented in Figure 8.5. As can be seen good separation between hZ and hA processes is achieved. It should be noted, however, that due to misassignment of events the hZ signal contributes to the hA analysis branch and vice versa. While testing Higgs boson mass hypotheses for which the hA production is kinematically inaccessible, $m_h + m_A > \sqrt{s}$, all events are assigned to the hZ branch.

Once an event is assigned to one of the two analyses branches it is subject of selection criteria optimised for each branch separately. For the hA analysis only events with

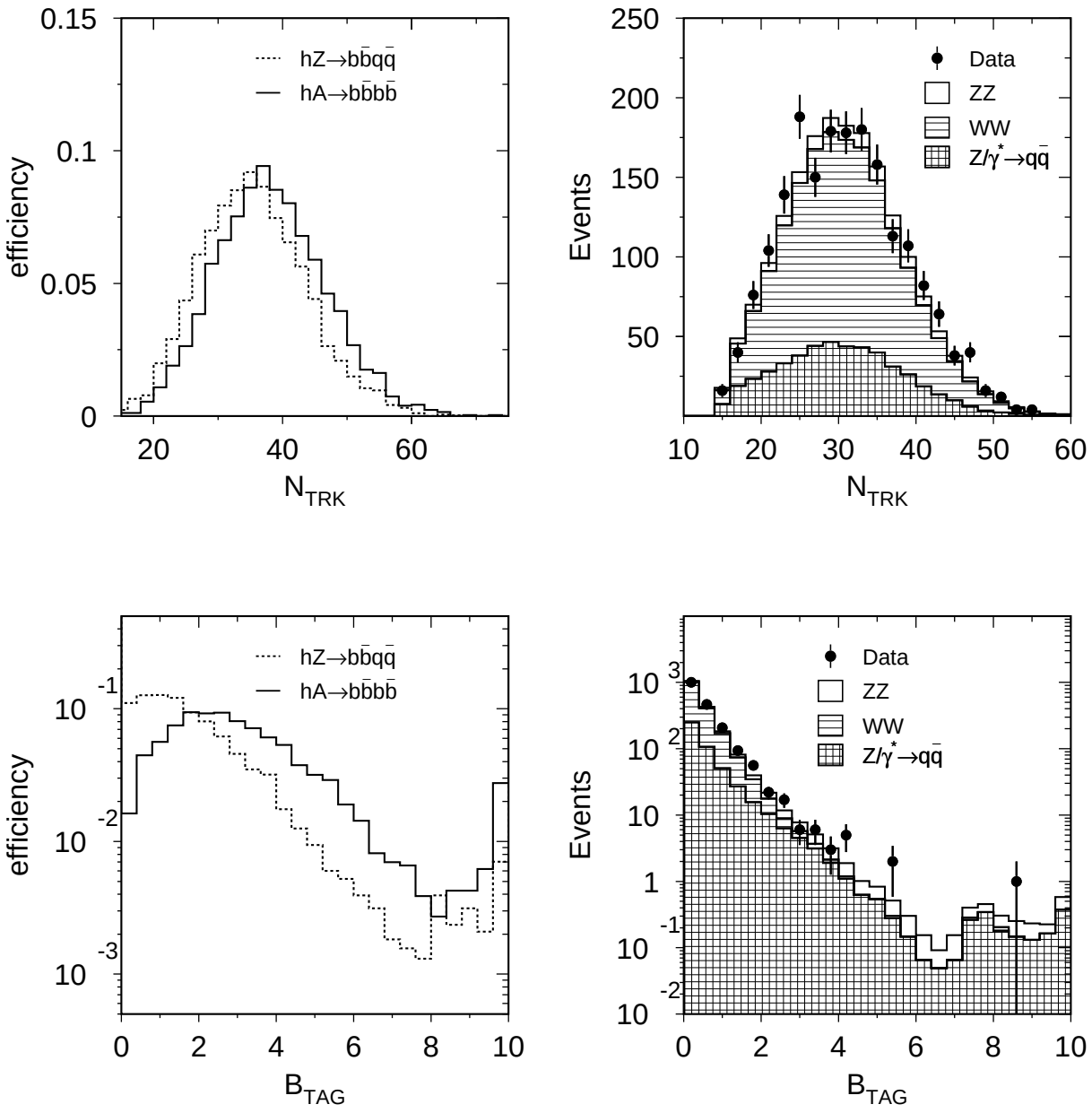

Figure 8.2: Distribution of N_{TRK} in terms of hZ and hA efficiencies (upper-left). Distribution of N_{TRK} for the expected background splitted into different sources and for data (upper-right). Distribution of B_{TAG} in terms of hZ and hA efficiencies (lower-left). Distribution of B_{TAG} for the expected background splitted into different sources and for data (lower-right). The signal distributions correspond to the Higgs boson mass hypothesis $(m_h, m_A) = (90,90)$ GeV. Samples are selected at $\sqrt{s} > 205$ GeV.

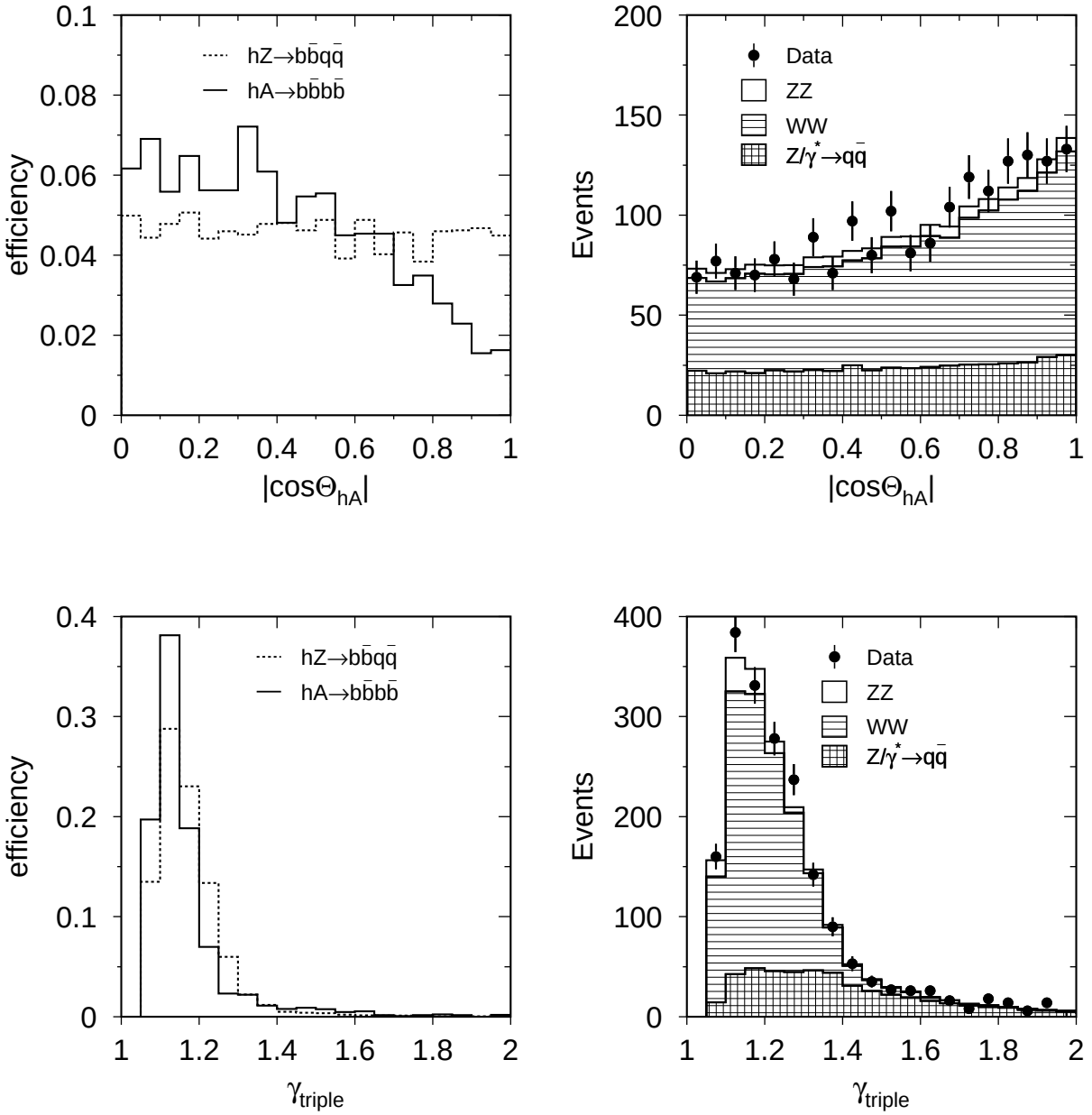

Figure 8.3: Distribution of $|\cos\Theta_{\mathrm{hA}}|$ in terms of hZ and hA efficiencies (upper-left). Distribution of $|\cos\Theta_{\mathrm{hA}}|$ for the expected background splitted into different sources and for data (upper-right). Distribution of γ_{triple} in terms of hZ and hA efficiencies (lower-left). Distribution of γ_{triple} for the expected background splitted into different sources and for data (lower-right). The distributions of $|\cos\Theta_{\mathrm{hA}}|$ correspond to Higgs mass hypothesis $(\mathrm{m_h}, \mathrm{m_A})$ = (90,90) GeV. The signal distributions of γ_{triple} correspond to the Higgs boson mass hypothesis $(\mathrm{m_h}, \mathrm{m_A})$ = (85,110) GeV. Samples are selected at $\sqrt{\mathrm{s}} >$ 205 GeV.

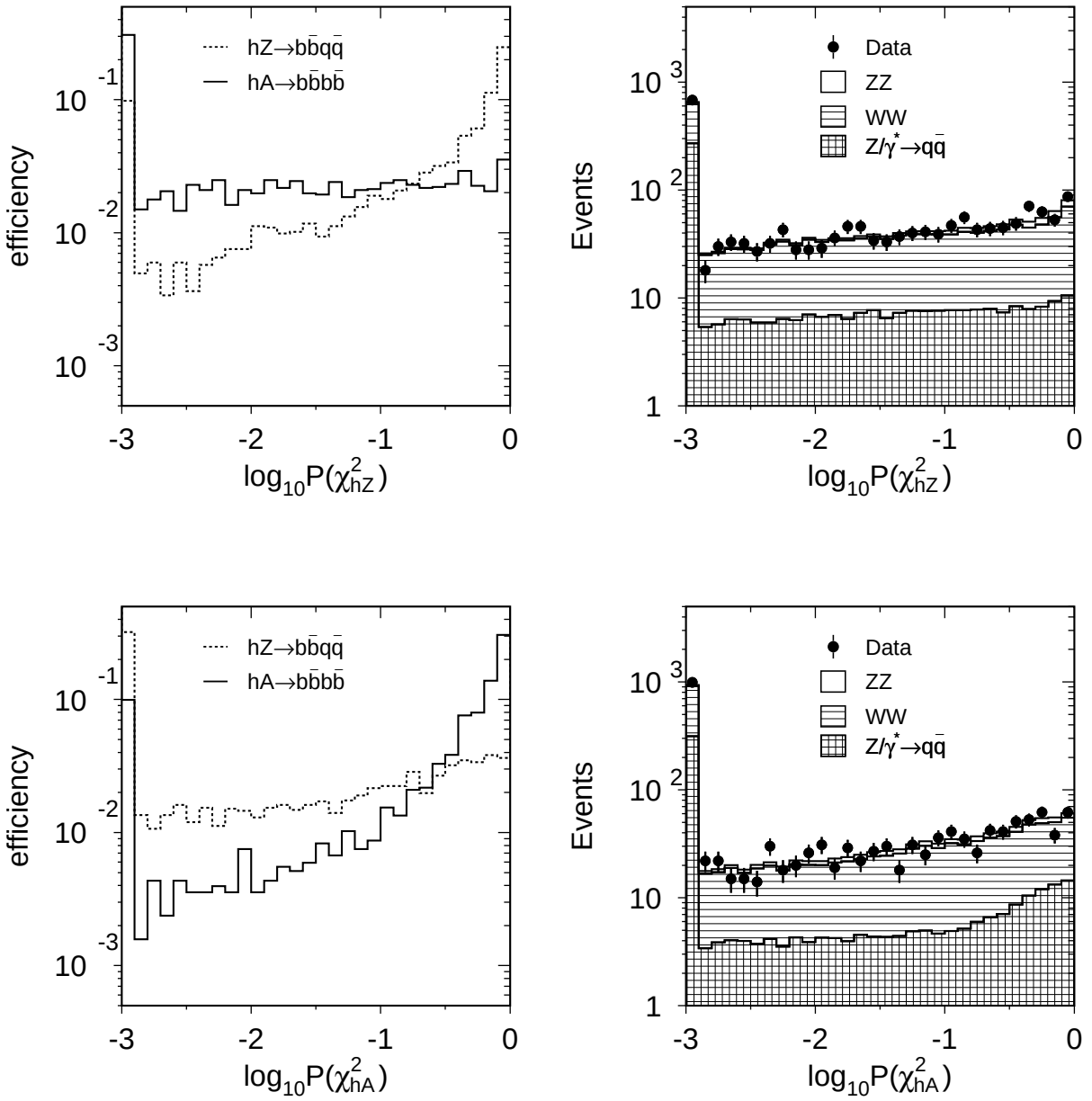

Figure 8.4: Distribution of $P(\chi^2_{hZ})$ in terms of hZ and hA efficiencies (upper-left). Distribution of $P(\chi^2_{hZ})$ for the expected background splitted into different sources and for data (upper-right). Distribution of $P(\chi^2_{hA})$ in terms of hZ and hA efficiencies (lower-left). Distribution of $P(\chi^2_{hA})$ for the expected background splitted into different sources and for data (lower-right). The distributions correspond to the Higgs boson mass hypothesis $(m_h, m_A) = (85,110)$ GeV. Samples are selected at $\sqrt{s} > 205$ GeV.

$P(\chi^2_{hA})$ larger than 1% and B_{TAG} larger than 1.0 are accepted. Then a selection likelihood L_{hA} is constructed to separate hA events from ZZ, WW and $q\bar{q}(\gamma)$ final states. L_{hA} is built from the following variables: N_{TRK}, B_{TAG}, $\log Y_{34}$, γ_{triple}, event sphericity and $|\cos\Theta_{hA}|$. Events are selected into the final sample if the L_{hA} is greater than the value 0.35, which is obtained from the optimisation of the sensitivity at (m_h, m_A) = (90,90) GeV. For these events the final discriminant, F_{hA}, is constructed using the binned likelihood technique and exploiting the following variables: b-tag variable of the most energetic jet, B_1, b-tag variable of the second highest energetic jet, B_2, b-tag variable of the third highest energetic jet, B_3, b-tag variable of the least energetic jet, B_4, $\log_{10}P(\chi^2_{hA})$ and $\log_{10}(1 - L_{hA})$. The distributions of some of these variables are shown in Figures 8.6- 8.7 for data and Monte Carlo events selected at (m_h, m_A) = (90,90) GeV.

The analysis in the hZ branch is very similar to that performed in the hA branch. Events are accepted if $P(\chi^2_{hZ})$ is larger than 1% and B_{TAG} is larger than 0.36. The likelihood L_{hZ} separating a hZ signal from ZZ, WW and $q\bar{q}\gamma$ backgrounds is obtained exploiting the variables: N_{TRK}, B_{TAG}, $\log Y_{34}$, $|\cos\Theta_{2B}|$, $E^{min}_{jet}/\sqrt{s}$, $\Delta E^{max}_{jet}/\sqrt{s}$ γ_{triple} and event sphericity. An event is accepted into the final sample if L_{hZ} exceeds the value 0.15 obtained from the optimisation of the search sensitivity at m_h = 110 GeV. The event category variable based on b-tag rankings of the jets assigned to the Higgs boson is then introduced as described in Section 7.1. In the last step, the final discriminant, F_{hZ}, is computed as a likelihood including b-tags of the individual jets, $P(\chi^2_{hZ})$ and the event category variable.

The analysis described above is repeated and final discriminants are recomputed at each Higgs boson mass hypothesis being tested. The number of events observed in data, expected background and signal efficiencies are summarised in Table 8.1 for five representative Higgs boson mass hypotheses.

$\sqrt{s} = 203 - 209$ GeV

(m_h, m_A) (GeV) =	(85,85)		(90,90)		(85,110)		(90,105)		(95,95)	
Analysis branch	hZ	hA	hZ	hA	hZ	hA	hZ	hA	hZ	hA
Data	339	33	275	30	334	41	281	28	278	24
Background	313	34	259	31	319	35	273	27	265	24
ϵ(hZ), %	44	15	37	25	54	11	53	10	42	21
ϵ(hA), %	15	55	23	51	11	63	10	59	16	55

Table 8.1: The number of events selected in data, the expected background and signal efficiencies for five tested Higgs boson mass hypotheses. The numbers are reported separately for the hZ and hA analysis branches and correspond to the full data sample of the year 2000.

Generally, good agreement between data and the expected SM background is observed in the distributions of the final discriminants. As an example Figure 8.8 shows the distribution of data, expected background and expected signal events selected into the final sample as a function of signal-to-background ratio, for the Higgs boson mass hypothesis of (m_h, m_A) = (85,85) GeV. The signal expectation is evaluated within the "m_h-max" scenario at $\tan\beta = 25$. For this choice of MSSM parameters the $e^+e^- \to hZ$

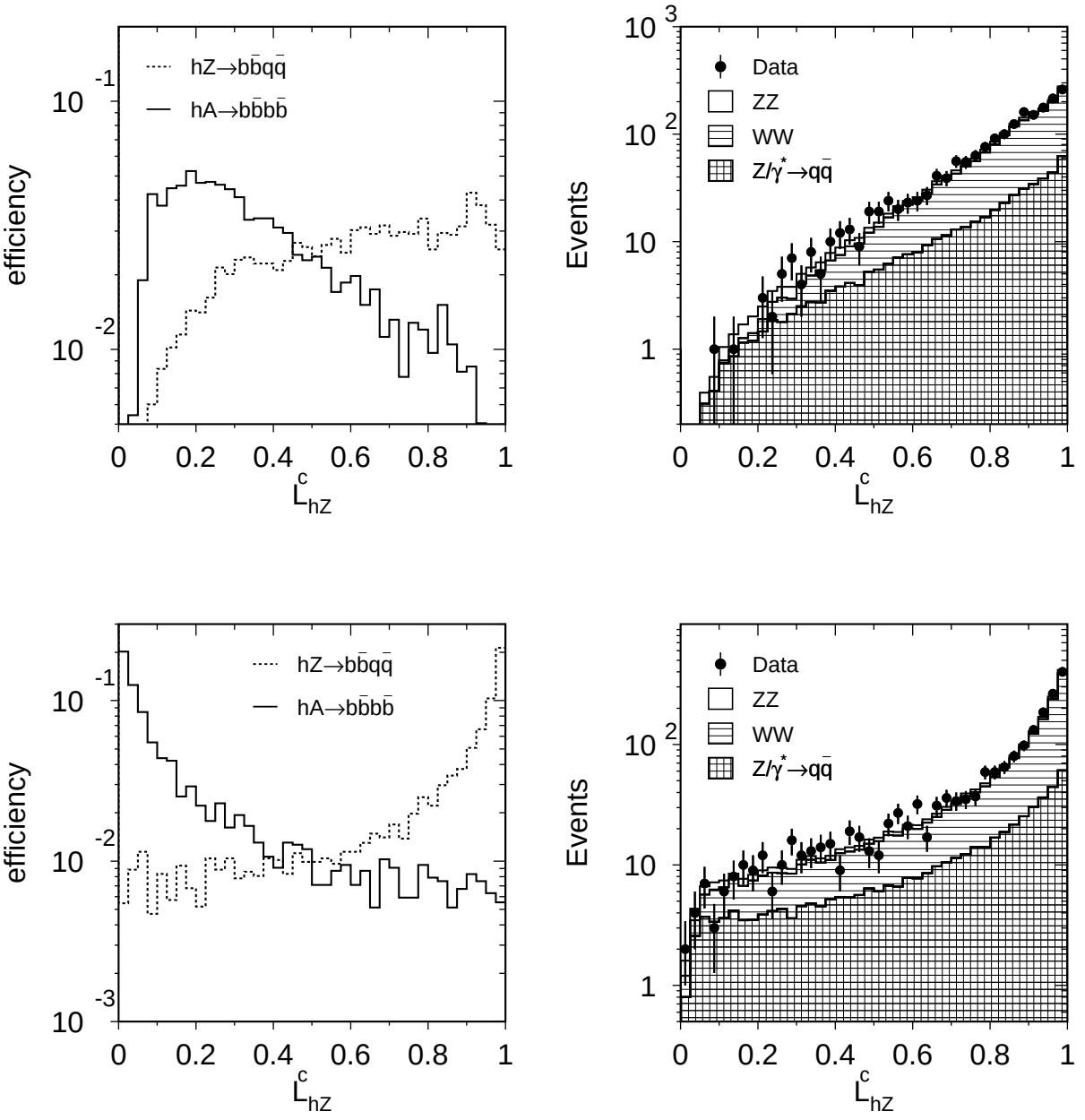

Figure 8.5: The distribution of the classification likelihood L^c_{hZ} in terms of hZ and hA efficiencies at $(m_h, m_A) = (90,90)$ GeV (upper-left). The distribution of the classification likelihood L^c_{hZ} for the expected background splitted into different sources and for data at $(m_h, m_A) = (90,90)$ GeV (upper-right). The distribution of the classification likelihood L^c_{hZ} in terms of hZ and hA efficiencies for $(m_h, m_A) = (85,110)$ GeV (lower-left). The distribution of the classification likelihood L^c_{hZ} for the expected background splitted into different sources and for data at $(m_h, m_A) = (85,110)$ GeV (lower-right). Samples are selected at $\sqrt{s} > 205$ GeV.

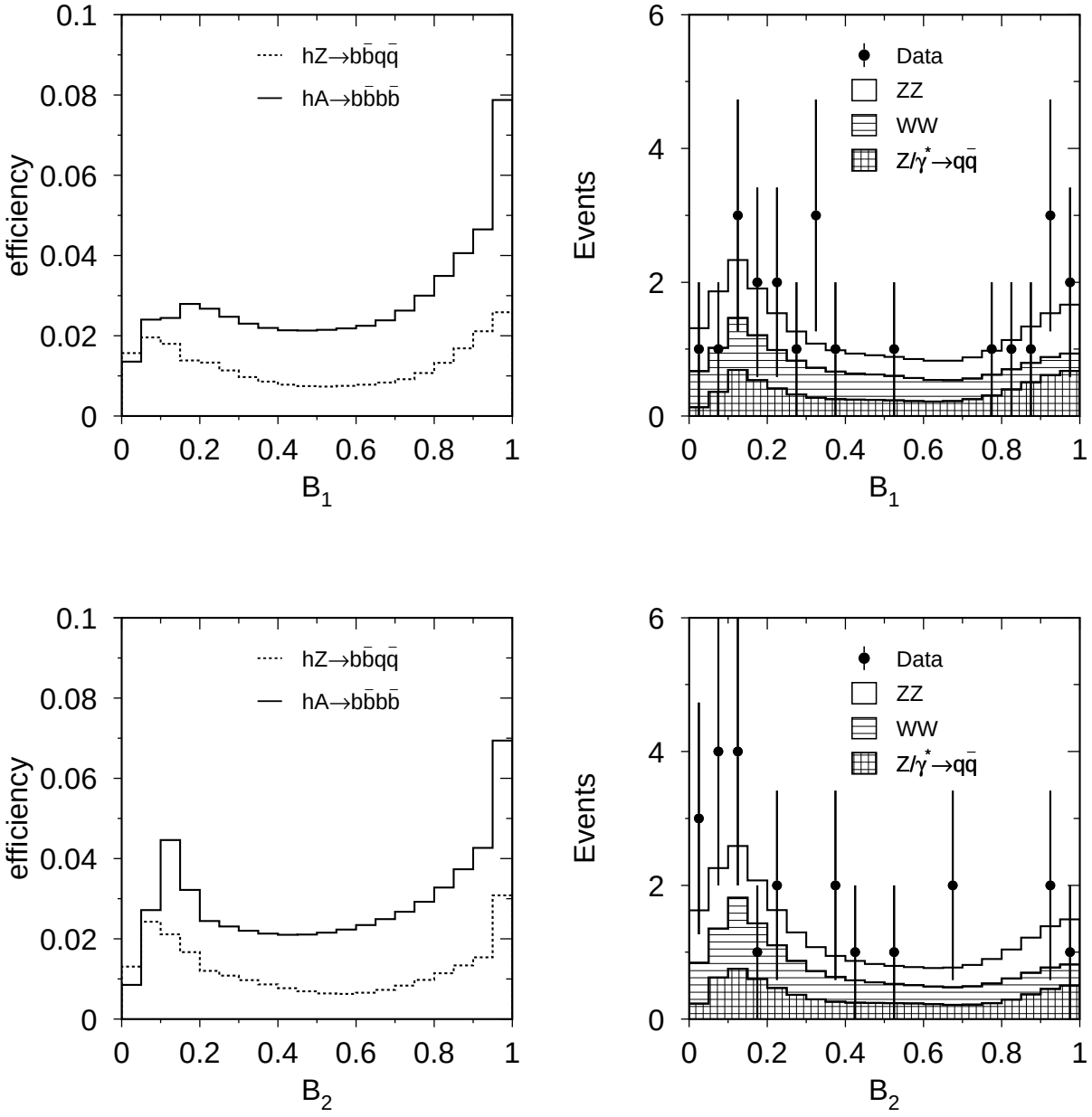

Figure 8.6: Distributions of the b-tag variable of the most energetic jet B_1 in terms of hZ and hA efficiencies (upper-left). Distributions of the b-tag variable of the most energetic jet B_1 for the expected background splitted into different sources and for data (upper-right). Distributions of the b-tag variable of the second energetic jet B_2 in terms of hZ and hA efficiencies (lower-left). Distributions of the b-tag variable of the second energetic jet B_2 for the expected background splitted into different sources and for data (lower-right). Data and Monte Carlo distributions include events selected into final sample of the hA analysis branch at the tested Higgs boson mass hypothesis of (m_h, m_A) = (90,90) GeV and at $\sqrt{s} > 205$ GeV.

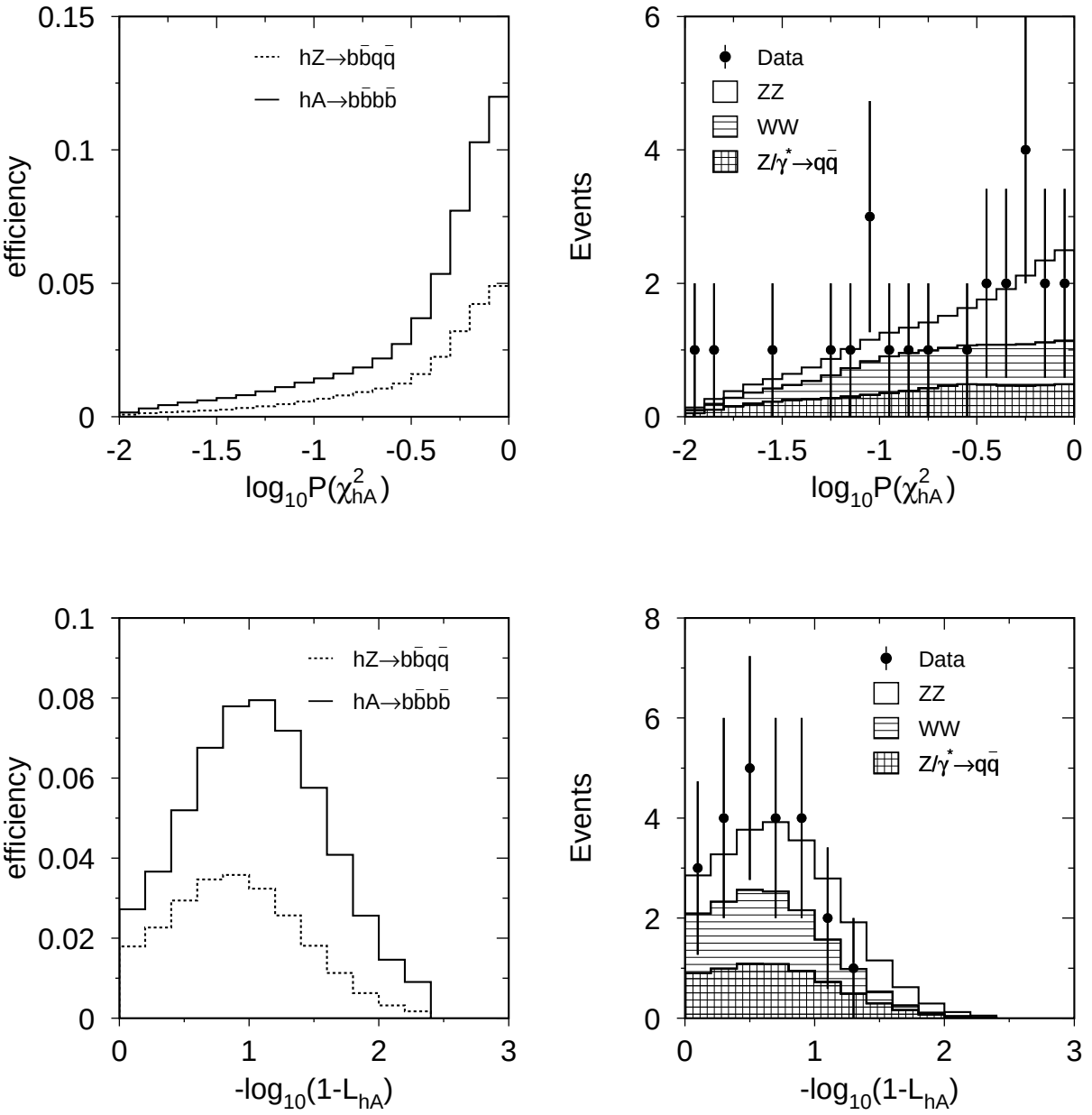

Figure 8.7: Distribution of $\log_{10}\mathrm{P}(\chi^2_{\mathrm{hA}})$ in terms of hZ and hA efficiencies (upper-left). Distribution of $\log_{10}\mathrm{P}(\chi^2_{\mathrm{hA}})$ for the expected background splitted into different sources and for data (upper-right). Distribution of $-\log_{10}(1-\mathrm{L_{hA}})$ in terms of hZ and hA efficiencies (lower-left). Distribution of $-\log_{10}(1-\mathrm{L_{hA}})$ for the expected background splitted into different sources and for data (lower-right). Data and Monte Carlo distributions include events selected into final sample of the hA analysis branch at the tested Higgs boson mass hypothesis of $(\mathrm{m_h}, \mathrm{m_A}) = (90,90)$ GeV and at $\sqrt{\mathrm{s}} > 205$ GeV.

process is suppressed by a small value of $\sin^2(\beta-\alpha)$ and only hA → bb̄bb̄ channel contributes to the signal.

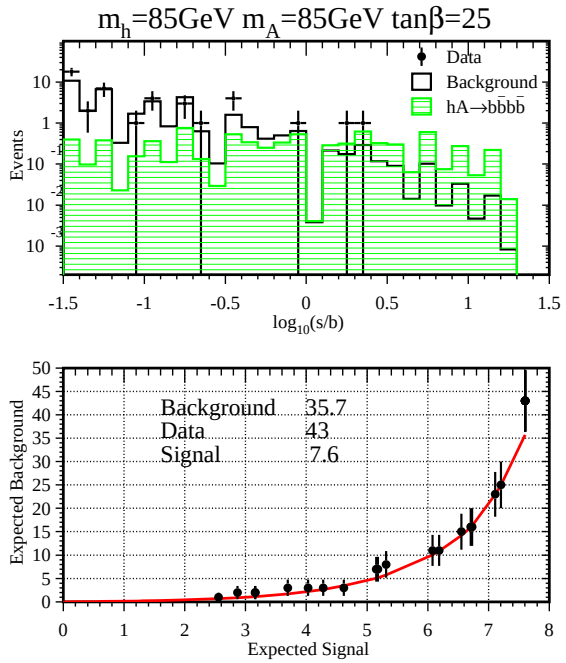

Figure 8.8: Distribution of $\log_{10}(s/b)$ for the full data sample of the year 2000 (top) in the hA → bb̄bb̄ channel. Only bins with signal-to-background ratio greater that 0.02 are retained. Dots represent data, the open histogram is the expected background and the hatched histogram is the expected signal. The bottom distribution is obtained by integrating the upper distribution from the right to the left side. Dots are data and the line is the expectation from the background. Distributions are obtained for Higgs mass hypothesis (m_h, m_A) = (85,85) GeV. The expected signal is calculated within the "m_h-max" scenario at $\tan\beta = 25$.

8.2 The hA → bb̄τ⁺τ⁻ and hZ → bb̄τ⁺τ⁻, τ⁺τ⁻qq̄ Channels

The signatures of hZ → bb̄τ⁺τ⁻, τ⁺τ⁻qq̄ and hA → bb̄τ⁺τ⁻ events are a pair of taus accompanied by two hadronic jets. For each of the channels hZ and hA an analysis is optimised based either on the tau identification or on the event topology by requiring four jets with two of them being narrow and of low multiplicity. The hZ → bb̄τ⁺τ⁻ and τ⁺τ⁻qq̄ selections are similar to those used in the SM Higgs search.

The hA selection is optimised for lower Higgs boson masses by omitting the cuts on the opening angles of the jets and tau pairs and on the invariant mass of the tau pair, $m_{\tau\tau}$. The invariant mass of the hadronic jets, m_{qq}, must be between 5 GeV and 125 GeV. The ratio of the sum of the energies of the tau decay products over the sum of the energies of the jets is required to be less than one and the value of the missing momentum vector in the rest frame of the Higgs boson must be less than 40 GeV.

Finally, the cosine of the polar angle of the Higgs boson, $|\cos\Theta|$, has to be less than 0.8. A sample containing 28 data events is selected while 27.4 events are expected from the SM background processes. The signal efficiency varies from 35% to 40% depending on the Higgs boson mass hypothesis.

There are in total four possible final states: $hZ \to b\bar{b}\tau^+\tau^-$, $hZ \to \tau^+\tau^- q\bar{q}$, $hA \to b\bar{b}\tau^+\tau^-$ and $hA \to \tau^+\tau^- b\bar{b}$. The overlap in selection of these final states is resolved by uniquely assigning events to one channel. This is done exploiting mass and b-tag information. In the last step, the final discriminant specific for each channel is constructed. For the $hZ \to b\bar{b}\tau^+\tau^-$, $hA \to b\bar{b}\tau^+\tau^-$ and $hA \to \tau^+\tau^- b\bar{b}$ final states, the final discriminant is combined from m_{qq}, $m_{\tau\tau}$ and b-tags of the two hadronic jets. For the $hZ \to \tau^+\tau^- q\bar{q}$ final state, $m_{\tau\tau}$ is used as the final discriminant. Good agreement is found in the final discriminant spectra between data and the expected background at all tested Higgs boson mass hypotheses.

8.3 The $hZ \to AAq\bar{q}$ Channel

To improve search sensitivity in the region of low $\tan\beta$ and low m_A where the $h \to AA$ channel becomes dominant and $A \to c\bar{c}$ supplants $A \to b\bar{b}$, a dedicated analysis is developed and performed on the data collected at $\sqrt{s}$ = 189 - 209 GeV. This analysis aims to select $hZ \to AAq\bar{q} \to q\bar{q}q'\bar{q}'q''\bar{q}''$ final states and is devised from the analysis used in the four-jet channel. To avoid degradation of signal efficiency for the $A \to c\bar{c}$ decay mode, b-tag information is not employed. At the first stage, the preselection of high multiplicity hadronic events described in Section 7.1 is applied with an additional cut on the event thrust, $T < 0.9$. In the next step, a signal likelihood L_{AAqq} is built to distinguish $hZ \to AAq\bar{q}$ signal from ZZ, WW and $q\bar{q}(\gamma)$ backgrounds. The L_{AAqq} includes the following variables: γ_{triple}, sphericity, N_{TRK}, $\cos\Theta_{2B}$, $\log Y_{34}$ and the logarithm of jet resolution parameter for which the event goes from six-jet to five-jet topology, $\log Y_{56}$. Among these variables N_{TRK} and $\log Y_{56}$ have the most discriminating power between the $hZ \to AAq\bar{q}$ signal and four-fermion and two-fermion backgrounds. The likelihood L_{AAqq} is used as the final discriminant. No evidence for the $hZ \to AAq\bar{q}$ signal is found in data. As an example Figure 8.9 shows the distributions of $\log Y_{56}$ and $L_{AAq\bar{q}}$ for the data collected in the year 2000, the expected background and the signal corresponding to the Higgs boson mass hypothesis (m_h, m_A) = (70,30) GeV.

8.4 L3 Combined Search for Neutral Higgs Bosons of the MSSM

The results of the search for neutral Higgs bosons of the MSSM are interpreted within the three benchmark scenarios discussed in Section 2.3.5. The mass of the light CP-even Higgs boson, m_h, the signal cross sections and Higgs boson decay branching fractions are calculated as a function of the two remaining free parameters, m_A and $\tan\beta$.

Table 8.2 reports the number of events selected in the $hA \to b\bar{b}b\bar{b}$ and $hA \to b\bar{b}\tau^+\tau^-$ channels for two representative Higgs mass hypotheses (m_h, m_A) = (85,85) GeV and

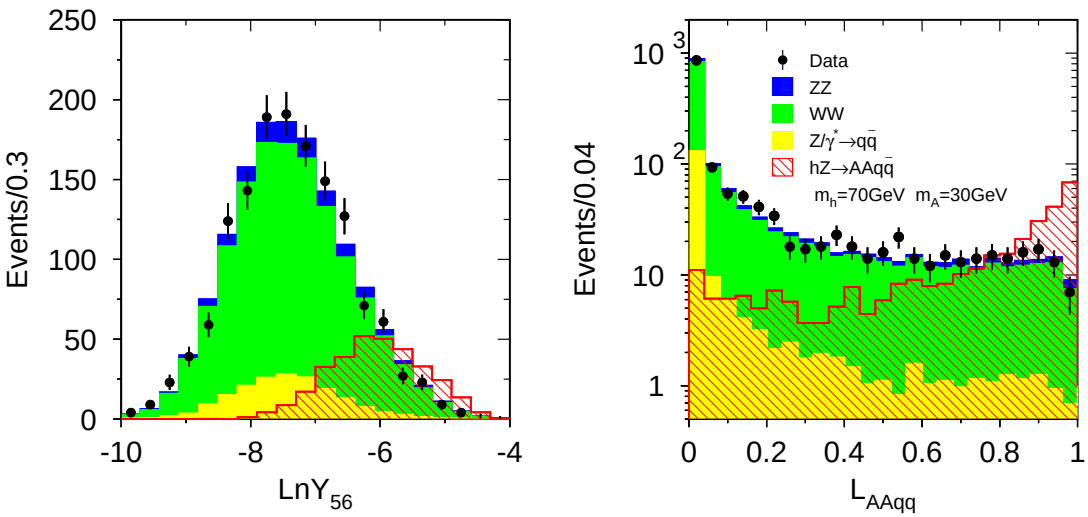

Figure 8.9: Distributions of $\log Y_{56}$ (left plot) and L_{AAqq} (right plot) in the $hZ \to AAq\bar{q} \to 6$ jets search. Dots represent data collected in the year 2000. The filled histograms are the expected background sources. The hatched histograms are the signal corresponding to the Higgs boson mass hypothesis $(m_h, m_A) = (70,30)$ GeV. The signal expectation is calculated within the "no mixing" scenario at $\tan\beta = 0.75$ and multiplied by a factor of 5.

(90,90) GeV[2] in the "m_h-max" scenario at $\tan\beta = 25$. For these hypotheses the hZ searches do not contribute. As can be seen good agreement between the number of observed candidates and the number of expected background events is found.

$\sqrt{s} = 203 - 209$ GeV	Mass hypothesis in "m_h -max" scenario at $\tan\beta = 25$					
	$(m_h, m_A) = (85,85)$ GeV			$(m_h, m_A) = (90,90)$ GeV		
Selection	N_D	N_B	N_S	N_D	N_B	N_S
$hA \to b\bar{b}b\bar{b}$	23	23.0	7.11	18	21.3	4.55
$hA \to b\bar{b}\tau^+\tau^-$	3	2.3	0.63	2	1.5	0.40
Total	26	25.3	7.74	20	22.8	4.95

Table 8.2: The number of observed candidates (N_D), expected background (N_B) and expected signal (N_S) events for the data collected by L3 in the year 2000, after a cut on the final discriminant corresponding to a signal-to-background ratio greater than 0.05. This cut is used to calculate the confidence levels. Numbers are given for two Higgs mass hypotheses $(m_h, m_A) = (85,85)$ GeV and (90,90) GeV in the "m_h-max" scenario at $\tan\beta = 25$.

[2]These mass hypotheses are very close to the upper limit of the search sensitivity in L3.

The systematic errors are estimated in the same way as in the SM Higgs search. They constitute 3% for the signal and 7% for the background. The analyses described in this chapter are combined with the hZ $\rightarrow$ b$\bar{\text{b}}\nu\bar{\nu}$ and hZ $\rightarrow$ b$\bar{\text{b}}\ell^+\ell^-(\ell = \text{e}, \mu)$ channels discussed in the chapter dedicated to the SM Higgs search. The results of previous searches [61] at $\sqrt{\text{s}}$ between 189 GeV and 202 GeV are also included in the calculation of confidence levels. Figure 8.10 shows the $(1 - \text{CL}_\text{b})$ significance contours as a function of m_h and m_A for the "m_h-max" scenario. An excess with a statistical significance of more than two standard deviations compared to the SM background hypothesis is observed in several regions in the $(\text{m}_\text{h}, \text{m}_\text{A})$ plane. However, all these excesses result each from events of only a single topology and a single data taking period. The largest excess is observed at $(\text{m}_\text{h}, \text{m}_\text{A}) \sim$ (68,68) GeV and amounts to about 2.4σ above the background expectation. This effect results mainly from candidates in the hA $\rightarrow$ b$\bar{\text{b}}$b$\bar{\text{b}}$ channel in the data collected by L3 in 1998 at $\sqrt{s} = 189$ GeV. The excess at $(\text{m}_\text{h}, \text{m}_\text{A}) \sim$ (75,82) GeV is mainly caused by candidates of the hA $\rightarrow$ b$\bar{\text{b}}\tau^+\tau^-$ topology in the data taken in 1999 at $\sqrt{\text{s}} = 192$ - 202 GeV. These two excesses are far below the expectation for the signal. There is also an excess of more than 2σ which appears as a band at m_h $\sim$ 99 GeV. This is due to several significant candidates in the hZ $\rightarrow$ b$\bar{\text{b}}\ell^+\ell^-(\ell = \text{e}, \mu)$ channels in the data collected in the year 1999. Finally, the excess at $(\text{m}_\text{h}, \text{m}_\text{A}) \sim$ 102 GeV is caused by candidates of the hA $\rightarrow$ b$\bar{\text{b}}$b$\bar{\text{b}}$ topology in the data sample of the year 2000.

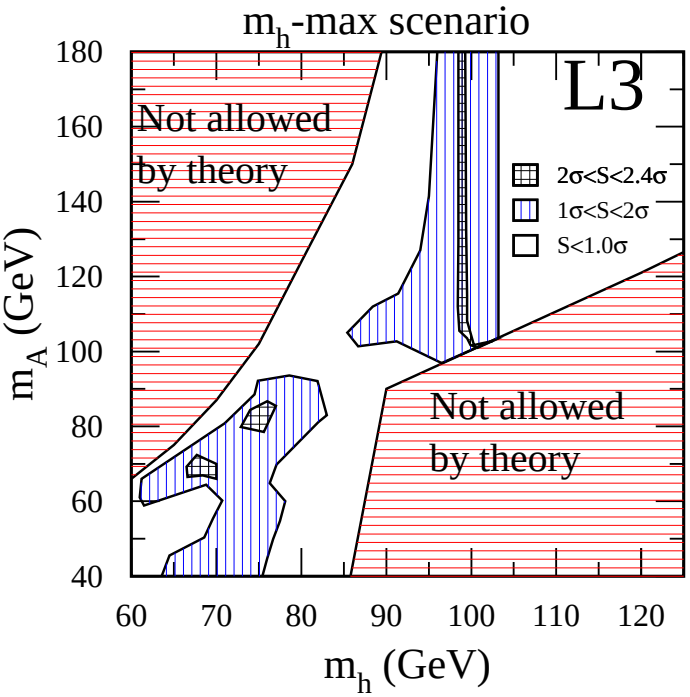

Figure 8.10: The $(1 - \text{CL}_\text{b})$ significance contours in the $(\text{m}_\text{A}, \text{m}_\text{h})$ plane for the "m_h -max" scenario. The data collected by L3 experiment at $\sqrt{\text{s}}$ = 189 - 209 GeV are combined. The horizontal hatched area is theoretically forbidden. The open area is the region where an excess of less than 1σ or deficit is observed compared to background expectation. The vertical hatched area represents the regions where an excess of more than 1σ is observed. The cross hatched area represents the regions where an excess of more than 2σ is observed.

Regarding these excesses as statistical fluctuations the data are interpreted in terms of exclusion of MSSM parameter regions. Figure 8.11 shows the area of the $(\tan\beta, \text{m}_\text{h})$

and $(\tan\beta, m_A)$ planes excluded at 95% C.L. for the "no mixing" and "m_h-max" scenarios. In the "m_h-max" scenario the observed lower limits on Higgs boson masses

$$m_h > 86.0 \text{ GeV}, \qquad m_A > 86.5 \text{ GeV}$$

are obtained at 95 % C.L. for any tanβ value considered. The expected lower mass bounds in the absence of signal are

$$m_h > 88.4 \text{ GeV}, \qquad m_A > 88.6 \text{ GeV}.$$

For $0.55 < \tan\beta < 2.2$ values of m_A up to 1 TeV are excluded thus allowing to rule out this tanβ range in the "m_h -max" scenario. The range $0.53 < \tan\beta < 2.2$ is expected to be ruled out in this scenario in the absence of signal. In the "no mixing" scenario the combined results establish lower mass bounds at 95 % of:

$$m_h > 85.5 \text{ GeV}, \qquad m_A > 86.3 \text{ GeV},$$

while expected limits are

$$m_h > 88.5 \text{ GeV}, \qquad m_A > 88.6 \text{ GeV}.$$

The tanβ range between 0.4 and 4.9 is excluded at 95 % C.L. compared to expected exclusion of $0.4 < \tan\beta < 6.6$. A more detailed view of L3 combined results for the case when $m_h \approx m_A$ and $\cos^2(\beta-\alpha) \approx 1$ is presented in Figure 8.12. It shows the confidence levels $(1 - CL_b)$, CL_s and CL_{med} as a function of m_h for the "m_h-max" scenario at $\tan\beta = 25$ and $m_h \leq 100$ GeV. A downward fluctuation of about 1σ compared to the background is observed in the data at $(m_h, m_A) \sim (89,89)$ GeV. There a deficit of candidates in the $hA \to b\bar{b}b\bar{b}$ channel at $\sqrt{s} = 203$ - 209 GeV is found resulting into observation of CL_s value smaller than 5% although no exclusion of this region at 95% C.L. is expected. This effect explains the irregularity in the exclusion plots at high tanβ and m_h between 86 GeV and 91 GeV. It should also be noted that in the "no mixing" scenario a large part of parameter space is ruled out in the intermediate range of tanβ , $5 \lesssim \tan\beta \lesssim 12$, for $m_h = 100$ - 112 GeV since for these models the quantity $\sin^2(\beta-\alpha)$ reaches 1 and the cross section of the hZ production is sufficiently high to provide sensitivity necessary for an exclusion. For the same region of the $(\tan\beta, m_h)$ plane in the "m_h-max" scenario, the cross section of the Higgs-strahlung process is essentially lower than in the "no mixing" scenario, making an exclusion impossible. The excess in the $hZ \to b\bar{b}\ell^+\ell^-$ channel discussed above and, to a lesser extent, in the $hZ \to b\bar{b}q\bar{q}$ channel in the data sample of the year 1999 result into a sizable reduction of the experimentally excluded range of tanβ for the mass range 90 GeV $\lesssim m_h \lesssim$ 100 GeV in both scenarios discussed. The area at $\tan\beta < 0.8$ and $m_A < 40$ GeV which was previously unexcluded by L3 [61] is now well covered with the $hZ \to AAq\bar{q}$ channel[3].

In the "large-μ" scenario, for those areas in the $(\tan\beta, m_A)$ plane where the $e^+e^- \to hA$ process is kinematically inaccessible and $e^+e^- \to hZ$ is suppressed by a small value of $\sin^2(\beta-\alpha)$, the heavy CP-even Higgs Boson, H, is expected to be produced via

[3]The $hZ \to AAq\bar{q}$ analysis was used instead of the four-jet one whenever it provided better sensitivity, i.e. gave smaller value of CL_{med}.

the Higgs-strahlung process with relatively high cross section. Hence, hZ analyses are also used to search for the HZ production. Figures 8.13a and 8.13b show the dependence of the quantities $(1 - CL_{med})$ and $(1 - CL_s)$ on m_A calculated at $\tan\beta = 15$ within the context of searches for h and H bosons. At each point of the ($\tan\beta$,m_A) scan we choose between h and H searches the one which gives the best sensitivity corresponding to the minimal value of CL_{med}. As dedicated analyses were optimised for the Higgs boson decay mode into a b anti-b quark pair, they do not provide sufficient sensitivity to exclude parameter regions where effective couplings $Hb\bar{b}$ and $hb\bar{b}$ are reduced. For $\tan\beta$ close to 15 and m_A around 94 GeV, this situation can be seen in Figures 8.13a and 8.13b.

Exclusion plots in the $(\tan\beta, m_h)$ and $(\tan\beta, m_A)$ planes for the "large-μ" scan are presented in Figures 8.13c and 8.13d, respectively. The 95 % C.L. limits on Higgs boson masses are

$$m_h > 84.5 \text{ GeV}, \qquad m_A > 86.5 \text{ GeV}.$$

The expected values are 87.2 GeV and 89.2 GeV, respectively. Furthermore, the range $0.7 < \tan\beta < 6.2$ is excluded. The expected excluded $\tan\beta$ range in the absence of the signal is $0.7 < \tan\beta < 14.7$. The experimentally allowed area spreading from $\tan\beta = 15$ to $\tan\beta = 50$ and inclined with respect to the m_A axis corresponds to the models with reduced $Hb\bar{b}$ or $hb\bar{b}$ couplings. The unexcluded region at $m_A \sim 88$ GeV and $\tan\beta \sim 15$ is caused by slight upward fluctuation in the data coming mainly from the $hA \rightarrow b\bar{b}b\bar{b}$ candidates selected during data taking period of the year 2000. The experimentally allowed vertical narrow band at $m_A = 107$ - 110 GeV and $\tan\beta \gtrsim 10$ represents the region where the hA production is kinematically inaccessible and $\cos^2(\beta - \alpha) \approx \sin^2(\beta - \alpha) \approx 0.5$ so that both the hZ and HZ production cross sections are reduced by a factor of 2 with respect to the HZ production cross section in the SM. Although the L3 combined search has a sensitivity for exclusion of this critical region as can be seen from Figure 8.13a, the expected median confidence level is only slightly lower than 5% and an insignificant upward fluctuation observed in the data pushes the observed confidence level, CL_s, above 5%, thus not allowing to exclude this region at 95% C.L.. Finally, the allowed area at $\tan\beta$ between 6 and 10 and m_h between 90 and 100 GeV arises due to the excesses already pointed out above.

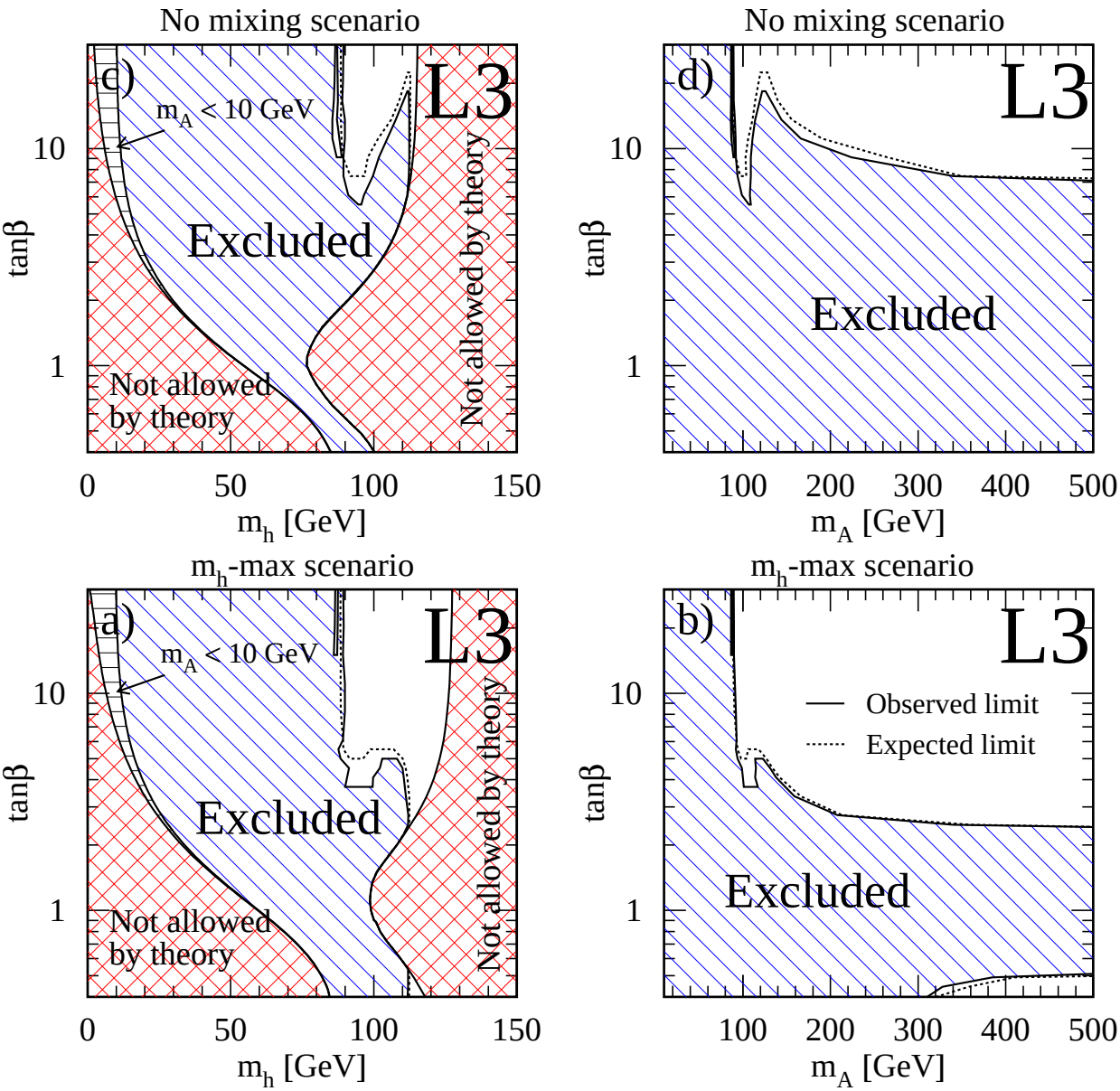

Figure 8.11: Exclusion plots in the $(\tan\beta, m_h)$ and the $(\tan\beta, m_A)$ planes at 95 % C.L. for the "no mixing" and "m_h – max" scenarios. The hatched area represents the exclusion and the crossed area is not allowed by theory. The horizontal hatched area corresponds to $m_A < 10$ GeV and was previously excluded by LEP [99]. The dashed line indicates the expected limit in the absence of signal.

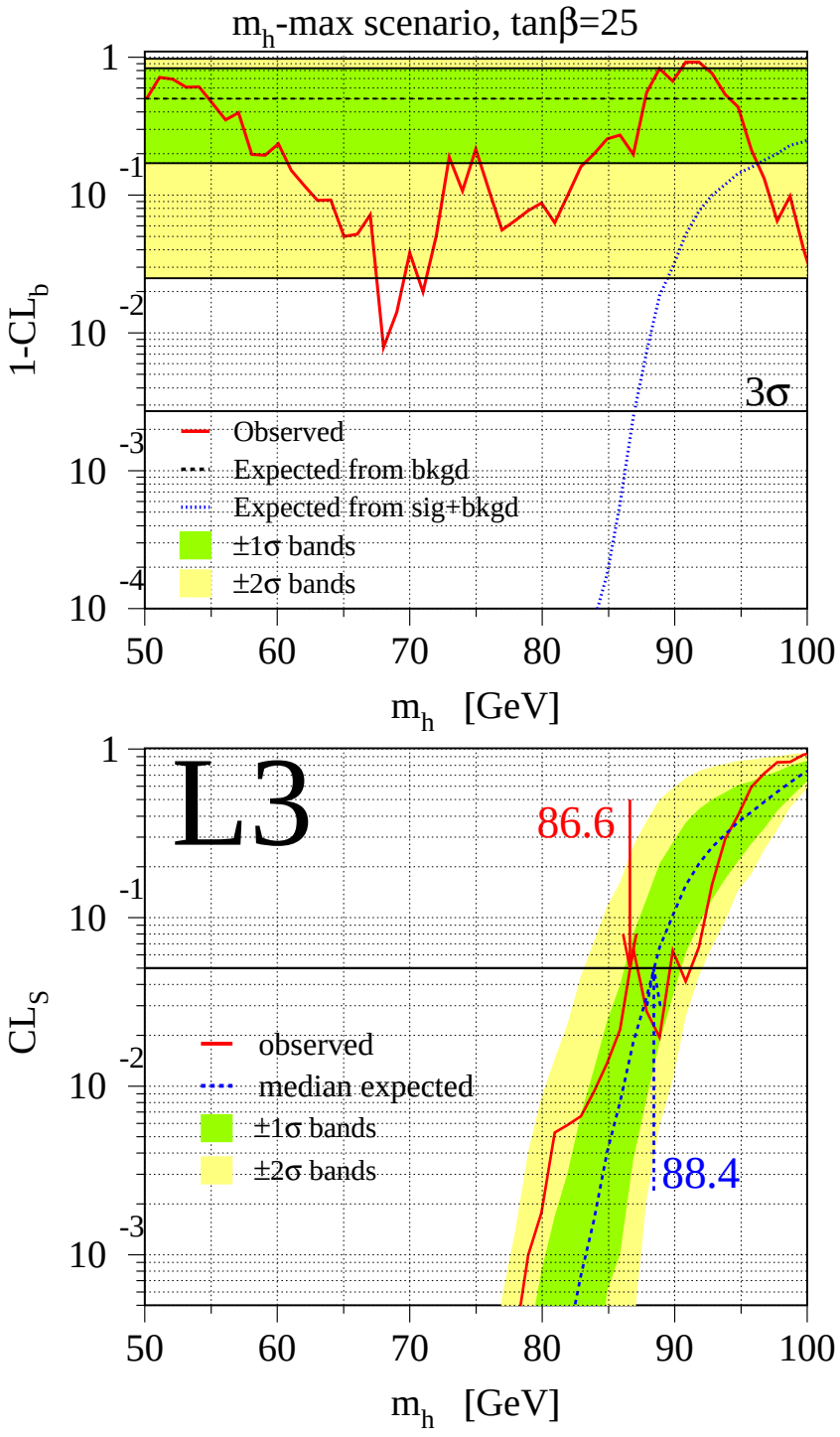

Figure 8.12: Upper plot: Confidence level for the background hypothesis, $(1 - \mathrm{CL_b})$, as a function of $\mathrm{m_h}$. The solid line corresponds to the observed $(1 - \mathrm{CL_b})$, the dashed line is the expectation from the "background-only" hypothesis, the dotted line is the expectation from the "signal+background" hypothesis. Also shown are $\pm 1\sigma$ and $\pm 2\sigma$ bands with respect to the "background-only" hypothesis. Lower plot: Confidence levels $\mathrm{CL_s}$ (solid line) and $\mathrm{CL_{med}}$ (dashed line) as a function of $\mathrm{m_h}$. Also shown are $\pm 1\sigma$ and $\pm 2\sigma$ bands with respect to the "background-only" hypothesis.

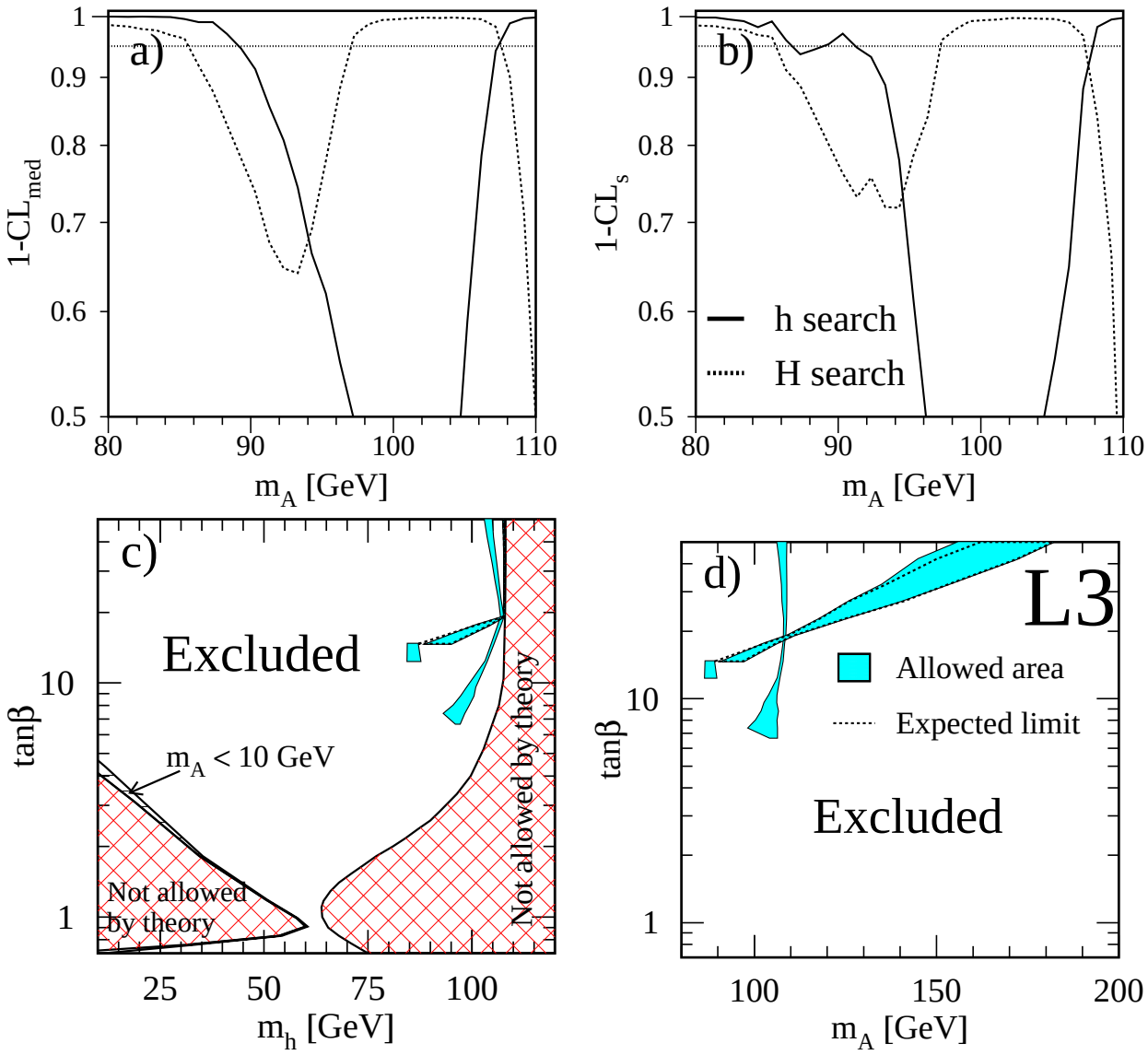

Figure 8.13: Confidence levels a) $(1 - \mathrm{CL_{med}})$ and b) $(1 - \mathrm{CL_s})$ as a function of $\mathrm{m_A}$ in the "large-μ" scenario at $\tan\beta = 15$. Confidence levels are calculated in context of searches for the heavy Higgs boson H (dotted line) and the light Higgs boson h (solid line). Since analyses rely upon b-tagging the sensitivity of the search for the HZ process degrades at $\mathrm{m_H}$ around 94 GeV due to the suppression of the $\mathrm{H} \to \mathrm{b\bar{b}}$ decay mode. Exclusion plots in c) $(\tan\beta, \mathrm{m_h})$ and d) $(\tan\beta, \mathrm{m_A})$ planes for the "large-μ" scenario. The hatched area is theoretically inaccessible. The open area is excluded at 95 % C.L.. The shaded area is allowed. The dashed line represents the expected boundary of the allowed region.

Chapter 9

Model Independent Higgs Searches

The searches for the SM Higgs boson and neutral Higgs bosons of the MSSM make use of a priori knowledge about signal cross sections and Higgs boson decay branching fractions which are unambiguously determined by m_H in the SM or by $\tan\beta$ and m_A in the MSSM benchmark scenarios. However, in some theoretical models such as 2HDM discussed in Section 2.2, the cross section of the Higgs-strahlung and associated Higgs boson pair production as well as Higgs boson decay branching fractions can be different from those in the SM or in MSSM benchmark scenarios. This motivated us to perform generalised searches for neutral CP-even and CP-odd scalar particles. Two production mechanisms, $e^+e^- \to hZ$ and $e^+e^- \to hA$, are considered. The hZZ and hAZ couplings are now probed instead of fixing them to the model predictions. The expressions for the cross section of the $e^+e^- \to hZ$ and $e^+e^- \to hA$ processes can be written in terms of these couplings as follows:

$$\sigma_{hZ} = \xi^2 \sigma^{SM}_{HZ}, \tag{9.1}$$

$$\sigma_{hA} = \eta^2 \bar{\lambda} \sigma^{SM}_{HZ}. \tag{9.2}$$

In these relations, ξ and η denote the ratio of the hZZ and hAZ couplings to the HZZ coupling in the SM: $\xi = g_{hZZ}/g^{SM}_{HZZ}$ and $\eta = g_{hAZ}/g^{SM}_{HZZ}$. The quantities $\bar{\lambda}$ and σ^{SM}_{HZ} have the same meaning as in Equations (3.8) and (3.10). It should be noted that in 2HDM, the quantities ξ and η depend on the parameters β and α:

$$\xi^2 = \sin^2(\beta - \alpha), \quad \eta^2 = \cos^2(\beta - \alpha) \tag{9.3}$$

and Relations (9.1) and (9.2) automatically transform into (3.8) and (3.10) respectively.

Two classes of analyses have been developed. The analyses of the first class rely upon b jet identification assuming the dominance of Higgs boson decay into $b\bar{b}$. The analyses of the second class, referred hereafter to as flavour independent analyses, ignore b tagging assuming that the Higgs boson decay into $b\bar{b}$ is suppressed. At the moment when this thesis was finalised, Monte Carlo samples with decays of Higgs bosons into light flavour quarks and gluons were produced with relatively low statistics. Therefore flavour independent analyses described in the following are performed using Monte Carlo samples with $h \to b\bar{b}$ and $A \to b\bar{b}$ decays. Some cross checks discussed later on in this chapter showed that the analysis performance is nearly independent on the flavour content of Higgs boson decay products. Nevertheless, these results are preliminary and

before the final publication analyses will be repeated with special samples of $h, A \to c\bar{c}$ and $h, A \to gg$ simulated signal events.

9.1 Model Independent Interpretation of SM Higgs Search Results

The results of the search for the SM Higgs boson at center-of-mass energies between 189 GeV and 209 GeV are also used to set limits on the quantity ξ^2. The upper 95 % C.L. limit on ξ^2 as a function of m_H is shown in Figure 9.1. This dependence was derived by fixing the branching fractions of the Higgs boson to the values predicted by the SM. Typically, ξ^2 values larger than 0.2 - 0.5 are excluded at 95 % C.L. for m_h ranging from 60 GeV to 90 GeV. The degradation of the analysis performance at $m_H \sim 91$ GeV is caused by the $ZZ \to b\bar{b}f\bar{f}$ final states. These represent a serious source of background, in particular for Higgs boson masses close to the Z boson mass, $m_H \approx m_Z$.

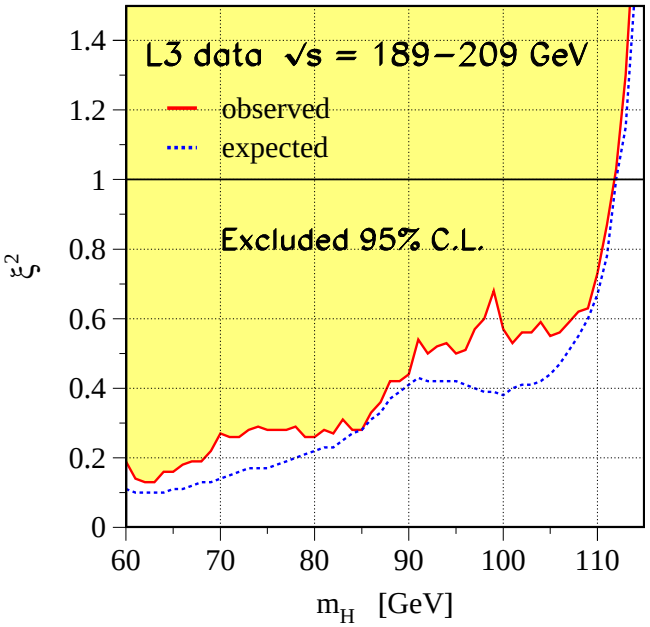

Figure 9.1: Upper limit on ξ^2 at 95% C.L. as a function of m_H. The dependence is derived in assumption of the SM branching fractions for the Higgs boson. The solid line is the observed limit and the dashed line is the expected limit. The shaded area is excluded at 95% C.L..

9.2 Flavour Independent Search for $e^+e^- \to hZ$

In this section a flavour independent search for the Higgs strahlung process with subsequent decay of the Higgs boson into hadrons is presented. Dedicated analyses are developed which investigate the following topologies: $hZ \to q\bar{q}q'\bar{q}'$, $hZ \to q\bar{q}\nu\bar{\nu}$ and $hZ \to q\bar{q}\ell^+\ell^-, \ell = e, \mu, \tau$.

9.2.1 Flavour Independent $hZ \to q\bar{q}q'\bar{q}'$ Analysis

The $hZ \to q\bar{q}q'\bar{q}'$ analysis proceeds in a similar way as that aimed to search for the SM Higgs boson. After the preselection described in Section 7.1 events are forced into four-jet topology using the Durham algorithm and a kinematic fit imposing four-momentum conservation is applied. The signal likelihood, L_{hZ}, is then constructed exploiting the same set of variables as listed in Section 7.1 apart from global event b-tag. An event is accepted if it passes optimised cut on the signal likelihood. The typical values of this cut lie between 0.3 and 0.5 depending on Higgs boson mass hypothesis and center-of-mass energy. The distribution of L_{hZ} for data, expected background and expected signal events is shown in Figure 9.2 for the entire data sample of the year 2000. The mass information is contained in the χ^2_{hZ} variable which is calculated using Equation (7.3). Only events with $P(\chi^2_{hZ}) > 10^{-2}$ are accepted. The quantity $\log_{10}P(\chi^2_{hZ})$ is used as the final discriminant.

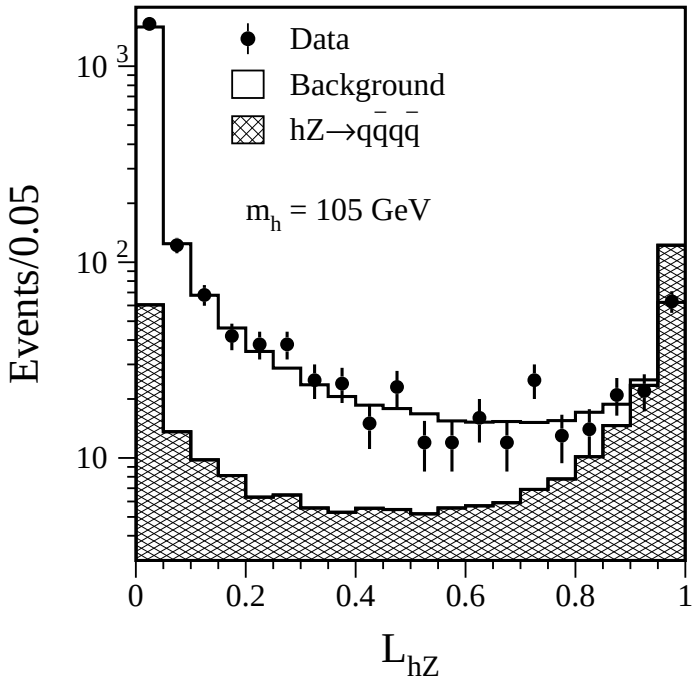

Figure 9.2: Distribution of L_{hZ} for the entire data sample of the year 2000. Dots are data. The open histogram is the expected background. The hatched histogram is the signal with $m_h = 105$ GeV. The signal is calculated assuming $\xi^2 = 1$ and $Br(h \to \text{hadrons}) = 100\%$ and multiplied by a factor of 10.

The number of events selected in data, the expected SM background, signal efficiency and the expected signal assuming $\xi^2 = 1$ $Br(h \to \text{hadrons}) = 100\%$ are summarised in Table 9.1 as a function of the tested Higgs boson mass. The largest background comes from hadronic decays of W-pairs.

As an example Figure 9.3 shows the spectrum of final discriminant bins ordered by signal-to-background ratio for data, expected SM background and signal at $m_h = 105$ GeV.

$\sqrt{s}$=203-209 GeV						
m_h =	70 GeV	80 GeV	90 GeV	100 GeV	105 GeV	110 GeV
SM background	655.8	542.9	427.6	273.4	215.8	128.2
Data	674	560	421	268	216	125
$\epsilon(hZ \to q\bar{q}q'\bar{q}')$	55%	59%	65%	62%	60%	55%
Signal	58.3	52.3	45.3	29.6	21.8	12.4

Table 9.1: Flavour independent $hZ \to q\bar{q}q'\bar{q}'$ search. The number of events selected in data, the expected SM background, signal efficiency and the expected signal as a function of the tested Higgs boson mass. The numbers correspond to the full data sample of the year 2000. The signal expectation is obtained for $\xi^2 = 1$ and Br(h $\to$ hadrons) = 100%.

The signal efficiencies computed with available Monte Carlo samples of $hZ \to b\bar{b}q\bar{q}$ final states are taken as generic hadronic efficiencies and applied also for $h \to c\bar{c}$ and $h \to gg$ decay modes. To verify the validity of this procedure, a number of cross checks have been done using statistically limited sample of $hZ \to c\bar{c}q\bar{q}$ events. At first, distributions of the crucial variables used in the analysis were compared between $hZ \to b\bar{b}q\bar{q}$

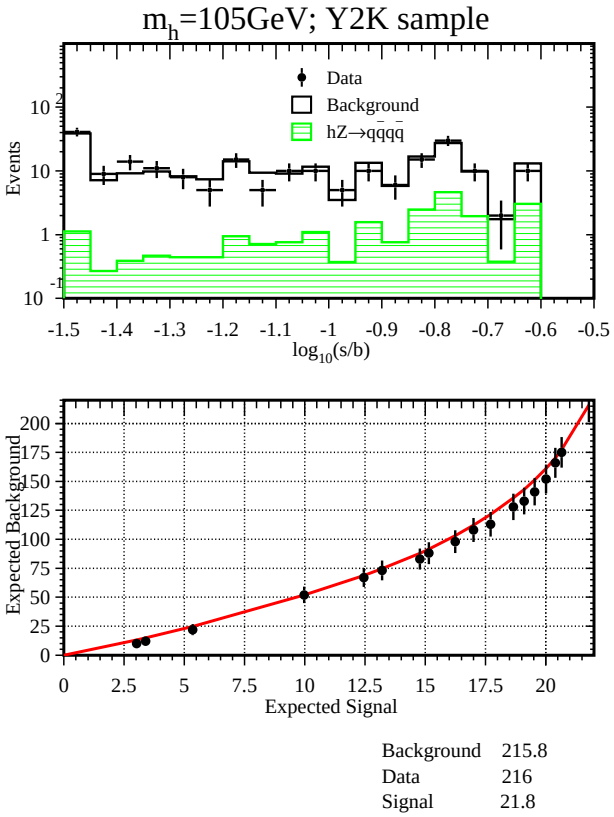

Figure 9.3: Distribution of $\log_{10}(s/b)$ for the full data sample of the year 2000 in the $hZ \to q\bar{q}q'\bar{q}'$ channel at m_h = 105 GeV (upper plot). Dots represent data, the open histogram is the expected background and the hatched histogram is the expected signal. The bottom distribution is obtained by integrating the upper distribution from the right to the left side. Dots are data and the line is the expectation from the background. The expected signal is estimated assuming $\xi^2 = 1$ and Br(h $\to$ hadrons) = 100%.

and $hZ \rightarrow c\bar{c}q\bar{q}$ Monte Carlo samples. The shapes of the distributions are found to be weakly dependent on the flavour of the quarks originating from the Higgs boson decay as illustrated in Figure 9.4. A small difference in shape is observed for the distribution of N_{TRK}. For the $hZ \rightarrow c\bar{c}q\bar{q}$ final states the distribution of charged track multiplicity is shifted to lower values by about 4 compared to the $hZ \rightarrow b\bar{b}q\bar{q}$ final states. To evaluate the impact of this difference on the analysis performance, the dependence of CL_{med} on the tested Higgs boson mass was calculated separately for $hZ \rightarrow b\bar{b}q\bar{q}$ and $hZ \rightarrow c\bar{c}q\bar{q}$ Monte Carlo samples. The cross section of the $e^+e^- \rightarrow hZ$ process was set to the value predicted by the SM and the branching fraction of h into quark anti-quark pair of a given flavour was set to 100 %. The comparison of CL_{med} between $hZ \rightarrow c\bar{c}q\bar{q}$ and $hZ \rightarrow b\bar{b}q\bar{q}$ Monte Carlo samples revealed only a negligible difference in the analysis performance as can be seen in Figure 9.5.

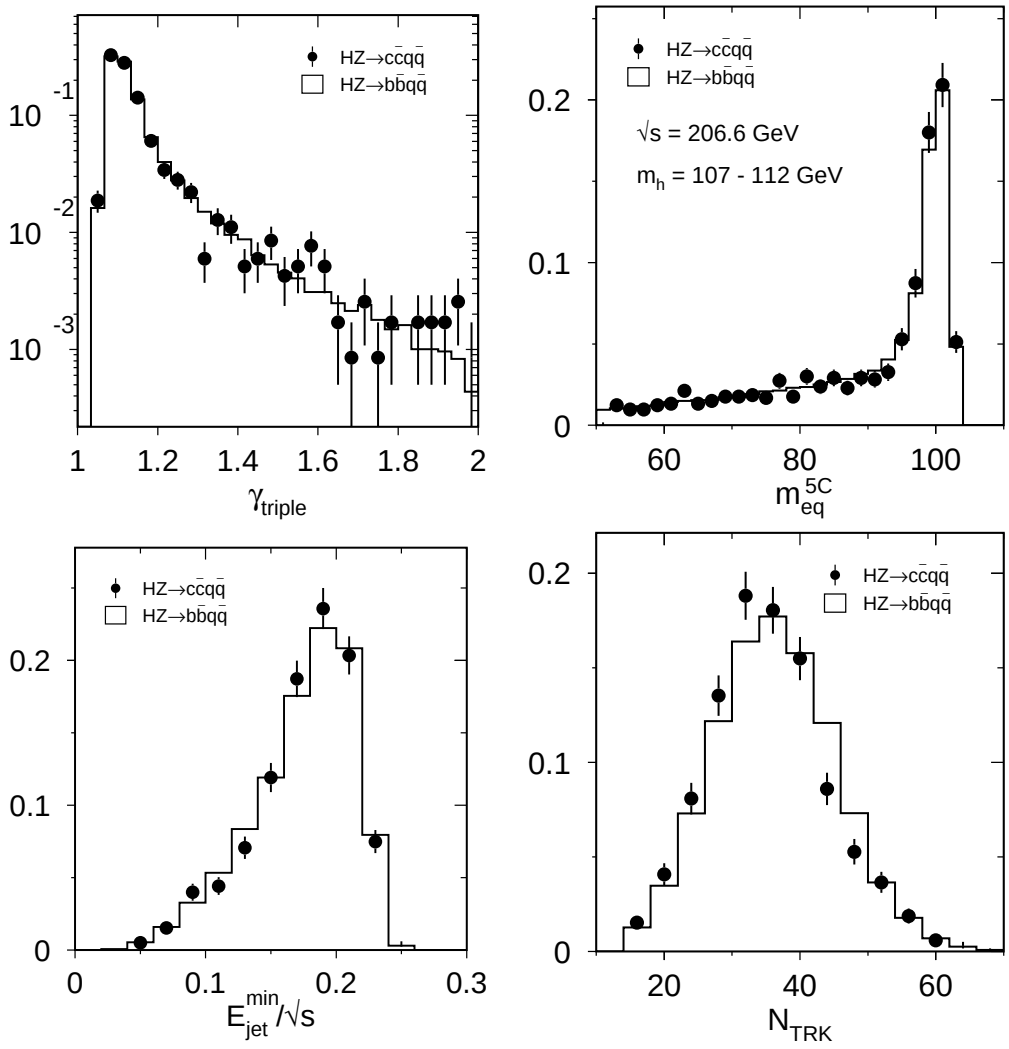

Figure 9.4: Normalised distributions of γ_{triple} (upper-left), m_{eq}^{5C} (upper-right), $E_{jet}^{min}/\sqrt{s}$ (lower-left) and N_{TRK} (lower-right) for $hZ \rightarrow b\bar{b}q\bar{q}$ (open histograms) and $hZ \rightarrow c\bar{c}q\bar{q}$ (dots) Monte Carlo samples generated at $\sqrt{s} = 206.6$ GeV. To enhance Monte Carlo statistics samples with Higgs boson masses between 107 and 112 GeV were merged.

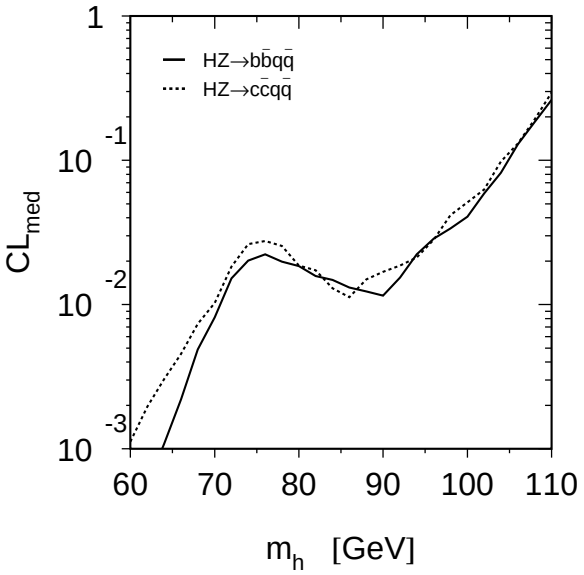

Figure 9.5: The dependence of CL_{med} on m_h for $hZ \to b\bar{b}q\bar{q}$ (solid line) and $hZ \to c\bar{c}q\bar{q}$ (dashed line) final states. The degradation of the analysis performance at m_h = 70 - 75 GeV is caused by a kinematic reflection of the W-peak while interpreting the $WW \to q\bar{q}q\bar{q}$ events within the context of the hZ production hypothesis.

9.2.2 Flavour Independent $hZ \to q\bar{q}\nu\bar{\nu}$ Analysis

In the first step high multiplicity hadronic events are selected. At least 10 tracks and 15 calorimetric clusters are required. The visible energy, E_{vis}, must exceed 25% and be less than 70% of the center-of-mass energy . The events are forced into two jets using the Durham algorithm. The contributions from leptonic two fermion final states as well as two-photon interactions are reduced by requiring the dijet invariant mass to be larger than 40 GeV. The events arising from $q\bar{q}(\gamma)$ background are also suppressed by demanding the mass recoiling against the hadronic system to be larger than 60 GeV.

The polar angle of the missing momentum must lie between 0.45 and 2.69 rad in order to avoid missing energy due to particles escaping in the beam pipe, and especially double radiative returns to the Z resonance. The energy in the very forward calorimeters is required to be smaller than 20 GeV and events with isolated photons with energy greater than 20 GeV are rejected. To further suppress radiative returns to Z resonance, the absolute value of the sine of the angle between the beam axis and the plane containing the dijet system, $|\sin\Psi|$, is required to be larger than 0.025.

A sample with 434 data events is selected while 417 events are expected from the SM background processes. The signal efficiency varies between 60 and 70 % for the Higgs boson mass ranging from 60 GeV to 114 GeV.

After the selection, variables having discriminating power between signal and background are combined into a feed forward neural network. The neural network inputs include: visible energy, longitudinal missing momentum normalised to the visible energy, transverse missing momentum normalised to the visible energy, absolute value of the cosine of the event acollinearity, event thrust, missing mass, sum of the opening angles between three jets after forcing event into 3-jet configuration and $|\sin\Psi|$.

The Higgs boson mass is reconstructed with the imposed condition that the missing mass equals to the mass of the Z boson. The output of the neural network is combined

with the reconstructed Higgs boson mass into the final discriminant.

9.2.3 Flavour Independent $hZ \to q\bar{q}\ell^+\ell^-(\ell = e, \mu, \tau)$ Analyses

The study of the $hZ \to q\bar{q}\ell^+\ell^-(\ell = e, \mu, \tau)$ final states is similar to the analyses optimised for the $h \to b\bar{b}$ decay mode. The only difference is that in the last step the final discriminant is built from the reconstructed masses of the dilepton and dijet systems ignoring the b-tag variables of the two hadronic jets.

9.2.4 L3 Combined Results of Flavour Independent Search for $e^+e^- \to hZ$

The flavour independent analyses described above are used to examine the hypothesis of $e^+e^- \to hZ$ production with subsequent hadronic decay of h. The branching fraction of h into hadrons is assumed to be 100 %. The Higgs boson masses are tested from 60 GeV to 114 GeV in 1 GeV steps. The number of events selected in each search channel at $m_h = 105$ GeV and 110 GeV is presented in Table 9.2 for the full data sample of the year 2000.

$\sqrt{s} = 203 - 209$ GeV	Mass hypothesis					
	$m_h = 105$ GeV			$m_h = 110$ GeV		
Selection	N_D	N_B	N_S	N_D	N_B	N_S
$hZ \to q\bar{q}q'\bar{q}'$	141	151.2	19.5	86	92.2	10.6
$hZ \to q\bar{q}\nu\bar{\nu}$	28	26.8	5.74	15	14.5	3.33
$hZ \to q\bar{q}e^+e^-$	1	1.81	1.11	0	1.06	0.68
$hZ \to q\bar{q}\mu^+\mu^-$	1	1.31	0.89	1	0.80	0.56
$hZ \to q\bar{q}\tau^+\tau^-$	2	2.22	0.38	2	1.41	0.24
Total	173	183.3	27.6	104	110.0	15.4

Table 9.2: Flavour independent search for $e^+e^- \to hZ$. The number of observed candidates (N_D), expected background (N_B) and expected signal (N_S) events for the data collected by L3 in the year 2000, after a cut on the final discriminant corresponding to a signal-to-background ratio greater than 0.05. This cut is used to calculate the confidence levels. The signal expectation is computed assuming $\xi^2 = 1$.

The systematic uncertainty of 3% is assigned to the signal and 7% to the background. Results from the data of the year 2000 are combined with our previous searches at $\sqrt{s}$ between 189 GeV and 202 GeV [100]. Figure 9.6 shows the dependence of $(1 - CL_b)$ on the tested Higgs boson mass. The data are found to be compatible with the SM background hypothesis within 2 standard deviations over the entire range of the tested Higgs boson masses. Results of the analyses are translated into upper limits on the quantity ξ^2. The 95% C.L. upper bound on ξ^2 as a function of m_h is presented in Figure 9.7. The analysis performance degrades at $m_h \approx 91$ GeV for the same reason as indicated in Section 9.1. On the other hand the drop in the analysis performance,

observed in the $hZ \to q\bar{q}q'\bar{q}'$ channel at $m_h = 70$ - 75 GeV, is flattened in the combination with the $hZ \to q\bar{q}\nu\bar{\nu}$ and $hZ \to q\bar{q}\ell^+\ell^-$ channels. At ξ=1, when the $e^+e^- \to hZ$ process has the same cross section as in the SM, Higgs boson masses less than 97 GeV are excluded at 95 % C.L. as can bee seen in Figure 9.8. The expected lower bound on m_h is 107 GeV. The sizable difference between the expected and observed mass limits is caused by tiny regions at $m_h \sim 99$ GeV and $m_h \sim 101$ GeV which are only ruled out at confidence levels lower than 95 %. There a few candidates in the $hZ \to q\bar{q}\ell^+\ell^-(\ell = e, \mu)$ channel at $\sqrt{s}$ = 192 - 202 GeV and the $hZ \to q\bar{q}\nu\bar{\nu}$ channel at $\sqrt{s}$ = 203 - 209 GeV, respectively, are found.

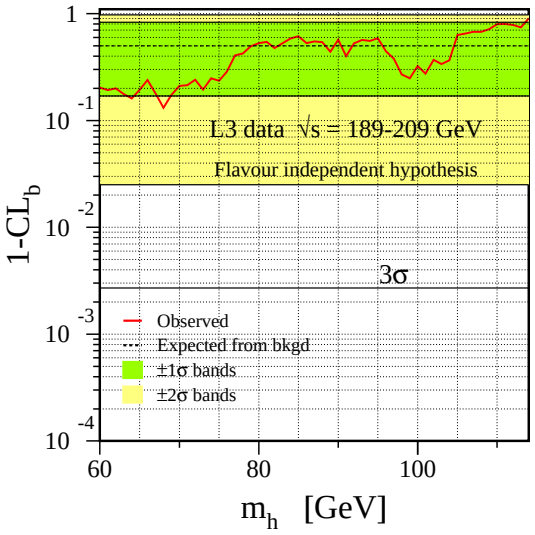

Figure 9.6: The confidence level for the "background-only" hypothesis, $(1 - CL_b)$, (solid line) as a function of m_h for the Higgs boson decaying into hadrons. The dashed line corresponds to the expectation from the SM background. The shaded areas represent 1σ and 2σ bands with respect to the SM background hypothesis.

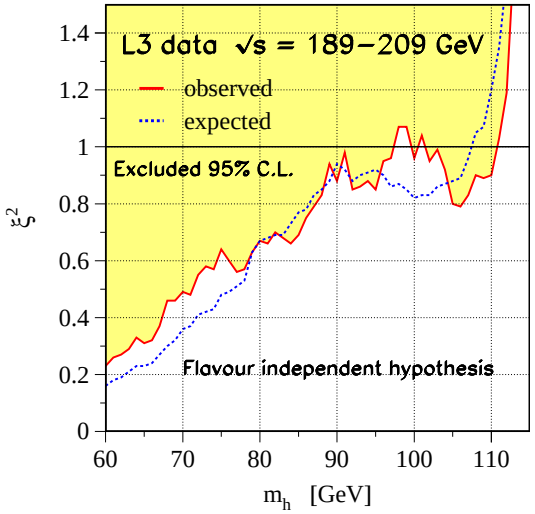

Figure 9.7: Upper limit on ξ^2 at 95 % C.L. as a function of m_h for the hadronically decaying Higgs boson. The solid line is the observed limit and the dashed line is the expected limit. The shaded area is excluded at 95 % C.L..

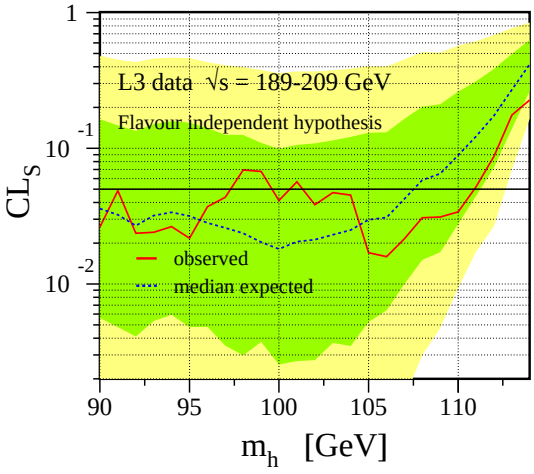

Figure 9.8: The confidence level observed in data, CL_s, (solid line) and the median expected confidence level, CL_{med}, (dashed line) as a function of m_h for hadronically decaying Higgs boson. The hZZ coupling is set to the value predicted by the SM. The shaded areas show 1σ and 2σ bands with respect to the expectation from the SM background in the absence of signal.

9.3 Exclusive Search for $e^+e^- \to hA$

In this section an exclusive search for the $e^+e^- \to hA$ process is discussed. The final states $hA \to b\bar{b}b\bar{b}$ and $hA \to b\bar{b}\tau^+\tau^-$ are analysed using the identification of b quarks. The flavour independent analyses, which ignore b tagging, are elaborated to study also the $hA \to q\bar{q}q'\bar{q}'$ and $hA \to q\bar{q}\tau^+\tau^-$ topologies.

The exclusive search for $e^+e^- \to hA$ implies that the process $e^+e^- \to hZ$ is not considered. Apart from this feature, the dedicated analyses closely follow those devised for MSSM Higgs boson searches.

The Higgs boson masses are scanned in the ranges

$$50 \text{ GeV} < m_h < 100 \text{ GeV} \text{ and } 50 \text{ GeV} < m_A < 100 \text{ GeV}$$

in 1 GeV steps.

9.3.1 The $hA \to b\bar{b}b\bar{b}$ and $hA \to q\bar{q}q'\bar{q}'$ Searches

The $hA \to b\bar{b}b\bar{b}$ search is performed on the data collected in the year 2000 and then combined with our previous searches [100]. The $(1 - CL_b)$ significance contours in the (m_h, m_A) plane are presented in Figure 9.9. For many tested Higgs boson mass hypotheses an excess of candidates with respect to the SM background expectation is observed. The largest excess, amounting to about 2.6σ, is found at $(m_h, m_A) = (68,68)$ GeV. As was already discussed in Section 8.4 this effect mainly originates from the data sample of the year 1998. Regarding this excess as a statistical fluctuation the results of the search are translated into an upper limit on the quantity η^2 as a function of Higgs boson masses assuming the topological branching fraction $Br(hA \to b\bar{b}b\bar{b})$ equal 100 %. The exclusion contours as a function of the tested Higgs boson masses are presented in Figure 9.10 for $\eta^2 \geq 0.4$, $\eta^2 \geq 0.7$ and $\eta^2 \geq 1.0$.

The search for $hA \to q\bar{q}q'\bar{q}'$ follows the strategy of the $hA \to b\bar{b}b\bar{b}$ analysis. The same set of variables, except for b-tag information, is exploited to distinguish the signal from the SM background processes. The quantity $\log_{10}P(\chi^2_{hA})$ is used as the final discriminant. Figure 9.11 shows as an example the distribution of the $\log_{10}P(\chi^2_{hA})$ variable

for data and Monte Carlo samples selected at $(m_h, m_A) = (70,50)$ GeV. The analysis done on the data of the year 2000 is combined with searches performed at lower center-of-mass energies [100]. Figure 9.12 presents the $(1 - CL_b)$ significance contours as a function of m_h and m_A.

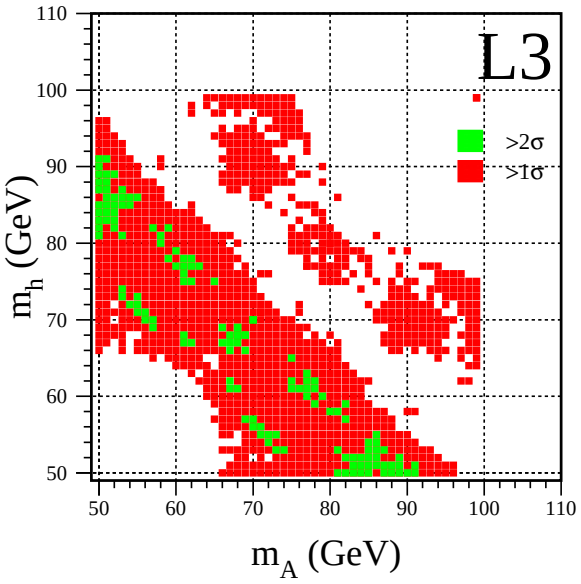

Figure 9.9: The $(1 - CL_b)$ significance contours in the (m_h, m_A) plane for the $hA \to b\bar{b}b\bar{b}$ search at $\sqrt{s}$ between 189 GeV and 209 GeV. The light-gray and gray areas indicate regions where an excess with a significance of more than 2σ and 1σ, respectively, is observed in data.

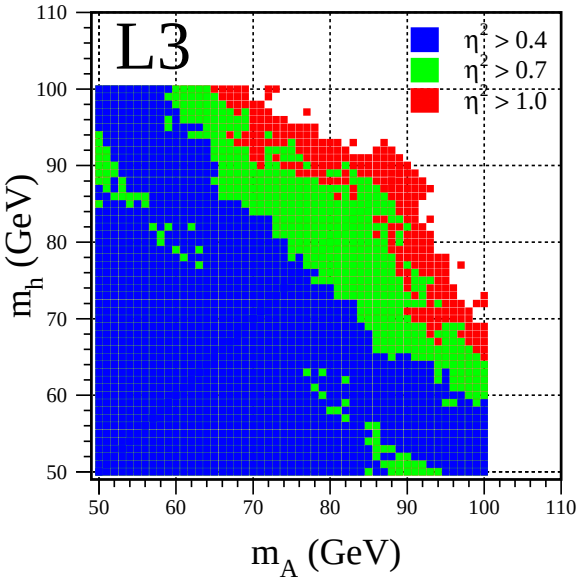

Figure 9.10: Points in the (m_h, m_A) plane where the $hA \to b\bar{b}b\bar{b}$ signal is excluded at 95 % C.L. for $\eta^2 \geq 0.4$ (dark area), $\eta^2 \geq 0.7$ (light-gray area) and $\eta^2 \geq 1.0$ (gray area).

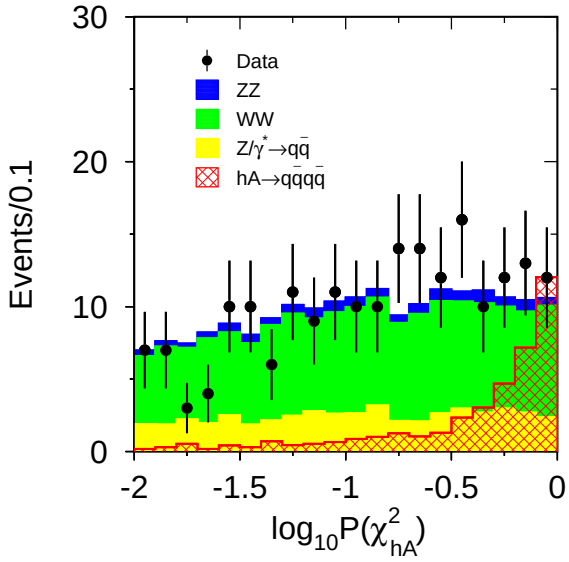

Figure 9.11: The distribution of $\log_{10}P(\chi^2_{hA})$ in the $hA \to q\bar{q}q'\bar{q}'$ channel for the full data sample of the year 2000. Dots represent data, the filled histograms are the expected background sources and the hatched histogram is the signal expected for $\eta^2 \times Br(hA \to q\bar{q}q'\bar{q}')$ = 1 and multiplied by a factor of 2. The Higgs boson mass hypothesis is (m_h, m_A) = (70,50) GeV.

With exception of few points in the (m_h, m_A) plane the data are compatible with the SM background expectation within 2σ[1]. The regions in the (m_h, m_A) plane excluded at 95 % C.L. for $\eta^2 \geq 0.3$, $\eta^2 \geq 0.7$ and $\eta^2 \geq 1.0$ and $Br(hA \to q\bar{q}q'\bar{q}') = 100\%$ are displayed in Figure 9.13.

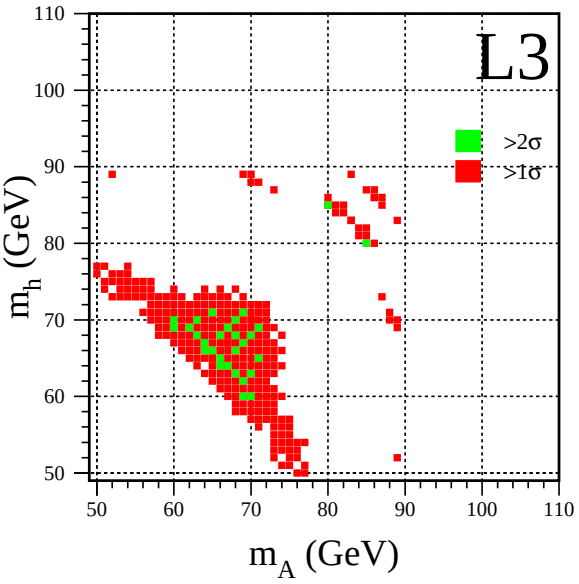

Figure 9.12: The $(1 - CL_b)$ significance contours in the (m_h, m_A) plane for the $hA \to q\bar{q}q'\bar{q}'$ search at $\sqrt{s}$ between 189 GeV and 209 GeV. The light-gray and gray areas indicate regions where an excess with a significance of more than 2σ and 1σ, respectively, is observed in data.

[1]The largest excess is found at (m_h, m_A) = (66,64) GeV and corresponds to 2.1σ effect.

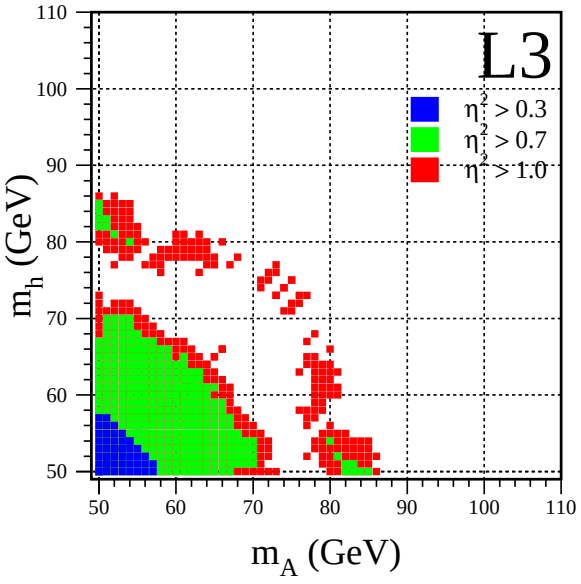

Figure 9.13: Points in the (m_h, m_A) plane where the $hA \to q\bar{q}q'\bar{q}'$ signal is excluded at 95 % C.L. for $\eta^2 \geq 0.3$ (dark area), $\eta^2 \geq 0.7$ (light-gray area) and $\eta^2 \geq 1.0$ (gray area).

9.3.2 The $hA \to b\bar{b}\tau^+\tau^-$ and $hA \to q\bar{q}\tau^+\tau^-$ Searches

The analyses are performed on the data collected at $\sqrt{s}$ between 189 GeV and 202 GeV[2] to search exclusively for $hA \to b\bar{b}\tau^+\tau^-$ and $hA \to q\bar{q}\tau^+\tau^-$ final states [100]. The selection of these final states is identical to that presented in Section 8.2. In the $hA \to b\bar{b}\tau^+\tau^-$ analysis, the final discriminant is built from the reconstructed masses of the dijet and dilepton systems, m_{qq}^{rec} and $m_{\tau\tau}^{rec}$, and b-tags of the two hadronic jets. The final discriminant for the $hA \to q\bar{q}\tau^+\tau^-$ search is constructed using only m_{qq}^{rec} and $m_{\tau\tau}^{rec}$.

Good agreement between observation and expectation from the background is found at all tested masses of the dilepton and dijet systems, $(m_{\tau\tau}, m_{qq})$, for both $hA \to b\bar{b}\tau^+\tau^-$ and $hA \to q\bar{q}\tau^+\tau^-$ searches. Hence, the results of the analyses are used to set limits on η^2. Figure 9.14a shows regions in the $(m_{\tau\tau}, m_{qq})$ plane excluded at 95 % for $\eta^2 \geq 0.4$, 0.7 and 1.0 using results of the $hA \to b\bar{b}\tau^+\tau^-$ analysis and assuming $Br(hA \to b\bar{b}\tau^+\tau^-) = 100\%$. The exclusion plot for the $hA \to q\bar{q}\tau^+\tau^-$ search is presented in Figure 9.14b.

[2] Analysis of the data collected in the year 2000 is not completed yet.

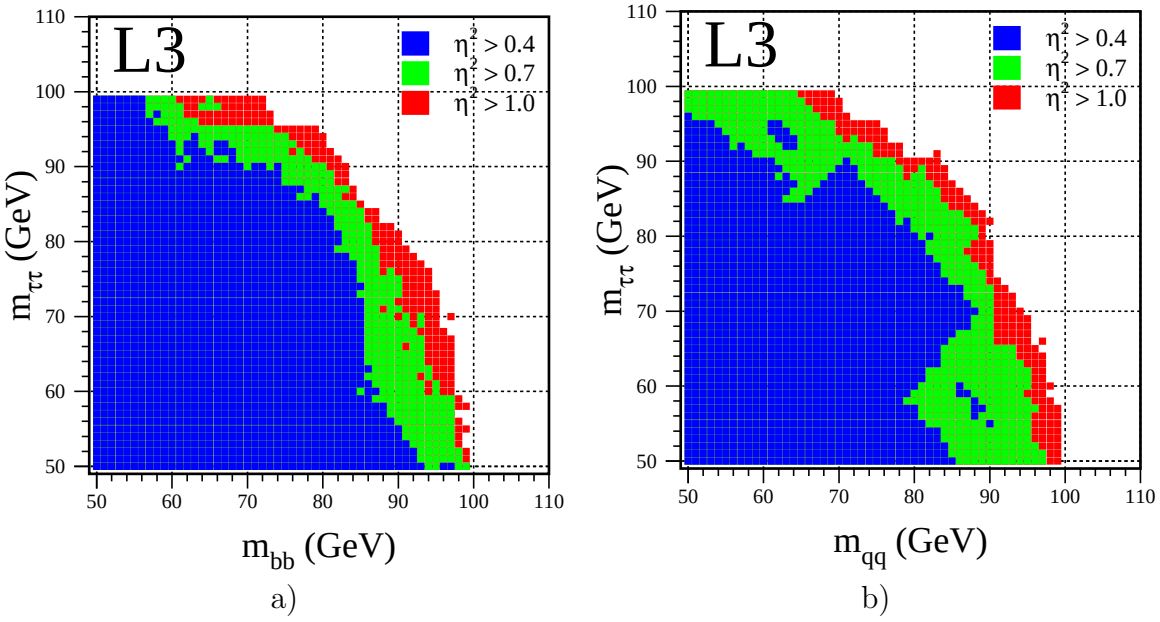

Figure 9.14: Points in the $(m_{\tau\tau}, m_{qq})$ plane where a) the hA → $b\bar{b}\tau^+\tau^-$ and b) the hA → $q\bar{q}\tau^+\tau^-$ signal is excluded at 95 % C.L. for $\eta^2 \geq 0.4$ (dark area), $\eta^2 \geq 0.7$ (light-gray area) and $\eta^2 \geq 1.0$ (gray area).

Chapter 10

LEP Combined Searches for Neutral Higgs Bosons

Before this thesis was finished ALEPH [101] and L3 [102, 103] collaborations had finalised their results of the searches for the SM Higgs boson and neutral Higgs bosons of the MSSM. Preliminary results were obtained by DELPHI [104] and OPAL [105] experiments.

In this chapter I briefly report on preliminary results of LEP combined searches for neutral Higgs bosons. A more detailed discussion of these results can be found in References [106].

An excess of 3σ beyond the background expectation consistent with the production of the Higgs boson with mass near 114 GeV was reported by the ALEPH collaboration [107]. This effect originates from events of the $HZ \to b\bar{b}q\bar{q}$ topology and is not confirmed neither by other search channels nor by other LEP collaborations. In the LEP combined search for the SM Higgs boson, the ALEPH excess is diminished to about 2σ due to background-like observations by other experiments. Since no strong indication of the signal is found, the LEP data are used to set limit on m_H. The dependence of CL_s and CL_{med} on m_H derived from a combination of LEP analyses is presented in Figure 10.1.

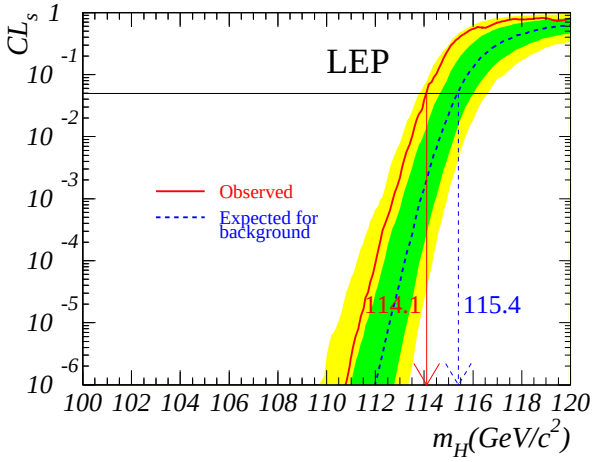

Figure 10.1: The dependence of CL_s and CL_{med} on m_H obtained from the LEP combined search for the SM Higgs boson.

The results of LEP combined search establish lower bound on m_H of

$$m_H > 114.1 \text{ GeV}$$

at 95 % C.L. compared to the expected limit in the absence of signal:

$$m_H > 115.4 \text{ GeV}.$$

The LEP combined data are also tested for the presence of MSSM Higgs boson signal. Three conventional benchmark scenarios are considered. No evidence of signal is found and constraints on MSSM parameters are derived. As an example Figure 10.2 shows the 95 % C.L. exclusion contours in the $(\tan\beta, m_h)$ projection for the "m_h-max" scenario.

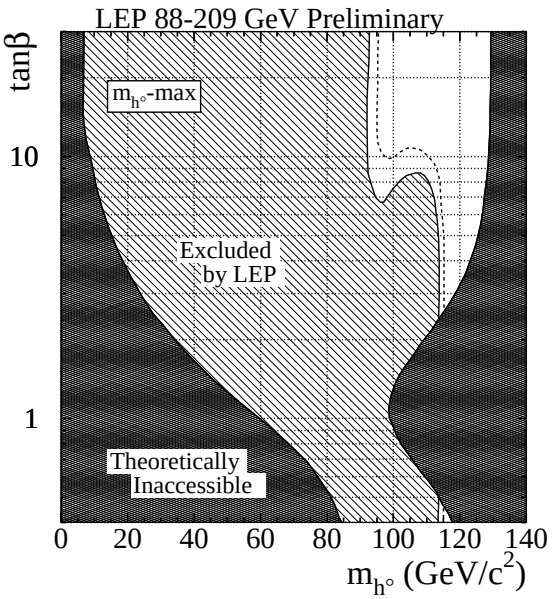

Figure 10.2: The 95 % C.L. exclusion contours in the $(\tan\beta, m_h)$ projection for the "m_h-max" scenario. The results of the four LEP experiments are combined.

The observed 95 % C.L. limits on Higgs boson masses for $\tan\beta > 0.7$ are:

$$m_h > 91.0 \text{ GeV}, \; m_A > 91.9 \text{ GeV},$$

compared to the expected values:

$$m_h > 94.6 \text{ GeV}, \; m_A > 95.0 \text{ GeV}.$$

The difference between the observed and expected mass limits is caused by the excess of candidates of the $hA \to b\bar{b}b\bar{b}$ topology at $(m_h, m_A) \sim (92,92)$ GeV in the data collected by OPAL at $\sqrt{s} = 196$ GeV [108]. This excess does not appear in other samples. The ranges $0.5 < \tan\beta < 2.4$ and $0.7 < \tan\beta < 10.5$ [1] are excluded in "m_h-max" and "no

[1] Preliminary results of the LEP combined search for MSSM Higgs bosons does not include the latest L3 analysis of the $hZ \to AAq\bar{q}$ topology. With inclusion of this analysis $\tan\beta$ range below 0.7 can be ruled out in the "no mixing" scenario.

mixing" scenarios, respectively, for a top quark mass less than or equal to 174.3 GeV. With the LEP combined data the "large-μ" scenario is entirely ruled out.

Each of the four LEP collaborations has obtained preliminary results of flavour independent search for $e^+e^- \to hZ$ process. The LEP working group for Higgs boson searches combined these results. No significant deviation from the SM background expectation is found in data and upper 95 % C.L. limit on the quantity $\xi^2 \times \mathrm{Br}(h \to \mathrm{hadrons})$ as a function of m_h is derived. This is shown in Figure 10.3. At $\xi^2 = 1$ and $\mathrm{Br}(h \to \mathrm{hadrons}) = 100$ %, a lower bound on the Higgs boson mass:

$$m_h > 112.9 \text{ GeV}$$

is obtained at 95 % C.L.. The expected limit is

$$m_h > 113 \text{ GeV}.$$

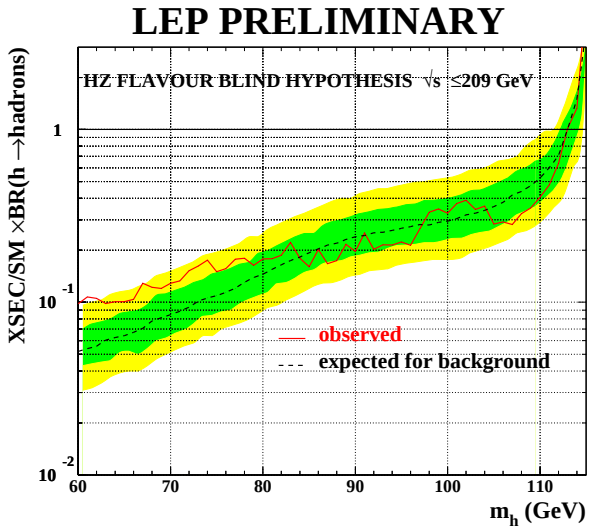

Figure 10.3: The 95 % C.L. upper limit on the quantity $\xi^2 \times \mathrm{Br}(h \to \mathrm{hadrons})$ as a function of m_h obtained from the LEP combined search for the $e^+e^- \to hZ$ process with subsequent hadronic decay of h.

Chapter 11

Prospects of Higgs Physics at TEVATRON and LHC

After LEP the Higgs boson searches will be continued at TEVATRON $p\bar{p}$ collider. About 0.1 fb^{-1} of data were collected by two experiments, CDF and D0, during Run1 at center-of-mass energy of 1.8 TeV. Results of Higgs searches performed on these data were briefly reported in Section 3.3 and are not competitive with the sensitivity at LEP. The TEVATRON accelerator has been upgraded to increase its center-of-mass energy to $\sqrt{s}$ = 2 TeV and to to attain higher beam intensity than in Run1 [109]. The upgrade of CDF and D0 detectors [110] improved their b-detection capability. The goal of Run2, which started in March 2001, is to eventually deliver the integrated luminosity of about 15 fb^{-1} to each experiment by 2007.

Although single Higgs boson production by gluon fusion, $gg \to H$, has the largest cross section, the more practicable channels are $q\bar{q}' \to HW$ and $q\bar{q} \to HZ$ production since a large fraction of copious QCD background can be suppressed by tagging leptons from the W and Z decays. The most promising final states for Higgs boson with $m_H \lesssim$ 130 GeV decaying mainly to $b\bar{b}$ are: $\ell\nu b\bar{b}$, $\ell^-\ell^+ b\bar{b}$ and $q\bar{q}b\bar{b}$. For $m_H \gtrsim 130$ GeV, the decays $H \to WW$ and $H \to ZZ$ become important. In this case the final states $\ell^+\nu\ell^-\bar{\nu}$, $\ell\nu q\bar{q}'$, $\ell^+\ell^- q\bar{q}$ and $\ell^+\ell^-\ell'^+\ell'^-$ can be exploited to detect the SM Higgs boson. The search sensitivity predicted for a combination of CDF and D0 results is quantified in Figure 11.1. The luminosity of 2 fb^{-1} per experiment will not be sufficient to go far beyond the sensitivity of LEP2. With 10 fb^{-1} the SM Higgs boson can be excluded up to $m_H \sim 180$ GeV and with 20 fb^{-1} evidence at the 3σ level for $m_H \lesssim 180$ GeV is feasible. Sensitivity for 3σ observation of the signal in a wide region of MSSM parameter space requires more than 10 fb^{-1}. The time needed to collect this amount of integrated luminosity will bring TEVATRON to the same time scale of the LHC at CERN. The LHC machine will produce proton-proton collisions at center-of-mass energy of 14 TeV. Four interaction points are foreseen. Two of them will be equipped with general-purpose detectors, ATLAS [112] and CMS [113]. They are designed primarily to search for the SM Higgs boson and new physics beyond the SM. The LHC, most likely starting in 2006, is expected to cover the entire SM and MSSM parameter space. As an example Figure 11.2 illustrates the sensitivity for the SM Higgs boson discovery as a function of m_H assuming integrated luminosity of 30 fb^{-1} for the ATLAS detector [114]. With this

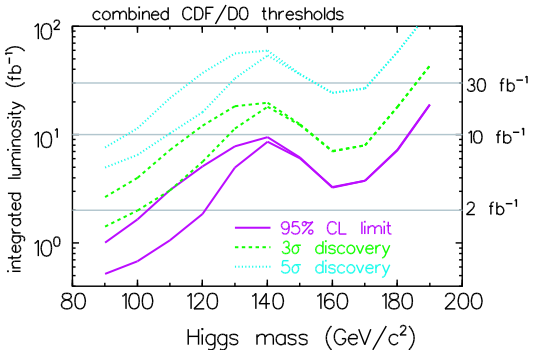

Figure 11.1: The sensitivity of the SM Higgs searches predicted for a combination of CDF and D0 results as a function of the Higgs boson mass and integrated luminosity delivered per experiment. Limits at 95 % C.L. (solid lines), 3σ evidence (dashed lines) and 5σ discovery (dotted lines) curves are plotted for cut-based (upper lines) and neural network (lower lines) analyses.

amount of luminosity, the mass range up to 1 TeV can be explored and in most areas with more than one channel. Due to a large QCD background inclusive Higgs boson production followed by the $H \to b\bar{b}$ and $H \to \tau^+\tau^-$ decays cannot be exploited to look for the SM Higgs boson at $m_H \lesssim 130$ GeV. The most favourable channel in this mass range will be the decay of the Higgs boson into a pair of photons. Although this channel is suppressed by the small branching ratio of the order of 10^{-3}, the natural width of the Higgs boson with $m_H \lesssim 130$ GeV is extremely narrow and it is possible to detect this channel over the enormous diphoton background as a narrow peak in the diphoton mass spectrum. Efficient photon identification and excellent performance of the electromagnetic calorimeter are crucial for this discovery mode. The associated production $t\bar{t}H$ followed by $H \to b\bar{b}$ can be also exploited at $m_H \lesssim 130$ GeV. The $H \to WW \to 2\ell 2\nu$ and $H \to ZZ \to 4\ell$ final states offer sensitivity over almost the full mass range. For very large masses, $m_H \gtrsim 500$ GeV, the search will be complemented with the $H \to ZZ \to \ell\ell\nu\nu$ and $H \to WW \to \ell\nu q\bar{q}'$ channels. In the MSSM, the entire parameter space can be covered with 30 fb^{-1} per experiment [115]. In many areas, several Higgs bosons and decay modes will be available. A large part of the parameter space can be explored already with 10 fb^{-1} per experiment. The measurements of moderate precision are possible in the Higgs sector and can constrain the other parameters of the SUSY model.

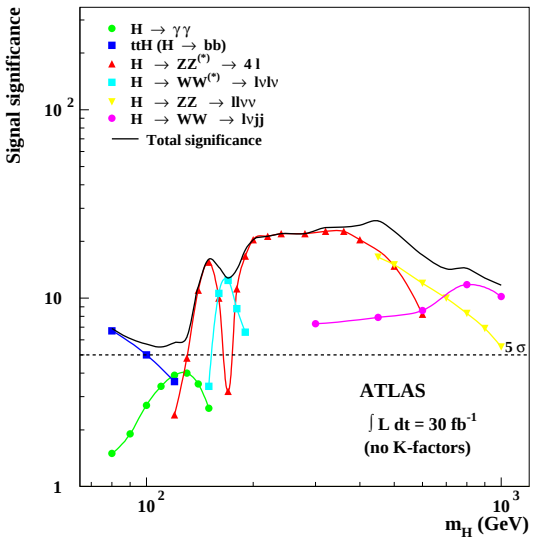

Figure 11.2: Sensitivity for the discovery of the SM Higgs boson with the ATLAS experiment as a function of m_H. The statistical significance of the signal is plotted for individual channels and for their combination assuming an integrated luminosity of 30 fb^{-1}.

Chapter 12

Higgs Physics at TESLA

Once Higgs bosons are discovered, a Linear e^+e^- Collider will be the most suitable device to study the properties of Higgs bosons. The TESLA project [19] recently worked out at DESY aims to design and built a superconducting linear e^+e^- collider operated at center-of-mass energy of 500 GeV extendable to 800 GeV, and a corresponding detector. In this chapter I discuss the potential of the TESLA experimental facility for determination of the Higgs boson profile.

12.1 TESLA Collider and Detector

Except for the Stanford Linear Collider (SLC), electron-positron colliders have so far been constructed as storage rings. This concept, however, is not suitable for reaching high collision energies, as electrons radiate electromagnetic energy when forced on a circular path. The energy loss of the accelerated electrons per turn due to synchrotron radiation is $\Delta E \simeq {E_b}^4/R$, where E_b is the beam energy and R the radius of the accelerator. At the highest LEP energies these losses reached with about 3 GeV per turn the limit of the RF power. Therefore, the only way to reach electron energies substantially above 100 GeV, is to accelerate them on a straight line. The main problems here are the high gradient of the acceleration cavities, in order to get the required energy with a technically reasonable length of the accelerator, and the luminosity. Electron and positron beams are brought into collision only once, hence the permanent regeneration of new beam particles is necessary to allow for high beam intensities. The advantages of the e^+e^- collider, in comparison to a proton machine, are the well defined initial state and the possibility to tune both $\sqrt{s}$ and the polarisation of electrons and positrons very precisely. Furthermore, also e^- e^-, $e^-\gamma$ and $\gamma\gamma$ scattering are options to extend the physics potential. A sketch of the TESLA linear collider is shown in Figure 12.1. The accelerator is foreseen to be built starting from DESY site in Hamburg in north-west direction. The total length will be about 30 km. The central part of the accelerator tunnel will be occupied with a detector designed to study e^+e^- annihilations.

The structure of the detector, of which a quadrant is shown in Figure 12.2, is very similar to that of LEP detectors.

The e^+e^- interaction region will be surrounded by a central tracker comprising a silicon tracker (VTX/SIT) as the innermost part and Time Projection Chamber (TPC). In radial direction follow electromagnetic (ECAL) and hadron (HCAL) calorimeters designed to measure energy and angles of electromagnetic particles and jets. All these subdetectors will be placed inside a superconducting solenoidal magnet of 3 T. A much better performance in comparison with LEP detectors is anticipated. The envisaged

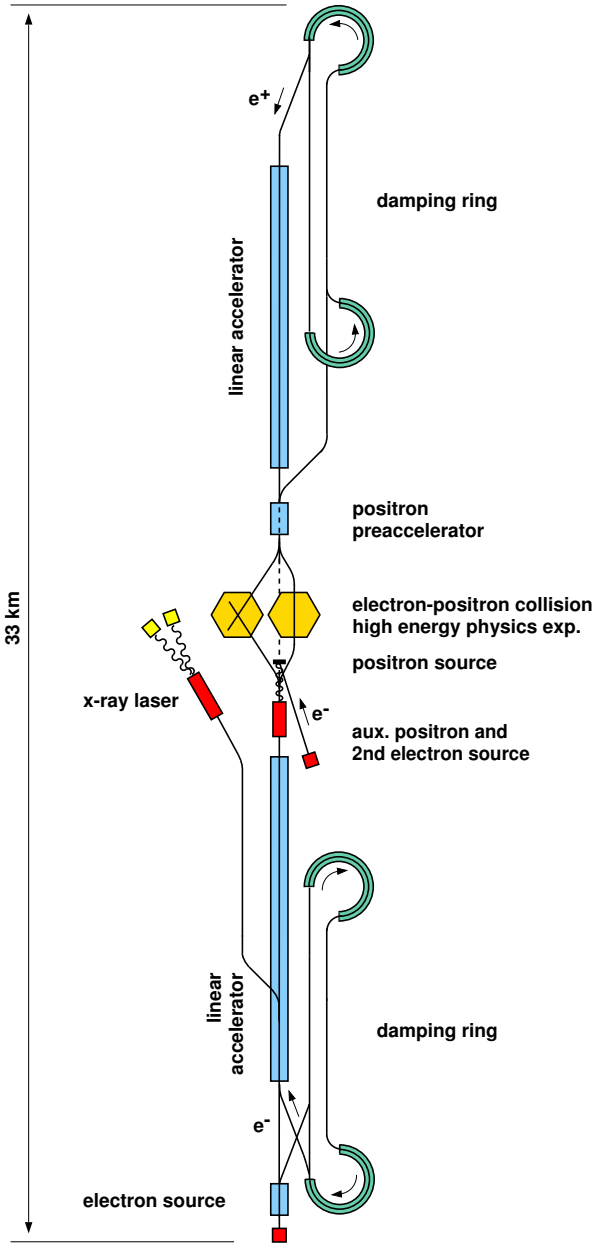

Figure 12.1: The layout of the TESLA linear collider at DESY.

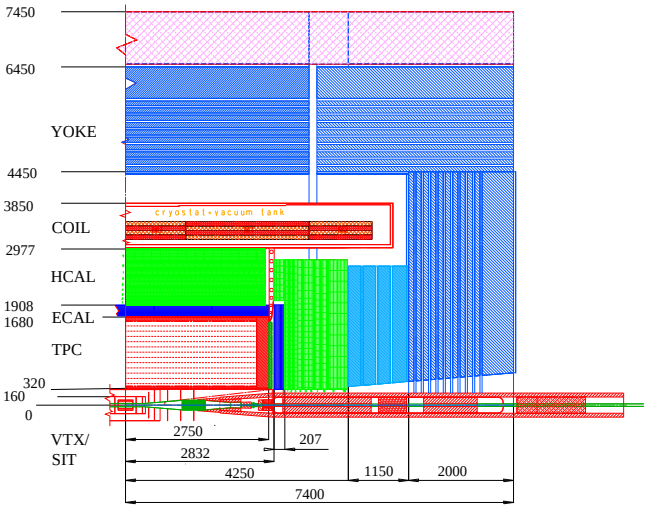

Figure 12.2: View of one quadrant of the TESLA detector. Dimensions are in mm.

momentum resolution is

$$\frac{\sigma_{p_t}}{p_t} = 4 \cdot 10^{-5} \cdot p_t \text{ [GeV]}, \tag{12.1}$$

the impact parameter resolution $\sigma = 2.9 \oplus \frac{3.9}{p \cdot sin^{3/2}\theta} \mu$m, the resolution of the energy measurement in the electromagnetic and hadron calorimeters

$$\frac{\sigma_{E_{el}}}{E_{el}} = \frac{11\%}{\sqrt{E_{el}}} + 0.6\ \%, \tag{12.2}$$

$$\frac{\sigma_{E_h}}{E_h} = \frac{35\%}{\sqrt{E_h}} + 3\ \%. \tag{12.3}$$

12.2 Determination of Higgs Boson Properties with TESLA

The study is performed for a linear collider operated at a center-of-mass energy of 350 GeV and an event sample corresponding to an integrated luminosity of 500 fb^{-1}. At the center-of-mass energy considered the dominant process for Higgs boson production in the Standard Model is $e^+e^- \to Z^* \to HZ$. Events of this process, hereafter referred to as signal, are generated using PYTHIA [76] for Higgs boson masses of 120, 150 and 180 GeV. The Z decays into electrons, muons and quarks are considered. For the Higgs boson all decay modes are simulated as expected in the Standard Model. The decay modes into $b\bar{b}$ and WW are investigated in detail. The Standard Model cross sections and the expected numbers of events are given in Table 12.1.

For background estimations events are generated with PYTHIA for the processes $e^+e^- \to (\gamma\gamma) \to e^+e^-f\bar{f}$, $e^+e^- \to f\bar{f}(\gamma)$, $e^+e^- \to W^+W^-$ and $e^+e^- \to ZZ$ and EXCALIBUR [81] for $e^+e^- \to Ze^+e^-$, $e^+e^- \to Z\nu\bar{\nu}$ and $e^+e^- \to We\nu$. The number of events expected in the most important background processes is given in Table 12.2.

Initial state Bremsstrahlung is simulated by PYTHIA. Beamstrahlung is taken into account using the CIRCE program [116].

Decay mode	topology	120 GeV	150 GeV	180 GeV
recoil mass	2ℓ + X	10.8	8.3	6.0
$e^+e^- \to HZ \to q\bar{q}\ell^+\ell^-$	2ℓ + 2-jets	8.1	1.7	0.04
$e^+e^- \to HZ \to b\bar{b}q\bar{q}$	4-jets	80.0	16.8	0.4
$e^+e^- \to HZ \to W^+W^-\ell^+\ell^-$, $W^\pm \to q\bar{q}'$	2ℓ + 4-jets	0.6	2.6	2.6
$e^+e^- \to HZ \to W^+W^-q\bar{q}$, $W^\pm \to q\bar{q}'$	6-jets	6.0	26.5	26.6
$e^+e^- \to HZ \to X$		160.3	123.7	89.0

Table 12.1: The cross section (in fb) times the branching ratio of the signal final states for Higgs boson masses of 120, 150 and 180 GeV as predicted in the Standard Model.

background process	events
$e^+e^- \to (\gamma\gamma) \to e^+e^-f\bar{f}$	2.0×10^9
$e^+e^- \to f\bar{f}(\gamma)$	2.0×10^7
$e^+e^- \to W^+W^-$	7.0×10^6
$e^+e^- \to ZZ$	5.0×10^5

Table 12.2: The number of events expected for several background sources.

Both signal and background events are processed by the detector simulation package SIMDET [117]. The output in terms of reconstructed track momenta and calorimetric cluster energies is used for the forthcoming analyses.

Methods of the measurements

The least model dependent technique for the measurements of the Higgs boson production cross section, $\sigma(HZ)$, is to use the spectrum of the recoil mass against the Z [118]. The Z decays into electrons and muons are well suited for this purpose, albeit the decay branching fractions are small. Furthermore, the recoil mass spectrum yields also a measurement of m_H.

Electrons are identified as energy depositions in the electromagnetic calorimeter whose shape is compatible with the expectation for an electromagnetic shower and with a matched track in the central tracker. The measured track momentum and shower energy must be in agreement within 5% and the shower leakage into the hadron calorimeter must be less than 2 GeV. Muons are tracks pointing to energy depositions in the calorimeters which are consistent with the expectation for a minimum ionising particle. Both electrons and muons must have momenta larger than 10 GeV and fulfil the polar angle cut $|\cos\theta| < 0.9$. To suppress ZZ background the production polar angle of the two lepton system must be $|\cos\theta_{\ell\ell}| < 0.6$.

In the study of the $HZ \to b\bar{b}q\bar{q}$, $HZ \to q\bar{q}\ell^+\ell^-$, $HZ \to W^+W^-q\bar{q}$ and $HZ \to W^+W^-\ell^+\ell^-$ channels a kinematic fit is used to improve mass resolution. Angular and energy resolutions are used as inputs in the routine performing the kinematic fit. They are different for isolated leptons and jets. The resolution functions obtained from Monte Carlo studies are presented in Table 12.3. The kinematic fit is performed using the software package described in Reference [119].

Measured object	$\frac{\sigma_E}{E}$	σ_Θ	σ_ϕ
Lepton	$10^{-4} \cdot E$ [GeV]	1 mrad	$\frac{1 \text{ mrad}}{\sin\Theta}$
Jet	$\frac{20\%}{\sqrt{E \text{ [GeV]}}}$	10 mrad	$\frac{10 \text{ mrad}}{\sin\Theta}$

Table 12.3: Energy and angular resolutions used in kinematic fit. Symbols E, Θ and ϕ denote energy, polar and azimuthal angles, respectively.

For the $HZ \to b\bar{b}q\bar{q}$ final states, the tagging of b quarks essentially improves signal-to-background ratio.

The recoil mass

To measure the cross section of $e^+e^- \to HZ$, the decays of the Z into an electron-positron pair and a pair of muons are exploited. These final states exhibit a clean signature in the detector, hence they are easily selected. The background is suppressed by requiring the invariant mass of the leptons to be consistent within 5 GeV with m_Z.

The spectrum of the recoil mass, m_R, against the Z,

$$m_R^2 = s - 2 \cdot \sqrt{s} \cdot E_Z + m_Z^2 \tag{12.4}$$

is used to detect the Higgs boson and to measure its production cross section. Here E_Z is the energy of the Z boson. The selection efficiencies for the processes $e^+e^- \to ZH \to e^+e^-X$ and $e^+e^- \to ZH \to \mu^+\mu^-X$ are about 50 % nearly independent on m_H. The recoil mass spectra are shown in Figure 12.3 for $m_H = 120$ GeV and 180 GeV. The Higgs signal is visible as a clear mass peak on the top of small and smooth background. The latter is dominated by $e^+e^- \to ZZ$.

The recoil mass spectra are fitted with a superposition of the signal and background distributions. The signal is parametrised with a Gaussian. To account for its asymmetric shape the upper side tail is approximated as the sum of a Gaussian and an exponential function. The fit of the mass has an error of 110 MeV at $m_H = 120$ GeV and 95 MeV at $m_H = 180$ GeV, the accuracy of the cross section measurement is $\Delta\sigma/\sigma = 2.6$ % and 3.8 %, respectively.

The $HZ \to b\bar{b}q\bar{q}$ and $HZ \to q\bar{q}\ell^+\ell^-$ final states

These final states are characterised by two isolated leptons and two jets or four jets. Leptons are identified as described above. Analyses aim to select high multiplicity events balanced in momentum and with full energy deposited in the detector. QCD background, resulting into two-jet and three-jet events, is suppressed by placing a cut

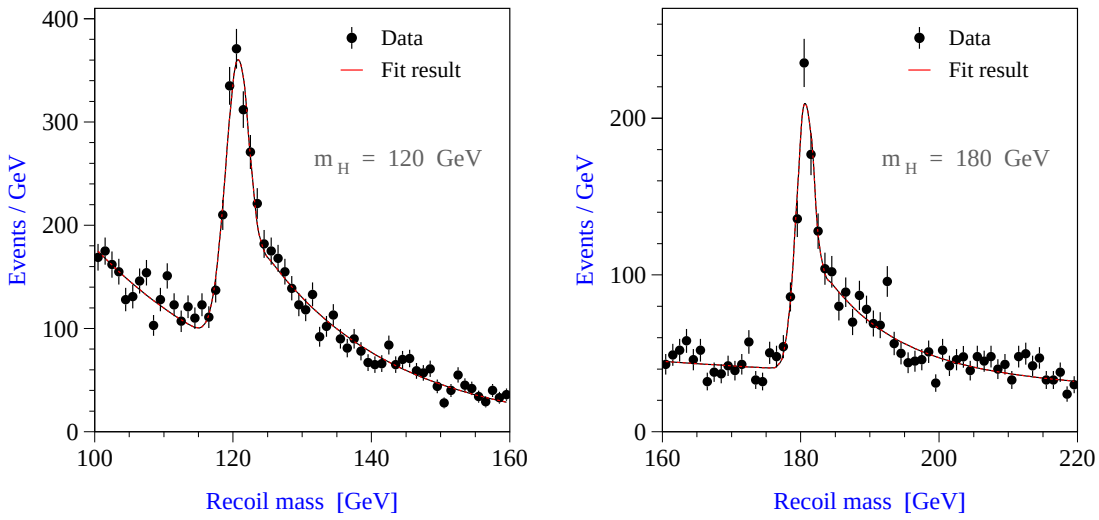

Figure 12.3: The distribution of the recoil mass against Z in selected sample of $e^+e^- \to HZ \to \ell^+\ell^- X, \ell = e, \mu$ events for $m_H = 120$ GeV (left) and $m_H = 180$ GeV (right).

on Y_{34} jet resolution parameter of $Y_{34} > 0.01$. Tracks and calorimetric energy deposits not classified as isolated leptons are then grouped into jets using the Cambridge [120] and Durham jet clustering algorithms. The events are subject of a kinematic fit imposing energy and momentum conservation. In addition, for four-jet final states the invariant mass of the two jets assigned to the Z decay is fixed to m_Z.

For the $HZ \to q\bar{q}\ell^+\ell^-$ channel the dijet invariant mass spectra after the 4C fit are shown in Figure 12.4 for $m_H = 120$ GeV and 150 GeV, respectively. The obtained mass spectra are fitted with the superposition of the signal and background distributions. For the signal a modified Gaussian parametrisation described above is used. The mass obtained from the fit has an error of 70 MeV at $m_H = 120$ GeV and 90 MeV at $m_H = 150$ GeV. The accuracy of the cross section measurement results to $\Delta\sigma/\sigma = 3.0$ % and 4.7 %, respectively.

In the four-jet sample, the signal is enhanced using the event b-tag [121], which quantifies the number of jets, for which a b quark decay is detected. The effect of requiring at least one or two jets tagged as a b quark decay is shown in Figure 12.5. The distribution of the invariant mass of the jets assigned to the Higgs boson after the 5C kinematic fit is shown in Figure 12.6 for $m_H = 120$ GeV accepting only events with at least two jets tagged as b quark decay.

The signal peak is fitted with a Gaussian. The fit of the mass has an error of 45 MeV at $m_H = 120$ GeV and 170 MeV at $m_H = 150$ GeV. The accuracy of the cross section measurement results to $\Delta\sigma/\sigma = 1.1$ % and 3.4 %, respectively.

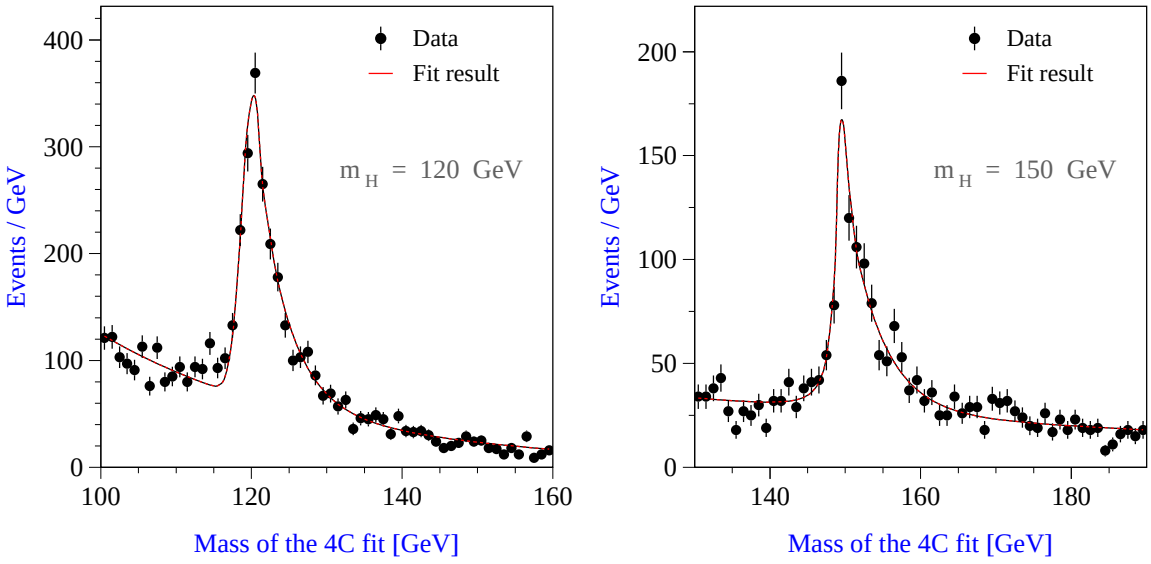

Figure 12.4: The dijet invariant mass from the HZ → $q\bar{q}\ell^+\ell^-$ final state after a 4C kinematic fit for m_H = 120 GeV (left) and 150 GeV (right).

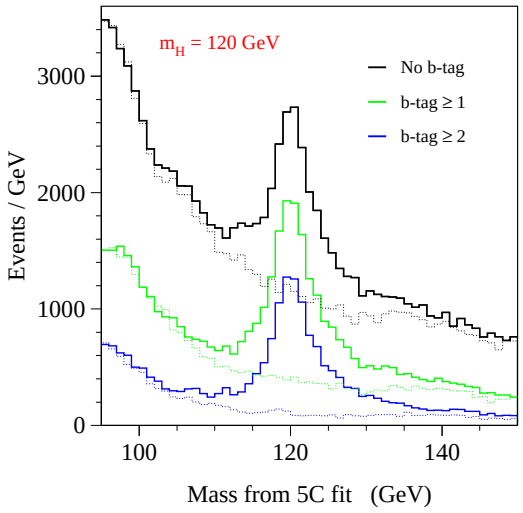

Figure 12.5: The invariant mass of the two jets assigned to the Higgs boson decay in the HZ → $b\bar{b}q\bar{q}$ final state with no requirement on b-tag, at least one jet and at least two jets tagged as b decay.

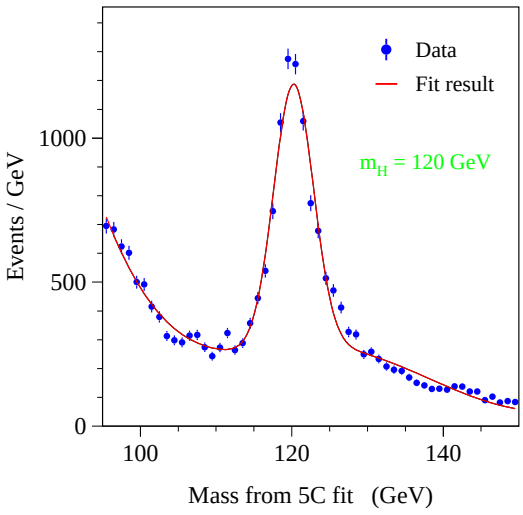

Figure 12.6: The invariant mass of the two jets assigned to the Higgs boson decay in the HZ → $b\bar{b}q\bar{q}$ final state after a 5C kinematic fit for m_H = 120 GeV. At least two jets are required to be tagged as b quark decay.

The HZ → $W^+W^-q\bar{q}$ and HZ → $W^+W^-\ell^+\ell^-$ final states

We consider W-boson decays into two quarks, hence the topologies of these final states are two isolated leptons and four or six jets. The requirements for electron and muon

identification are the same as in the previous sections.

Details of the analysis of these final states are given in Reference [122]. Events of the process $HZ \to W^+W^-\ell^+\ell^-$ are selected by requiring high multiplicity in the tracking device and the calorimeters, the energy deposited in the detector to be greater than 85% of the centre-of-mass energy and two isolated electrons or muons. Furthermore the cuts on global event shape variables thrust and the second Fox-Wolfram moment [76] are used to suppress the dominant background from the semileptonic decays of the Z-pairs. The values of the cuts depend on the Higgs boson mass hypothesis and are more stringent at $m_H = 120$ GeV than at $m_H = 180$ GeV. In the same Higgs boson mass range the selection efficiency for signal events varies from 25% to 72%. The two leptons are expected to stem from the Z. Requiring their invariant mass to be within 10 GeV equal to m_Z the background is suppressed considerably. Tracks and calorimetric energy deposits not stemming from the leptons are grouped into four jets using the Durham algorithm. Then a 4C kinematic fit is performed imposing energy and momentum conservation. The four-jet invariant mass distributions are shown in Figure 12.7 for $m_H = 150$ GeV and $m_H = 180$ GeV, respectively.

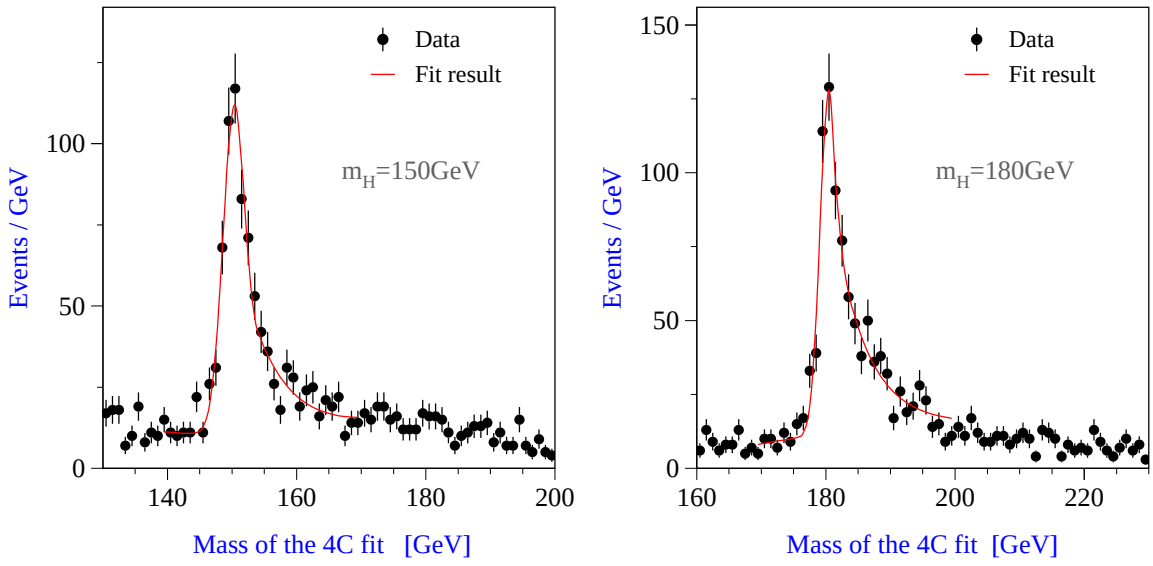

Figure 12.7: The four-jet invariant mass from the $HZ \to W^+W^-\ell^+\ell^-, \ell = e, \mu$ final state after a 4C kinematic fit for $m_H = 150$ GeV (left) and 180 GeV (right).

The signal is fitted using a modified Gaussian parametrisation. The uncertainty of the mass amounts to about 100 MeV for both mass values and the uncertainty of the cross section to 5.2% and 4% for $m_H = 150$ and 180 GeV, respectively.

The six-jet channel is selected first by requiring high-multiplicity events with a total energy deposits in the detector greater than 80% of the centre-of-mass energy. The event thrust must be less than 0.9, there must be no isolated leptons and the logarithm of the Durham jet resolution parameter $\log Y_{56}$ must be larger than -0.8. Then a likelihood discriminant is defined using as input the number of energy-flow objects, the second Fox-Wolfram moment, the event sphericity, the thrust, the jet resolution parameters

Y_{34} and Y_{56}. Depending on the mass of the Higgs boson, events are accepted when the value of this discriminant is larger than a given threshold. The six jets are now grouped in three dijet pairs following criteria which depend on the mass of the Higgs boson. If $m_H < 2m_W$ only one W is expected to be on the mass shell. Therefore the quantity

$$\chi^2 = (m_{ij} - m_Z)^2/\sigma_Z^2 + (m_{kl} - m_W)^2/\sigma_W^2 \tag{12.5}$$

is calculated for all possible dijet combinations, where m_{ij} is the invariant mass of the two jets assigned to the Z and m_{kl} the invariant mass of two jets assigned to a W. The quantities σ_Z^2 and σ_W^2 are the convolution of the bosonic widths and the mass resolutions. They are estimated to be about 4GeV. For $m_H > 2m_W$ both W bosons are on shell. Again all dijet combinations are taken and the quantity

$$\chi^2 = (m_{ij} - m_Z)^2/\sigma_Z^2 + (m_{kl} - m_W)^2/\sigma_W^2 + (m_{mn} - m_W)^2/\sigma_W^2 \tag{12.6}$$

is calculated, where m_{mn} is the mass of the two jets stemming from the second W.

The jet pairing with the smallest value of χ^2 is chosen and subject of a kinematic fit imposing energy-momentum conservation and constraining the mass of the two jets stemming from the Z to m_Z. The selection efficiency for the signal is 4%, 30% and 21% for m_H = 120 GeV, 150 GeV and 180 GeV, respectively. The spectra of the invariant mass of the four-jet system are shown in Figure 12.8 for m_H = 150 GeV, 180 GeV, respectively. From a fit with a Gaussian the uncertainty of the mass is about 100 MeV

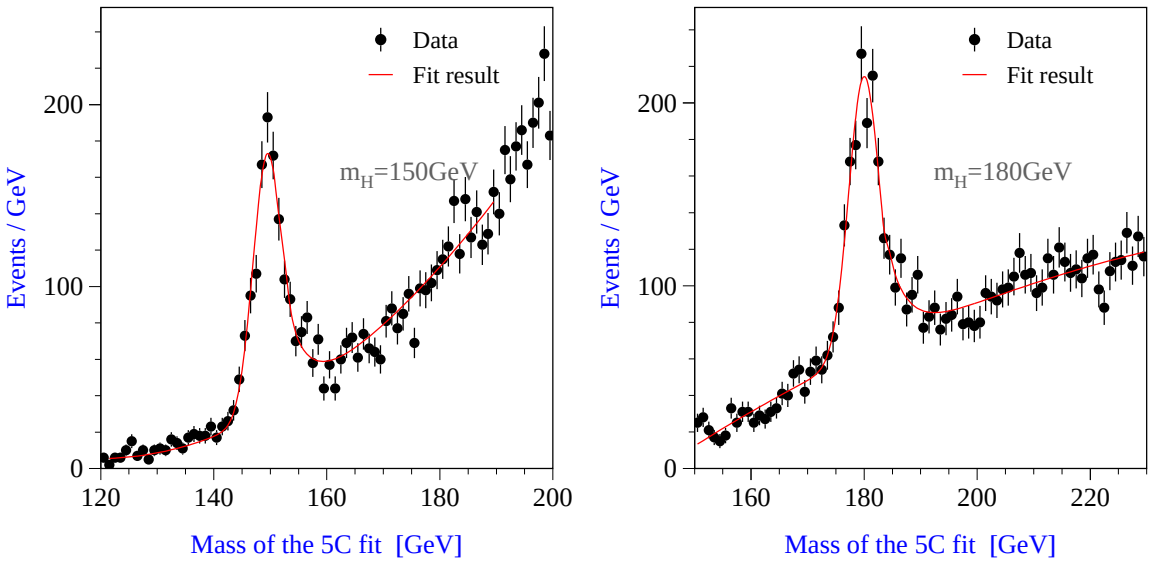

Figure 12.8: The four jet invariant mass from the $HZ \to W^+W^-q\bar{q}$ final state after a 5C kinematic fit for m_H = 150 GeV (left) and m_H = 180 GeV (right).

and of the cross section about 4% for both mass values.

Combined results of mass and cross section measurements

Table 12.4 summarises the accuracy in the determination of m_H for the different final states and their combination, for Higgs boson masses of 120, 150 and 180 GeV. The

relative uncertainties on the topological cross sections are listed in Table 12.5.

	Δm_H in MeV		
Decay mode	120 GeV	150 GeV	180 GeV
$HZ \to Z\ell^+\ell^-, \ell = e, \mu$	110	90	95
$HZ \to q\bar{q}\ell^+\ell^-$	70	90	–
$HZ \to b\bar{b}q\bar{q}$	45	170	–
$HZ \to W^+W^-\ell^+\ell^-$, $W^\pm \to q\bar{q}'$	310	95	100
$HZ \to W^+W^-q\bar{q}$, $W^\pm \to q\bar{q}'$	250	100	110
Combined	$\simeq 40$	$\simeq 50$	$\simeq 70$

Table 12.4: Uncertainties on the determination of m_H for $m_H = 120$, 150 and 180 GeV.

	$\Delta\sigma/\sigma$ in %		
Process	120 GeV	150 GeV	180 GeV
$e^+e^- \to HZ \to X\ell^+\ell^-, \ell = e, \mu$	2.6	3.2	3.8
$e^+e^- \to HZ \to q\bar{q}\ell^+\ell^-$	3.0	4.7	–
$e^+e^- \to HZ \to b\bar{b}q\bar{q}$	1.1	3.4	–
$e^+e^- \to HZ \to W^+W^-\ell^+\ell^-$, $W^\pm \to q\bar{q}'$	13.0	5.2	4.0
$e^+e^- \to HZ \to W^+W^-q\bar{q}$, $W^\pm \to q\bar{q}'$	12.0	4.6	4.4
Combined	$\simeq 1$	$\simeq 2$	$\simeq 3$

Table 12.5: Uncertainties on the cross section for $m_H = 120$, 150 and 180 GeV. The combined uncertainties are obtained by setting branching fractions of the Higgs boson to the values predicted by the SM.

Determination of Higgs boson spin

If a signal is detected as a clear peak in a mass spectrum the measurement of the spin is crucial for its identification as the Higgs boson. It can be performed by analysing the energy dependence of the Higgs boson production cross section just above the kinematic threshold. For a spin zero particle the rise of the cross section is expected to be $\sim \beta$, where β is the velocity of the boson in the centre-of-mass system [1]. For a spin one particle the rise is $\sim \beta^3$ and for spin two like $\sim \beta^5$. With a very small luminosity of about 20 fb^{-1} per energy point the scalar nature of the Higgs boson can be established and other spin hypotheses are disfavoured, as shown in Figure 12.9.

Measurement of Higgs boson width

The width of the Higgs boson, Γ_H, is of several GeV for masses $m_H > 250$ GeV and detector performance allows to measure it directly from the invariant mass spectra. At

[1] There are particular scenarios for s=1 and 2, which show a threshold behaviour similar in shape to the s=0 one. This can be disentangled using angular information in addition.

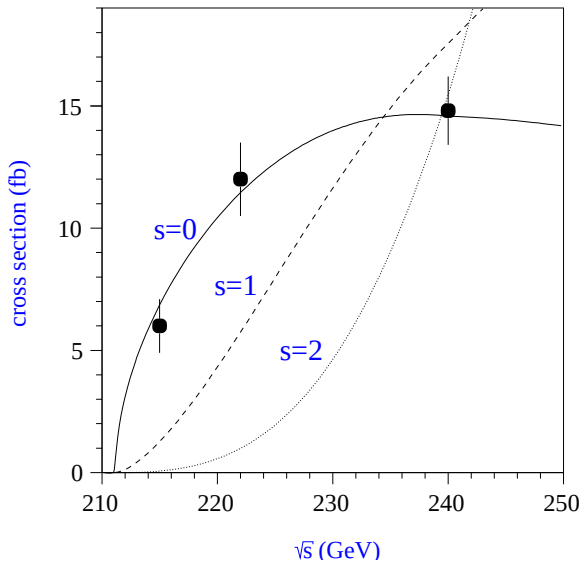

Figure 12.9: The cross section of $e^+e^- \to HZ \to q\bar{q}\ell^+\ell^-$ just above the threshold assuming $m_H = 120$ GeV. The dots correspond to a measurement and the curves are predictions for several spins. Figure is taken from Reference [123].

lower masses, however, the detector resolution is much larger than Γ_H. But using the relation

$$\Gamma_H = \frac{\Gamma(H \to X)}{Br(H \to X)} \tag{12.7}$$

with X = ZZ, WW or $\gamma\gamma$ the width can be determined indirectly. For example, the partial width $\Gamma(H \to \gamma\gamma)$ can be measured with $\gamma\gamma$ collider whereas the branching fraction $Br(H \to \gamma\gamma)$ is accessible in e^+e^- collider from the diphoton invariant mass spectrum. The same procedure can be performed for WW fusion process and $H \to WW$ decay mode. Depending on m_H the accuracy in determination of Γ_H between 4% and 10% can be reached.

Chapter 13

Summary

Searches for the neutral Higgs bosons of various theoretical models were performed in experimentally related channels using the data collected by the L3 detector at LEP. The main conclusion of this thesis is that no evidence for Higgs boson production is found. The data therefore were interpreted in terms of exclusion of the signal.

The SM Higgs boson was searched for in the $HZ \to q\bar{q}q\bar{q}$ channel. Results of this analysis were combined with the $HZ \to q\bar{q}\nu\bar{\nu}$, $HZ \to q\bar{q}\ell^+\ell^-(\ell = e, \mu, \tau)$ and $HZ \to \tau^+\tau^- q\bar{q}$ search channels leading to a 95 % C.L. lower bound on m_H of

$$m_H > 112.0 \text{ GeV}.$$

The search results were also translated into an upper limit on the HZZ coupling as a function of the Higgs boson mass.

In the search for the neutral Higgs bosons predicted by the MSSM, the analyses aimed to search for the $e^+e^- \to hZ$ process are complemented with the investigation of the $hA \to b\bar{b}b\bar{b}$ and $hA \to b\bar{b}\tau^+\tau^-$ topologies. The L3 combined data were used to exclude MSSM parameter regions in three benchmark scenarios. Lower limits on the Higgs boson masses

$$m_h > 84.5 \text{ GeV}, \qquad m_h > 86.3 \text{ GeV}$$

were set at 95 % C.L. for $\tan\beta > 0.7$.

The search for $e^+e^- \to hZ$ process with subsequent decay of h into hadrons was carried out in the $hZ \to q\bar{q}q'\bar{q}'$ channel and then combined with the $hZ \to q\bar{q}\nu\bar{\nu}$ and $hZ \to q\bar{q}\ell^+\ell^-(\ell = e, \mu, \tau)$ channels. Results of these analyses were used to derive an upper limit on the hZZ coupling as a function of m_h assuming $Br(h \to \text{hadrons}) = 100\%$. Setting the hZZ coupling to the value predicted in the SM the lower mass limit

$$m_h > 97 \text{ GeV}$$

is obtained at 95% C.L..

Analyses were elaborated to search exclusively for $e^+e^- \to hA$ production in the $hA \to b\bar{b}b\bar{b}$, $hA \to q\bar{q}q'\bar{q}'$, $hA \to b\bar{b}\tau^+\tau^-$ and $hA \to q\bar{q}\tau^+\tau^-$ channels. Results of these analyses were used to set a limit on the hAZ coupling as a function of Higgs boson masses.

SM Higgs searches					
	ALEPH	DELPHI	L3	OPAL	LEP combined
observed limit $m_H >$	111.5	114.3	112.0	109.7	114.1
expected limit $m_H >$	114.2	113.5	112.4	112.5	115.4
MSSM Higgs searches					
observed limit $m_h >$	89.8	89.7	84.5	79.3	91.0
expected limit $m_h >$	91.3	88.8	87.2	85.1	94.6
observed limit $m_A >$	90.1	90.7	86.3	80.6	91.9
expected limit $m_A >$	91.6	89.7	88.6	86.9	95.0
Flavour independent search for $e^+e^- \to hZ$					
observed limit $m_h >$	109.3	109.6	97	109.4	112.9
expected limit $m_h >$	108.4	108.8	107	108.5	113.0

Table 13.1: The results of the Higgs boson searches from the four LEP collaborations and LEP combined results expressed in terms of 95% C.L. limits on the Higgs boson masses (in GeV). With exception of L3 experiment, results of flavour independent searches are obtained without inclusion of systematic errors.

The searches performed by the four LEP collaborations were combined. No strong indication of the signal was found in the LEP combined data. The results of LEP analyses expressed in terms of limits on Higgs boson masses are summarised in Table 13.1.

The search for Higgs bosons with CDF and D0 detectors at the TEVATRON collider will be one of the main objectives during Run2 data taking period. An observation of Higgs boson signal at 3σ significance level is possible in a wide domain of SM and MSSM parameter space with 20 fb^{-1} of data delivered per experiment. However, with the ultimate integrated luminosity foreseen in Run2 it will be difficult to make a 5σ discovery. The searches for Higgs bosons will be continued at the LHC at CERN. The LHC will provide the sensitivity for the detection of Higgs bosons over the entire range of SM and MSSM parameter space and in most areas with several search channels.

Once Higgs bosons are found, a Linear e^+e^- Collider will be an ideal machine for detailed studies of their properties. The potential of the TESLA detector foreseen at TESLA collider for determination of Higgs boson profile is investigated. The measurement of Higgs boson mass with accuracy of 40 MeV - 70 MeV for m_H ranging from 120 GeV to 180 GeV is possible with integrated luminosity of about 500 fb^{-1}. The method for model independent determination of $e^+e^- \to HZ$ cross section was proposed which is based on the measurement of inclusive $HZ \to X\ell^+\ell^-(\ell = e, \mu)$ final states. It was shown that cross section can be measured with the relative accuracy of 2.6% - 3.8% depending on m_H. The four-fermion and six-fermion final states resulting from the $e^+e^- \to HZ$ were studied. We demonstrated that the measurements of topological cross sections are feasible with relative error ranging from 1% for the $HZ \to b\bar{b}q\bar{q}$ channel at $m_H = 120$ GeV to 13% for the $HZ \to W^+W^-\ell^+\ell^-(\ell = e, \mu; W \to q\bar{q}')$ channel at $m_H = 120$ GeV.

The author of this thesis is sure that much interesting physics will be done with forthcoming challenging experiments. History of physics however teaches us that Nature is much reacher than human imagination and possibly along with anticipated and foreseen

discoveries in the field of particle physics many surprises and unexpected observations are awaiting us in the future.

Bibliography

[1] S. L. Glashow, Nucl. Phys. **22** (1961) 579.

[2] S. Weinberg, Phys. Rev. Lett. **19** (1967) 1264.

[3] A. Salam, in Elementary Particle Theory, ed. N. Svartholm, (Almqvist and Wiksell, Stockholm, 1968), p. 367.

[4] The UA1 Collaboration, G. Arnison *et al.*, Phys. Lett. **B 122** (1983) 103.

[5] The UA1 Collaboration, G. Arnison *et al.*, Phys. Lett. **B 126** (1983) 398.

[6] The TASSO Collaboration, R. Brandelik *et al.*, Phys. Lett. **B 97** (1980) 453.

[7] The CDF Collaboration, F. Abe *et al.*, Phys. Rev. Lett. **74** (1995) 2626.

[8] The Super-Kamiokande Collaboration, Y. Fukuda *et al.*, Phys. Rev. Lett. **81** (1998) 1562.

[9] P. W. Higgs, Phys. Lett. **12** (1964) 132.

[10] P. W. Higgs, Phys. Rev. Lett. **13** (1964) 508.

[11] P. W. Higgs, Phys. Rev. **145** (1966) 1156.

[12] S. Dawson, J.F. Gunion, H.E. Haber and G.L. Kane, "The Physics of the Higgs Bosons: Higgs Hunter's Guide", (Addison Wesley, Menlo Park, 1989).

[13] S. Weinberg, Phys. Rev. **D 13** (1976).

[14] L. Susskind, Phys. Rev. **D 20** (1979).

[15] H. E. Haber and M. Schmitt, Eur. Phys. Jour. **C 3** (1998) 743.

[16] H.P. Nilles, Phys. Rep. **110** (1984) 1.

[17] H. E. Haber and G. L. Kane, Phys. Rep. **117** (1985) 75.

[18] R. Barbieri, Riv. Nuovo Cim. **11 n°4** (1988) 1.

[19] "The Superconducting Electron-Positron Linear Collider with an Integrated X-Ray Laser Laboratory", Technical Design Report", 2001, DESY 2001-11, ECFA 2001-209, TESLA Report 2001-23, TESLA-FEL 2001-05.

[20] M. Kobayashi and T. Maskawa, Prog. Theor. Phys. **49** (1973) 652.

[21] N. Cabibbo, Phys. Rev. Lett. **10** (1963) 531.

[22] G.L. Kane, "Modern Elementary Particle Physics", (Addison Wesley Publishing Company Inc., Menlo Park, 1987).

[23] J.F. Gunion, R. Vega and J. Wudka, Phys. Rev. **D 42** (1990) 1673.

[24] V. Barger, J.L. Hewett and R.J.N. Phillips, Phys. Rev. **D 41** (1990) 3421.

[25] S. Glashow and S. Weinberg, Phys. Rev. **D 15** (1977) 1958.

[26] H. Georgi, Hadronic J. **1** (1978) 155.

[27] S. Dawson, J.F. Gunion, H.E. Haber and G.L. Kane, "The Physics of the Higgs Bosons: Higgs Hunter's Guide", p. 307, (Addison Wesley, Menlo Park, 1989).

[28] F. Wilczek, Phys. Rev. Lett. **40** (1978) 279.

[29] K. Inoue *et al.*, Prog. Theor. Phys. **68** (1982) 927.

[30] H. Georgi and S.L. Glashow, Phys. Rev. Lett. **32** (1974) 438.

[31] H. Georgi, H. Quinn and S. Weinberg, Phys. Rev. Lett. **33** (1974) 451.

[32] R. Haag, J. Lopuszanski and M. Sohnius, Nucl. Phys. **B 88** (1975) 257.

[33] J. Wess and J. Bagger, "Supersymmetry and Supergravity", (Princton University press, 2nd edition, 1991).

[34] P. Fayetm and S. Ferrara, Phys. Rep. **32** (1977) 251.

[35] S. Weinberg, "The quantum theory of fields", volume II, chapter 22, (Cambridge University Press, 1996).

[36] A.H. Chamseddine, R. Arnowitt, P. Nath, Phys. Rev. Lett. **49** (1982) 970
L.J. Hall, J. Lykken, S. Weinberg, Phys. Rev. **D 27** (1983) 2359
M. Dine, A. Nelson, Y. Shirman, Phys. Rev. **D 48** (1993) 1277
M. Dine *et al.*, Phys. Rev. **D 53** (1996) 2658.

[37] L. Ibanez and G.G. Ross, Phys. Lett. **B 110** (1982) 215.

[38] M.Carena, M.Quiros and C.E.M. Wagner, Nucl. Phys. **B 461** (1996) 407.

[39] S.Heinememeyer, W.Hollik and G. Weiglein, Eur. Phys. Jour. **C 9** (1999) 343.

[40] M.Carena, S.Heinemeyer, C.E.M. Wagner and G. Weiglein, CERN-TH-99-374, DESY-99-186, Dec 1999. 10pp., Contribution to Workshop on New Theoretical Developments for Higgs Physics, Geneva, Switzerland, 27 Oct 1999.

[41] S.Heinememeyer, W.Hollik and G. Weiglein, Phys. Rev. **D 58** (1998) 091701.

[42] S.Heinememeyer, W.Hollik and G. Weiglein, Phys. Lett. **B 440** (1998) 296.

[43] D.E. Groom *et al.*, Eur. Phys. Jour. **C 15** (2000) 1, available om the PDG WWW pages (http://pdg.lbl.gov).

[44] G. Altarelli, T. Sjöstrand, F. Zwirner, *Physics at LEP2*, CERN 96-01, Vol. 1.

[45] L. Resnick, M.K. Sundaresan and P.J.S. Watson, Phys. Rev. **D 8** (1973) 172.

[46] E. Braaten, J. P. Leveille, Phys. Rev. **D 22** (1980) 715;
N. Sakai, Phys. Rev. **D 22** (1980) 2220;
T. Inami, T. Kubota, Nucl. Phys. **B 179** (1981) 171;
M. Drees, K. Hikasa, Phys. Lett. **B 240** (1990) 455;
S. G. Gorishny, A. L. Kataev, S. A. Larin, L. R. Surguladze, Mod. Phys. Lett. **5** (1990) 2703;
A. L. Kataev, V. T. Kim, Mod. Phys. Lett. **A 9** (1994) 1309;
L. R. Surguladze, Phys. Lett. **B 341** (1994) 61.

[47] S. Narison, Phys. Lett. **B 341** (1994) 61.

[48] M. Carena, S. Mrenna and C.E.M. Wagner, Phys. Rev. **D 60** (1999) 075010.

[49] M. Carena, S.Mrenna, C.E.M. Wagner, CERN-TH/99-203, hep-ph/9907422.

[50] M. Veltmann, Acta Phys. Polon. **B 8** (1977) 75;
B. W. Lee, C. Quigg and H. Thacker, Phys. Rev. **D 16** (1977) 1519;
D. Dicus and V. Mathur, phys. Rev. **D 7** (1972) 3111.

[51] L. Maiani, G. Parisi and R. Petronzio, Nucl. Phys. **B 136** (1978) 115;
R. Dashen and H. Neuberger, Phys. Rev. Lett. **50** (1983) 1897.

[52] U. M. Heller, M. Klomfass, H. Neuberger and P. Vranus, Nucl. Phys. **B 405** (1993) 555;
J. Kuti, L. Lin and Y. Shen, Phys. Rev. Lett. **61** (1988) 678;
M. Gockeler, K. Jansen and T. Neuhaus, Phys. Lett. **B 273** (1991) 450;
U. M. Heller, H. Neuberger and P. Vranas, Phys. Lett. **B283** (1992) 335.

[53] ZFITTER: D. Bardin *et al.*, Comp. Phys. Comm. **133** (2001) 229;
BHM: W. Hollik, Fortschr. Phys. (1990) **38**;
TOPAZ0 Version 4.0i: G. Montagna, O. Nicrosini, G. Passarino, F. Piccini, R. Pittau, Nucl. Phys. **B401** (1993) 3.

[54] M. Steinhauser, Phys. Lett. **B 429** (1998) 158.

[55] The LEP Collaborations ALEPH, DELPHI, L3 and OPAL, the LEP Electroweak Working Group, the SLD Heavy Flavour and Electroweak Groups, CERN-EP/2001-098.

[56] S. Eidelmann and F. Jegerlehner, Z. Phys. **C 67** (1995) 585.

[57] The BES Collaboration, hep-ex/0102003.

[58] A.D. Martin, J. Outhwaite and M.G. Ryskin, Phys. Lett. **B 492** (2000) 69.

[59] The ALEPH Collaboration, R. Barate *et al.*, Phys. Lett. **B 499** (2001) 53.

[60] The DELPHI Collaboration, P. Abreu *et al.*, Preprint CERN-EP/2000-087 (2001), accepted by Eur. Phys. J.

[61] The L3 Collaboration, M. Acciarri *et al.*, Phys. Lett. **B 503** (2001) 21.

[62] The L3 Collaboration, M. Acciarri *et al.*, Phys. Lett. **B 507** (2001) 225.

[63] The OPAL Collaboration, G. Abbiendi *et al.*, Eur. Phys. Jour. **C 12** (2000) 567.

[64] The CDF Collaboration, F. Abe *et al.*, Phys. Rev. Lett. **79** (1997) 3819
The D0 Collaboration, S. Abachi *et al.*, Fermilab-Conf-96/258-E.

[65] The ALEPH Collaboration, Nucl. Inst. Meth. **A 294** (1990) 121.

[66] The DELPHI Collaboration, Nucl. Inst. Meth. **A 303** (1991) 233.

[67] L3 Collaboration, B. Adeva *et al.*, Nucl. Instr. Meth. **A 289** (1990) 35;
J.A. Bakken *et al.*, Nucl. Instr. Meth. **A 275** (1989) 81;
O. Adriani *et al.*, Nucl. Instr. Meth. **A 302** (1991) 53;
B. Adeva *et al.*, Nucl. Instr. Meth. **A 323** (1992) 109;
K. Deiters *et al.*, Nucl. Instr. Meth. **A 323** (1992) 162;
M. Chemarin *et al.*, Nucl. Instr. Meth. **A 349** (1994) 345;
B. Acciari *et al.*, Nucl. Instr. Meth. **A 351** (1994) 300;
G. Basti *et al.*, Nucl. Instr. Meth. **A 374** (1996) 293;
A. Adam *et al.*, Nucl. Instr. Meth. **A 383** (1996) 342.

[68] The OPAL Collaboration, Nucl. Inst. Meth. **A 305** (1991) 275.

[69] A. Adam *et al.*, Nucl. Inst. Meth. **A 344** (1994) 521.

[70] A. Kopp, *Aufbau und Test der elektronischen Auslese der L3 Z-Kammer im Bunch-Train-Regime von LEP*, Diplomarbeit, Humboldt-Universität zu Berlin, 1995.

[71] The L3 Collaboration, O. Adriani *et al.*, Phys. Rep. **236** (1993) 1.

[72] G. Basti *et al.*, Nucl. Inst. Meth. **A 374** (1996) 293.

[73] W. Lustermann, *Das anomale magnetische moment des τ Leptons*, Ph. D. thesis, ETH Zürich (1996), DISS. ETH Nr. 11645.

[74] I. Brock, *et al.*, Nucl. Inst. Meth. **A 381** (1996) 236.

[75] P. Janot, *The HZHA generator* CERN 96-01, 1996, vol. 2, p.309.

[76] T. Sjöstrand, Preprint CERN-TH/93-7112 (1993).

[77] T. Sjöstrand, Comp. Phys. Comm. **82** (1994) 74.

[78] S. Jadach *et al.*, Phys. Lett. **B 449** (1999) 97.

[79] M. Skrzypek *et al.*, Comp. Phys. Comm. **94** (1996) 216.

[80] R. Engel, Z. Phys. **C 66** (1995) 203;
R. Engel and J. Ranft, Phys. Rev. **D 54** (1996) 4244.

[81] R. Kleiss and R. Pittau, Comp. Phys. Comm. **83** (1994) 141;
see also F.A. Berends, R. Kleiss and R. Pittau in "Physics at LEP2", CERN 96-01, Vol. 2, eds. G. Altarelli, T. Sjöstrand and F. Zwirner.

[82] The L3 detector simulation is based on GEANT Version 3.15.
See R. Brun *et al.*, "GEANT 3", CERN DD/EE/84-1 (Revised), September 1987.

[83] H. Fesefeldt, RWTH Aachen Report PITHA 85/02 (1985).

[84] A. Read, "Modified Frequentist Analysis of Search Results (The CLs Method)" in *Workshop on Confidence Limits*, eds. F. James, L.Lyons and Y.Perrin, CERN 2000-05, p. 81.

[85] S. Bethke, *et al.*, Nucl. Phys. **B 370** (1992) 310.

[86] R. Faccini, L3 Internal Note 2044 (1997).

[87] S. Likhoded, W. Lohmann, L3 Internal Note 2664 (2001).

[88] N. J. Kjaer and R. Moller, DELPHI Internal Note 91-17 (1991).

[89] R.M. Barnet *et al.*, Phys. Rev. **D 54** (1996), 1997 off-year partial update for the 1996 edition available on the PDG WWW pages (http://pdg.lbl.gov)
C. Caso *et al.*, Eur. Phys. Jour. **C 3** (1998) 1.

[90] J. Branson, A. Dominguez, I. Fisk and G. Raven, L3 Internal Note 2108 (1997).

[91] L. Lönnblad, C. Peterson and T. Rognvaldsson, Nucl. Phys. **B 349** (1991) 675;
C. Peterson *et al.*, Comp. Phys. Comm. **81** (1994) 185.

[92] The OPAL Collaboration, K. Ackerstaff *et al.*, Eur. Phys. Jour. **C 1** (1998) 425.

[93] T. Aziz, M. Wadhwa, L3 Internal Note 2481 (2000).

[94] A. Kopp, Ph. D. Thesis, DESY-THESIS-2000-009 (2000).

[95] The LEP Energy Working Group Collaboration, A. Blondel *et al.*, Preprint CERN-EP/98-191, CERN-SL/98-073, CERN 1998;
The LEP Energy Working Group Collaboration, A. Blondel *et al.*, Preprint LEP ECAL/97-04, LEP ECAL, 1997;
The LEP Energy Working group Collaboration, A. Blondel *et al.*, Preprint LEP ECAL/98-01, LEP ECAL, 1998;

The LEP Energy Working Group Collaboration, A. Blondel *et al.*, Preprint LEP ECAL/99-01, LEP ECAL, 1999.

[96] B. A. Kniehl, Phys. Rep. **C 240** (1994) 211;
E. Gross, B. A. Kniehl and G. Wolf, Z. Phys. **C 63** (1994) 417, *erratum-ibid* **C 66** (1995) 321.

[97] A. Djouadi *et al.*, Z. Phys. **C 70** (1996) 427.

[98] The ALEPH Collaboration, R. Barate *et al.*, Phys. Lett. **B 447** (1999) 336.

[99] G. Alexander *et al.*, Z. Phys. **C 73** (1997) 189.

[100] W. Lohmann *et al.*, L3 Internal Note 2576 (2000).

[101] The ALEPH Collaboration, R. Barate *et al.*, Phys. Lett. **B 526** (2002) 191.

[102] The L3 Collaboration, P.Achard *et al.*, Phys. Lett. **B 517** (2001) 319.

[103] The L3 Collaboration, P.Achard *et al.*, Phys. Lett. **B 545** (2002) 30.

[104] The DELPHI Collaboration, P. Abreu *et al.*, Phys. Lett. **B 499** (2001) 23.

[105] The OPAL Collaboration, G. Abbiendi *et al.*, Phys. Lett. **B 499** (2001) 38.

[106] The ALEPH, DELPHI, L3 and OPAL Collaborations, the LEP working group for Higgs boson searches, *"Search for the Standard Model Higgs Boson at LEP"*, CERN-EP/2001-055, LHWG Note 2001-05, ALEPH 2001-066 CONF 2001-046, DELPHI 2001-113 CONF 536, L3 Internal Note 2699, OPAL Physics Note PN479, July 11, 2001;
The ALEPH, DELPHI, L3 and OPAL Collaborations, the LEP working group for Higgs boson searches, *"Searches for the Neutral Higgs Bosons of the MSSM: Preliminary Combined Results Using LEP Data Collected at Energies up to 209 GeV"*, LHWG Note 2001-04, ALEPH 2001-057 CONF 2001-037, DELPHI 2001-114 CONF 537, L3 Internal Note 2700, OPAL Technical Note TN699, July 9, 2001;
The ALEPH, DELPHI, L3 and OPAL Collaborations, the LEP working group for Higgs boson searches, *"Flavour Independent Search for Hadronically Decaying Neutral Higgs Bosons at LEP"*, LHWG Note 2001-07, ALEPH 2001-058 CONF 2001-038, DELPHI 2001-118 CONF 541, L3 Internal Note 2703, OPAL Technical Note TN700, July 5, 2001.

[107] The ALEPH Collaboration, R. Barate *et al.*, Phys. Lett. **B 495** (2000) 1.

[108] The OPAL Collaboration, OPAL Physics Note PN426, March 3, 2000.

[109] *"The Run II Handbook"*, http://www-bd.fnal.gov/upgrades/tdr/tdr.html.

[110] *"The CDF II Detector Technical Design Report"*, Fermilab-Pub-96/390-E.

[111] *"The D0 II Upgrade: The Detector and its Physics"*, Fermilab-Pub-96/357-E.

[112] ATLAS Technical Proposal CERN/LHCC/94-43.

[113] CMS Technical Proposal CERN/LHCC/94-38.

[114] ATLAS Detector and Physics Performance Technical Design Report CERN/LHCC 99-15.

[115] K. Lassila-Perini *"Higgs Physics at LHC"* CMS Conference Report, CMS CR 2001/018.

[116] T. Ohl, Comp. Phys. Comm. **94** (1996) 53.

[117] M. Pohl and H.J. Schreiber, SIMDET V3.2, DESY-99-030 (1999).

[118] P. Garcia-Abia and W. Lohmann, EPJdirect **C 2** (2000) 1.

[119] V. Blobel, "Constrained Least Squares and Error Propagation", Hamburg (1997), http://www.desy.de/∼blobel.

[120] Yu.L. Dokshitzer, G.D. Leder, S. Moretti and B.R. Webber, Cavendish-HEP-97/06.

[121] R. Hawkings, LC Note LC-PHSM-2000-021-TESLA (2000).

[122] A. Raspereza, LC Note LC-PHSM-2001-034 (2001).

[123] M. T. Dova, P. Garcia-Abia, W.Lohmann, LC Note LC-PHSM-2001-055 (2001).

Appendix A

Selection of Reference Samples

This section describes the selection of reference samples used to verify the b-tagging performance in the high-energy sample of the year 2000.

Radiative $e^+e^- \to q\bar{q}\gamma$ Events:
This class of events is characterised by high multiplicity and a large longitudinal imbalance due the initial state photon, which escapes in most of the cases undetected through the beam pipe. The events at $\sqrt{s} > 203$ GeV have been selected by requiring at least 5 tracks, 15 calorimetric clusters and the visible energy, E_{vis}, between $0.5\sqrt{s}$ and $0.9\sqrt{s}$. The missing momentum vector along the beam pipe must be at least 50 GeV, but less than $0.7 \cdot E_{vis}$. The visible mass of the event is required to lie within 25 and 120 GeV. In order to suppress two-photon interactions the direction of the event thrust must satisfy $|\cos\Theta_T| \leq 0.85$ and there should be not more than 60 GeV energy deposited in the luminosity monitor.

The $W^+W^- \to q\bar{q}'\ell\nu$ Events:
The signatures of this topology are two hadronic jets, isolated energetic lepton and missing energy. The $W^+W^- \to q\bar{q}'\ell\nu$ events are selected by requiring the number of charged tracks and calorimetric clusters to be greater than 5 and 10, respectively. An event is rejected if the visible energy is less than $0.3\sqrt{s}$. The presence of isolated electron or muon with energy larger than 15 GeV is required. Lepton is considered isolated if the ratio of its energy to the energy deposited in 10^o cone around its momentum is larger than 0.8. The polar angle of the missing momentum vector must fulfil the requirement $|\cos\Theta_{mis}| \leq 0.95$. The invariant mass of the jets must be between 40 GeV and 120 GeV. The invariant mass of leptonic system has to be greater than 40 GeV.

The number of events selected in data and Monte Carlo predictions for the Standard Model processes are summarised in Tables A.1 and A.2 for the $e^+e^- \to q\bar{q}\gamma$ and $W^+W^- \to q\bar{q}'\ell\nu$ samples, respectively.

The $e^+e^- \to q\bar{q}\gamma$ sample	
Data	3343
Monte Carlo prediction	3310
$e^+e^- \to q\bar{q}\gamma$	3150
Purity	95 %

Table A.1: The $e^+e^- \to q\bar{q}\gamma$ reference sample at $\sqrt{s} > 203$ GeV. The number of events selected in data, the Monte Carlo prediction for the SM processes and the purity obtained for this sample.

The $W^+W^- \to q\bar{q}'\ell\nu$ sample	
Data	931
Monte Carlo prediction	925
$W^+W^- \to q\bar{q}'e\nu_e$	412
$W^+W^- \to q\bar{q}'\mu\nu_\mu$	389
$W^+W^- \to q\bar{q}'\tau\nu_\tau$	62
Purity	93 %

Table A.2: The $W^+W^- \to q\bar{q}'\ell\nu$ reference sample at $\sqrt{s} > 203$ GeV. The number of events selected in data, the Monte Carlo prediction for the SM processes and the purity obtained for this sample.

Selbständigkeitserklärung

Hiermit erkläre ich, die vorliegende Arbeit selbständig ohne fremde Hilfe verfaßt und nur die angegebene Literatur und Hilfsmittel verwendet zu haben.

Alexei Raspereza
30. März 2002